Lire
la première partie
de la thèse

5.5 Results for two-phase flow polydisperse case

In this section, the downstream evolution of the air and particulate flow fields at a moderate mass loading ($M_j = 22\%$) for a polydisperse test case is presented and discussed. Numerical results of the AVBP-EL and CDP solvers are compared to experiments. Axial and radial profiles of the gaseous and dispersed phases are presented in Subsections 5.5.1-5.5.3. Subsection 5.5.4 discusses the influence of the number of samples on the axial and radial velocity profiles. Particle-dispersion characteristics are analysed in Subsection 5.5.5, focusing on the dependence of particle trajectories and the slip velocities upon particle sizes.

Figure 5.32 shows the initial particle number distribution used by both solvers at the corresponding injection plane. Levels are quite similar to the experimental ones (see Fig. 5.4 (b)) except for the two smallest classes ($d_p = 20$ and 30 μm) but this is assumed to have minor effects in the simulation due to their negligible contribution to the overall mass distribution (see Fig. 5.4 (a)). Both solvers use the same particle injection parameters in order to make easier the comparison of particles profiles. Note however, that the injection planes are not the same (see Fig. 5.14). For the sake of clarity, only 4 classes are analysed in the following: $d_p = 20, 40, 60$ and 80 μm.

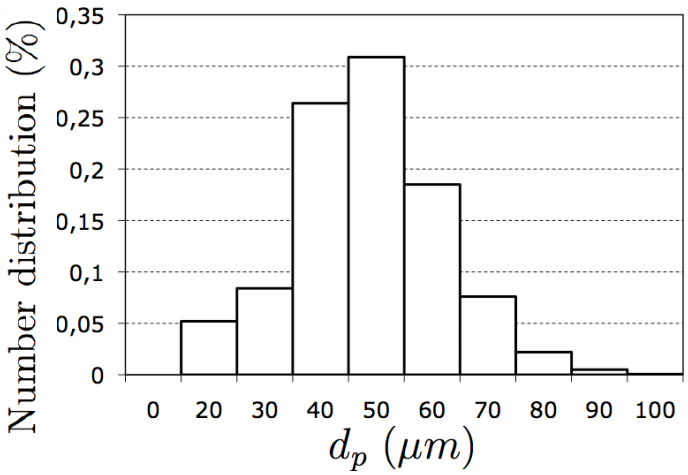

Figure 5.32 - *Initial number distribution of the particle size injected numerically by both solvers.*

5.5.1 Gaseous phase

Figure 5.33 presents the axial evolution of the mean (a) and RMS (b) velocity of the gaseous phase. At first sight, there is a clear similarity between these results and the ones obtained for the LES solvers in the monodisperse case (see Fig. 5.15). The difference observed between AVBP-EL and CDP in the location of the recirculation zone is still the same as in the monodisperse simulation. Again, CDP predicts better its location and the AVBP-EL solver displays a difference in the prediction of the first and second stagnation points located respectively, 40 and 60 mm before the experimental values. As mentioned for the monodisperse calculation, the prediction of stagnation points is a critical issue in bluff-body simulations due to the sensitivity to the ratio between the mean velocity of the inner jet and the coflow. However, an important detail must be highlighted when comparing the monodisperse and the polydisperse simulations: the levels of mean gas velocity

in the recirculation zone are lower than expected (-1 m/s instead of -1.4 m/s for the peaks near $z \approx 180$ mm) with both codes (Fig. 5.33 (a)). This implies a reduction in the size of the recirculation bubble and it has an effect in the axial velocity profiles of the different particle classes (as discussed in the next subsection). It can be observed that the location of the maximum RMS in Fig. 5.33 (b) (first stagnation point) has not changed. The levels of RMS at $z > 180$ mm are lower than the experimental values and lower than the ones obtained for the monodisperse simulation; however, AVBP-EL seems to capture the small variation between 180 mm $< z <$ 280 mm even if the level of turbulence fluctuations is not the same.

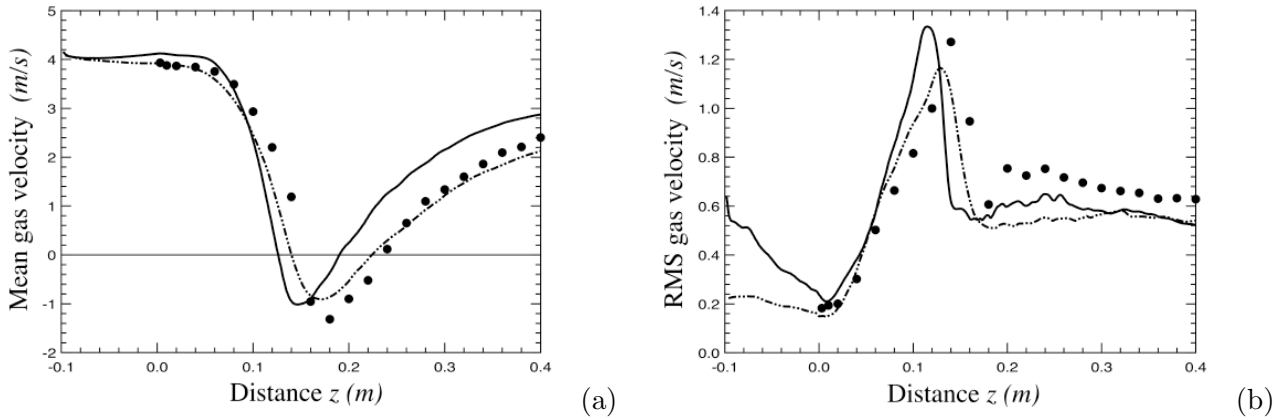

Figure 5.33 - *Axial evolution of mean (a) and RMS (b) gas velocities at $M_j = 22\%$. Symbols: experiment; solid line: AVBP-EL; dot-dashed line: CDP.*

Figs. 5.34-5.37 show the radial profiles of the mean and RMS, axial and radial gas velocities. In Fig. 5.34, the negative values of the mean axial gas velocity profiles at $z = 80$ mm and $z = 160$ mm indicate the location and radial extent of the recirculation zone. The second stagnation point near $z = 240$ mm is visible for the experimental profiles but it is located close to $z = 200$ mm for the AVBP-EL results. Mean radial gas profiles (Fig. 5.36) show only negative values for $z > 160$ mm. This inward flow converges to the centerline where values are close to zero. The reduction of radial velocity values and their convergence indicate also the boundary of the recirculation bubble which is associated to a radial compression. Both solvers have some difficulties to capture the maximum of the negative values in the last four cross-sections, probably due to a lower prediction of pressure values. RMS axial and radial profiles (Figs. 5.35 and 5.37) are similar to the experimental values.

These radial profiles are almost exactly the same as the ones presented in Section 5.4 for the monodisperse case (see Figs. 5.17-5.20). This may lead us to think that considering a monodisperse distribution is sufficient to capture the mean flow effects on the gas for the moderate mass loading. However, they do not reflect the reduction of the recirculation zone observed in Fig. 5.33.

As a technical remark, the averaging time to obtain particle profiles with the AVBP-EL solver in this polydisperse case ($t = 3.89$ s) is almost eight times the one considered for the monodisperse case, $t = 0.4642$ s (see Table 5.2). The number of samples of classes $d_p = 20$ and 80 μm would not be enough for converged statistics if the physical time was equal to the one used in the monodisperse case. To support this statement, results of the radial velocity of mean and RMS axial profiles for three different physical times: $t \approx 0.26$, 1 and 4 s, are presented in Subsection 5.5.4.

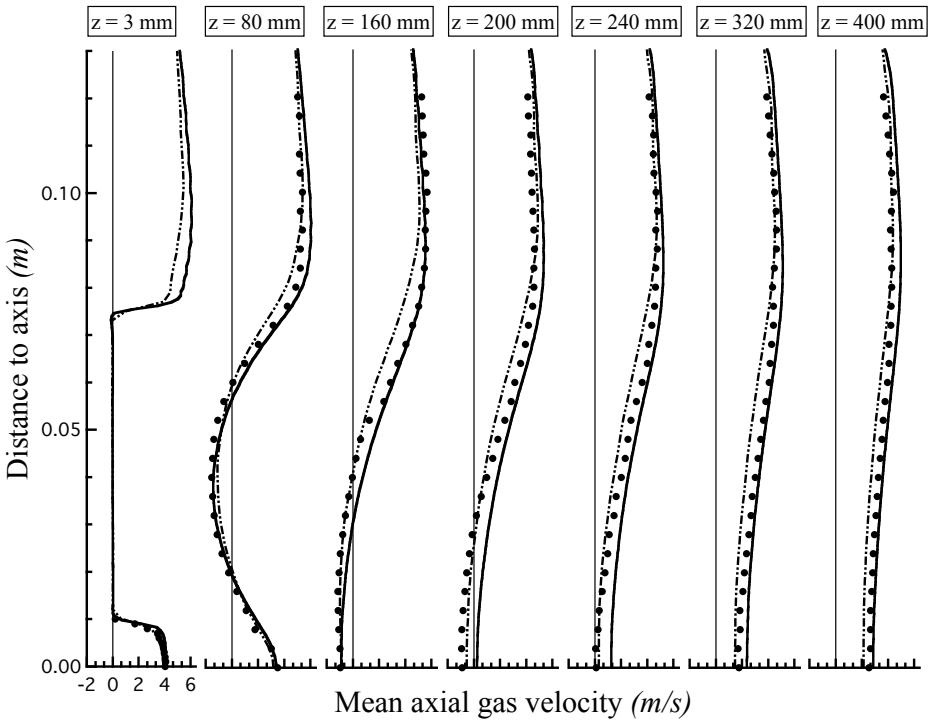

Figure 5.34 - *Radial profiles of mean axial gas velocities at seven stations along z axis at $M_j = 22\%$. Symbols: experiment; solid line: AVBP-EL; dot-dashed line: CDP.*

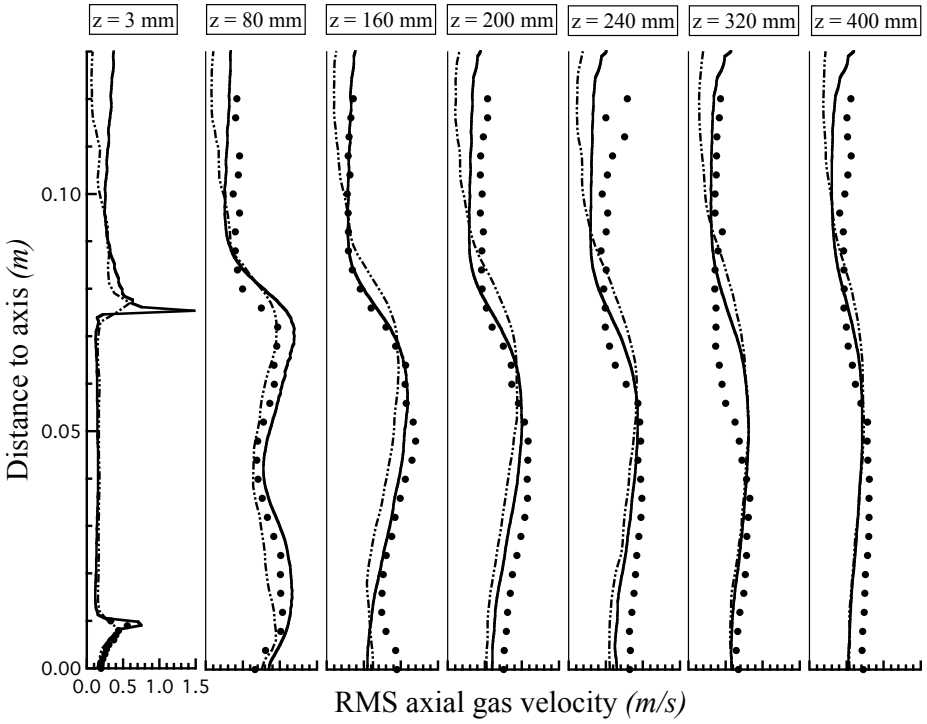

Figure 5.35 - *Radial profiles of RMS axial gas velocities at seven stations along z axis at $M_j = 22\%$. Symbols: experiment; solid line: AVBP-EL; dot-dashed line: CDP.*

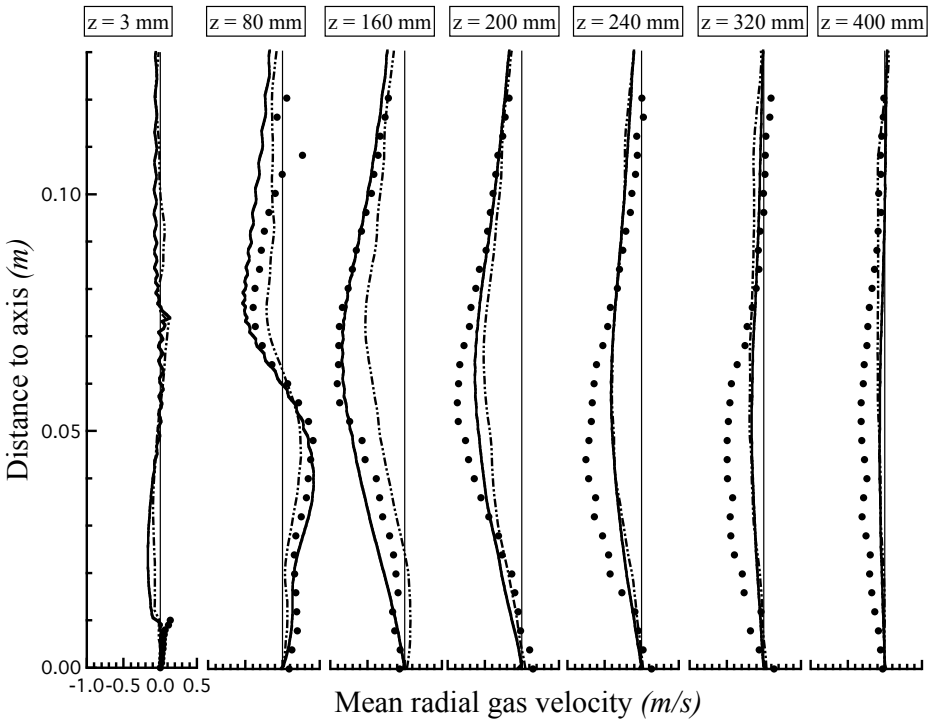

Figure 5.36 - *Radial profiles of mean radial gas velocities at seven stations along z axis at $M_j = 22\%$. Symbols: experiment; solid line: AVBP-EL; dot-dashed line: CDP.*

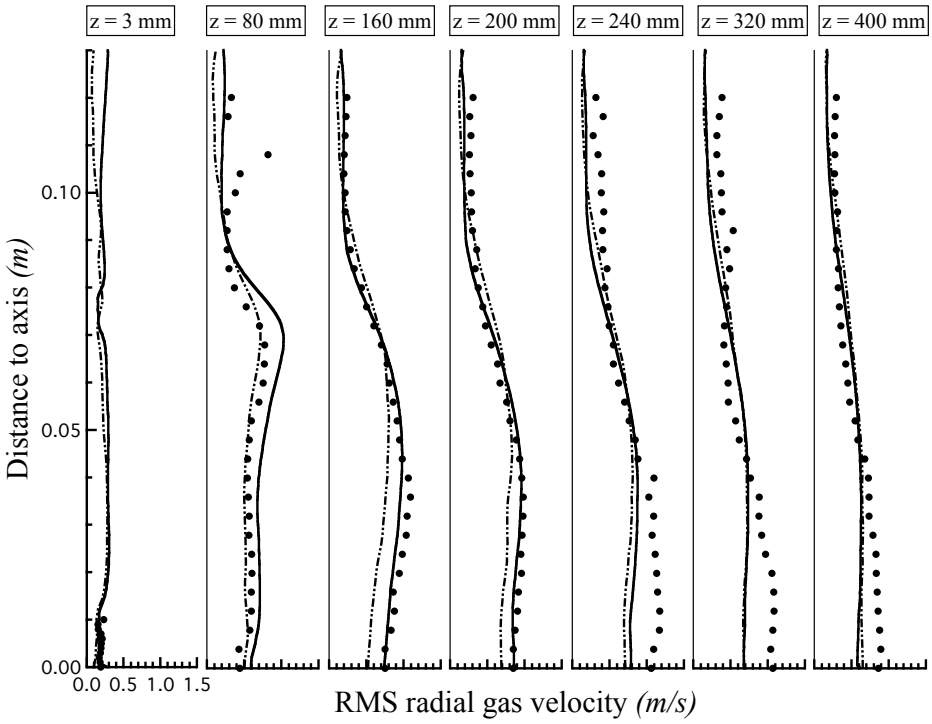

Figure 5.37 - *Radial profiles of RMS radial gas velocities at seven stations along z axis at $M_j = 22\%$. Symbols: experiment; solid line: AVBP-EL; dot-dashed line: CDP.*

5.5.2 Dispersed phase: axial velocity profiles

Regarding the results of the dispersed phase, the motion of the smallest particles with diameter $d_p = 20$ μm is expected to be very different from the largest ones, with diameter $d_p = 80$ μm. While the smallest particles (Fig. 5.38 (a)) almost follow the gas flow (see Fig. 5.33 (a)) the inertia of the largest particles (Fig. 5.41 (a)) decorrelates them from the fluid flow as can be observed in the axial evolution of the mean particle velocities. The reduction in the extent and location of the recirculation zone observed by the particles (near $z = 200$ mm) is evident while comparing Figs. 5.38 (a)-5.41 (a). CDP is able to better capture this recirculation bubble with similar results than the experimental ones, however, the delay in the occurrence of the recirculation zone for the gaseous phase with AVBP-EL (see Fig. 5.33) is still visible in these particle velocity profiles.

Another trace of the different particle inertia effects can be observed near the exit of the inner pipe ($0 < z < 60$ mm) in Figs. 5.38 (b)-5.41 (b). In spite of differences in the injection location (see Fig. 5.14), neither CDP, nor AVBP-EL display the accurate levels of particle fluctuations at the exit of the inner pipe but particle behaviour is the same in both solvers while trying to capture the RMS values in the first millimeters of the jet exit. The smallest particles adapt very quickly to the flow fluctuations, mid-size particles take around 40 mm and the largest ones need more than 60 mm to achieve the same level as the one detected by the experiments.

As mentioned for other graphs of this section, AVBP-EL mean and RMS profiles results look more scattered than CDP profiles (mainly for the classes $d_p = 20$ and 80 μm) due to a lower number of samples. Nevertheless, we emphasize that both solvers present the same differences in the RMS values at $z > 200$ mm where numerical results are 20% lower than experimental ones. Following Borée *et al.* [22], particle velocity fluctuations in this region seems to be controlled by the dragging of large-scale fluid turbulent motion, therefore, the differences observed may be related to an underestimation of these large-eddies effects.

Regarding the differences between the monodisperse and the polydisperse cases, particles with diameter $d_p = 60$ μm show quite similar profiles to the one presented in the monodisperse test case (see Fig. 5.27).

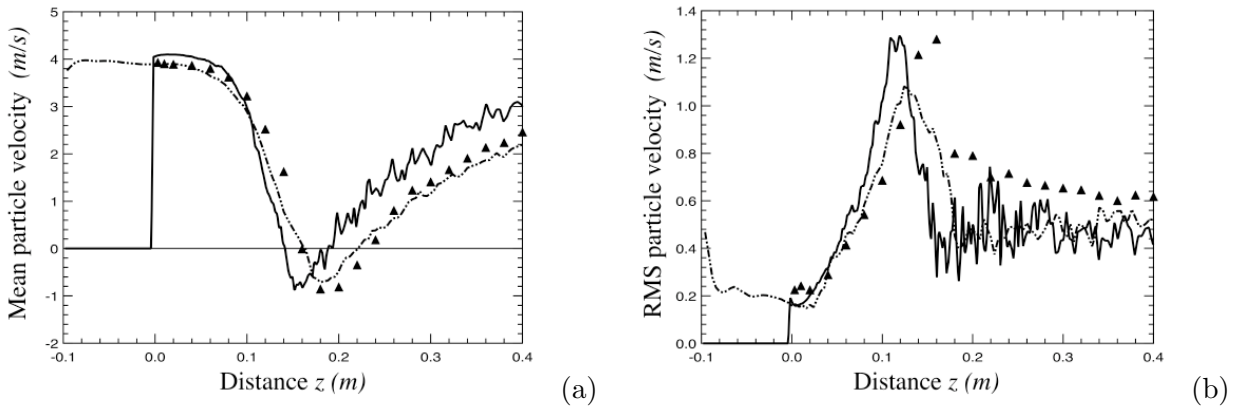

Figure 5.38 - *Axial evolution of mean (a) and RMS (b) particle velocities at $M_j = 22\%$ for $dp = 20$ μm. Symbols: experiment; solid line: AVBP-EL; dot-dashed line: CDP.*

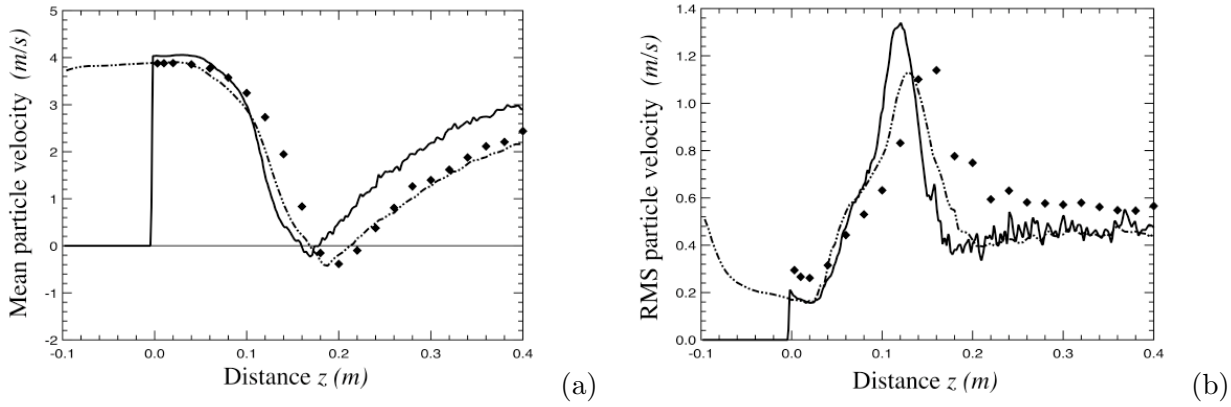

Figure 5.39 - *Axial evolution of mean (a) and RMS (b) particle velocities at $M_j = 22\%$ for $dp = 40$ μm. Symbols: experiment; solid line: AVBP-EL; dot-dashed line: CDP.*

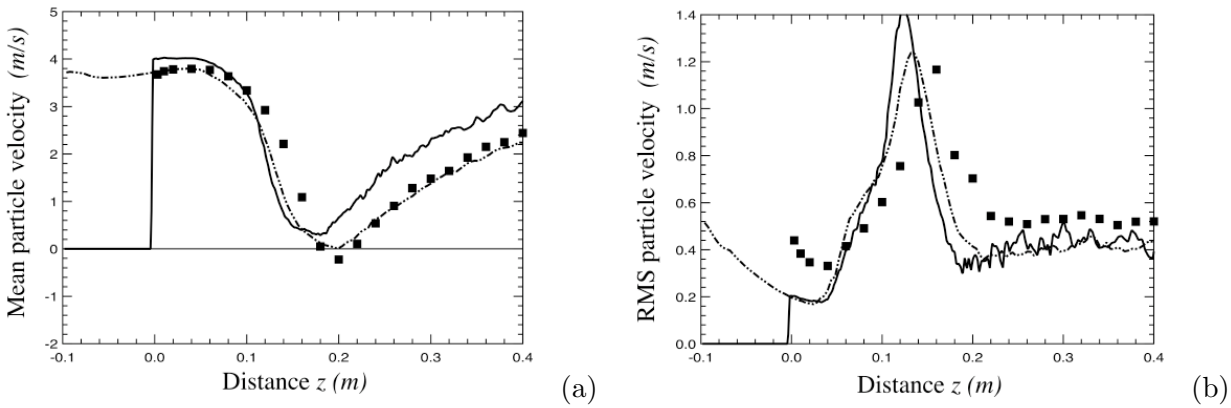

Figure 5.40 - *Axial evolution of mean (a) and RMS (b) particle velocities at $M_j = 22\%$ for $dp = 60$ μm. Symbols: experiment; solid line: AVBP-EL; dot-dashed line: CDP.*

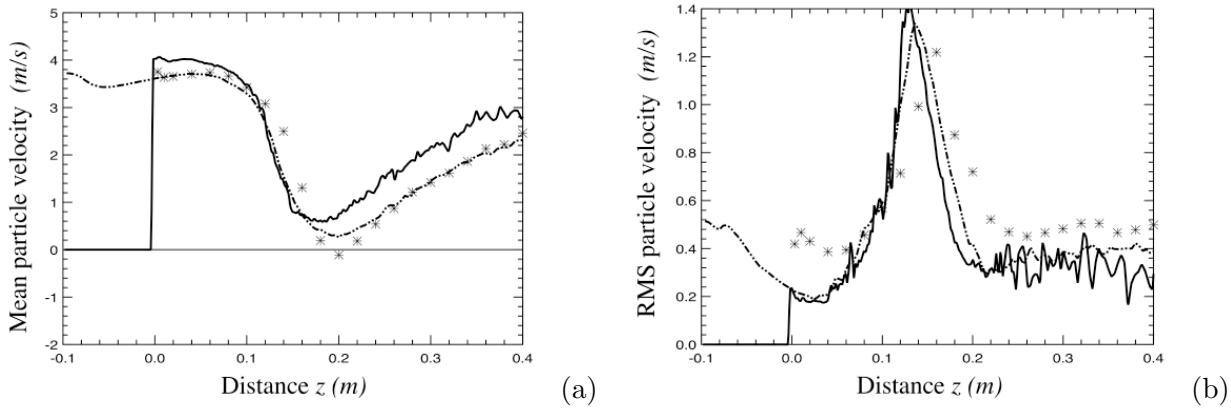

Figure 5.41 - *Axial evolution of mean (a) and RMS (b) particle velocities at $M_j = 22\%$ for $dp = 80$ μm. Symbols: experiment; solid line: AVBP-EL; dot-dashed line: CDP.*

5.5.3 Dispersed phase: radial velocity profiles

In the following subsection, the mean and RMS, axial and radial velocity profiles of the four classes previously mentioned are presented. Again, numerical results obtained with both Lagrangian solvers are compared to experiments.

Figs. 5.42-5.45: $d_p = 20$ μm

Mean axial velocity profiles (Fig. 5.42) of the smallest particle diameter are in good agreement with the experimental ones, with AVBP-EL giving better results at most stations. The lack of numerical samples in the outer region ($r > 80$ mm) is visible in some cross-sections. CDP profiles go farther since the averaging time is three times greater than the AVBP-EL averaging time. This lack of samples is more evident in the RMS axial profiles (Fig. 5.43). It is difficult to capture particles in this region since they are quickly accelerated by the large-scale structured presented in the separated region. Mean radial profiles (Fig. 5.44) of both solvers still underestimate the experimental results as can be expected since these particles behaves almost like the gaseous phase. RMS radial profiles (Fig. 5.45) are also quite similar to the experiments except in the centerline after the second stagnation point like for the gaseous phase.

Figs. 5.46-5.49: $d_p = 40$ μm

Mean axial velocity profiles (Fig. 5.46) are also in good agreement with experiments. The number of samples of the numerical results is greater than for the previous class, covering more experimental data than the smallest particles do. This can also be observed for the RMS results (Fig. 5.47). Results of the radial and RMS particle velocities (Figs. 5.48 and 5.49) are in very good agreement with experimental data and they are lower than for the 20 μm class since 40 μm particles are less controlled by the fluid flow.

Figs. 5.50-5.53: $d_p = 60$ μm

No relevant differences have been observed between these figures and the ones presented in the monodisperse case (see Figs. 5.28-5.31 and comments in Subsection 5.4.2).

Figs. 5.54-5.57: $d_p = 80$ μm

Mean axial velocity profiles (Fig. 5.54) of the largest particle diameter considered here are in good agreement with the experimental data. The lack of numerical samples in the outer region ($r > 70$ mm) is evident but even Borée *et al.* [22] make a reference to the poor statistical converge of large particles to limit duration of data acquisition. Results of the RMS axial particle velocities (Fig. 5.55) show scattered profiles due to this reason. It can be observed that the mean radial particle velocities (Fig. 5.56) are close to zero. This shows that the large particles motion is mainly controlled by the axial velocity component of the bluff-body flow. RMS radial profiles (Fig. 5.57) are also quite similar to the experiments, with highest values mainly on the axis and with some differences after $z > 240$ mm, as stated for the other classes.

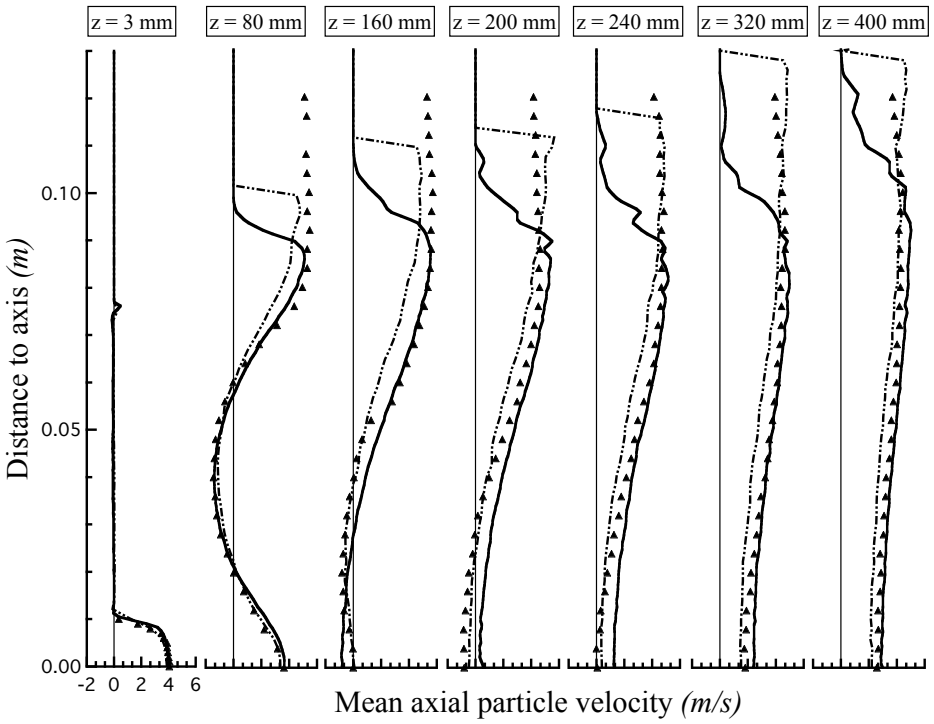

Figure 5.42 - *Radial profiles of mean axial particle velocities at seven stations along z axis at $M_j = 22\%$ for $d_p = 20$ μm. Symbols: experiment; solid line: AVBP-EL; dot-dashed line: CDP.*

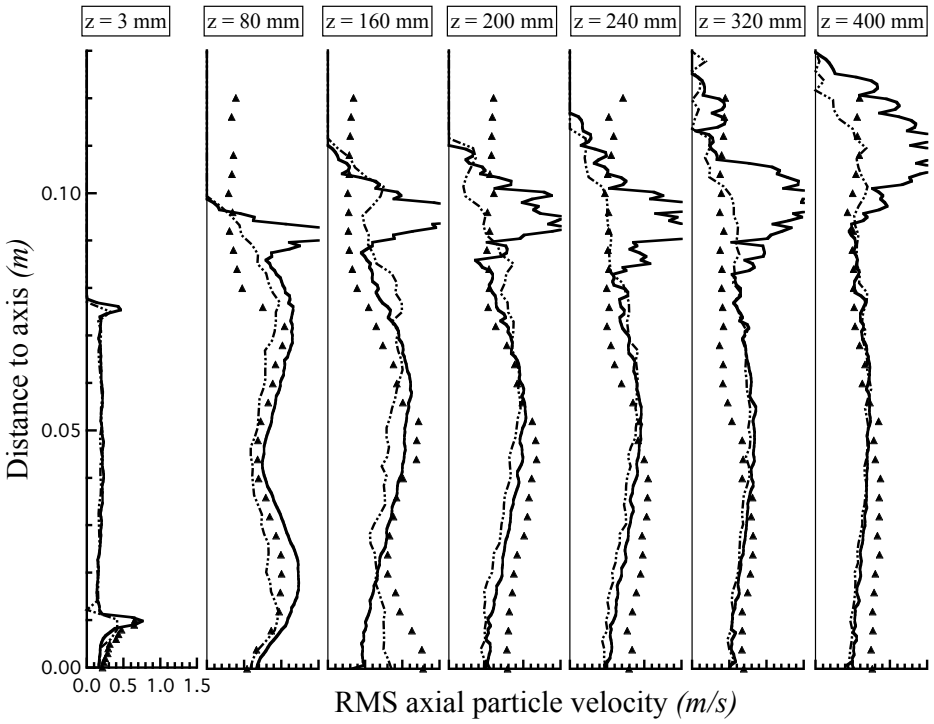

Figure 5.43 - *Radial profiles of RMS axial particle velocities at seven stations along z axis at $M_j = 22\%$ for $d_p = 20$ μm. Symbols: experiment; solid line: AVBP-EL; dot-dashed line: CDP.*

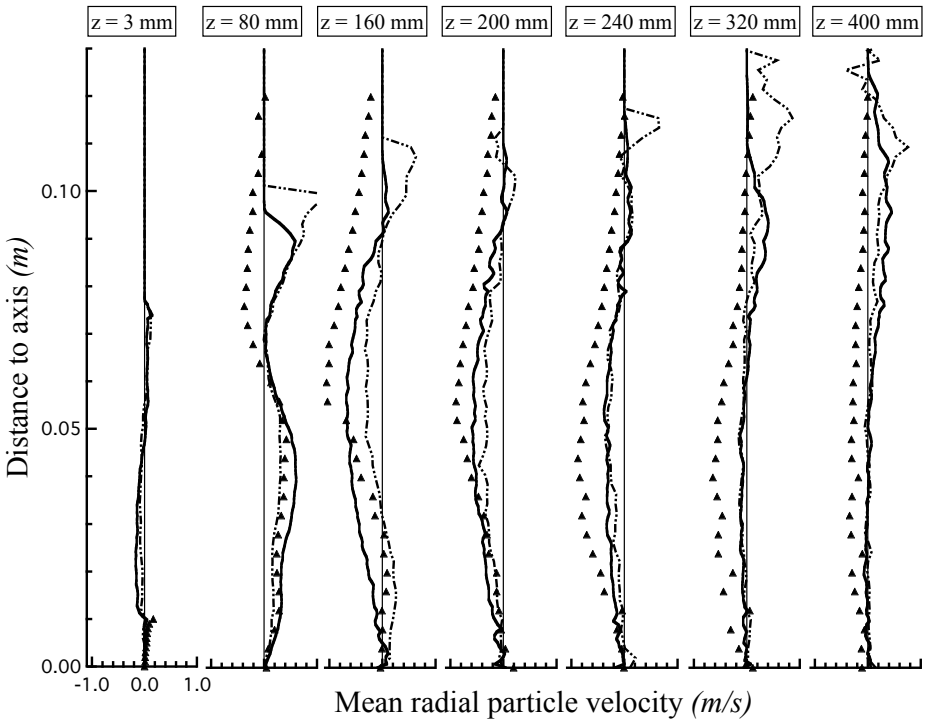

Figure 5.44 - *Radial profiles of mean radial particle velocities at seven stations along z axis at $M_j = 22\%$ for $d_p = 20$ μm. Symbols: experiment; solid line: AVBP-EL; dot-dashed line: CDP.*

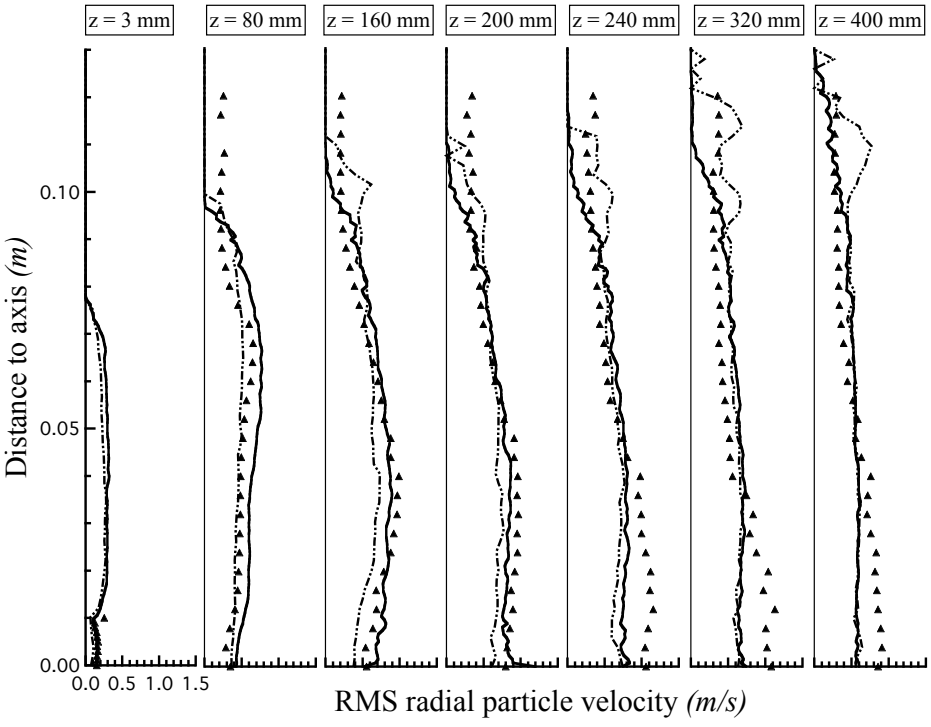

Figure 5.45 - *Radial profiles of RMS radial particle velocities at seven stations along z axis at $M_j = 22\%$ for $d_p = 20$ μm. Symbols: experiment; solid line: AVBP-EL; dot-dashed line: CDP.*

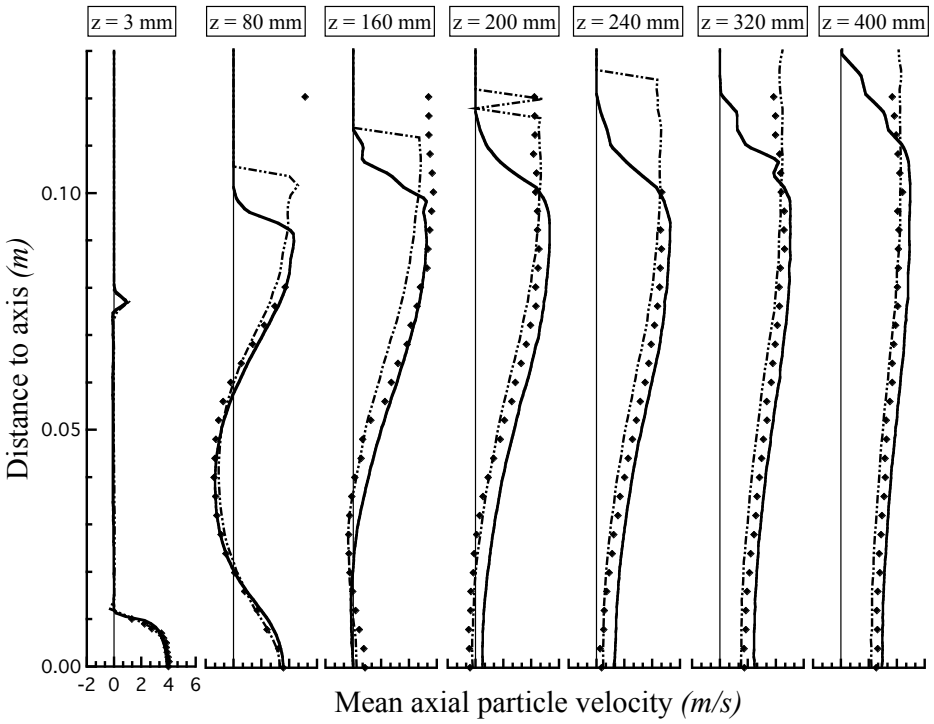

Figure 5.46 - *Radial profiles of mean axial particle velocities at seven stations along z axis at $M_j = 22\%$ for $d_p = 40$ μm. Symbols: experiment; solid line: AVBP-EL; dot-dashed line: CDP.*

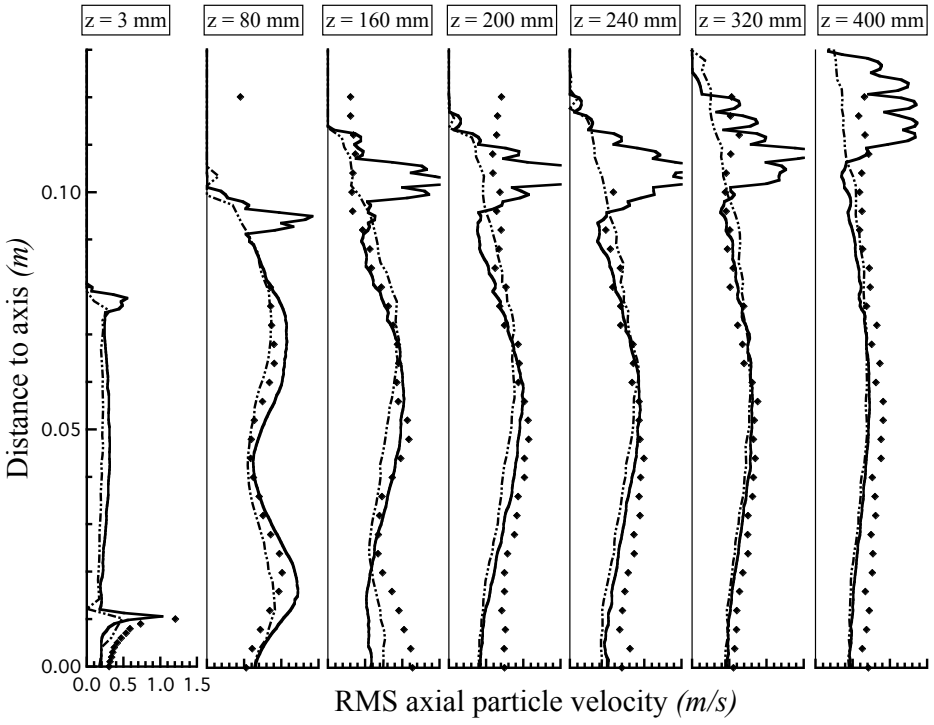

Figure 5.47 - *Radial profiles of RMS axial particle velocities at seven stations along z axis at $M_j = 22\%$ for $d_p = 40$ μm. Symbols: experiment; solid line: AVBP-EL; dot-dashed line: CDP.*

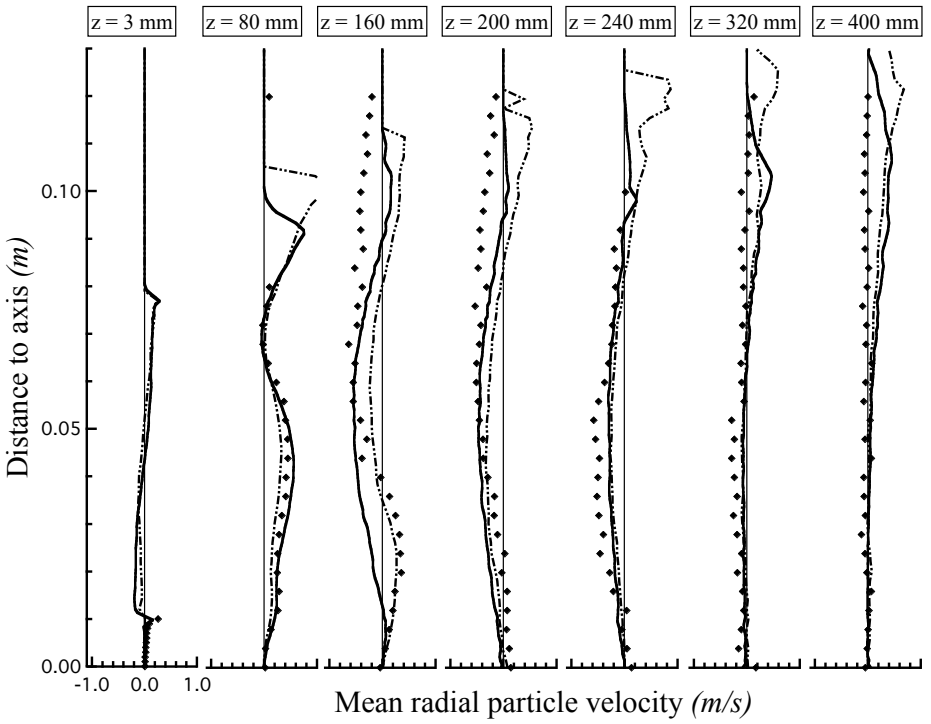

Figure 5.48 - *Radial profiles of mean radial particle velocities at seven stations along z axis at $M_j = 22\%$ for $d_p = 40$ μm. Symbols: experiment; solid line: AVBP-EL; dot-dashed line: CDP.*

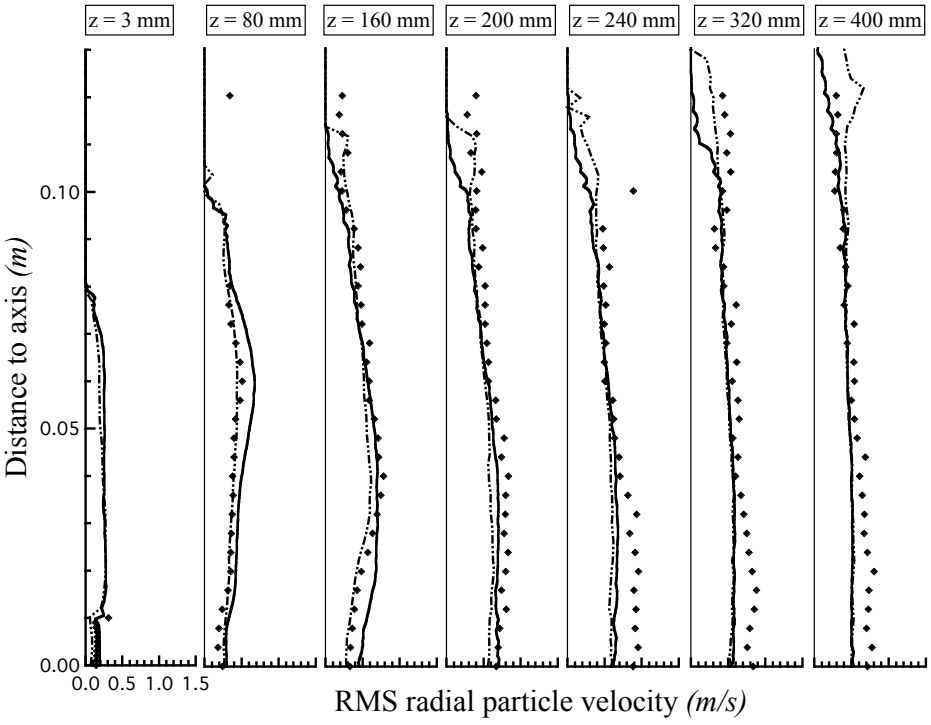

Figure 5.49 - *Radial profiles of RMS radial particle velocities at seven stations along z axis at $M_j = 22\%$ for $d_p = 40$ μm. Symbols: experiment; solid line: AVBP-EL; dot-dashed line: CDP.*

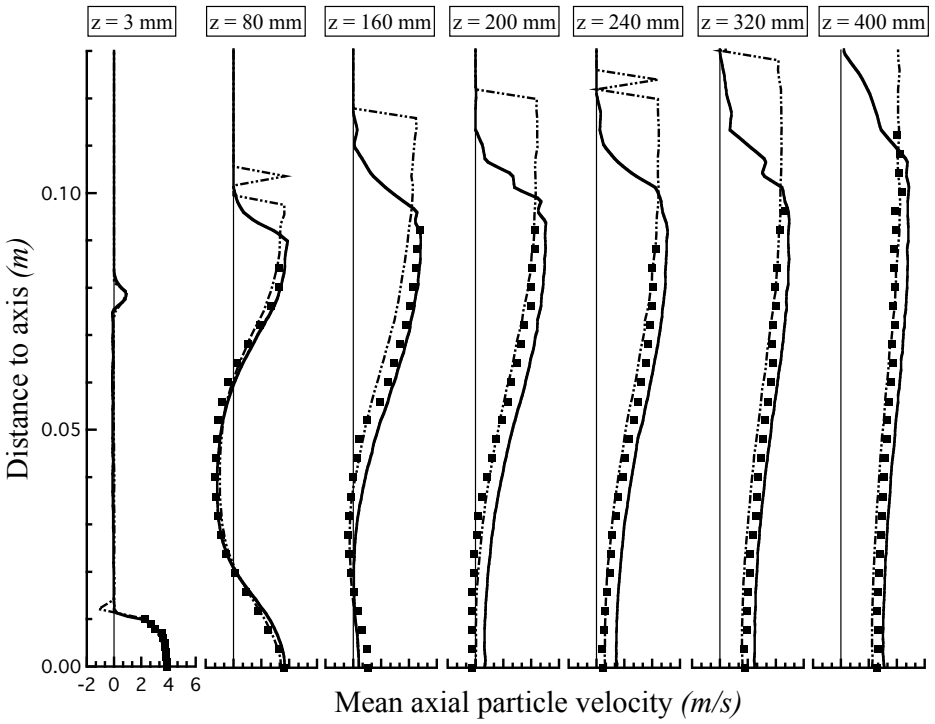

Figure 5.50 - *Radial profiles of mean axial particle velocities at seven stations along z axis at $M_j = 22\%$ for $d_p = 60$ μm. Symbols: experiment; solid line: AVBP-EL; dot-dashed line: CDP.*

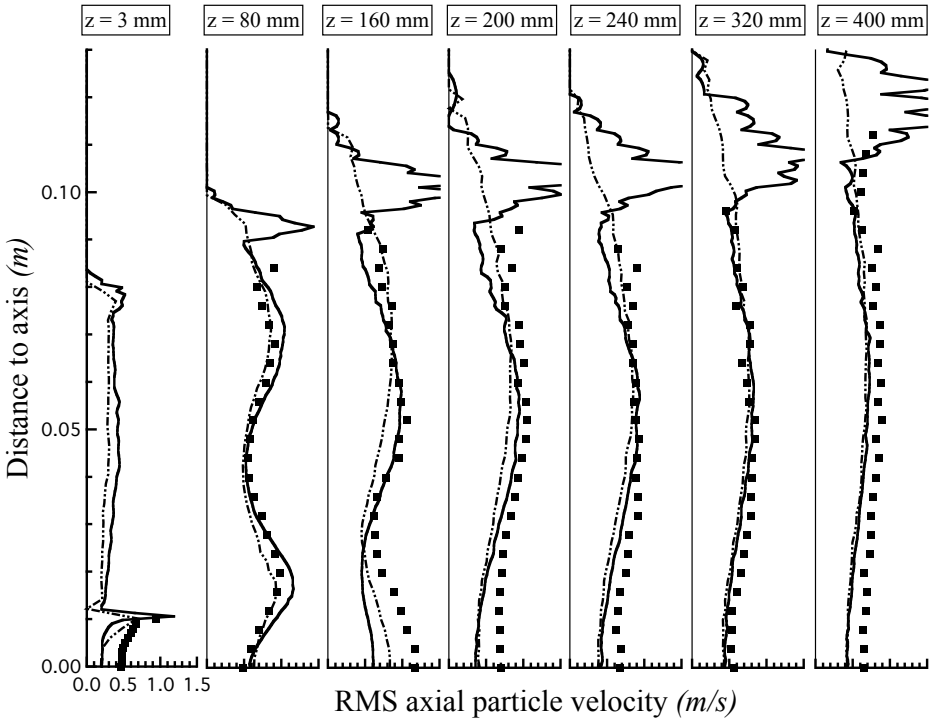

Figure 5.51 - *Radial profiles of RMS axial particle velocities at seven stations along z axis at $M_j = 22\%$ for $d_p = 60$ μm. Symbols: experiment; solid line: AVBP-EL; dot-dashed line: CDP.*

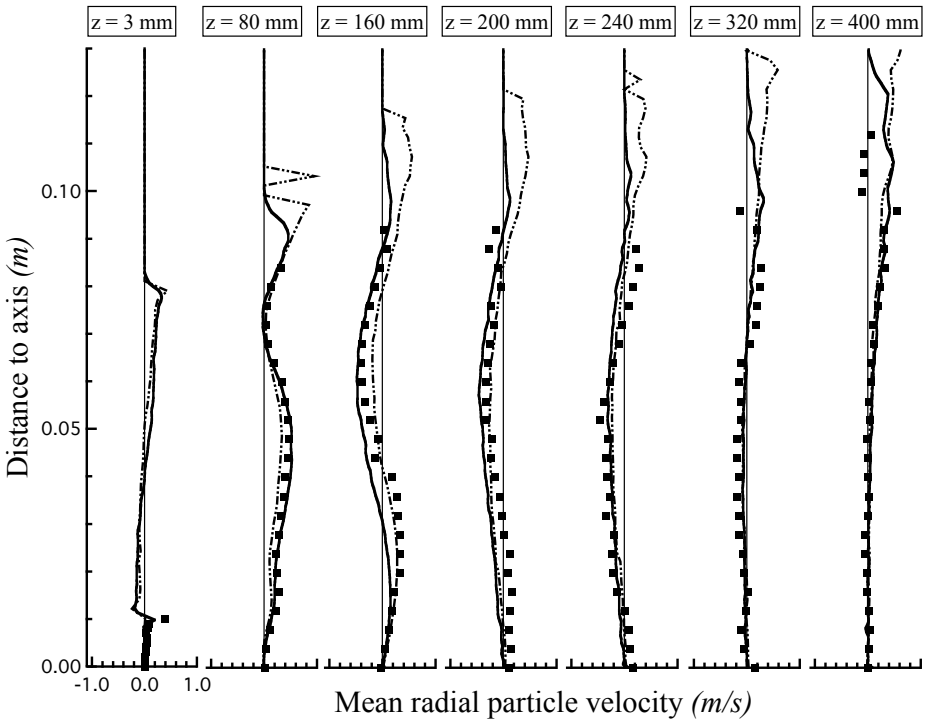

Figure 5.52 - *Radial profiles of mean radial particle velocities at seven stations along z axis at $M_j = 22\%$ for $d_p = 60$ μm. Symbols: experiment; solid line: AVBP-EL; dot-dashed line: CDP.*

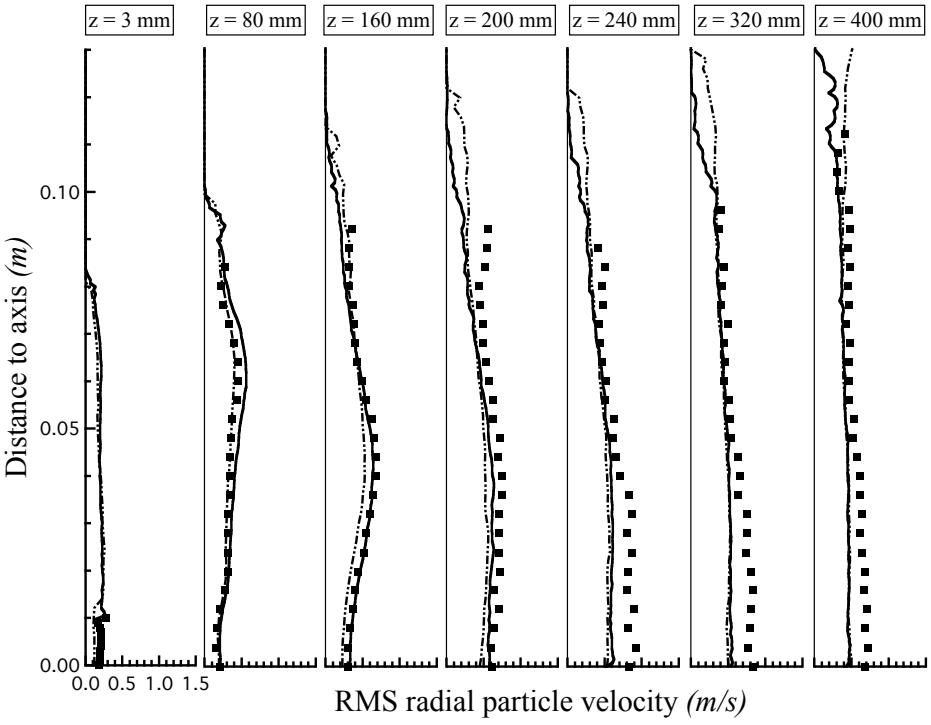

Figure 5.53 - *Radial profiles of RMS radial particle velocities at seven stations along z axis at $M_j = 22\%$ for $d_p = 60$ μm. Symbols: experiment; solid line: AVBP-EL; dot-dashed line: CDP.*

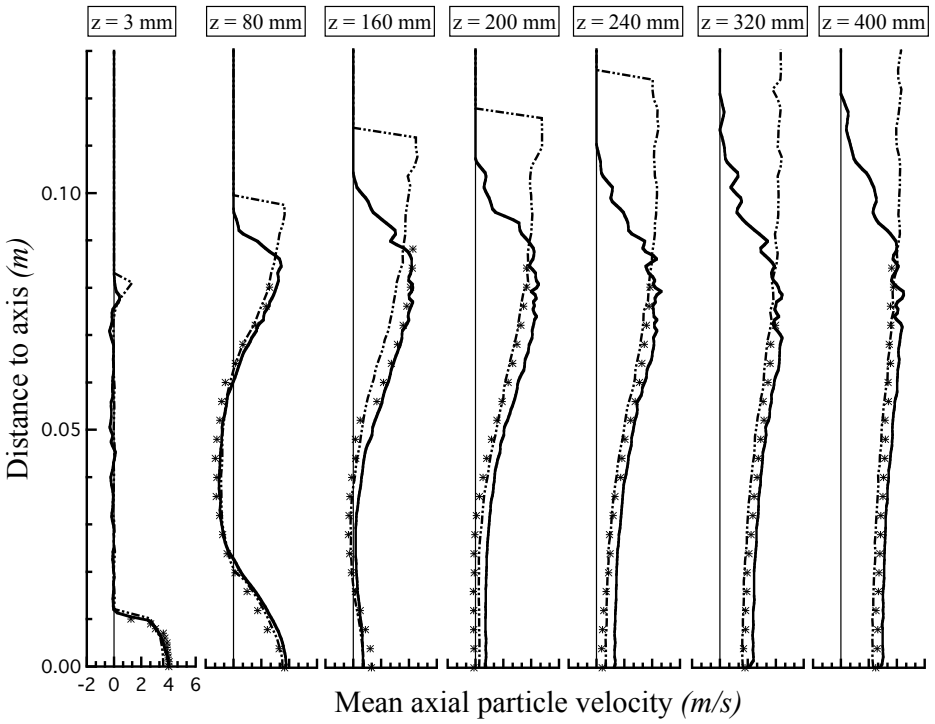

Figure 5.54 - *Radial profiles of mean axial particle velocities at seven stations along z axis at $M_j = 22\%$ for $d_p = 80$ μm. Symbols: experiment; solid line: AVBP-EL; dot-dashed line: CDP.*

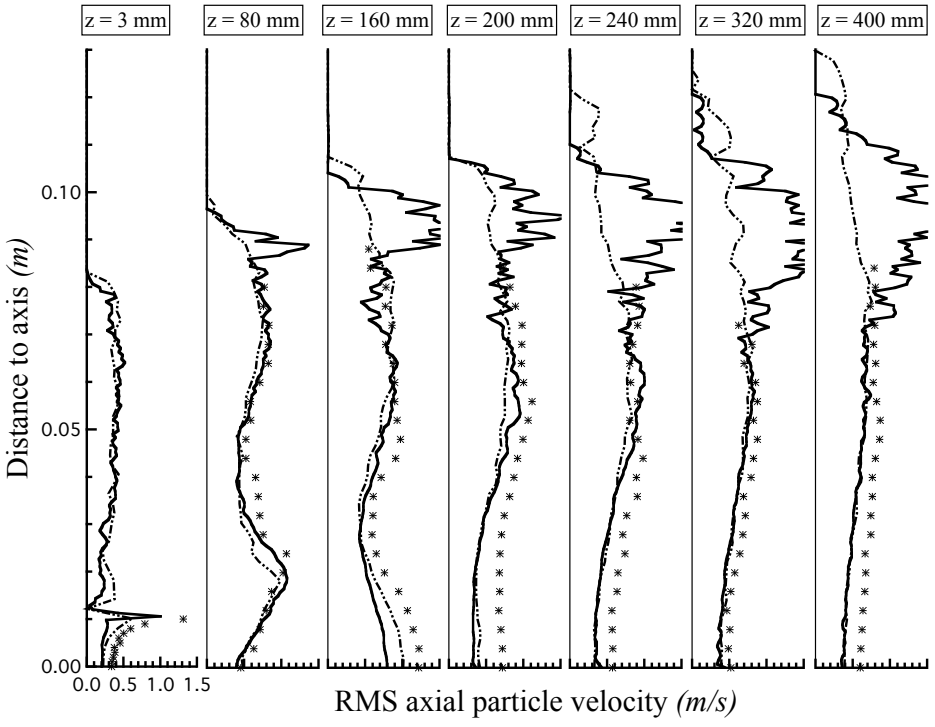

Figure 5.55 - *Radial profiles of RMS axial particle velocities at seven stations along z axis at $M_j = 22\%$ for $d_p = 80$ μm. Symbols: experiment; solid line: AVBP-EL; dot-dashed line: CDP.*

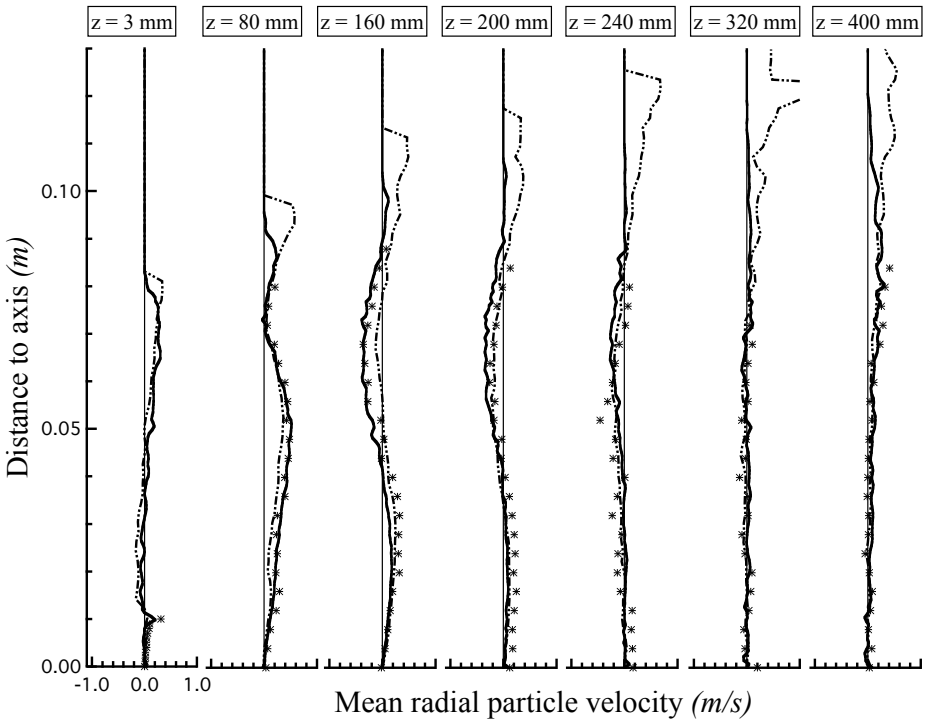

Figure 5.56 - *Radial profiles of mean radial particle velocities at seven stations along z axis at $M_j = 22\%$ for $d_p = 80$ μm. Symbols: experiment; solid line: AVBP-EL; dot-dashed line: CDP.*

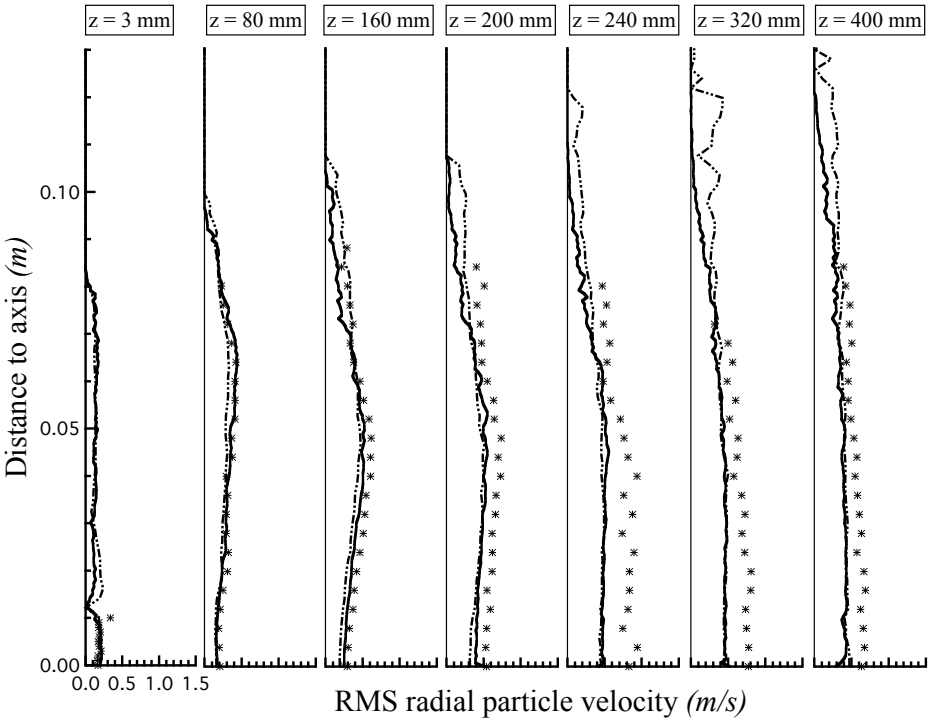

Figure 5.57 - *Radial profiles of RMS radial particle velocities at seven stations along z axis at $M_j = 22\%$ for $d_p = 80$ μm. Symbols: experiment; solid line: AVBP-EL; dot-dashed line: CDP.*

5.5.4 Influence of the number of samples

The following paragraphs discuss the effect of the number of samples on the radial velocity profiles presented in previous subsections. Table 5.4 summarises the physical time of the three simulations compared hereafter. Only the numerical results of the AVBP-EL solver are compared to the experimental data. The number of iterations and the CPU time (in hours) spent for a 32-processor simulation are also included in this table.

Physical time (s)	0.26	1	3.89
N^o *of time steps*	63,000	234,000	922,000
CPU time with 32 processors (h)	≈ 74	≈ 274	≈ 1078

Table 5.4 - *Summary of parameters of AVBP-EL with the hexahedron-based grid on an IBM JS21.*

Figs. 5.58-5.65:

These figures show the mean and RMS axial velocity profiles[2] of classes: $d_p = 20, 40, 60$ and 80 μm. The differences between the three times, and therefore, the influence of an increasing number of samples are evident in all the figures. In most cases, an averaging time of one second appears to be sufficient. The first two cross-sections in the lightest particles (Figs. 5.58 and 5.59) are quite similar since the number of particles used to create the average profiles is high enough and the improvement of results is only visible in the outer region ($z > 80$ mm). On the contrary, mean and RMS profiles in the rest of stations ($z \geq 160$ mm) show an important improvement while increasing the average time, especially in the last stations. Results of the classes: 40 and 60 μm (Figs. 5.60-5.63) are quite similar. Both of them contain an important number of samples after one second of physical time. Again, the first cross-sections are always the less scattered. The number of samples in the heaviest particles (Figs. 5.64 and 5.65) leads to important differences between the three cases. These differences are even stronger than for the lightest particles since their number distribution is one of the lowest.

Figs. 5.66-5.69:

These figures[3] display the number of samples used to calculate average statistics. As expected, profiles at four seconds are close to four times the one second profiles. Results presented in these graphs confirm the tendencies observed in the previous ones: (i) the classes with the highest number of samples are: 40 and 60 μm; (ii) the number of particles captured in the first cross-sections is greater and that is why, mean profiles of Figs. 5.58-5.65 were less scattered. In addition, particles are mainly located near the centerline with a radial dispersion as long as the axial distance to the origin increases. Profiles of the 80 μm particles display a lower radial dispersion than the other classes. As mentioned in previous subsections, their large inertia causes these particles to penetrate more in the axial direction.

[2] Results of the mean and RMS radial velocity profiles are not presented here due to their similarity.
[3] Note that the x-axis do not have the same scale.

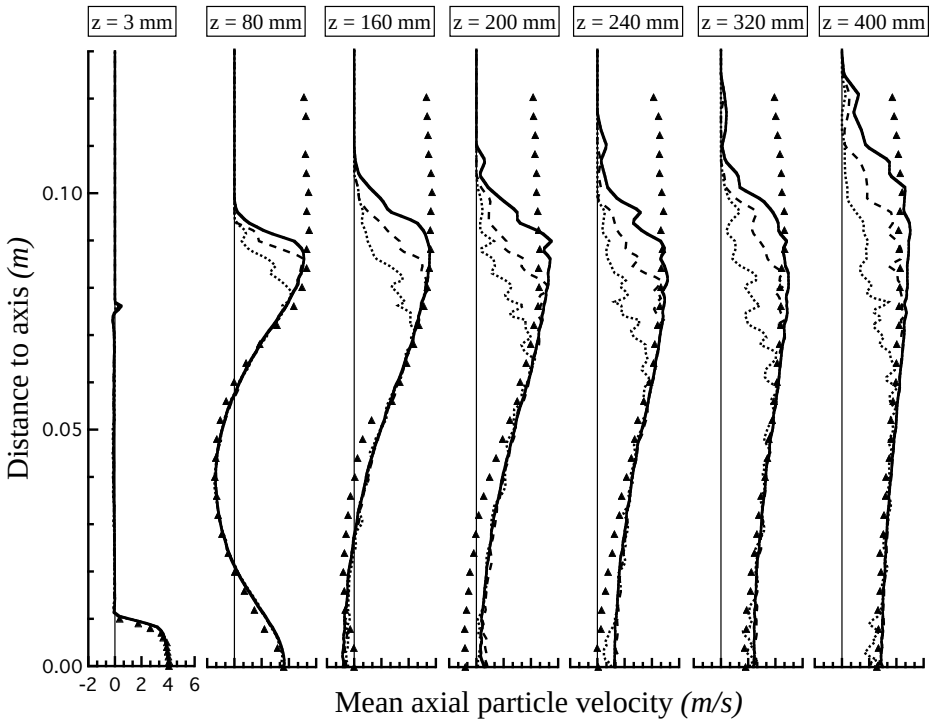

Figure 5.58 - *Radial profiles of mean axial particle velocities at seven stations along z axis at $M_j = 22\%$ for $d_p = 20$ μm. Symbols: experiment; lines: AVBP-EL at $t \approx 0.26$ s (dotted), $t \approx 1$ s (dashed), $t \approx 4$ s (solid).*

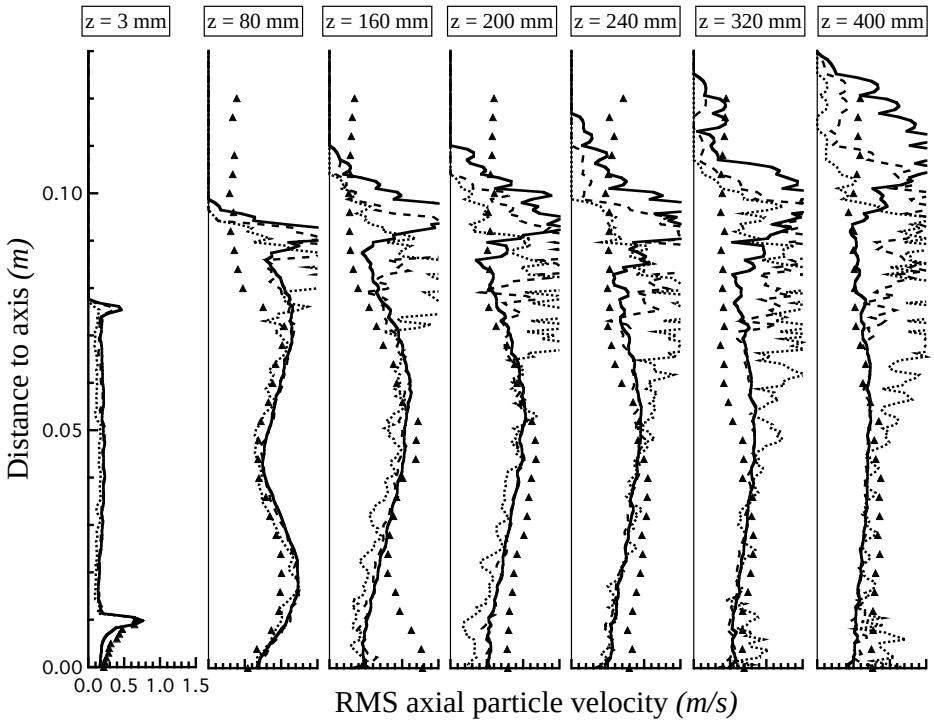

Figure 5.59 - *Radial profiles of RMS axial particle velocities at seven stations along z axis at $M_j = 22\%$ for $d_p = 20$ μm. Symbols: experiment; lines: AVBP-EL at $t \approx 0.26$ s (dotted), $t \approx 1$ s (dashed), $t \approx 4$ s (solid).*

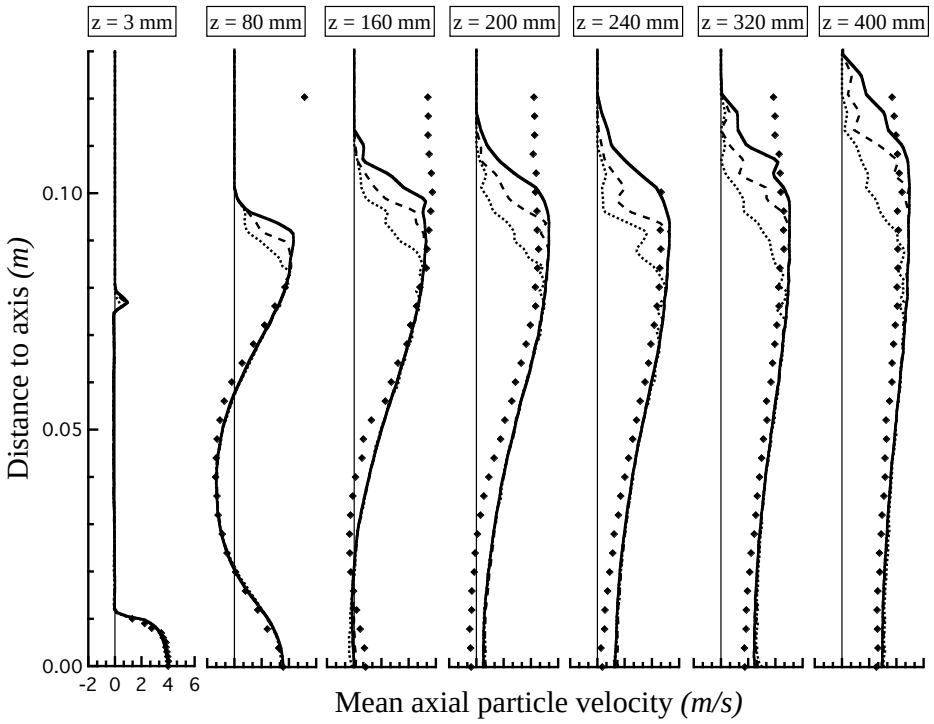

Figure 5.60 - *Radial profiles of mean axial particle velocities at seven stations along z axis at $M_j = 22\%$ for $d_p = 40$ μm. Symbols: experiment; lines: AVBP-EL at $t \approx 0.26$ s (dotted), $t \approx 1$ s (dashed), $t \approx 4$ s (solid).*

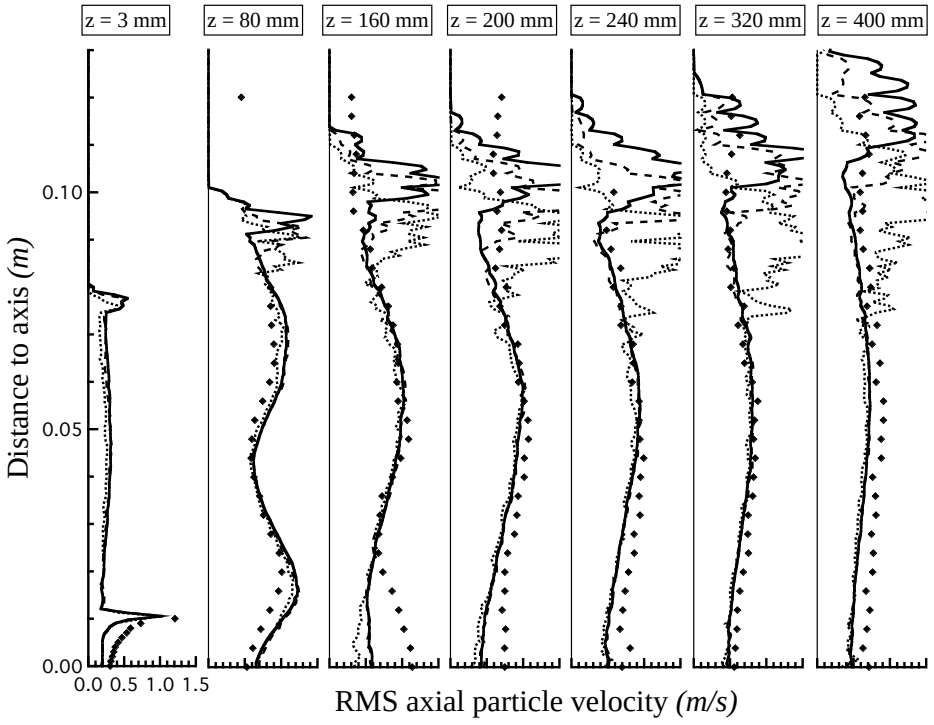

Figure 5.61 - *Radial profiles of RMS axial particle velocities at seven stations along z axis at $M_j = 22\%$ for $d_p = 40$ μm. Symbols: experiment; lines: AVBP-EL at $t \approx 0.26$ s (dotted), $t \approx 1$ s (dashed), $t \approx 4$ s (solid).*

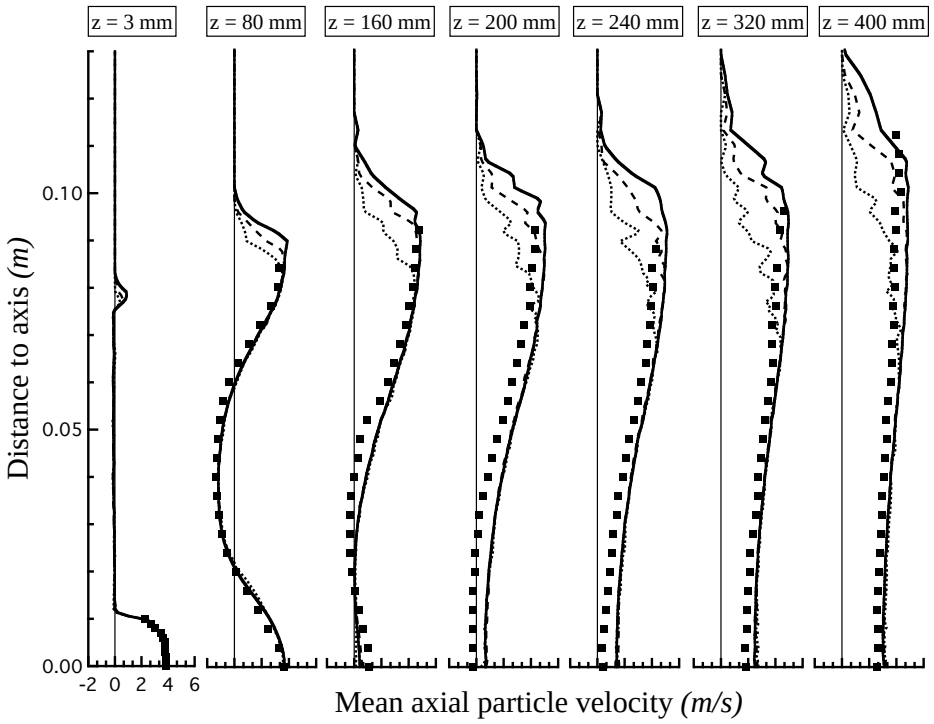

Figure 5.62 - *Radial profiles of mean axial particle velocities at seven stations along z axis at $M_j = 22\%$ for $d_p = 60$ μm. Symbols: experiment; lines: AVBP-EL at $t \approx 0.26$ s (dotted), $t \approx 1$ s (dashed), $t \approx 4$ s (solid).*

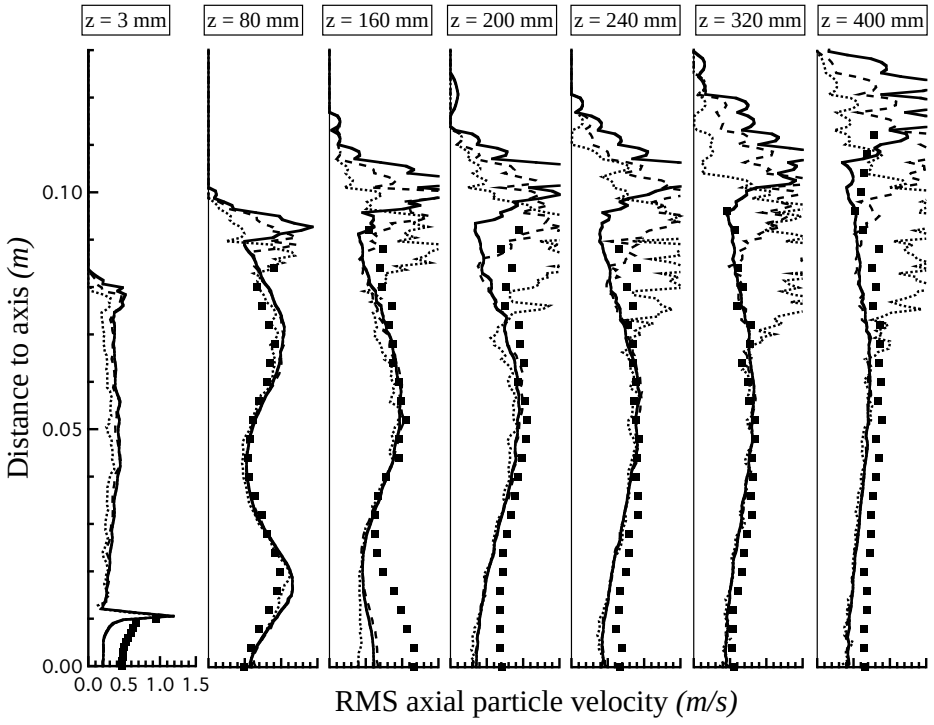

Figure 5.63 - *Radial profiles of RMS axial particle velocities at seven stations along z axis at $M_j = 22\%$ for $d_p = 60$ μm. Symbols: experiment; lines: AVBP-EL at $t \approx 0.26$ s (dotted), $t \approx 1$ s (dashed), $t \approx 4$ s (solid).*

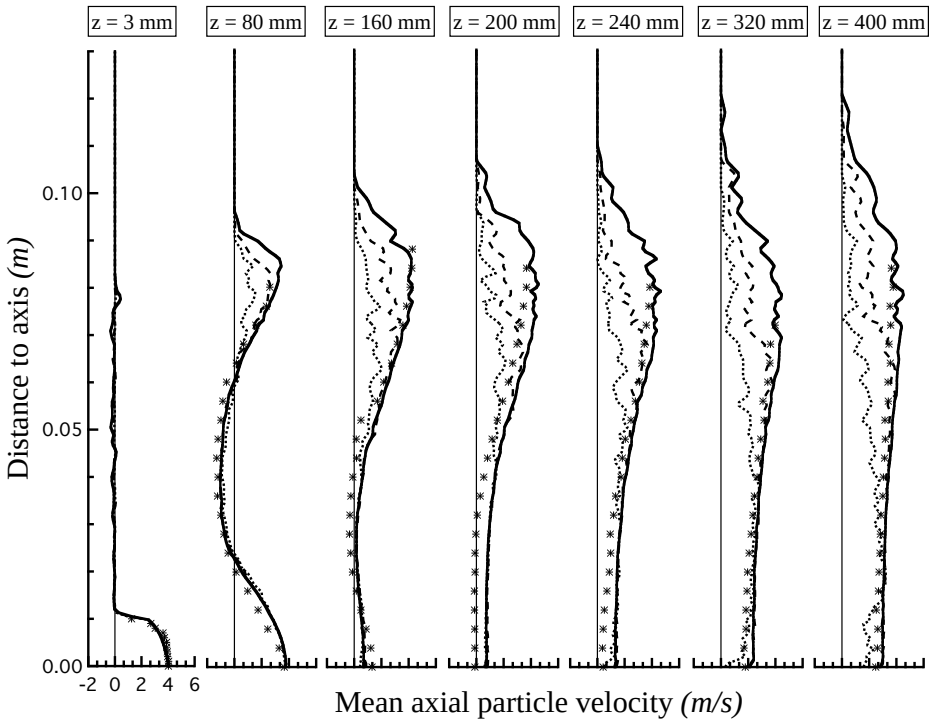

Figure 5.64 - *Radial profiles of mean axial particle velocities at seven stations along z axis at $M_j = 22\%$ for $d_p = 80$ μm. Symbols: experiment; lines: AVBP-EL at $t \approx 0.26$ s (dotted), $t \approx 1$ s (dashed), $t \approx 4$ s (solid).*

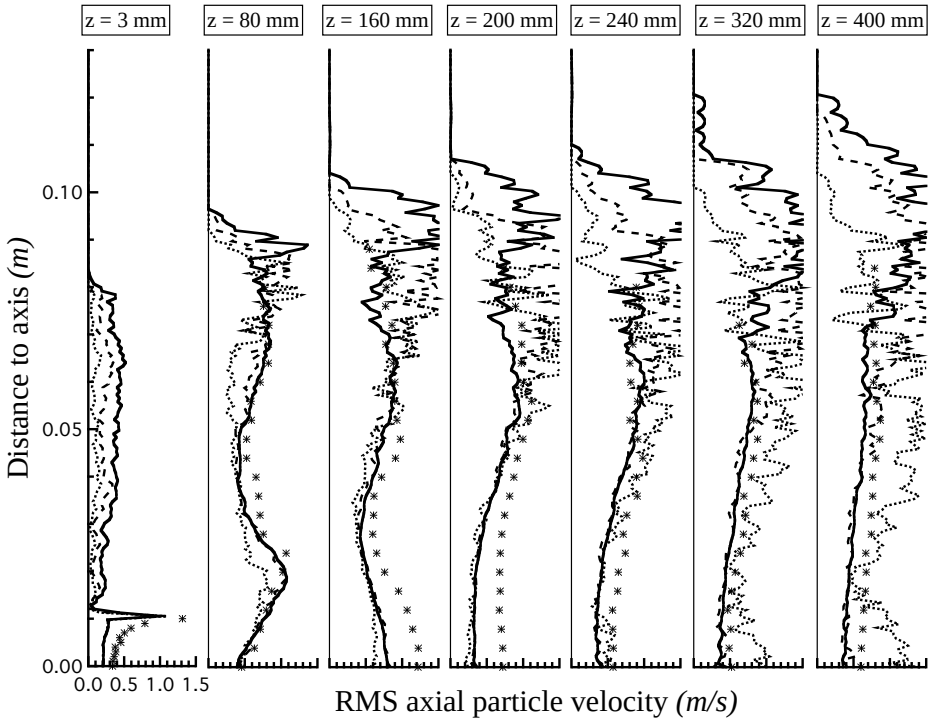

Figure 5.65 - *Radial profiles of RMS axial particle velocities at seven stations along z axis at $M_j = 22\%$ for $d_p = 80$ μm. Symbols: experiment; lines: AVBP-EL at $t \approx 0.26$ s (dotted), $t \approx 1$ s (dashed), $t \approx 4$ s (solid).*

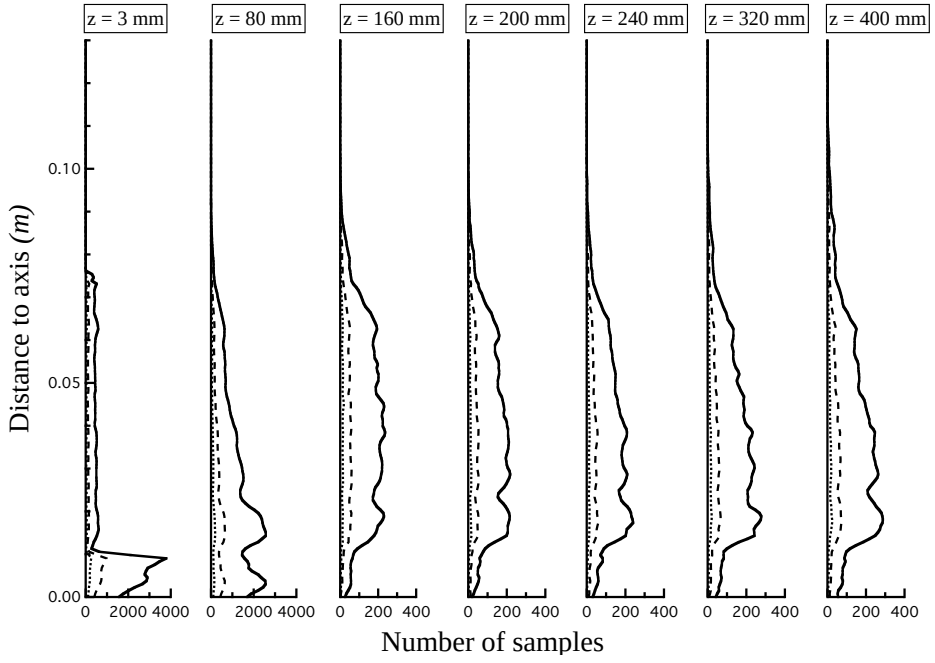

Figure 5.66 - *Number of samples at seven stations along z axis at $M_j = 22\%$ for $d_p = 20$ μm. Lines: AVBP-EL at $t \approx 0.26$ s (dotted), $t \approx 1$ s (dashed), $t \approx 4$ s (solid).*

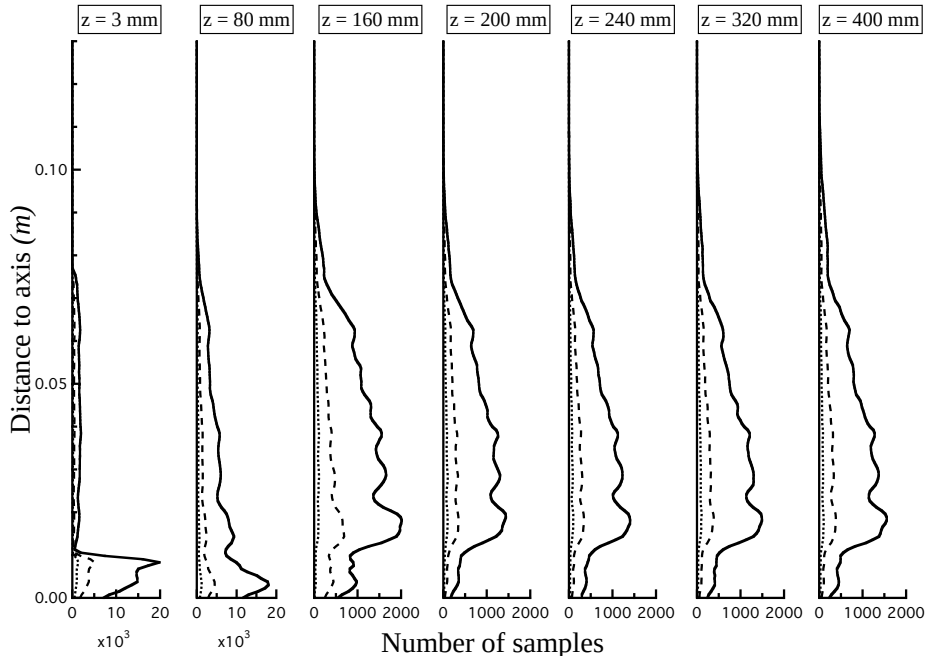

Figure 5.67 - *Number of samples at seven stations along z axis at $M_j = 22\%$ for $d_p = 40$ μm. Lines: AVBP-EL at $t \approx 0.26$ s (dotted), $t \approx 1$ s (dashed), $t \approx 4$ s (solid).*

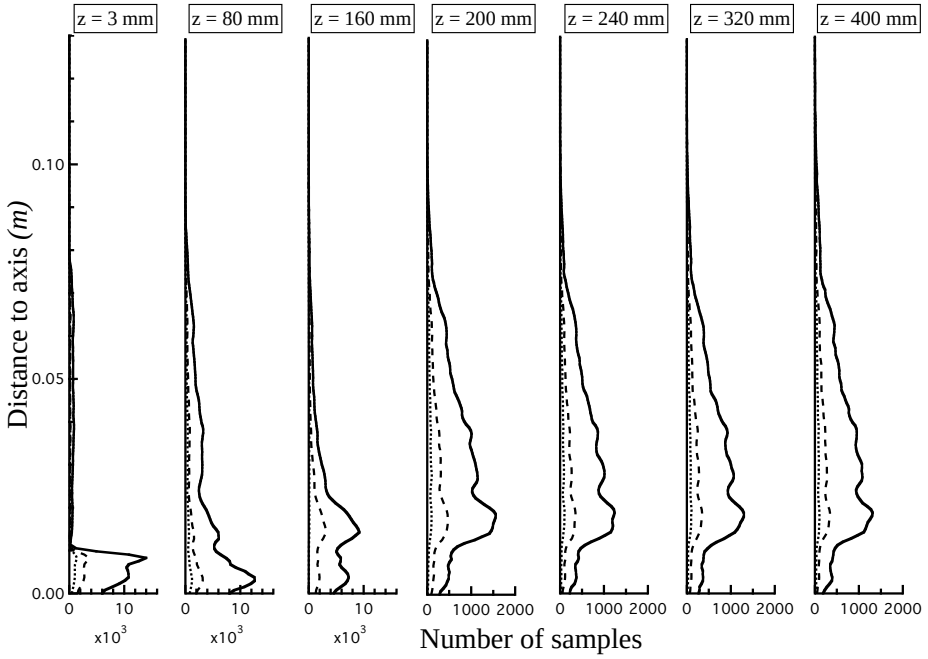

Figure 5.68 - *Number of samples at seven stations along z axis at $M_j = 22\%$ for $d_p = 60$ μm. Lines: AVBP-EL at $t \approx 0.26$ s (dotted), $t \approx 1$ s (dashed), $t \approx 4$ s (solid).*

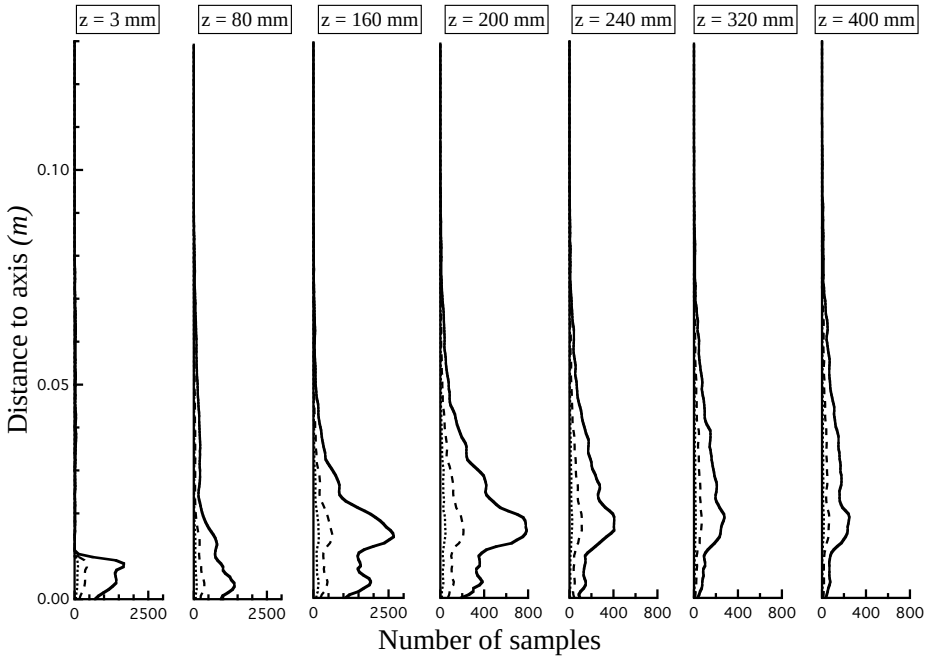

Figure 5.69 - *Number of samples at seven stations along z axis at $M_j = 22\%$ for $d_p = 80$ μm. Lines: AVBP-EL at $t \approx 0.26$ s (dotted), $t \approx 1$ s (dashed), $t \approx 4$ s (solid).*

5.5.5 Particle trajectories

Figure 5.70 (a) shows the probability density function (PDF) of the slip velocities of all particle classes. The peak of the curve is near a value of 0.5 m/s which confirms that a high number of particles follow the fluid motion. The PDFs of the slip velocities of four different particle classes are presented in Fig. 5.70 (b). Smallest particles follow the fluid very close with low values of the slip velocity (≈ 0.2 m/s). As long as the particle diameter increases, the peak of the PDF decreases and the slip velocity associated to it increases, making them more independent of the flow.

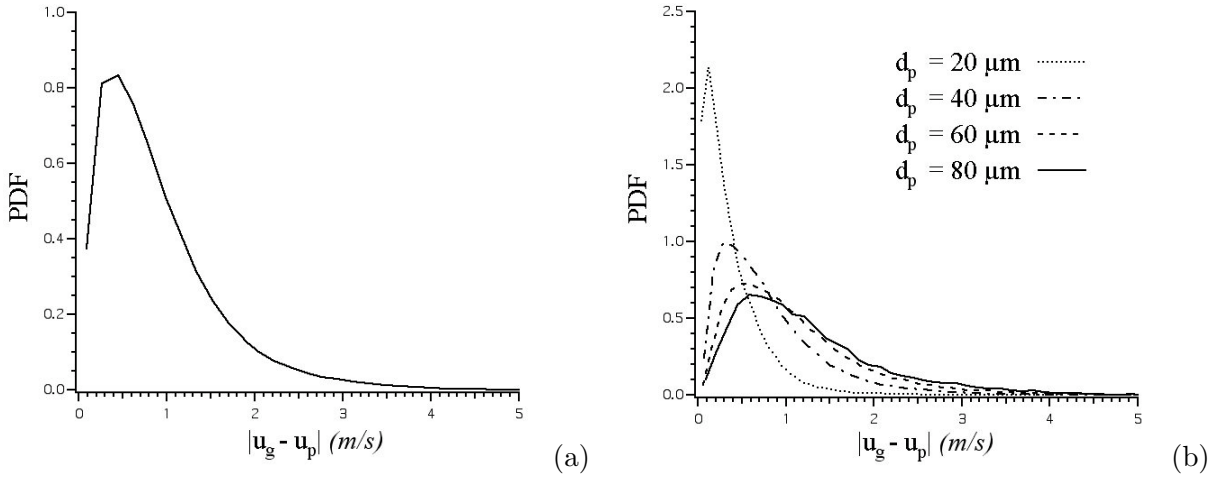

Figure 5.70 - *Probability density function (PDF) of (a) all classes and (b) only four particle classes.*

Figs. 5.71 and 5.72 display 25 tracks of particles with diameters: $d_p = 20, 40, 60$ and 80 μm at a moderate mass loading and for the same physical time: $t = 0.44$ s. Left and right panels present the projections of particle pathlines in the $y - z$ and $y - x$ axes, respectively. Initially, all particles follow the axial direction without turning away from the axis. Due to their different nature, lighter particles respond to the flow faster and are decelerated to zero axial velocity sooner (Fig. 5.71). Furthermore, their trajectories are deviated and more influenced by turbulence as it can be observed from their twisted pathlines inside the recirculation bubble.

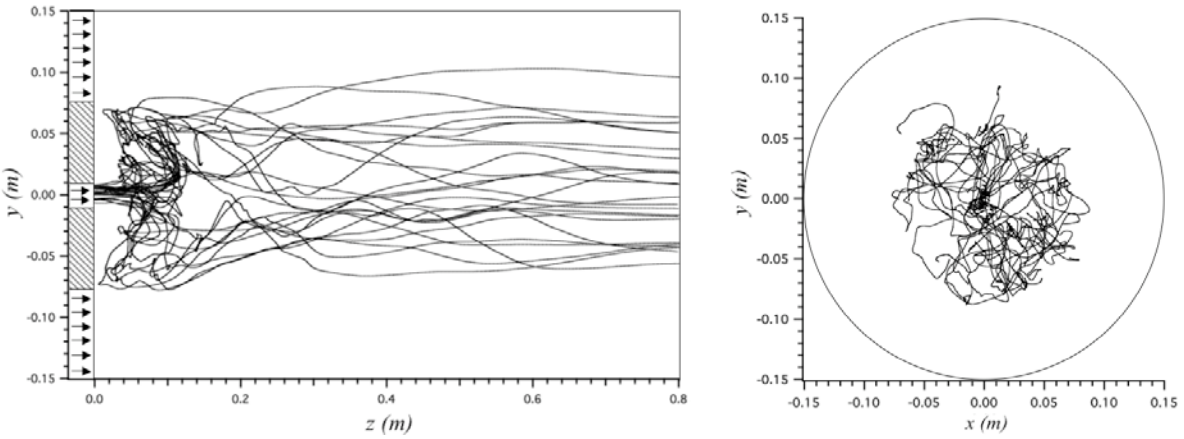

Figure 5.71 - *Some particle trajectories calculated at $M_j = 22\%$ for $d_p = 20$ μm at $t = 0.44$ s. Left: y-z view. Right: y-x view.*

On the contrary, heavier particles (Fig. 5.72) penetrate more into the recirculation bubble due to their large inertia before coming to rest. The highest penetration is clearly presented for 80 μm particles (bottom panel). This class also presents a particularity because these particles do not reach the wall between the inner and the annular jets since they are captured before by large eddies of the coflow boundary and transported downstream.

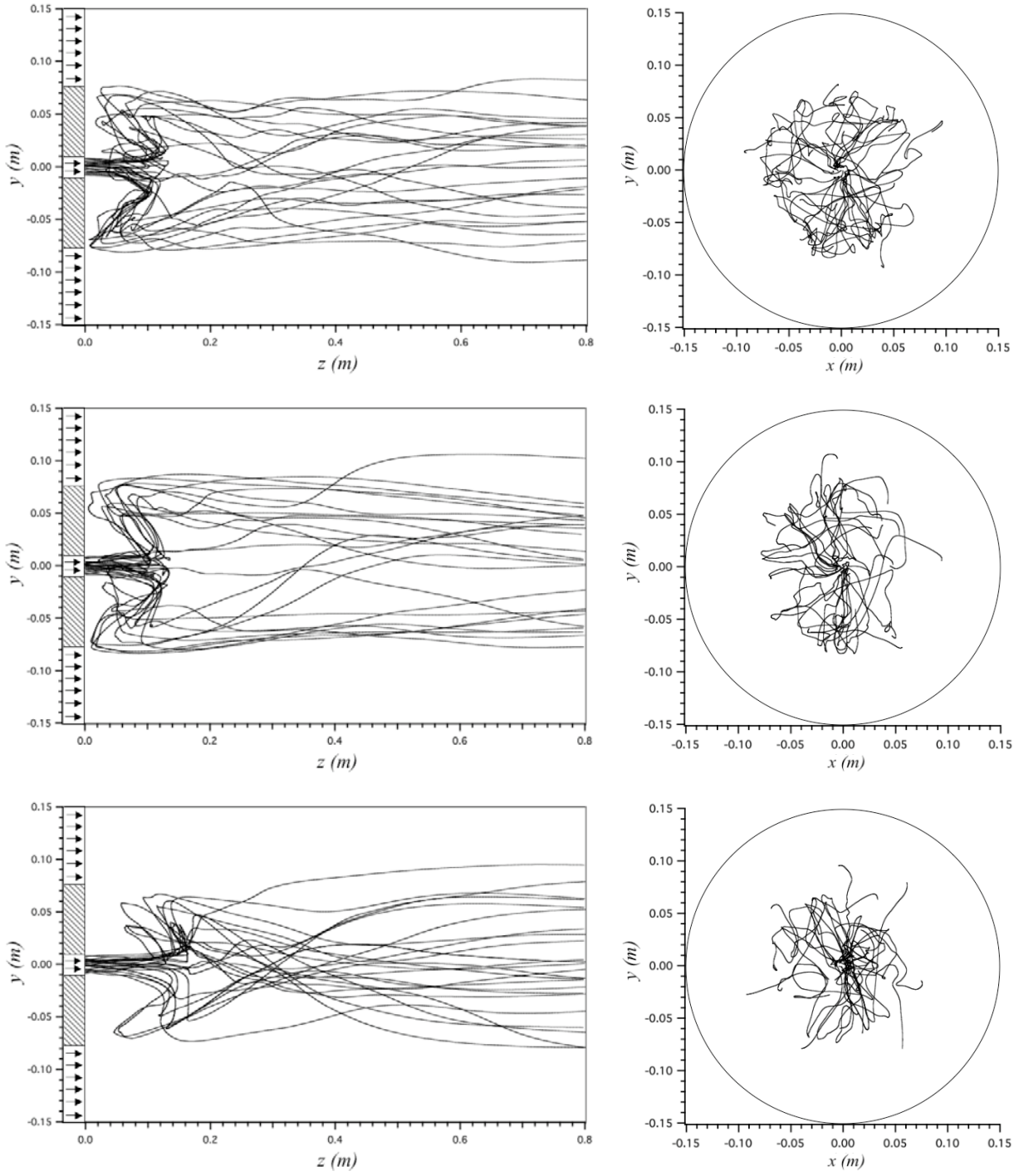

Figure 5.72 - *Some particle trajectories calculated at $M_j = 22\%$ at $t = 0.44$ s. Top panel: $d_p = 40$ μm; middle panel: $d_p = 60$ μm; bottom panel: $d_p = 80$ μm. Left: y-z view. Right: y-x view.*

5.6 Performance

One interesting issue in the development of Lagrangian methods is the analysis of scalability and computational performance. The implementation on massively parallel machines of the dispersed phase with Eulerian approaches is not technically problematic because the flow and the droplets are solved on the same grid using the same spatial discretization scheme. On the other hand, Lagrangian approaches are less well-suited to parallel computers since the two phases must be coupled, which increases the complexity of the implementation. Thus, before implementing a Lagrangian module into a new solver one of the strategies presented in Subsection 2.6.1 should be adopted for the dispersed phase treatment. The most used are:

- Task parallelism in which some processors compute the gaseous phase and others compute the particles or droplets.

- Data parallelism in which particles are computed together with the gas flow on geometrical subdomains mapped on parallel processors. Individual particles or parcels are tracked as they cross the computational domain and must be exchanged between processors when leaving a subdomain to enter an adjacent one.

Particle tracking within an unstructured solver (like AVBP) reveals an additional constraint since particle coordinates cannot be easily used to locate them inside a cell, and time (and memory) consuming searching algorithm must be used. However, for LES it is easy to show that only the strategy based on data parallelism is efficient on large grids because task parallelism would require the communication of very large three-dimensional data sets at each iteration between all processors, increasing the cost of communications and reducing considerably the speedup. It is well known that codes treating particles with a data parallelism technique and based on domain partitioning are difficult to optimize on massively parallel architectures when droplets are clustered in one part of the domain (typically, near the fuel injectors) due to load imbalance. Moreover, the distribution of droplets may change during the computation: for a gas turbine reignition sequence, for example, the chamber is filled with droplets when the ignition begins thus ensuring an almost uniform droplet distribution; these droplets then evaporate rapidly during the computation, leaving droplets only in the near injector regions. This may lead to a poor speedup on a parallel machine if the domain is decomposed in the same way for the entire computation since some processors should compute a high number of particles while others are waiting for this task to finish. As a result, load balancing strategies are required to redecompose the domain by taking into account particles information to preserve a high parallel efficiency [76].

In this section, the notions of scalability and CPU time introduced in Section 2.6 will be applied to analyse performance of the implementation of the Lagrangian module. This scalability study has been performed in a CRAY XD1[4] supercomputer for a number of processors up to 64. Subsection 5.6.1 summarises results of the simulations performed with a one-constraint partitioning algorithm (RIB), i.e., without balancing the number of particles across the subdomains; and subsection 5.6.2 presents the effect of a two-constraint partitioning algorithm which takes into account the particle information while partitioning the grid.

[4] This machine has 58 nodes with 2 processors/node and 2 GB/processor.

5.6.1 Scalability with a one-constraint partitioning algorithm

Results of the moderate mass loading test case has been calculated in two different grids (tetrahedron and hexahedron-based grids) and results are presented hereafter. The total number of particles presented in the domain is of the order of 560,000 and 430,000, respectively. Variations smaller than 0.5% in the number of particles were observed between the beginning and the end of the simulation, which implies that it is statistically stationary. The lower number of particles used in the tetrahedron grid is due to the difference in the length between the two grids (see Fig. 5.5). Even if the length of the chamber is half the dimension of the tetrahedron-based grid, the number of particles is three-fourth since they are mainly concentrated inside the recirculation zone. Figure 5.73 shows a front view of both computational meshes after the partitioning into 32 subdomains by the RIB partitioning algorithm (see Subsection 2.4.2). A more complete study of a simulation with the tetrahedron-based grid can be consulted in Appendix C.

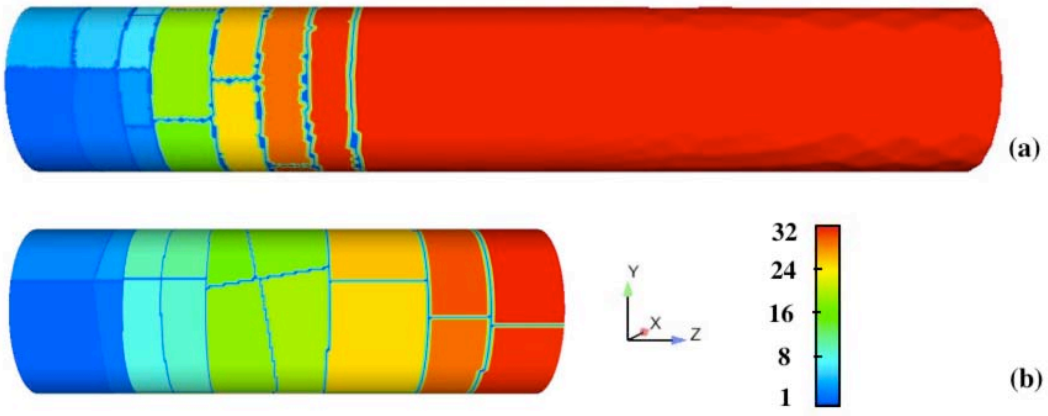

Figure 5.73 - *Front view of a computational mesh divided into 32-subdomains by using the RIB partitioning algorithm for (a) a tetrahedron and (b) a hexahedron-based grid. Configuration of Borée* et al. *[22].*

Figure 5.74 shows the speedup of the single-phase and the monodisperse test cases with the tetrahedron (Fig. 5.74 (a)) and the hexahedron-based grid (Fig. 5.74 (b)). Scaling of the hexahedron grid is reported relative to the 8 processor case ($n = 8$), which was the smallest number of CRAY XD1 processors that could run this problem due to high memory requirements. In both cases, the good scalability of the single-phase is unquestionable. The drop of performance observed in Fig. 5.74 (a) for the two-phase flow simulation is not related to large communications costs between processors but merely to the parallel load imbalance generated by the partitioning algorithm [69], as will be demonstrated in the next subsection. The same simulation with a different grid can lead to a completely different speedup graph, as observed from Fig. 5.74 (b).

The differences between the two speedup graphs can also be explained by plotting the number of nodes (or cells) and particles presented in each processor. As AVBP is based on a *cell-vertex* formulation, comparing the number of nodes to the number of particles is more representative of the computational loading since almost all arrays are dimensioned as a function of the number of nodes per processor. Figure 5.75 reports the number of nodes and particles per processor for a 32-processors simulation with RIB, for the tetrahedron and the hexahedron-based grids, respectively.

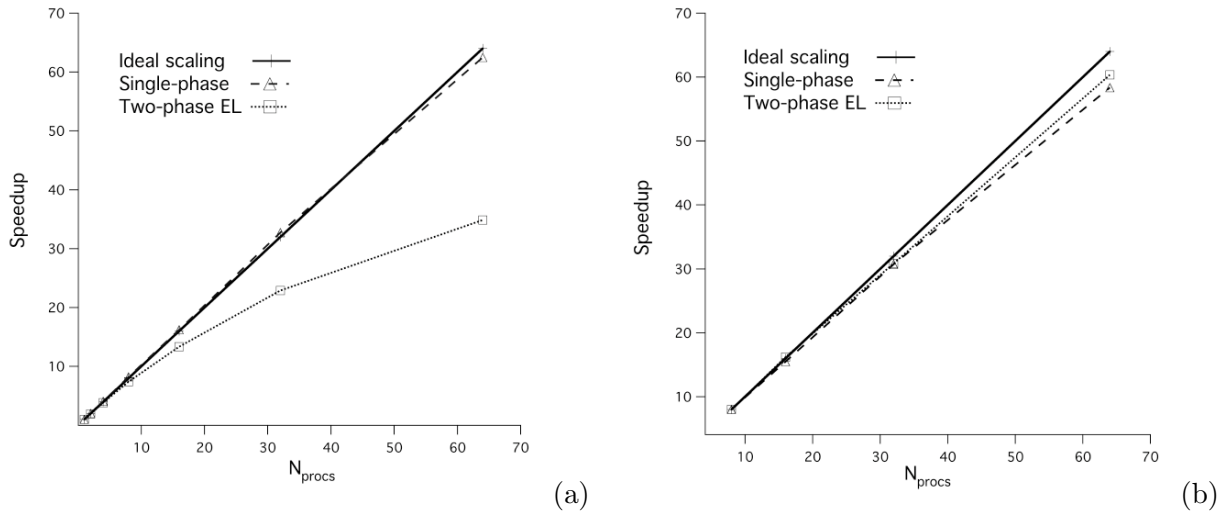

Figure 5.74 - *Speedup of the single-phase and the monodisperse test case with (a) the tetrahedron and (b) the hexahedron-based grid on a CRAY XD1 supercomputer.*

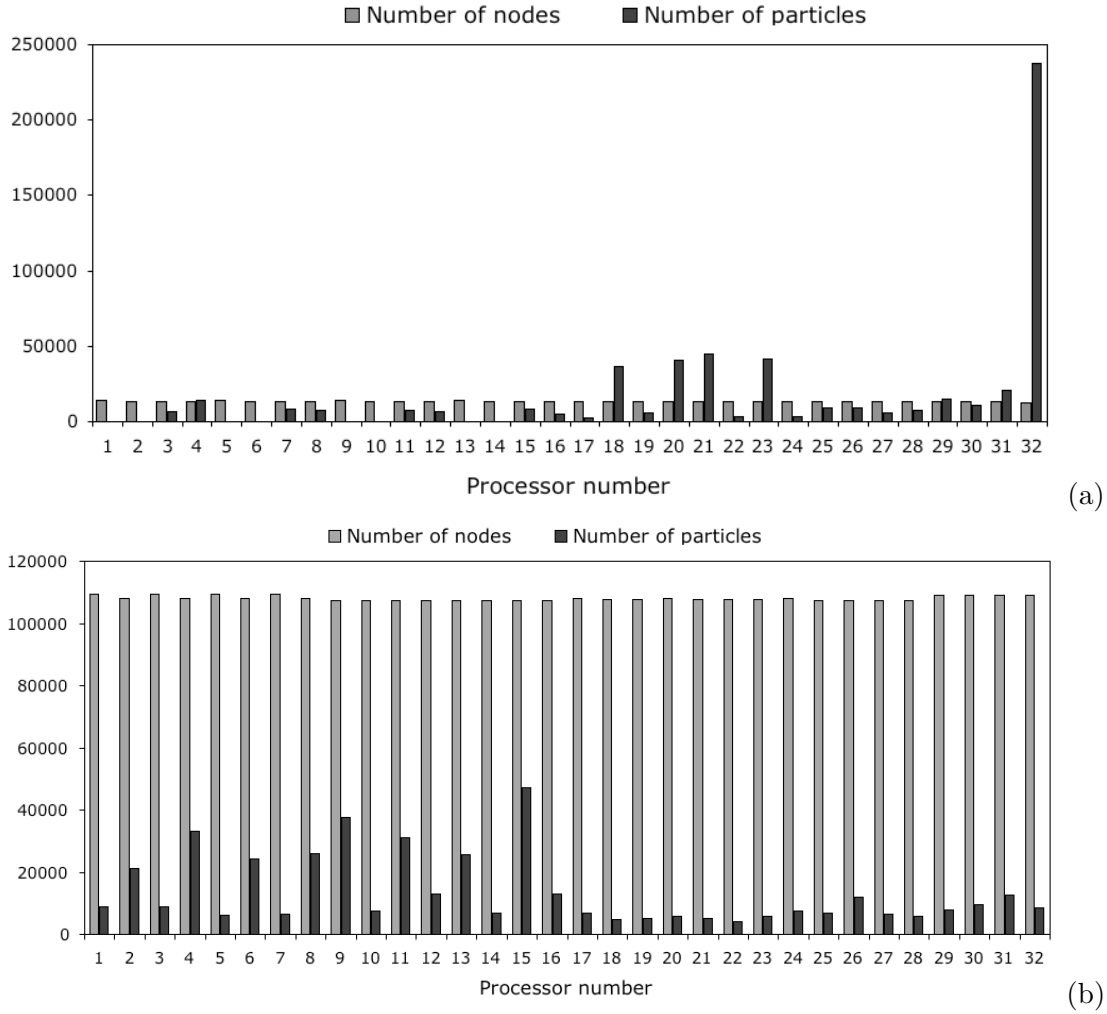

Figure 5.75 - *Number of nodes and particles per processor for a 32-processors simulation by using the RIB partitioning algorithm for the (a) tetrahedron and the (b) hexahedron-based grids.*

As expected from Fig. 5.74, Fig. 5.75 shows an excellent load balancing for the gaseous phase: all processors contain about the same number of nodes. On the contrary, it shows a strong particle load imbalance (Fig. 5.75 (a)) where one single processor contains almost half the total number of particles of the simulation. This fact is related to the grid downstream coarsening which increases significantly the memory requirements and the floating-point operations for this processor. This case confirms the need of load balancing strategies for two-phase flow simulations with a Lagrangian approach. Even if the dispersed phase presents a small load imbalance in Fig. 5.75 (b), it is hidden by the higher computational loading needed to calculate the gaseous phase. This is one of the reasons of the good speedup observed in Fig. 5.74 (b).

Tables 5.5 and 5.6 summarised the CPU time ratios with both grids. Additional time to perform the two-phase flow simulation can vary from 5% (for a sequential simulation) up to 87% (for a 64-processors simulation) with the Lagrangian formulation in the tetrahedron-based grid but it is not higher than 5% with the hexahedron-based grid which confirms the tendencies observed with the speedup graphs. The same simulations with the Eulerian approach has a constant added cost of the order of 80% since this approach is independent of the mass loading. Therefore, at this moderate mass loading the Lagrangian approach proved to be faster than the Eulerian formulation.

N_{procs}	1	2	4	8	16	32	64
Single-phase	1	0.50	0.25	0.12	0.06	0.030	0.016
Two-phase AVBP-EL	1.05	0.54	0.27	0.14	0.08	0.046	0.030

Table 5.5 - *Summary of the CPU time ratios of AVBP-EL with a tetrahedron-based grid on a CRAY XD1 supercomputer.*

N_{procs}	8	16	32	64
Single-phase	1	0.51	0.26	0.137
Two-phase AVBP-EL	1.06	0.524	0.275	0.14

Table 5.6 - *Summary of the CPU time ratios of AVBP-EL with a hexahedron-based grid on a CRAY XD1 supercomputer.*

5.6.2 Scalability with a two-constraint partitioning algorithm

As demonstrated in the previous subsection, partitioning algorithms able to balance only a single quantity can result in good or bad speedup graphs for two-phase flow simulations depending on the application. This problem is not new: in fact, many important types of multi-phase and multi-physics computations require that multiple quantities be load-balanced simultaneously. The critical point is that each processor has the same amount of work from each phase. Two examples are particle-in-cells [225] and contact impact [62] simulations. The aim of this subsection is the implementation of a multi-constraint partitioning algorithm into the Lagrangian module of AVBP to show the effect of particles load balancing. The multi-constraint partitioning algorithm chosen is one of those available inside the METIS package (see Subsection 2.4.4). In the following, only two constraints are used: one to balance the number of grid elements and the other the number of particles, respectively.

Figure 5.76 presents in a simple way the problem encountered in a PIC application and the information recovered by the multi-constraint algorithm to perform the partitioning. A grid containing some particles (represented by small red circles) is displayed on the left panel. The right panel shows the dual graph of the mesh with two weights on each vertex. The first weight represents the work associated with the mesh-based computation (gaseous phase) for the corresponding element[5]. The second weight represents the work associated with the particle-based computation (dispersed phase). This value is estimated by the number of particles that fall within each element. With this information, the multi-constraint algorithm is able to partition the grid by balancing elements and particles between subdomains (the interface is represented by a bold line): ten elements and eight particles on each subdomain.

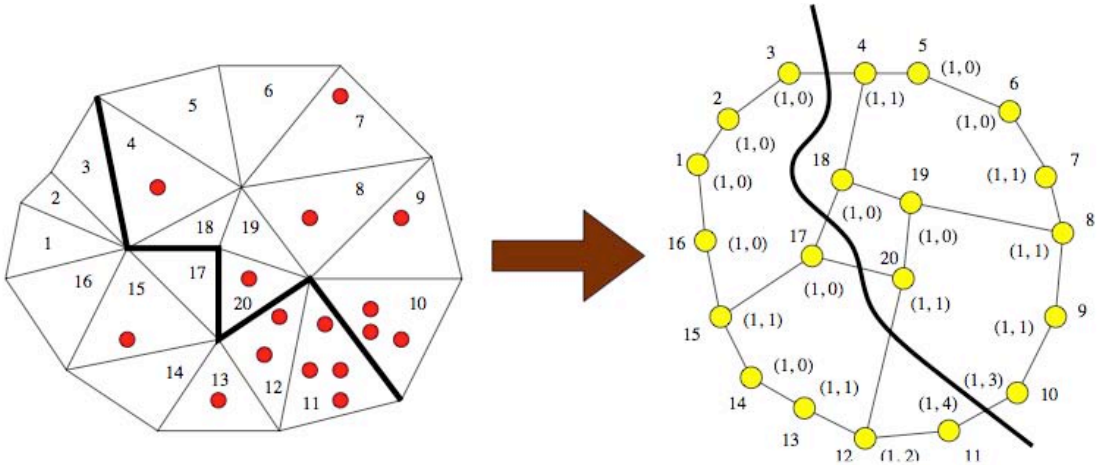

Figure 5.76 - *A dual graph with vertex weight vectors of size two (right) is constructed from the mesh. A multi-constraint partitioning has been computed for this graph, and this partitioning has been projected back to the mesh. From [97].*

Applying the same principle to the imbalance test case observed in Fig. 5.74 (a) for the tetrahedron-based grid we obtain the following mesh partitioned into 32-subdomains (Fig. 5.77). At first sight, it can be observed that this new view of the computational mesh is quite different from the one displayed in Fig. 5.73 (a), illustrating one of the differences between multilevel and geometric partitioning algorithms. Another difference can be found in the number of duplicated nodes: that is a reduction of 2.7% (RIB: 424,163; METIS: 412,603) even when using the new weight imposed by particle treatment (however, the increase or reduction in the number of these new nodes depends on the test case).

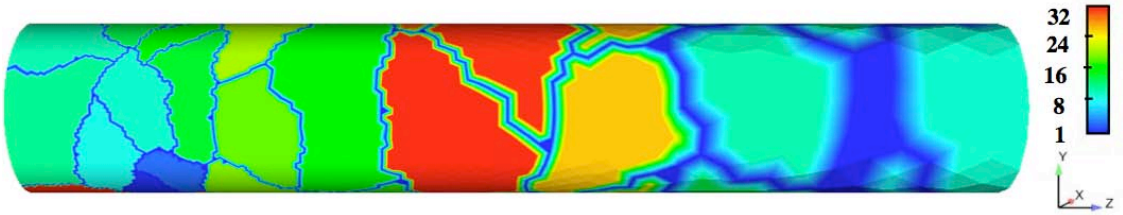

Figure 5.77 - *Front view of a computational mesh divided into 32-subdomains by using a multi-constraint partitioning algorithm (from METIS) to take into account particles. Configuration of Borée* et al. *[22].*

[5] All values are one because we assume that all the elements have the same amount of work associated with them.

Figure 5.78 presents the speedup of a single-phase simulation and two two-phase simulations performed with the Lagrangian version developed during this thesis[6]. The differences between the two two-phase simulations is on the algorithms used to partition the grid:

- A one-constraint recursive bisection algorithm (RIB) explained in Subsection 2.4.2.
- A multi-constraint multilevel recursive bisection algorithm, from the METIS package.

The improvement observed by using an algorithm to balance particles across subdomains is clearly evident. This is a remarking result since load imbalance is an inherent problem to Lagrangian simulations and it has always been considered as a major drawback. The success in the use of multi-constraint partitioning algorithm to improve Lagrangian computation performance on massively parallel machines had already been demonstrated by Ham *et al.* [76]. Results obtained in this thesis confirm the competitive position of Lagrangian formulation compared to its principal competitor, the Eulerian formulation, reducing the disadvantages associated with the Lagrangian formulation.

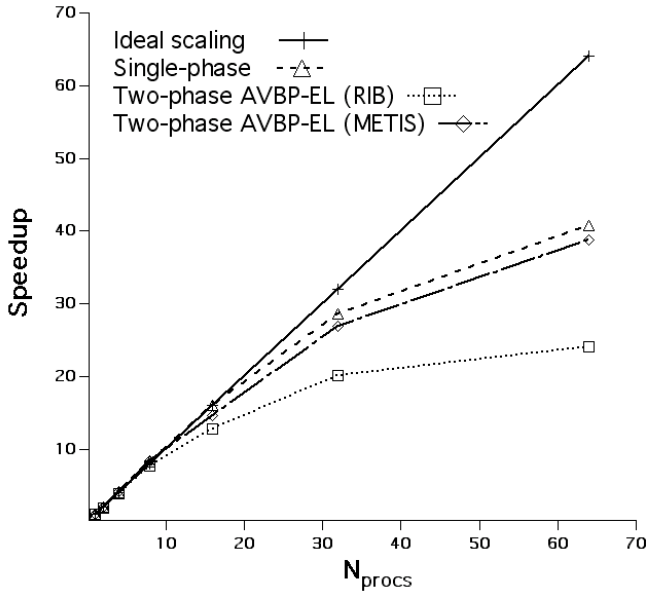

Figure 5.78 - *Speedup of the single-phase and the monodisperse test case with two two-phase simulations: one with the RIB algorithm and the other with a multi-constraint partitioning algorithms from METIS.*

Figure 5.79 reports the number of nodes and particles per processor for a 32-processors simulation with the multi-constraint partitioning algorithm for the tetrahedron-based grid. As expected from the speedup graph, this figure shows an excellent load-balancing for both, gaseous and dispersed phases. Comparing this figure with Fig. 5.75 (a) it can be observed that processor number 32 has reduced in more than 10 times the number of particles to treat. The main consequences of this reduction is that other processors will not wait for this one to finish, increasing the efficiency of the overall computation.

[6] The input files of the single-phase computation and the two-phase AVBP-EL (RIB) computation are the same as the ones used for the simulations presented in Fig. 5.74 (a) but the version of AVBP (for gaseous and dispersed-phase subroutines) is more recent in these last results. However, the differences observed between them are due to a hardware problem detected in this machine after some upgrades. The computer support group (CSG) at CERFACS is working with CRAY to detect the source of the problem.

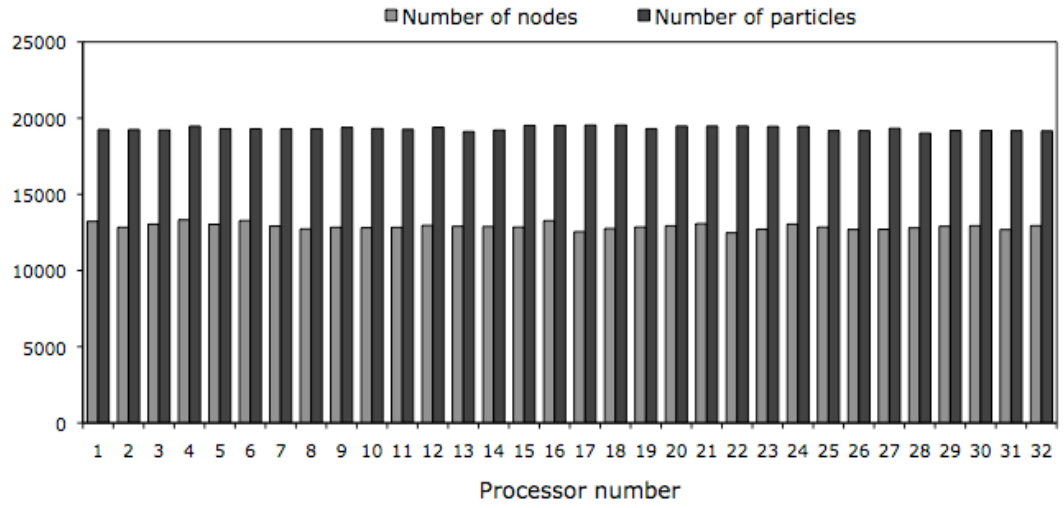

Figure 5.79 - *Number of nodes and particles per processor for a 32-processors simulation by using a two-constraint partitioning algorithm from METIS on the tetrahedron-based grid.*

Table 5.7 summarised the CPU time ratios of the simulations previously mentioned. Additional time to perform the one-constraint two-phase flow computation with 32 processors was 55%. On the contrary, with the use of the two-constraint algorithm, the two-phase computation needs only 16% more than the single-phase computation, which is a reasonable cost to study the moderate mass loading case with this configuration.

N_{procs}	1	2	4	8	16	32	64
Single-phase	1	0.504	0.257	0.122	0.063	0.035	0.025
Two-phase AVBP-EL (RIB)	1.09	0.557	0.278	0.143	0.086	0.054	0.045
Two-phase AVBP-EL (METIS)	1.09	0.533	0.266	0.131	0.075	0.041	0.028

Table 5.7 - *Summary of the CPU time ratios of AVBP-EL with a tetrahedron-based grid on a CRAY XD1 supercomputer.*

5.7 Conclusions

The main conclusions of this chapter are summarised here:

- In this configuration where particles are inertial, but still much dependent on the gas flow, prediction of particles motion strongly depend on the results for the gas phase. Results obtained with the Lagrangian version of AVBP (AVBP-EL) are in good agreement with the experiments, and with the results provided by the LES solver CDP. The accuracy in the single-phase case for radial and axial profiles of mean and fluctuating velocities are as good as the results from CDP except for the location of the recirculation zone which is slightly shifted upstream with the AVBP-EL solver.

- As a general remark, the axial evolution and the radial profiles of the mean and RMS particle velocities of the monodisperse and polydisperse cases are in good agreement with CDP results which validates all developments of the Lagrangian module implemented on the code. Concerning the gaseous results, the monodisperse and the polydisperse cases are very similar. The main important difference is in the levels of the mean gas velocity in the recirculation zone which are lower than expected. This implies a reduction in the size of the recirculation bubble in the polydisperse case. Since there are no differences in CPU time between the monodisperse and the polydisperse cases, trying to simulate this flow with a polydisperse particle distribution is closer to the experiments and the reality.

- The effect of the number of particles on the radial velocity profiles at three physical times ($t = 0.26,\ 1$, and 3.89 (s)) has been studied for the polydisperse case. Mean and RMS particle velocity profiles show an important improvement while increasing the average time, specially for the lightest ($d_p = 20\ \mu$m) and the heaviest particles ($d_p = 80\ \mu$m) since their number distributions are one of the lowest. Results of the classes 40 and 60 μm are less scattered since both of them contain an important number of samples after one second of physical time.

- A scalability study of the AVBP-EL solver has been performed on a CRAY XD1 supercomputer at CERFACS up to 64 processors. No particular problems related to load-balancing have been observed with the hexahedron-based grid and speedup results are very good. This results on two-phase flow simulations without almost any additional cost and open good perspectives for other future Lagrangian test cases in massively parallel machines. Results with the tetrahedron-based grid leads to a poor speedup if the domain is decomposed without considering particles information and a high load imbalance is presented. On the contrary, balancing particles with a multi-constraint partitioning algorithm improves considerably the speedup. As a result, to preserve a high parallel efficiency on massively parallel machines in cases intrinsically imbalance, the use of load balancing strategies is essential. Results obtained in this thesis confirm the competitive position of Lagrangian formulation compared to its principal competitor, the Eulerian formulation, reducing the disadvantages associated with the Lagrangian formulation.

- For the present case with moderate mass loading, the total number of particles per processor is moderate. The CPU and memory requirements to track particles is lower than for the gaseous phase even with the load balancing problem observed with one of the grids studied. Although the additional cost of Eulerian formulations is independent on the mass loading, for such a dilute case, the Lagrangian approach proved to be faster.

Conclusions and perspectives

Conclusions

Understanding combustion phenomena is the key to progress in terms of power supply, better performance and reduction of consumption in most of today industrial devices, but also directly conditions the control of the pollutants formation. Combustion is a highly non-linear and complex process in which chemistry, fluid mechanics, thermodynamics, radiation and phase change are deeply coupled. The first steps in combustion knowledge were obtained experimentally, but the potential of numerical simulation as a tool to investigate these phenomena, has grown significantly in the last few years with the application of direct numerical simulation (DNS) and large-eddy simulation (LES) to two-phase flow combustion. In many industrial devices, fuel is stored in condensed form and injected as a dispersed liquid phase in the combustion chamber where it mixes with the oxidizer and burns usually through a turbulent combustion process. In order to understand the physics of reactive two-phase flows, a Lagrangian formulation is proposed to treat the dispersed phase. One of the motivations of this study is the rapid increase in computing power which opens a new way for simulations that were prohibitive one decade ago.

The objective of the present thesis is the development and validation of a two-phase Lagrangian formulation on a parallel and unstructured solver, named AVBP, for large-eddy simulations of reacting flows. This solver is a parallel Computational Fluid Dynamics (CFD) code that solves turbulent compressible Navier-Stokes equations in two and three space dimensions. The handling of unstructured or hybrid grids is a key feature of AVBP and represents a major challenge in the implementation of the Lagrangian data structure. A related problem analysed in this thesis is the study of new partitioning algorithms to improve performance on massively parallel machines by reducing the size of partitions and the time of the algorithm to partition. An analysis of performance of the current partitioning algorithms is done and the need of a new partitioning algorithm is highlighted. The chosen algorithm is part of the software package METIS which offers multi-constraint partitioning algorithms and parallel facilities. This feature was used to add load-balancing capabilities to the Lagrangian version developed during this thesis. A comparative study between the new partitioning algorithm and those already available has shown a significant reduction of the CPU time used to partition the test grid and a reduction in the number of duplicated nodes resulting for the partition.

The use of a LES solver and different analysis of parallelism, reordering techniques of partitioning algorithms and computer precision lead indirectly to the study of sensitivity of chaotic systems to initial conditions. Any turbulent flow computed in LES exhibits significant sensitivity to small perturbations, leading to instantaneous solutions which can be totally different. On the contrary, laminar flows are almost insensitive to these parameters even for periodic simulations. One reason of

the divergence of solutions is the propagation of rounding errors in a naturally unstable (turbulent) flow induced by domain partitioning and scheduling of operations. The effect of different parameters is studied and results have been the object of a publication in *AIAA Journal* (see Appendix D).

The two-phase flow Lagrangian module was validated in an Homogeneous Isotropic Turbulence (HIT) which allows a simple analysis of several aspects of performance and particle behaviour. Firstly, a performance analysis of particle search algorithm at the beginning of the simulation was performed. The octree algorithm implemented in this thesis was compared to the simple brute force algorithm for a different number of particles per cell, and for a different number of processors. The octree algorithm showed to be noticeably faster than the brute-force algorithm, as expected. Then, the results of the fluid and particle kinetic energies were analysed and compared to another high-resolution Lagrangian solver, NTMIX3D. Results will show that the third-order spatial scheme (TTGC) performs perfectly well for this test case, providing results which are close to those obtained with the sixth-order scheme of NTMIX3D, which validates the Lagrangian formulation.

The second test case was chosen to validate the Lagrangian module in configurations similar to those encountered in real combustion chambers, in particular the turbulent dispersion properties predicted by the code. The test consists in a particle-laden bluff-body configuration from Borée *et al.* [22] where glass beads are injected into a complex recirculating flow. In this configuration where particles are inertial, although much dependent on the gas flow, the prediction of particles motion strongly depends on the gas phase. Results obtained with the Lagrangian formulation are in good agreement with the experiments, and with the results provided by the LES solver CDP developed at Stanford University. As a general remark, the axial evolution and the radial profiles of the mean and RMS particle velocities of the monodisperse and polydisperse cases are in good agreement with CDP results which validates all developments of the Lagrangian module implemented on the code. Concerning the gaseous results, the monodisperse and the polydisperse cases are very similar. The main difference is in the levels of the mean gas velocity in the recirculation zone which are lower than expected. This implies a reduction in the size of the recirculation bubble in the polydisperse case. Since there are no differences in CPU time between the monodisperse and the polydisperse cases, trying to simulate this flow with a polydisperse particle distribution is closer to the experiments and to reality. The effect of the number of particles on the radial velocity profiles at three physical times has been studied for the polydisperse case. Mean and RMS particle velocity profiles show an important improvement while increasing the average time.

A scalability study of the AVBP-EL solver has been performed on a CRAY XD1 supercomputer at CERFACS up to 64 processors. No particular problems related to load-balancing have been observed with the hexahedron-based grid and speedup is very good. Results with the tetrahedron-based grid leads to a poor speedup if the domain is decomposed without considering the information of particles position and a high load imbalance is presented. Nevertheless, balancing particles with a multi-constraint partitioning algorithm improves considerably the speedup. As a result, to preserve a high parallel efficiency on massively parallel machines in highly imbalanced simulations, the use of load balancing strategies is essential. The results obtained in this thesis confirm the competitive position of Lagrangian formulation compared to the Eulerian formulation once such strategies are efficiently implemented. All these results have been the object of a publication in *Journal of Computational Physics* (see Appendix E).

Perspectives

Despite all the work done in this thesis, a number of important developments deserve to be undertaken. Here we mentioned some of them: the introduction of an evaporation model to simulate two-phase reactive flows, the treatment of particle-wall interactions, the introduction of collision and coalescence models, improvement of particle injection (new geometries, new particle size distributions and multi-injection capabilities), introduction of unfiltered gas fluctuating velocity on particle velocity components, improvement of current search algorithms, etc.

During this thesis, at the beginning of 2007, two new PhD students from the FP6 European project ECCOMET (Efficient and clean combustion experts training) start to work on the Lagrangian version giving solution to an important number of these problems:

- F. Jaegle has introduced an evaporating model that has been validated in academic test cases and is currently working on particle-wall features.
- J.-M. Senoner is focused on the improvement of particle injection options.

In both cases, some of their developments are integrating part of the official Lagrangian version and the others will be included in a near future.

Bibliography

[1] K. Akselvoll & P. Moin (1996) Large-eddy simulation of turbulent confined coannular jets. *J. Fluid Mech.* **315**, 387–411.

[2] A. Albrecht, B. Bédat, T. Poinsot & O. Simonin (1999) Direct numerical simulation and modelling of evaporating droplets in homogeneous turbulence: application to turbulent flames. In *15th Annual Conference on Liquid Atomization and Spray System - ILASS Europe*. Toulouse, France.

[3] C. J. Alpert & A. B. Kahng (1995) Recent directions in netlist partitioning: a survey integration. *Integration: the VLSI Journal* **19** (1-2), 1–81.

[4] E. Anderson (2002) LAPACK3E a Fortran 90-enhanced version of LAPACK. *Tech. Rep.*.

[5] E. Anderson, Z. Bai, C. Bischof, S. Blackford, J. Demmel, J. Dongarra, J. Du Croz, A. Greenbaum, S. Hammarling, A. McKenney & D. Sorensen (1999) *LAPACK Users' guide, third edition*. SIAM, Philadelphia.

[6] S. V. Apte, K. Mahesh & T. Lundgren (2003) A Eulerian-Lagrangian model to simulate two-phase/particulate flows. In *Annual Research Briefs*, pp. 161–171. Center for Turbulence Research, NASA Ames/Stanford Univ.

[7] S. V. Apte, K. Mahesh, P. Moin & J. C. Oefelein (2003) Large-eddy simulation of swirling particle-laden flows in a coaxial-jet combustor. *Int. J. Multiphase Flow* **29** (8), 1311–1331.

[8] V. A. Barker, L. S. Blackford, J. J. Dongarra, J. Du Croz, S. Hammarling, M. Marinova, J. Wasniewski & P. Yalamov (2001) *LAPACK95 Users' guide*. SIAM, Philadelphia.

[9] S. T. Barnard & H. D. Simon (1993) A fast multilivel implementation of recursive spectral bisection for partitioning unstructured problems. In *Proc. of the 6th SIAM conference on Parallel Processing for Scientific Computing*, pp. 711–718.

[10] G. K. Batchelor (1949) Diffusion in a field of homogeneous turbulence. Eulerian analysis. *Aust. J. Sci. Res* **2**, 437–450.

[11] M. Baum & T. Poinsot (1992) A direct numerical simulation code for studies of combustion phenomena. *Tech. Rep.* 920201. Laboratoire EM2C du CNRS et de l'École Centrale de Paris.

[12] J. L. Bentley (1975) Multidimensional binary search trees used for associative searching. *Communications of the ACM* **18**, 509–517.

[13] M. J. Berger & S. H. Bokhari (1987) A partitioning strategy for nonuniform problems on multiprocessors. *IEEE Trans. on Computers* **C-36** (5), 570–580.

[14] P. Berkhin (2002) *Survey of clustering data-mining techniques*. Accrue Software, San Jose, USA.

[15] M. Bern & P. Blassmann (2000) Mesh generation. In *Handbook of Computational Geometry* (ed. Sack & Urrutia), chap. 6. Elsevier Science.

[16] J. Bertin (1981) *Graphics and Graphic Information Processing*. Berlin: Walter de Gruyter & Co., originally: *La graphique et le traitemente graphique de l'information*, 1967, translated in English by William J. Berg and Paul Scott.

[17] J. Bertin (1983) *Semiology of Graphics–Diagrams Networks Maps*. Madison: The University of Wisconsin Press., originally: *Semiologue graphique*, 1967, translated in English by William J. Berg.

[18] M. Boileau (2007) Simulation aux grandes échelles de l'allumage diphasique des foyers aéronautiques. Phd thesis, INP Toulouse.

[19] M. Boivin, O. Simonin & K. D. Squires (1998) Direct numerical simulation of turbulence modulation by particles in isotropic turbulence. *J. Fluid Mech.* **375**, 235–263.

[20] M. Boivin, O. Simonin & K. D. Squires (2000) On the prediction of gas-solid flows with two-way coupling using large eddy simulation. *Phys. Fluids* **12** (8), 2080–2090.

[21] J. Bonet & J. Periare (1991) An alternating digital tree (ADT) algorithm for 3D geometric searching and intersection problems. *Int. J. Numer. Meth. Eng.* **31** (1), 1–17.

[22] J. Borée, T. Ishima & I. Flour (2001) The effect of mass loading and inter-particle collisions on the development of the polydispersed two-phase flow downstream of a confined bluff body. *J. Fluid Mech.* **443**, 129–165.

[23] H. Boughanem (1998) Évaluation des termes de transport et de dissipation de surface de flamme par simulation numérique directe de la combustion turbulente. Phd thesis, Université de Rouen.

[24] H. Boughanem & A. Trouvé (1996) Validation du code de simulation directe NTMIX3D pour le calcul des écoulements turbulents réactifs. *Tech. Rep.* 42907. Institut Français du Pétrole.

[25] J. Boussinesq (1877) Essai sur la théorie des eaux courantes. *26ème édn. Acad. Sci. Paris* .

[26] A. N. Brooks & T. Hugues (1982) Streamline upwind/Petrov-Galerkin formulations for convection dominated flows with particular emphasis on the incompressible Navier-Stokes equations. *Comput. Methods Appl. Mech. Eng.* **32**.

[27] A. B. Chace (1979) *The Rhind Mathematical Papyrus*. National Council of Teachers of Mathematics, Reston, VA, The cited quote is from Volume 1, pp. 48-49.

[28] S. de Chaisemartin, L. Fréret, D. Kah, F. Laurent, R. O. Fox, J. Réveillon & M. Massot (2008) Turbulent combustion of polydisperse evaporating sprays with droplets crossing: Eulerian modeling and validation in the infinite Knudsen limit. In *Proc. of the Summer Program*. Center for Turbulence Research, NASA Ames/Stanford Univ.

[29] J. R. Chasnov (1991) Simulation of the Kolmogorov inertial subrange using an improved subgrid model. *Phys. Fluids A* **3** (1), 188–200.

[30] C. H. Chen (2002) Generalized association plots: Information visualization via iteratively generated correlation matrices. *Statistica Sinica* **12**, 7–29.

[31] K. H. Chen & J. S. Shuen (1993) Analysis of transcritical spray phenomena in turbulent mixing layers. *31st AIAA Aerospace Sciences Meeting* (AIAA 93-0108).

[32] R. Clift, J. R. Grace & M. E. Weber (1978) *Bubbles, Drops, and Particles*. Academic Press.

[33] O. Colin & M. Rudgyard (2000) Development of high-order Taylor-Galerkin schemes for unsteady calculations. *J. Comput. Phys.* **162** (2), 338–371.

[34] G. Comte-Bellot (1965) Écoulement turbulent entre deux parois parallèles. *Publ. Sci. Tech. Min. Air.* (419).

[35] C. Crowe, M. Sommerfeld & Y. Tsuji (1998) *Multiphase Flows with Droplets and Particles*.

[36] B. Cuenot & T. Poinsot (1996) Asymptotic and numerical study of diffusion flames with variable Lewis number and finite rate chemistry. *Combust. Flame* **104**, 111–137.

[37] D. E. Culler & A. Gupta J. P. Singh (1999) *Parallel Computer Architecture: A Hardware/Software Approach*. Morgan Kaufmann Publishers.

[38] E. Cuthill & J. McKee (1969) Reducing the bandwidth of sparse symmetric matrices. In *Proceedings of the 24th National Conference of the ACM*, pp. 157–172.

[39] J. Deardorff (1970) A numerical study of three-dimensional turbulent channel flow at large Reynolds numbers. *J. Fluid Mech.* **41**, 453–480.

[40] J. W. Deardorff (1974) Three-dimensional numerical study of the height and mean structure of a heated planetary boundary layer. *Boundary-Layer Meteorology* **7** (1), 81–106.

[41] P. Dellenback, D. Metzger & G. Neitzel (1988) Measurement in turbulent swirling flows through an abrupt axisymmetric expansion. *AIAA Journal* **13** (4), 669–681.

[42] E. Deutsch (1992) Dispersion de particules dans une turbulence homogène isotrope stationnaire calculée par simulation numérique directe des grandes échelles. Phd thesis, EDF-DRD.

[43] J. Donea (1984) Taylor-Galerkin method for convective transport problems. *Int. J. Numer. Meth. Fluids* **20** (1), 101–119.

[44] J. Donea, L. Quartapelle & V. Selmin (1987) An analysis of time discretization in the finite element solution of hyperbolic problems. *J. Comput. Phys.* **70**, 463–499.

[45] H. L. Dryden & A. M. Kuethe (1930) Effect of turbulence in wind tunnel measurements. *Tech. Rep.* 342. Natl. Advisory Comm. Aeronaut.

[46] F. Ducros, P. Comte & M. Lesieur (1996) Large-eddy simulation of transition to turbulence in a boundary layer developing spatially over a flat plate. *J. Fluid Mech.* **326**, 1–36.

[47] F. Ducros, F. Nicoud & T. Poinsot (1998) Wall-adapting local eddy-viscosity models for simulations in complex geometries. In *ICFD*, pp. 293–300. Baines M. J.

[48] I. S. Duff, A. M. Erisman & J. K. Reid (1986) *Direct methods for sparse matrices*. Oxford University Press.

[49] A. E. Dunlop & B. W. Kernighan (1985) A procedure for placement of standard-cell VLSI circuits. *IEEE Trans. on Computers - Aided Design of Integrated Circuits and Systems* **CAD-4** (1), 92–98.

[50] J. K. Eaton & J. R. Fessler (1994) Preferential concentration of particles by turbulence. *Int. J. Multiphase Flow* **20**, 169–209.

[51] S. Elghobashi & G. C. Truesdell (1992) Direct simulation of particle dispersion in a decaying isotropic turbulence. *J. Fluid Mech.* **242**, 655–700.

[52] S. Elghobashi & G. C. Truesdell (1993) On the two-way interaction between homogeneous turbulence and dispersed solid particles. I: Turbulence modification. *Phys. Fluids* **5** (7), 1790–1801.

[53] E. Elmroth & F. Gustavson (2001) A faster and simpler recursive algorithm for the LAPACK routine DGELS. *BIT Numerical Mathematics* **41** (5), 936–949.

[54] G. M. Faeth (1983) Evaporation and combustion of sprays. *Prog. Energy Comb. Sci.* **9**, 1–76.

[55] G. M. Faeth (1987) Mixing, transport and combustion sprays. *Prog. Energy Comb. Sci.* **13** (4), 293–345.

[56] A. Favre (1969) Statistical equations of turbulent gases. In *Problems of hydrodynamics and continuum mechanics*, pp. 231–266. Philadelphia: SIAM.

[57] H. Faxen (1922) Der Widerstand gegen die Bewegung einer starren Kugel in einer zähen Flüssigkeit, die zwischen zwei parallelen ebenen Wänden eingeschlossen ist. *Annalen der Physik* **68**, 89–119.

[58] P. Fede & O. Simonin (2006) Numerical study of the subgrid fluid turbulence effects on the statistics of heavy colliding particles. *Phys. Fluids* **18** (045103).

[59] Y. T. Feng & D. R. J. Owen (2002) An augmented spatial digital tree algorithm for contact detection in computational mechanics. *Int. J. Numer. Meth. Eng.* **55**, 159–176.

[60] P. Février & O. Simonin (2000) Statistical and continuum modelling of turbulent reactive particulate flows. Part 2: Application of a two-phase second-moment transport model for prediction of turbulent gas-particle flows. In *Theoretical and Experimental Modeling of Particulate Flows, Lecture Series 2000-06, von Karman Institute for Fluid Dynamics, Rhode Saint Genese (Belgium)*.

[61] P. Février, O. Simonin & K. Squires (2005) Partitioning of particle velocities in gas-solid turbulent flows into a continuous field and a spatially uncorrelated random distribution: Theoretical formalism and numerical study. *J. Fluid Mech.* **533**, 1–46.

[62] J. Fingberg, A. Basermann, G. Lonsdale, J. Clinckermaillie, J. Gratien & R. Ducloux (2000) Dynamic load-balancing for parallel structural mechanics simulations with DRAMA. In *ECT2000*.

[63] R. Finkel & J. L. Bentley (1974) Quad trees: A data structure for retrieval of composite keys. *Acta Informatica* **4** (1), 1–9.

[64] M. J. FLynn (1972) Some computer organizations and their effectiveness. *IEEE Trans. on Computers* **C-21** (9), 948–960.

[65] L. Fréret, F. Laurent, S. de Chaisemartin, D. Kah, R. O. Fox, P. Vedula, J. Reveillon, O. Thomine & M. Massot (2008) Turbulent combustion of polydisperse evaporating sprays with droplet crossing: Eulerian modeling of collisions at finite Knudsen and validation. In *Proc. of the Summer Program*. Center for Turbulence Research, NASA Ames/Stanford Univ.

[66] J. C. H. Fung, J. C. R. Hunt, N. A. Malik & R. J. Perkins (1992) Kinematic simulation of homogeneous turbulence by unsteady random Fourier modes. *J. Fluid Mech.* **236**, 281–318.

[67] M. García (2003) Analysis of precision differences observed for the AVBP code. *Tech. Rep.* TR/CFD/03/84. CERFACS, Toulouse, France.

[68] M. García (2007) Interpolateur parallèle de solutions. Projet ANR CAMPAS, Livrable L3 CR/CFD/07/149. CERFACS, Toulouse, France.

[69] M. García, Y. Sommerer, T. Schönfeld & T. Poinsot (2005) Evaluation of Euler/Euler and Euler/Lagrange strategies for large eddy simulations of turbulent reacting flows. In *ECCOMAS Thematic Conference on Computational Combustion*.

[70] R. Gatignol (1983) The Faxén formulae for a rigid particle in an unsteady non-uniform Stokes flow. *J. Méc. Théor. Appl.* **1** (2), 143–160.

[71] A. George (1971) Computer implementation of the finite element method. *Tech. Rep.* STAN-CS-208. Stanford University, Department of Computer Science.

[72] M. Germano, U. Piomelli, P. Moin & W. Cabot (1991) A dynamic subgrid-scale eddy viscosity model. *Phys. Fluids* **3** (7), 1760–1765.

[73] N. Gibbs, W. Poole & P. Stockmeyer (1976) A comparison of several bandwidth and profile reduction algorithms. *ACM Trans. Math. Software* **2**, 322–330.

[74] L. Giraud, P. Noyret, E. Sevault & V. Van Kemenade (1995) IPM - User's guide and reference manual. *Tech. Rep.* TR/PA/95/01. CERFACS, Toulouse, France.

[75] A. K. Gupta, D. G. Lilley & N. Syred (1984) *Swirl flows*. Abacus Press.

[76] F. Ham, S. V. Apte, G. Iaccarino, X. Wu, M. Herrmann, G. Constantinescu, K. Mahesh & P. Moin (2003) Unstructured LES of reacting multiphase flows in realistic gas turbine combustors. In *Annual Research Briefs*, pp. 139–160. Center for Turbulence Research, NASA Ames/Stanford Univ.

[77] F. Ham & G. Iaccarino (2004) Energy conservation in collocated discretization schemes on unstructured meshes. In *Annual Research Briefs*, pp. 3–14. Center for Turbulence Research, NASA Ames/Stanford Univ.

[78] G. Hanrot, V. Lefèvre, D. Stehlé & P. Zimmermann (2007) Worst cases for a periodic function with large arguments. In *Proceedings of the 18th IEEE Symposium on Computer Arithmetic* (ed. Peter Kornerup & Jean-Michel Muller), pp. 133–140. Los Alamitos, CA: IEEE Computer Society Press.

[79] R. J. Hanson & A. Thomas (1984) Flame development in swirling flows in closed vessels. *Combust. Flame* **55**, 255–277.

[80] R. von Hanxleden & L. R. Scott (1991) Load balancing on message passing architectures. *J. Parallel and Distributed Computing* **13** (3), 312–324.

[81] J. A. Hartigan (1972) Direct clustering of a data matrix. *Journal of the American Statistical Association* **67** (337), 123–129.

[82] A. Haselbacher, F. M. Najjar & J. P. Ferry (2007) An efficient and robust particle-localization algorithm for unstructured grids. *J. Comput. Phys.* **225** (2), 2198–2213.

[83] D. C. Haworth & K. Jansen (2000) Large-eddy simulation on unstructured deforming meshes: towards reciprocating IC engines. *Comput. Fluids* **29**, 493–524.

[84] B. T. Helenbrook & C. F. Edwards (2002) Quasi-steady deformation and drag of uncontaminated liquid drops. *Int. J. Multiphase Flow* **28** (10), 1631–1657.

[85] B. Hendrickson & K. Devine (2000) Dynamic load balancing in computational mechanics. *Comput. Methods Appl. Mech. Eng.* **2-4** (184), 485–500.

[86] B. Hendrickson & R. Leland (1993) A multilevel algorithm for partitioning graphs. *Tech. Rep.* SAND93-1301. Sandia National Laboratories, Albuquerque, NM.

[87] B. Hendrickson & R. Leland (1995) The Chaco user's guide, version 2.0. *Tech. Rep.* SAND95-2344. Sandia National Laboratories, Albuquerque, NM.

[88] J. O. Hinze (1987) *Turbulence*. McGraw-Hill Classic Textbook Reissue.

[89] C. Hirsch (2007) Finite volume method and conservative discretization with an introduction to finite element method. In *Numerical Computation of internal & external flows: Fundamentals of Computational Fluid Dynamics, second edition*, chap. 5, pp. 203–248. New York: John Wiley & Sons.

[90] J. C. R. Hunt, J. C. Buell & A. A. Wray (1987) Big whorls carry little whorls. In *Proc. of the Summer Program*, pp. 77–94. Center for Turbulence Research, NASA Ames/Stanford Univ.

[91] IEEE (1985) *IEEE Standard for Binary Floating-Point Arithmetic*. ANSI/IEEE Std 754-1985. Institute of Electrical and Electronics Engineers, New York.

[92] T. Ishima, J. Borée, P. Fanouillère & I. Flour (1999) Presentation of a two phase flow data base obtained on the flow loop Hercule. In *Proc. of the 9th Workshop on Two-Phase Flow Predictions*. Merseburg, Germany.

[93] J. Jiménez (2004) Turbulence and vortex dynamics. *Tech. Rep.*. École Polytechnique, Madrid.

[94] R. W. Johnson (1998) *The handbook of fluid dynamics*. CRC Press.

[95] G. Karypis & V. Kumar (1998) A fast and high quality multilevel scheme for partitioning irregular graphs. *SIAM Journal on Scientific Computing* **20** (1), 359–392.

[96] G. Karypis & V. Kumar (1998) Multilevel algorithms for multi-constraint graph partitioning. *Tech. Rep.* 98-019. University of Minnesota, Department of Computer Science/Army HPC Research Center.

[97] G. Karypis, K. Schloegel & V. Kumar (2003) *Parmetis: Parallel Graph Partitioning and Sparse Matrix Ordering Library*. Univ. of Minnesota, Department of Computer Science and Engineering, USA, (version 3.1).

[98] A. Kaufmann (2004) Vers la simulation des grandes échelles en formulation Euler/Euler des écoulements réactifs diphasiques. Phd thesis, INP Toulouse.

[99] J. de Keyser & D. Roose (1992) Grid partitioning by inertial recursive bisection. *K. U. Leuven, Dept. of Computer Science, Belgium* **Report TW 174**.

[100] J. Kim & P. Moin (1985) Application of a fractional-step method to incompressible Navier-Stokes equations. *J. Comput. Phys.* **59** (2), 308–323.

[101] D. E. Knuth (1997) *The Art of Computer Programming: Fundamental Algorithms*. Addison-Wesley, Reading, MA, third edition, Vol. 1.

[102] D. E. Knuth (1998) *The Art of Computer Programming: Sorting and Searching*. Addison-Wesley, Reading, MA, second edition, Vol. 3.

[103] A. N. Kolmogorov (1941) The local structure of turbulence in incompressible viscous fluid for very large Reynolds numbers. *C.R. Acad. Sci. USSR* **30**, 301.

[104] R. H. Kraichnan (1976) Eddy viscosity in two and three dimensions. *J. Atmos. Sci.* **33**, 1521–1536.

[105] V. Kumar (2000) Graph partitioning for dynamic, adaptive and multi-phase computations. In *Workshop "Resource Recovery"*. Material from IMA Talks.

[106] K. K. Kuo (1986) *Principles of Combustion*. New York: John Wiley.

[107] N. Lamarque (2007) Schémas numériques et conditions limites pour la simulation aux grandes échelles de la combustion diphasique dans les foyers d'hélicoptère. Phd thesis, INP Toulouse.

[108] J. Lavedrine (2008) Simulations aux grandes échelles de l'écoulement diphasique dans des modèles d'injecteur de moteurs aéronautiques. Phd thesis, INP Toulouse.

[109] J. Laviéville (1997) Simulations numériques et modélisation des interactions entre l'entrainement par la turbulence et les collisions interparticulaires en écoulement gaz-solide. Phd thesis, Université de Rouen.

[110] P. D. Lax & B. Wendroff (1960) Systems of conservation laws. *Commun. Pure Appl. Math.* **13**, 217–237.

[111] P. D. Lax & B. Wendroff (1964) Difference schemes for hyperbolic equations with high order of accuracy. *Commun. Pure Appl. Math.* **17**, 381–398.

[112] A. H. Lefebvre (1989) *Atomization and Sprays*. Taylor & Francis.

[113] C. Leith (1971) Atmospheric predictability and two-dimensional turbulence. *J. Atmos. Sci.* **28** (2), 145–161.

[114] S. Lele (1992) Compact finite difference schemes with spectral like resolution. *J. Comput. Phys.* **103**, 16–42.

[115] A. Leonard (1974) Energy cascade in large eddy simulations of turbulent fluid flows. *Adv. Geophys.* **18** (A), 237–248.

[116] J. G. Lewis (1982) The Gibbs-Poole-Stockmeyer and Gibbs-King algorithms for reordering sparse matrices. *ACM Trans. Math. Software* **8** (2), 190–194.

[117] D. K. Lilly (1967) The representation of small-scale turbulence in numerical simulation experiments. In *Proceedings of the IBM Scientific Computing Symposium on Environmental Sciences*, pp. 195–210. Yorktown Heights, USA.

[118] D. K. Lilly (1992) A proposed modification of the Germano sub-grid closure method. *Phys. Fluids* **4** (3), 633–635.

[119] W.-H. Liu & A. H. Sherman (1976) Comparative analysis of the Cuthill-McKee and the reverse Cuthill-McKee ordering algorithms for sparse matrices. *SIAM Journal of Numerical Analysis* **13** (2), 198–213.

[120] R. Löhner (1995) Robust Vectorised Search Algorithms for Interpolation on Unstructured Grids. *J. Comput. Phys.* **118** (2), 380–387.

[121] R. Löhner & J. Ambrosiano (1990) A Vectorised Particle Tracer for Unstructured Grids. *J. Comput. Phys.* **91** (1), 22–31.

[122] E. N. Lorenz (1963) Deterministic nonperiodic flow. *J. Atmos. Sci.* **20** (2), 130–141.

[123] E. N. Lorenz (1993) *The essence of chaos*. University of Washington Press, Chapters 1-2.

[124] T. S. Lundgren (2003) Linear forced isotropic turbulence. In *Annual Research Briefs*, pp. 461–473. Center for Turbulence Research, NASA Ames/Stanford Univ.

[125] K. Mahesh, G. Constantinescu & P. Moin (2004) A numerical method for large-eddy simulation in complex geometries. *J. Comput. Phys.* **197** (1), 215–240.

[126] P. J. Mason (1994) Large-eddy simulation: a critical review of the technique. *Quarterly Journal of the Royal Meteorology Society* **120 (A)** (515), 1–26.

[127] A. Massol (2004) Simulation d'écoulement autour de réseaux de particules sphériques. Phd thesis, INP Toulouse.

[128] M. R. Maxey (1987) The gravitational settling of aerosol particles in homogeneous turbulence and random flow fields. *J. Fluid Mech.* **174**, 441–465.

[129] M. R. Maxey & J. J. Riley (1983) Equation of motion for a small rigid sphere in a nonuniform flow. *Phys. Fluids* **26** (4), 883–889.

[130] R. Mei, R. J. Adrian & T. J. Hanratty (1991) Particle dispersion in isotropic turbulence under Stokes drag and Basset force with gravitational settling. *J. Fluid Mech.* **225**, 481–495.

[131] O. Métais & M. Lesieur (1986) Statistical probability of decaying turbulence. *Journal of Atmospheric Science* **43** (9), 857–870.

[132] P. Moin (2004) Large eddy simulation of multi-phase turbulent flows in realistic combustors. *Prog. Comput. Fluid Dynamics* **4**, 237–240.

[133] P. Moin & S. V. Apte (2006) Large-eddy simulation of realistic gas turbine combustors. *Am. Inst. Aeronaut. Astronaut. J.* **44** (4), 698–708.

[134] P. Moin & J. Kim (1982) Numerical investigation of turbulent channel flow. *J. Fluid Mech.* **118**, 341–377.

[135] M. Moreau (2006) Modélisation numérique directe et des grandes échelles des écoulements turbulents gaz-particules dans le formalisme eulérien mésoscopique. Phd thesis, INP Toulouse.

[136] J.-B. Mossa (2005) Extension polydisperse pour la description Euler-Euler des écoulements diphasiques réactifs. Phd thesis, INP Toulouse.

[137] V. Moureau (2004) Simulation aux grandes échelles de l'aérodynamique interne des moteurs à piston. Phd thesis, École Centrale Paris.

[138] V. Moureau, G. Lartigue, Y. Sommerer, C. Angelberger, O. Colin & T. Poinsot (2005) High-order methods for DNS and LES of compressible multi-component reacting flows on fixed and moving grids. *J. Comput. Phys.* **202** (2), 710–736.

[139] R. A. Mugele & H. D. Evans (1951) Droplet size distribution in sprays. *Ind. Engr. Chem.* **43** (6), 1317–1324.

[140] J. A. Mulholland, R. K. Srivastava & J. O. L. Wendt (1988) Influence of droplet spacing on drag coefficient in nonevaporating, monodisperse streams. *AIAA Journal* **26** (10), 1231–1237.

[141] J.-D. Müller (2008) *A User's guide to hip*. CERFACS, Toulouse, France, (version 1.23 "Kaa").

[142] C. Narayanan, D. Lakehal & G. Yadigaroglu (2002) Linear stability analysis of particle-laden mixing layers using Lagrangian particle tracking. *Powder Technology* **125** (2-3), 122–130.

[143] F. Nicoud (1999) Defining wave amplitude in characteristic boundary conditions. *J. Comput. Phys.* **149** (2), 418–422.

[144] J. C. Oefelein & V. Yang (1996) Analysis of transcritical spray phenomena in turbulent mixing layers. *34th AIAA Aerospace Sciences Meeting* (AIAA 96-0085).

[145] C. W. Oseen (1910) Über die Stokes'sche Formel und über eine verwandte Aufgabe in der Hydrodynamik. *Arkiv. Mat. Astron. Physik* **6** (29).

[146] M. L. Overton (2001) *Numerical Computing with IEEE Floating Point Arithmetic*. SIAM, Philadelphia.

[147] R. Pandya & F. Mashayek (2002) Two-fluid large-eddy simulation approach for particle-laden turbulent flows. *Int. J. Heat and Mass Transfer* **45**, 4753–4759.

[148] S. Pannala & S. Menon (1998) Large eddy simulations of two-phase turbulent flows. *36th AIAA Aerospace Sciences Meeting* (AIAA 98-0163).

[149] Y. H. Pao (1965) Structure of turbulent velocity and scalar fields at large wavenumbers. *Phys. Fluids* **8**, 1063–1075.

[150] Y. H. Pao (1968) Transfert of turbulent energy and scalar quantities at large wavenumbers. *Phys. Fluids* **11**, 1371–1372.

[151] R. Paoli, J. Hélie & T. Poinsot (2004) Contrail formation in aircraft wakes. *J. Fluid Mech.* **502**, 361–373.

[152] R. Paoli & K. Shariff (2004) Direct numerical simulation of turbulent condensation in clouds. In *Annual Research Briefs*, pp. 305–316. Center for Turbulence Research, NASA Ames/Stanford Univ.

[153] R. Paoli & K. Shariff (2008) Turbulent condensation of droplets: direct simulation and a stochastic model. *J. Atmos. Sci.* **DOI 10.1175/2008JAS2734.1**.

[154] S. Pascaud (2006) Vers la simulation aux grandes échelles des écoulements turbulents diphasiques réactifs: application aux foyers aéronautiques. Phd thesis, INP Toulouse.

[155] T. Passot & A. Pouquet (1987) Numerical simulation of compressible homogeneous flows in the turbulent regime. *J. Fluid Mech.* **181**, 441–466.

[156] F. Pellegrini (2007) Scotch and libscotch 5.0 user's guide. *Tech. Rep.*. ENSEIRB and LaBRI, Université Bordeaux I, Talence, France.

[157] C. D. Pierce & P. Moin (1998) Large eddy simulation of a confined coaxial jet with swirl and heat release. In *29th Fluid Dynamics Conference* (ed. AIAA Paper 98-2892). Albuquerque, NM.

[158] U. Piomelli (1993) High Reynolds number calculations using the dynamic subgrid-scale stress model. *Phys. Fluids A* **5**, 1484–1490.

[159] H. Pitsch & N. Peters (1998) A consistent flamelet formulation for non-premixed combustion considering differential diffusion effects. *Combust. Flame* **114**, 26–40.

[160] R. W. Pitz & J. W. Daily (1983) Combustion in a turbulent mixing layer formed at a rearward facing step. *AIAA Journal* **21**, 1565–1570.

[161] T. Poinsot (1987) Analyse des instabilités de combustion de foyers turbulents prémélangés. Thèse d'état, Université d'Orsay.

[162] T. Poinsot, D. Haworth & G. Bruneaux (1993) Direct simulation and modelling of flame-wall interaction for premixed turbulent combustion. *Combust. Flame* **95** (1/2), 118–133.

[163] T. Poinsot & S. Lele (1992) Boundary conditions for direct simulations of compressible viscous flows. *J. Comput. Phys.* **101** (1), 104–129.

[164] T. Poinsot & D. Veynante (1999) Combustion numérique. *Cours de DEA, ENSEEIHT-IMFT* .

[165] T. Poinsot & D. Veynante (2005) *Theoretical and numerical combustion*. R.T. Edwards, 2nd edition.

[166] A. Pothen, H. D. Simon & K.-P. Liou (1990) Partitioning sparse matrices with eigenvectors of graphs. *SIAM J. Matrix Anal. Appl.* **11** (3), 430–452.

[167] R. Preis & R. Diekmann (1996) The PARTY partitioning-library, user guide - version 1.1. *Tech. Rep.* tr-rsfb-96-024. Dept. of Computer Science, Univ. of Paderborn, Paderborn, Germany.

[168] W. H. Press, S. A. Teukolsky, W. T. Vetterling & B. P. Flannery (1996) *Numerical recipes in Fortran 90 (second edition): the art of parallel scientific computing*. New York, NY, USA: Cambridge University Press.

[169] W. H. Press, S. A. Teukolsky, W. T. Vetterling & B. P. Flannery (2003) *Numerical Recipes in Fortran 77, The Art of Scientific Computing, second edition*. Cambridge: Cambridge University Press.

[170] C. Prière (2005) Simulation aux grandes échelles : application au jet transverse. Phd thesis, INP Toulouse.

[171] L. Quartapelle & V. Selmin (1993) High-order Taylor-Galerkin methods for non-linear multidimensional problems.

[172] A. Quarteroni & A. Valli (1999) *Domain Decomposition Methods for Partial Differential Equations*. Oxford Science Publications.

[173] M. W. Reeks (1991) On a kinetic equation for the transport of particles in turbulent flows. *Phys. Fluids* **3** (3).

[174] M. W. Reeks (1993) On the constitutive relations for dispersed particles in nonuniform flows. I. dispersion in a simple shear flow. *Phys. Fluids* **5** (3), 750–761.

[175] M. W. Reeks & S. McKee (1984) The dispersive effects of Basset history forces on particle motion in a turbulent flow. *J. Fluid Mech.* **27** (7), 1573–1582.

[176] J. Réveillon, C. Pera, M. Massot & R. Knikker (2004) Eulerian analysis of the dispersion of evaporating polydispersed sprays in a statistically stationary turbulent flow. *J. Turb.* **5** (1), 1–27.

[177] O. Reynolds (1883) An experimental investigation of the circumstances which determine the motion of water shall be direct or sinuous, and the law of resistance in parallel channels. *Philos. Trans. R. Soc. London Ser. A* **174**, 935–982.

[178] O. Reynolds (1894) On the dynamical theory of incompressible viscous flows and the determination of the criterion. *Philos. Trans. R. Soc. London Ser. A* **186**, 123–161.

[179] E. Riber (2007) Développement de la méthode de simulation aux grandes échelles pour les écoulements diphasiques turbulents. Phd thesis, INP Toulouse.

[180] E. Riber, M. Moreau, O. Simonin & B. Cuenot (2005) Towards large eddy simulation of non-homogeneous particle laden turbulent gas flows using Euler-Euler approach. In *11th Workshop on Two-Phase Flow Predictions*. Merseburg, Germany.

[181] L. F. Richardson (1922) *Weather Prediction by Numerical Process*. Cambridge University Press.

[182] S. Roux, G. Lartigue, T. Poinsot, U. Meier & C. Bérat (2005) Studies of mean and unsteady flow in a swirled combustor using experiments, acoustic analysis and large eddy simulations. *Combust. Flame* **141**, 40–54.

[183] M. Rudgyard (1990) Cell vertex methods for compressible gas flows. Phd thesis, Oxford University Computing Laboratory.

[184] M. Rudgyard (1993) Cell vertex methods for steady inviscid flow. In *Lectures Series 1993-04*. Von Karman Institute for Fluid Dynamics.

[185] A. Safjan & J. T. Oden (1994) High-order Taylor-Galerkin methods for linear hyperbolic systems. *J. Comput. Phys.* **120**, 206–230.

[186] P. Sagaut (1998) *Introduction à la simulation des grandes échelles*, mathématiques & applications edn. Springer.

[187] P. Sagaut (1998) *Large Eddy Simulation for Incompressible Flows*. Berlin: Springer.

[188] H. Samet (1984) The quadtree and related hierarchical data structures. *J. Comput. Phys.* **16** (2), 187–260.

[189] V. Sankaran & S. Menon (2002) LES of spray combustion in swirling flows. *J. Turb.* **3**, 011.

[190] R. W. Schefer, M. Namazian & J. Kelly (1994) Velocity measurements in turbulent bluff-body stabilized flows. *Am. Inst. Aeronaut. Astronaut. J.* **32** (9), 1844–1851.

[191] L. Schiller & A. Naumann (1935) A drag coefficient correlation. *VDI Zeitung* **77**, 318–320.

[192] K. Schloegel, G. Karypis & V. Kumar (2002) Graph partitioning for high-performance scientific simulations. In *Sourcebook on Parallel Computing* (ed. J. Dongarra, I. Foster, G. Fox, W. Gropp, K. Kennedy, L. Torczon & A. White), chap. 18, pp. 491–541. San Francisco, CA: Morgan Kaufmann.

[193] T. Schönfeld & M. Rudgyard (1998) COUPL and its use within hybrid mesh CFD applications. In *Proc. of the 10th International Conference on Parallel CFD 98* (ed. A. Ecer, D. Emerson, J. Périaux & N. Satofuka). Hsinchu, Taiwan: Elsevier, Amsterdam.

[194] T. Schönfeld & M. Rudgyard (1999) Steady and unsteady flows simulations using the hybrid flow solver AVBP. *AIAA Journal* **37** (11), 1378–1385.

[195] U. Schumann (1975) Subgrid scale model for finite difference simulations of turbulent flows in plane channels and annuli. *J. Comput. Phys.* **18**, 376–404.

[196] D. Seldner & T. Westermann (1988) Algorithms for Interpolation and Localization in Irregular 2D Meshes. *J. Comput. Phys.* **79** (1), 1–11.

[197] L. Selle, G. Lartigue, T. Poinsot, P. Kaufmann, W. Krebs & D. Veynante (2002) Large-eddy simulation of turbulent combustion for gas turbines with reduced chemistry. In *Proc. of the Summer Program*, pp. 333–344. Center for Turbulence Research, NASA Ames/Stanford Univ.

[198] J.-M. Senoner, M. García, S. Mendez, G. Staffelbach, O. Vermorel & T. Poinsot (2008) Growth of Rounding Errors and Repetitivity of Large-Eddy Simulations. *AIAA Journal* **46** (7), 1773–1781.

[199] J. Shi & J. Malik (1997) Normalized cuts and image segmentation. In *Proc. of the 1997 IEEE Computer Society Conference on Computer Vision and Pattern Recognition*, pp. 731–737. IEEE Computer Society Press.

[200] H. D. Simon (1991) Partitioning of unstructured problems for parallel processing. *Computing Systems in Eng.* **2/3**, 135–148.

[201] H. D. Simon & S.-H. Teng (1997) How good is recursive bisection? *SIAM J. Sci. Comput.* **18** (5), 1436–1445.

[202] O. Simonin (1991) Prediction of the dispersed phase turbulence in particle-laden jets. In *Proc. 1st Int. Symp. Gas-Solid Flows*, pp. 197–206. ASME.

[203] D. G. Sloan, P. J. Smith & L. D. Smoot (1986) Modeling of swirl in turbulent flow systems. *Prog. Energy Comb. Sci.* **12**, 163–250.

[204] J. Smagorinsky (1963) General circulation experiments with the primitive equations: I. The basic experiment. *Mon. Weather Rev.* **91** (3), 99–164.

[205] W. H. Snyder & J. L. Lumley (1971) Some measurements of particle velocity autocorrelation functions in a turbulent flow. *J. Fluid Mech.* **48** (1), 41–71.

[206] K. D. Squires & J. K. Eaton (1990) Particle response and turbulence modification in isotropic turbulence. *Phys. Fluids A* **2** (7), 1191–1203.

[207] K. D. Squires & J. K. Eaton (1991) Measurements of particle dispersion obtained from direct numerical simulations of isotropic turbulence. *J. Fluid Mech.* **226**, 1–35.

[208] K. D. Squires & J. K. Eaton (1991) Preferential concentration of particles by turbulence. *Phys. Fluids A* **3** (5), 1169–1178.

[209] J. S. Stoer & R. Bulirsch (1980) *An introduction to numerical analysis*. Berlin: Springer.

[210] A. Stoessel, M. Hilka & M. Baum (1994) 2D direct numerical simulation of turbulent combustion on massively parallel processing platforms. In *1994 EUROSIM Conference on Massively Parallel Computing*, pp. 793–800. Delft: Elsevier Science B.V.

[211] G. G. Stokes (1851) On the effect of the inertial friction of fluids on the motions of pendulums. *Trans. Cambridge Phil. Soc.* **9**, 8–23.

[212] R. Struijs, I. d'Ast, T. Schönfeld, M. Rudgyard, F. Nicoud, G. Hernandez & O. Colin (1996) AVBP Version 3.0 results on some basic test cases. *Tech. Rep.* TR/CFD/96/10. CERFACS.

[213] S. Sundaram & L. R. Collins (1999) A numerical study of the modulation of isotropic turbulence by suspended particles. *J. Fluid Mech.* **379**, 105–143.

[214] G. I. Taylor (1921) Diffusion by continuous movements. *Proc. London Math. Soc* **20**, 196–211.

[215] V. E. Taylor & B. Nour-Omid (1994) A study of the factorization fill-in for a parallel implementation of the finite element method. *Int. J. Numer. Meth. Eng.* **37** (22), 3809–3823.

[216] C.-M. Tchen (1947) Mean value and correlation problems connected with the motion of small particles suspended in a turbulent fluid. Phd thesis, Technical University of Delft, Netherlands.

[217] P. J. Thomas (1992) On the influence of the Basset history force on the motion of the particle through a fluid. *Phys. Fluids* **4** (9), 2090–2093.

[218] M. Van Dyke (1982) *An Album of Fluid Motion*. The Parabolic Press, Stanford, CA.

[219] M. W. Vance, K. D. Squires & O. Simonin (2006) Properties of the particle velocity field in gas-solid turbulent channel flow. *Phys. Fluids* **18** (063302).

[220] O. Vermorel, B. Bédat, O. Simonin & T. Poinsot (2003) Numerical study and modelling of turbulence modulation in a particle laden slab flow. *J. Turb.* **4, 025**.

[221] J.-F. Virepinte (1999) Étude du comportement dynamique et thermique de gouttes en régime d'interaction dans le cas de jets rectilignes. Phd thesis, École Nationale Supérieure de l'Aéronautique et de l'Espace.

[222] C. Walshaw & M. Cross (2007) JOSTLE: Parallel multilevel graph-partitioning software – an overview. In *Mesh Partitioning Techniques and Domain Decomposition Techniques* (ed. F. Magoules), pp. 27–58. Civil-Comp Ltd., (Invited chapter).

[223] Q. Wang & K. D. Squires (1996) Large eddy simulation of particle-laden turbulent channel flow. *Phys. Fluids* **8** (5), 1207–1223.

[224] W. Wang & R. Pletcher (1996) On the large eddy simulation of a turbulent channel flow with significant heat transfer. *Phys. Fluids* **8** (12), 3354–3366.

[225] J. Watts, M. Rieffel & S. Taylor (1997) A load balancing technique for multi-phase computations. In *Proc. of High Performance Computing '97*, pp. 15–20.

[226] M. R. Wells & D. E. Stock (1983) The effects of crossing trajectories on the dispersion of particles in a turbulent flow. *J. Fluid Mech.* **136**, 31–62.

[227] T. Westermann (1992) Localization schemes in 2D boundary-fitted grids. *J. Comput. Phys.* **101** (2), 307–313.

[228] J. H. Wilkinson (1964) *Rounding Errors in Algebraic Processes*. Englewood Cliffs, NJ: Prentice-Hall.

[229] R. D. Williams (1991) Performance of dynamic load balancing algorithms for unstructured mesh calculations. *Concurrency: Practice, and Experience* **3** (5), 451–481.

[230] Y. Yamamoto, M. Potthoff, T. Tanaka, T. Kajishima & Y. Tsuji (2001) Large-eddy simulation of turbulent gas-particle flow in a vertical channel: effect of considering inter-particle collisions. *J. Fluid Mech.* **442**, 303–334.

[231] H. Zha, X. He, C. Ding, M. Gu & H. Simon (2001) Bipartite graph partitioning and data clustering. In *Proc. of the 10th ACM International Conference on Information and Knowledge Management*, pp. 25–31.

Appendices

Appendix A

Suggestion of treatment of other Lagrangian boundary conditions

Figure A.1 (a) shows an example of hexahedron-based grid where the outlet, and the external and internal walls are highlighted. The idea proposed is to label in a particular way the cells of boundary conditions to check them when relocating particles. An example of this is presented in Figure A.1 (b) where BC cells are colored in grayscale. Cells of the outlet are in dark gray and cells of the different walls are in light gray.

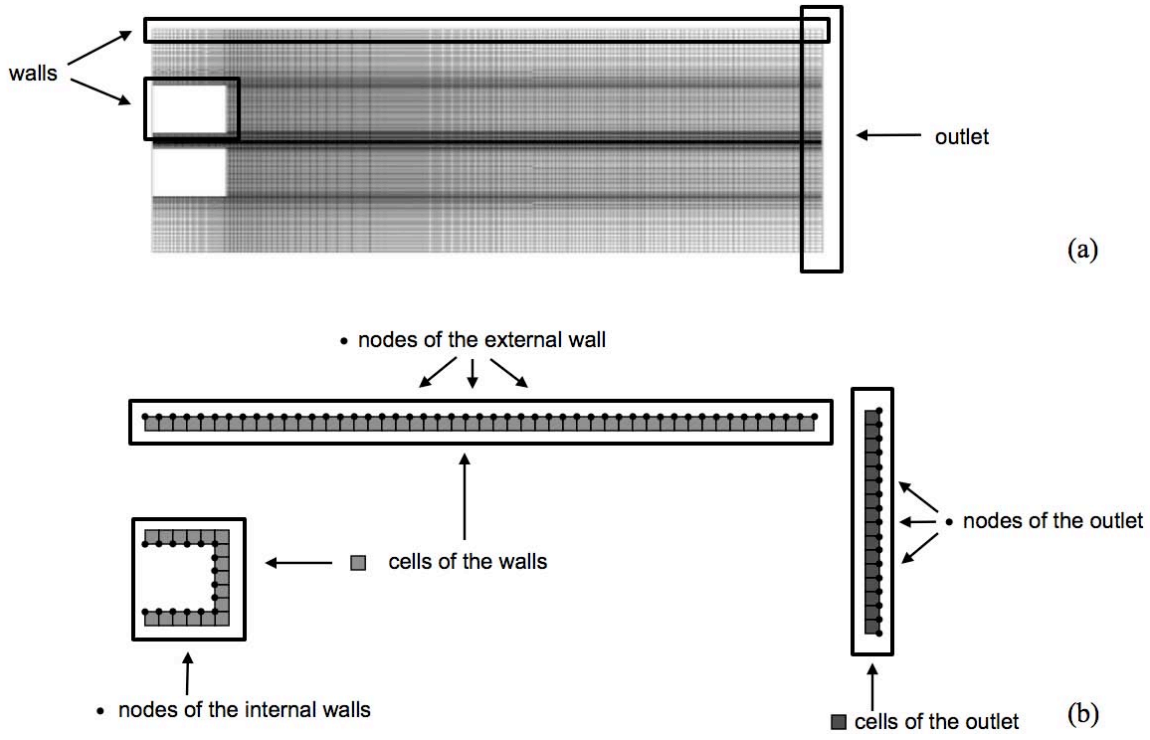

Figure A.1 - *(a) Mesh with outlet and wall positions highlighted; (b) illustration of the cells and nodes of the boundary conditions presented. Two gray scales are used to distinguish the outlet or wall cells.*

This procedure can be extended to any other boundary condition: symmetry, periodicity; or even to distinguish different kind of particle-wall treatments: rebound, films, splash, etc. For development purpose, integer values can be used: zero for cells which are not boundaries, one for outlets, two for walls, three for symmetry, and so on. This allows the use of only one array with dimension of the number of cell of each subdomain.

One advantage of this procedure is that it benefits from the existent data structure of AVBP. Firstly, all the nodes with a boundary condition (also called *patch*) are known at the beginning of the simulation and the cells associated to a particular patch could be flagged by using the same arrays and while recovering information of the patch. The array with the cells labeled could then be filled at this time, reducing memory and time requirements. Secondly, only one array is needed to store information about the particle-cell treatment. Then, the kind of treatment to apply to a particle is accessible with an *if* statement.

Another possibility is to label only the cells of the boundaries to reduce memory storage but this may increase time requirements since for every cell of the boundary and for every particle, a loop should be done to detect if the cell is flagged. In addition and focusing on massively parallel machines, the higher the number of partitions, the lower the number of cells associated to each subdomain and the lower the impact of the array proposed on the whole memory storage.

Appendix B

Proc. of the Summer Program 2006, pp. 197-211

Évaluation des méthodes numériques pour la simulation aux grandes échelles des écoulements diphasiques réactifs turbulents

La combustion turbulente est parfois effectuée avec des réactifs purement gazeux (dans les turbines à gaz industrielles par exemple) mais elle est aussi souvent basée sur l'emploi de réactifs liquides. En effet, pour des raisons de stockage et de manipulation, le carburant est en général injecté sous forme liquide avant d'être brûlé. L'aspect diphasique devient alors essentiel et parfois prédominant face à la combustion. La prédiction de la dispersion du carburant dans les écoulements diphasiques turbulents (la plupart comprenant des zones de recirculation) est donc une question clé dans le cadre de notre étude.

Les méthodes les plus classiques pour la description de la phase dispersée dans ce type d'écoulements sont les approches Euler/Euler (EE) et Euler/Lagrange (EL). Dans la première approche, la phase gazeuse et la phase liquide sont décrites sur le même maillage sur lequel on cherche à résoudre un lot d'équations différentielles partielles. Dans la seconde approche, le gaz est résolu comme toujours sur un maillage Eulérien alors que la phase liquide est simulée au moyen de particules Lagrangiennes. Dans les deux cas, le couplage est nécessaire et intervient au travers d'échanges d'information entre le système fluide et liquide. La plupart des codes RANS (pour Reynolds-averaged Navier-Stokes) utilise les approches EL. Cependant, l'histoire du développement du RANS a montré que les deux approches sont disponibles dans les codes commerciaux. Dans le cas de la simulation aux grandes échelles (LES pour Large-Eddy Simulation) - qui permet une analyse plus complète des phénomènes instables (instabilités, flashback or quenching) à l'intérieur des chambres de combustion - les deux formulations ont été développées dans le but de comparer les résultats numériques dans un cas test de référence disposant d'un ensemble complet de données expérimentales pour un calcul gazeux et un calcul diphasique.

Dans cette étude, le cas test choisi pour la comparaison des deux approches avec la stratégie LES est décrit dans Borée *et al.* [22]. Dans cette configuration, un jet d'air avec des particules de verre est injecté dans la chambre par le biais d'un tube d'injection entouré d'un co-courant d'air. Le rapport de vitesse entre le tube d'injection et le co-courant a été choisi de manière à créer une large zone centrale de recirculation (entre le jet central et le co-courant). Ces tests sont effectués

sans combustion ni évaporation, mais sont obligatoires avant de réaliser ce type de calculs dans des géométries complexes proches de celles des chambres de combustion. Le diamètre des particules de verre est compris entre 20 et 100 microns et leur masse volumique est de 2470 kg/m^3. Cette configuration dispose de deux bases de données complètes pour un cas faiblement chargé en masse ($M_j = 22\%$) et un autre fortement chargé en masse ($M_j = 110\%$). Les comparaisons présentées dans cet article se limitent au calcul faiblement chargé où l'écoulement diphasique consideré est suffisamment dilué pour négliger les collisions inter-particulaires. Les simulations numériques ont été réalisées uniquement avec des particules de 60 microns. Des études non rapportées ici ont montré qu'un calcul monodispersé avec la taille moyenne des particules est suffisant pour capturer l'effet moyen de la phase gazeuse et la dynamique des particules.

Deux codes de calcul différents ont également été testés sur la configuration de Borée *et al.* [22].

- Le solveur implicite CDP (développé à l'Université de Stanford) résout les équations de Navier-Stokes de façon incompressible. L'avancement en temps de CDP est basé sur la méthode de pas de temps fractionné (fractional-step method) et l'avancement en espace est fait par un schéma centré à l'ordre 2. Le modèle de sous-maille utilisé est celui de Smagorinsky dynamique (Germano *et al.* [72]).
- Le code de calcul explicite AVBP (développé au centre de recherche : CERFACS) résout les équations de Navier-Stokes de façon compressible. Le schéma utilisé dans cette étude est à l'ordre 3 en espace avec un avancement en temps de type Runge-Kutta. Le modèle de sous-maille est celui de Smagorinsky et les conditions limites sont du type NSCBC (Poinsot & Veynante [165], Moureau *et al.* [138]).

Les points qui sont étudiés avec la LES de cet écoulement diphasique sont les suivants :

- Comparaison des performances et des temps de calcul des approches EE et EL.
- Évaluation de l'influence du type des cellules du maillage (hexaèdres vs tétraèdres)
- Comparaison des formulations implicite et explicite pour l'avancement en temps.
- Étude des effets des conditions limites sur la phase dispersée.

Après une description détaillée des équations de la phase dispersée dans les deux approches, les résultats des calculs gazeux et diphasique sont présentés en les comparant aux résultats expérimentaux sur sept profils radiaux de vitesses moyenne et fluctuante.

Les résultats montrent que l'écoulement est bien prédit par les deux solveurs. La phase dispersée est bien prédite avec les deux approches, mais la formulation Lagrangienne prédit les valeurs fluctuantes (RMS) plus précisément. En fait, la formulation Eulérienne montre une sous-estimation de l'agitation des particules, et de leur dispersion radiale, qui semble liée au fait que dans cet étude l'effet de l'agitation décorrélée (RUV) de la phase dispersée ne soit pas prise en compte. L'importance des conditions limites d'entrée pour le gaz et la phase dispersée apparait à travers différents cas tests. Dans ce cas faiblement chargé où le nombre de particules reste faible pas rapport au nombre de cellules, l'approche Lagrangienne reste moins coûteuse (en temps et en mémoire) que l'approche Eulérienne.

Center for Turbulence Research
Proceedings of the Summer Program 2006

Evaluation of numerical strategies for LES of two-phase reacting flows

By E. Riber∗, †, M. García∗, V. Moureau, H. Pitsch, O. Simonin† AND T. Poinsot†

Predicting particle dispersion in recirculating two-phase flows is a key issue for reacting flows. In this study, Euler/Euler and Euler/Lagrange LES formulations have been compared in the bluff-body configuration from Borée *et al.* (2001) where glass beads are injected into a complex recirculating flow. These tests are performed for non-reacting, non-evaporating sprays but are mandatory validations before computing realistic combustion chambers. Two different solvers (one explicit and compressible and the other implicit and incompressible) have also been tested on the same configuration. Results show that the gas flow is well predicted by both solvers. The dispersed phase is also well predicted but the Lagrange solver predicts RMS values more precisely. The importance of inlet boundary conditions for the gas and the dispersed phase is revealed through various tests.

1. Motivations and objectives

Today, RANS (Reynolds-averaged Navier-Stokes) equations are routinely solved to design combustion chambers, for both gaseous and liquid fuels. Recently, in order to provide better accuracy for the prediction of mean flows but also to give access to unsteady phenomena occurring in combustion devices (such as instabilities, flashback or quenching), Large-Eddy Simulation (LES) has been extended to reacting flows. The success of these approaches for gaseous flames in the last years (Caraeni *et al.* 2000; Chakravarthy & Menon 2000; Colin *et al.* 2000; Forkel & Janicka 2000; Pitsch & Duchamp de la Geneste 2002; Mahesh *et al.* 2004; Selle *et al.* 2004; Sommerer *et al.* 2004; Moureau *et al.* 2005; Roux *et al.* 2005; Poinsot & Veynante 2005) is a clear illustration of their potential. LES gives access to the large scales structures of the flow reducing the importance of modeling, and naturally capturing a significant part of the physics controlling these flames. Even though LES has already demonstrated its potential for gaseous flames, its extension to two-phase flames is still largely to be done. First, the physical submodels required to describe the atomization of a liquid fuel jet, the dispersion of solid particles, their interaction with walls, evaporation and combustion are as difficult to build in LES as in RANS because they are essentially subgrid phenomena. Second, the numerical implementation of two-phase flow LES remains a challenge. The equations for both the gaseous and the dispersed phases must be solved together at each time step in a strongly coupled manner. This differs from classical RANS where the resolution of the two phases can be done in a weak procedure, bringing first the gas flow to convergence, then the solid particles and finally iterating until convergence of both phases. Finally, in the context of parallel super-computing, numerical efficiency is an additional constraint. For single-phase flows, efficient and accurate solvers have been developed and speedups of

† IMF Toulouse, UMR CNRS/INPT/UPS, 31400 Toulouse, France
∗ CERFACS, CFD team, 42 Av. Gaspard Coriolis, 31057 Toulouse, France

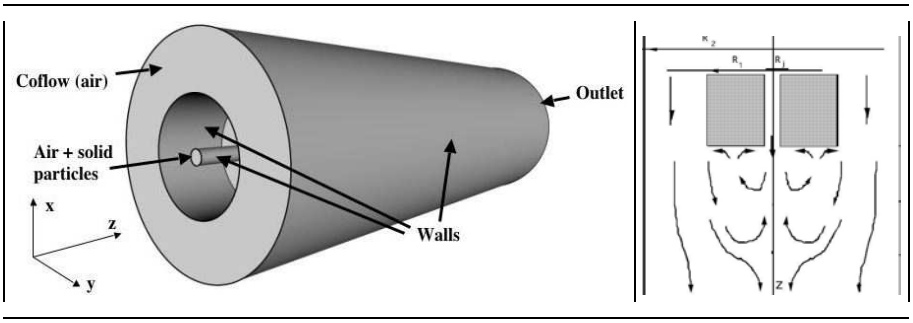

FIGURE 1. Configuration of Borée (Borée *et al.* 2001). The dimensions are : $R_j = 10$ mm, $R_1 = 75$ mm, $R_2 = 150$ mm. The total length of the experiment is 1.5 m.

the order of 5000 are not uncommon (www.cerfacs.fr/cfd/parallel.html). Maintaining a similar parallel efficiency for a two-phase flow solver while representing the main physics of the flow raises additional questions.

In LES of two-phase flows, physics and numerics interact strongly: the first question is to choose a paradigm to describe the two-phase flow. Most RANS codes use Euler/Lagrange (EL) methods in which the flow is solved using an Eulerian method and the particles are tracked using a Lagrangian approach. An alternative technique is to use two-fluid models in which both the gas and the dispersed phases are solved using an Eulerian method (Euler/Euler or EE). The history of RANS development has shown that both EE and EL are useful and either is found today in most commercial codes. For LES, both EE and EL formulations are being developed and the focus of this study is to test them in a reference case where complete sets of solutions for gas and dispersed phase are available. This exercise is performed here without evaporation or combustion.

2. Configuration and work objectives

In this study two solvers developed at CTR and CERFACS are used to investigate some critical issues for LES of two-phase flows on massively parallel computers:

- an implicit incompressible solver (CDP) using a EL formulation. For this study, hexahedron-based grids are used in CDP.
- an explicit compressible solver (AVBP) using both EL and EE formulations (Kaufmann *et al.* 2003). For the present study, AVBP is used on tetrahedron-based grids.

These solvers are used to study a bluff-body configuration (Borée *et al.* 2001) where a jet of air and solid particles are injected in a coflow of air (Fig. 1). The jet velocity on the axis is 4 m/s and the coflow maximum velocity is 6 m/s. The experiment is designed to provide large recirculation zones between the central jet and the coflow. The dispersed phase consists of solid particles (glass beads with diameter ranging from 20 to 100 microns with a mean value of 60 microns) so that evaporation, coalescence and break up do not have to be considered. The material density of the glass particle is $\rho_p = 2470$ kg.m^{-3}. The mass loading ratio of particles in the inner jet is 0.22 corresponding to a solid volumetric fraction less than 10^{-4}. Thus collision effects will be assumed to be negligible in the modelling approaches.

The issues which can be studied are still very relevant for LES of two-phase flows:

- Compare performances and cost of EE and EL approaches.

- Evaluate influence of mesh type (hexahedra vs tetrahedra).
- Compare implicit and explicit formulations for time advancement.
- Study effects of boundary conditions for the dispersed phase: should the particle velocities at the domain inlet be modulated to account for turbulence or not?

3. Description of solvers and models

Numerical methods used in both LES solvers for the gas phase have been extensively described in the literature (Moureau *et al.* 2005; Selle *et al.* 2004; Schmitt *et al.* 2006; Mahesh *et al.* 2004; Ham & Iaccarino 2004) and will only be summarized here.
The LES solver CDP solves implicitly the incompressible Navier-Stokes equations. The time integration of CDP is based on the fractional-step method (Kim & Moin 1985) and the space integration relies on a second-order central scheme which conserves the kinetic energy (Mahesh *et al.* 2004; Ham & Iaccarino 2004). The dynamic Smagorinsky model (Germano *et al.* 1991) is used to model the subgrid stress tensor.
The explicit LES solver AVBP solves the compressible Navier-Stokes equations with a third-order scheme for spatial differencing and a Runge-Kutta time advancement (Colin & Rudgyard 2000; Moureau *et al.* 2005). For the present case, the Smagorinsky model is used to model SGS tensors. Walls are treated using the law-of-the-wall formulation of Schmitt *et al.* (2006). The boundary conditions are handled with the NSCBC formulation (Poinsot & Veynante 2005; Moureau *et al.* 2005).
The influence of the particles on the gas phase is taken into account in the EL simulations by using the point-force approximation in the general framework of the particle-in-cell method (PIC) (Boivin *et al.* 1998; Vermorel *et al.* 2003), with standard single-phase subgrid turbulence modelling approaches. According to Boivin *et al.* (2000), such an assumption is valid for small mass loading ratio of particles (typically, $\alpha_p \rho_p / \rho_g \leq 1$) with response time larger than the subgrid turbulence characteristic time scale.
The influence of the particles on the gas phase is taken into account through the drag force in the EE simulations. Modification of the gas subgrid-scale turbulence model by the particles is neglected.
This section focuses on techniques used for the dispersed phase.

Euler/Lagrange approach

The dispersed phase consists of particles which are assumed to be rigid spheres with diameter comparable or smaller than the Kolmogorov length scale. If the particle density is much larger than the fluid density, the forces acting on particles reduce to drag and gravity. With these assumptions, the particle equations of motion can then be written for a single particle as:

$$\frac{dx_{p,i}}{dt} = u_{p,i} \tag{3.1}$$

$$\frac{du_{p,i}}{dt} = -\frac{3}{4}\,\frac{\rho_g}{\rho_p}\,\frac{C_D}{d_p}\,|\mathbf{v}_r|\;\mathrm{v}_{r,i} + g_i = -\frac{u_{p,i} - \tilde{u}_{g,i}}{\tau_p} + g_i\ . \tag{3.2}$$

The local drag coefficient in Eq. (3.2) is C_D and may be expressed in terms of the particle Reynolds number Re_p following Schiller & Nauman (1935):

$$C_D = \frac{24}{Re_p}\left[1 + 0.15 Re_p^{0.687}\right], \qquad Re_p = \frac{|\mathbf{v}_r|\; d_p}{\nu_g} \leq 800\ . \tag{3.3}$$

The local instantaneous relative velocity between the particle and the surrounding fluid is $\mathrm{v}_{r,i} = u_{p,i} - \tilde{u}_{g,i}$ where g_i is the gravity vector and $\tilde{u}_{g,i}$ is the filtered fluid velocity at the position of the particle assuming that the flow field is locally undisturbed by the presence of this particle (Gatignol 1983; Maxey & Riley 1983) and that the subgrid fluid velocity seen by the particles is negligible (Fede *et al.* 2006). The particle relaxation time τ_p is defined as the Stokes characteristic time:

$$\tau_p = \frac{4}{3}\,\frac{\rho_p}{\rho_g}\,\frac{d_p}{C_D}\,|\mathbf{v}_r| \tag{3.4}$$

where d_p is the particle diameter, ρ_p is the density of the particle, ν_g is the kinematic viscosity of the fluid at the particle location.

Euler/Euler approach

The treatment of the dispersed phase is based on an Eulerian approach: Eulerian equations for the dispersed phase may be derived by several means. A popular and simple way consists in volume filtering of the separate, local, instantaneous phase equations accounting for the inter-facial jump conditions (Druzhinin & Elghobashi 1999). Such an averaging approach is restrictive because particle sizes and particle distances have to be smaller than the smallest length scale of the turbulence. Besides, they do not account for the Random Uncorrelated Motion (Février *et al.* 2005). In the present study, a statistical approach analogous to kinetic theory (Chapman & Cowling 1939) is used to construct a probability density function (pdf) $\breve{f}_p(\mathbf{c}_p, \mathbf{x}, t)$ which gives the local instantaneous probable number of particles with the given translation velocity $\mathbf{u}_p = \mathbf{c}_p$. The resulting model (Février *et al.* 2005; Moreau *et al.* 2005) leads to equations for the particle number density $\bar{n}_p$ and the correlated velocity $\hat{\mathbf{u}}_p$:

$$\frac{\partial}{\partial t}\bar{n}_p + \frac{\partial}{\partial x_j}\bar{n}_p\hat{u}_{p,j} = 0 \tag{3.5}$$

$$\begin{aligned}\frac{\partial}{\partial t}\bar{n}_p\hat{u}_{p,i} + \frac{\partial}{\partial x_j}\bar{n}_p\hat{u}_{p,i}\hat{u}_{p,j} = &-\frac{\bar{n}_p}{\tau_p}\left(\hat{u}_{p,i} - \hat{u}_{f,i}\right) + \bar{n}_p g_i - \frac{\partial}{\partial x_j}T_{p,ij} \\ &-\frac{\partial}{\partial x_j}\bar{n}_p\widehat{\delta R}^{*}_{p,ij} - \frac{\partial}{\partial x_i}\frac{2}{3}\bar{n}_p\widehat{\delta\theta}_p\end{aligned} \tag{3.6}$$

where $\bar{n}_p$, $\hat{\mathbf{u}}_p$ and $\widehat{\delta\theta}_p$ are respectively the filtered particle number density, correlated velocity and Random Uncorrelated Energy (RUE). The two first terms of the rhs of Eq. (3.6) are the drag force and gravity effects on large scales, the third one accounts for the SGS effects, the fourth one takes into account the RUE effects and the last one is a dissipation term by RUE. $T_{p,ij}$ stands for the particle subgrid stress tensor:

$$T_{p,ij} = \bar{n}_p(\widehat{u_{p,i}u_{p,j}} - \hat{u}_{p,i}\hat{u}_{p,j}) \tag{3.7}$$

As in fluid anisotherm turbulence, an additional equation on energy is needed. The transport equation of filtered RUE is:

$$\begin{aligned}\frac{\partial}{\partial t}\overline{n}_p\widehat{\delta\theta}_p + \frac{\partial}{\partial x_j}\overline{n}_p\hat{u}_{p,j}\widehat{\delta\theta}_p = &-2\frac{\overline{n}_p}{\tau_p}\widehat{\delta\theta}_p - \frac{2}{3}\overline{n}_p\widehat{\delta\theta}_p\frac{\partial\hat{u}_{p,j}}{\partial x_j} \\ &-\overline{n}_p\widehat{\delta R}^{*}_{p,ij}\frac{\partial\hat{u}_{p,i}}{\partial x_j} - \frac{1}{2}\frac{\partial}{\partial x_j}\overline{n}_p\widehat{\delta S}_{p,iij} + \Pi_{\delta\theta_p} - \frac{\partial}{\partial x_j}Q_{p,j}\end{aligned} \tag{3.8}$$

The first rhs term is the RUE destruction by drag force, the second one is a RUE-dilatation term, the third one is a production term by filtered Random Uncorrelated Velocity (RUV) tensor, the next one is the diffusion by filtered RUV third correlation tensor. $\Pi_{\delta\theta_p}$ and $Q_{p,j}$ are respectively production and diffusion terms by subgrid scales:

$$\Pi_{\delta\theta_p} = \left(\overline{\breve{n}_p \delta R_{p,ij} \frac{\partial \breve{u}_{p,i}}{\partial x_j}} - \bar{n}_p \delta\widehat{R_{p,ij}} \frac{\partial \hat{u}_{p,i}}{\partial x_j}\right) \quad \text{and} \quad Q_{p,i} = \bar{n}_p \left(\widehat{u_{p,i}\delta\theta}_p - \hat{u}_{p,i}\widehat{\delta\theta}_p\right) \quad (3.9)$$

Closure of filtered RUV terms

Using an equilibrium assumption, Kaufmann (2004) model $\delta R^*_{p,ij}$ by a viscous term and $\delta S_{p,iij}$ by a diffusive term similar to Fick's law. For LES approach these models are adapted by replacing non filtered quantities by filtered ones leading to (Moreau *et al.* 2005):

$$\widehat{\delta R}^*_{p,ij} = -\hat{\nu}_{RUM}\left(\frac{\partial \hat{u}_{p,i}}{\partial x_j} + \frac{\partial \hat{u}_{p,j}}{\partial x_i} - \frac{\partial \hat{u}_{p,k}}{\partial x_k}\frac{\delta_{ij}}{3}\right) \quad \text{and} \quad \frac{1}{2}\widehat{\delta S}_{p,iij} = -\hat{\kappa}_{RUM}\frac{\partial \widehat{\delta\theta}_p}{\partial x_j} \quad (3.10)$$

where the RUM viscosity, $\hat{\nu}_{RUM}$, and the RUM diffusion coefficient, $\hat{\kappa}_{RUM}$, are given by:

$$\hat{\nu}_{RUM} = \frac{\tau_p}{3}\widehat{\delta\theta}_p \quad \text{and} \quad \hat{\kappa}_{RUM} = \frac{10}{27}\tau_p\widehat{\delta\theta}_p \quad (3.11)$$

Subgrid terms modeling

By analogy to single phase flows (Moin *et al.* 1991; Vreman *et al.* 1995), Riber *et al.* (2005) propose a viscosity model for the SGS tensor $T_{p,ij}$. The trace-free SGS tensor is modeled using a viscosity assumption (compressible Smagorinsky model), while the subgrid energy is parametrized by a Yoshizawa model (Yoshizawa 1986):

$$T_{p,ij} = -C_S 2\Delta_f^2 \bar{n}_p |\hat{S}_p|\left(\hat{S}_{p,ij} - \frac{\delta_{ij}}{3}\hat{S}_{p,kk}\right) + C_I 2\Delta_f^2 \bar{n}_p |\hat{S}_p|^2 \delta_{ij} \quad (3.12)$$

where $\hat{S}_p$ is the filtered particle strain rate tensor, $|\hat{S}_p|^2 = 2S_{p,ij}S_{p,ij}$ and Δ_f the filter characteristic length. The model constants have been evaluated in a priori tests (Riber *et al.* 2006) leading to the values $C_S = 0.02$, $C_I = 0.012$.

The subgrid diffusion term in the filtered RUE is modeled by an eddy-diffusivity model:

$$Q_{p,j} = -\frac{\bar{n}_p C_S 2\Delta_f^2 |\hat{S}_p|}{P^{SGS}_{r,p}} \frac{\partial \widehat{\delta\theta}_p}{\partial x_j} \quad (3.13)$$

with the particle turbulent Prandtl number $P^{SGS}_{r,p} = 0.8$. The subgrid production of filtered RUE term $\Pi_{\delta\theta_p}$ acts like a dissipation term in the subgrid energy equation. Using an equilibrium assumption on the particle correlated subgrid energy and neglecting diffusion terms leads to:

$$-\frac{\bar{n}_p}{\tau_p}\left(\frac{T_{p,kk}}{\bar{n}_p} - q_{fp,SGS}\right) + \Pi_{\delta\theta_p} - T_{p,ij}\frac{\partial \hat{u}_{p,i}}{\partial x_j} = 0 \quad (3.14)$$

where the subgrid covariance is $q_{fp,SGS} = \widehat{u_{p,k}u_{f,k}} - \hat{u}_{p,k}\hat{u}_{f,k}$. To first order, the drag force term can be neglected and $\Pi_{\delta\theta_p}$ can be modeled by: $\Pi_{\delta\theta_p} \approx T_{p,ij}\partial\hat{u}_{p,i}/\partial x_j$ with the SGS tensor modeled by Eq. (3.12). This model ensures that the correlated energy dissipated by subgrid effects is fully transfered into RUE.

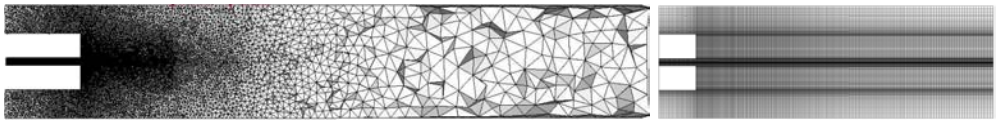

FIGURE 2. Grids used by AVBP (Tetrahedra, left) and CDP (Hexahedra, right).

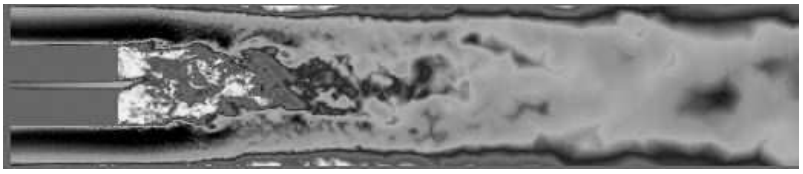

FIGURE 3. Instantaneous field of velocity modulus (AVBP). Maximum value (black): 6 m/s. Minimum value: 0.

	CDP	AVBP
Grid type	Hexahedra	Tetrahedra
Number of cells / nodes	3207960 / 3437576	2058883 / 367313
Time step (microseconds) / CFL	147 / 50	3,2 / 0.7
Averaging time (s) / Iterations	2,65 / 18000	1,03 / 320000
LES model / Wall model	Dynamic Smagorinsky/None	Smagorinsky/Law-of-the-wall

TABLE 1. Summary of parameters and models used for the 'no-particles' computation.

4. Comparison of gas flow without particles

Before discussing results for the dispersed phase, the accuracy of the LES solvers for the gas phase is evaluated by computing the flow without particles and comparing it to the same data provided in Borée *et al.* (2001). The two codes (AVBP and CDP) are used on two different grids (Fig. 2) (see summary in Table 1). A typical snapshot of the velocity field (modulus) in the central plane is displayed in Fig. 3 for an AVBP result (CDP fields are very similar). The complex structure of the recirculating flow is obvious: on the axis, the flow is recirculating down to $z = 200$ mm. On the sides of the channel, the flow also seems to separate from $z = 50$ mm to $z = 400$ mm.

Figures 4 to 7 present the results of the two LES codes along with the experimental measurements. The two LES solvers capture most of the flow physics: the axial mean and RMS velocities (Fig. 4 and 5) agree with the LDV measurements. The length of the recirculation zone (evidenced by the negative values of axial velocities on the axis) is well predicted. In the coflow, the RMS values predicted by LES are too low because no turbulence is injected at the inlet of the domain for these computations.

The mean radial velocity levels (Fig. 6) remain small (less than 1 m/s) and the two LES codes capture the radial velocity fields correctly except at the corner of the coflow and the step (first station at $z = 3$ mm) where the RMS velocities are underpredicted by CDP (Fig. 7). The stagnation point (around $z = 170$ mm) is a delicate zone where both

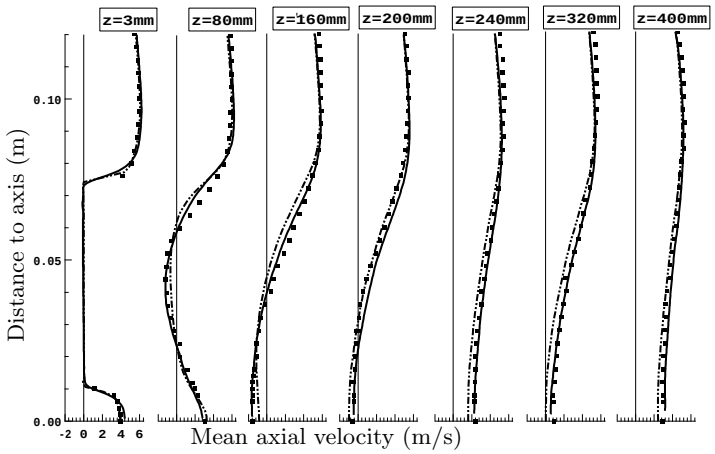

FIGURE 4. Radial profiles of mean axial gas velocities at 7 stations along z axis. Symbols: experiment; solid line: AVBP; dot-dashed line: CDP.

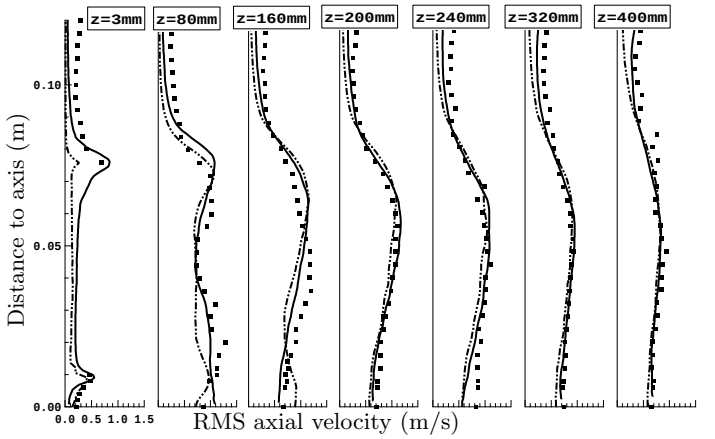

FIGURE 5. Radial profiles of RMS axial gas velocities at 7 stations along z axis. Symbols: experiment; solid line: AVBP; dot-dashed line: CDP.

codes have difficulties. The source of this problem is the exact position of the stagnation point: any small mismatch in this position leads to large changes in profiles measured around this point. Upstream and downstream of this point, the agreement is very good. The overall result is that both codes provide similar results even though they use totally different grids and methods. This indicates that grid independence for the gas is achieved for this test case and that tests for the dispersed phase can be performed with reasonable confidence.

5. Results for two-phase flow cases

This section presents results for the 22 percent mass loading of the central jet, obtained with three different computations summarized in Table 2. The grids and the time steps

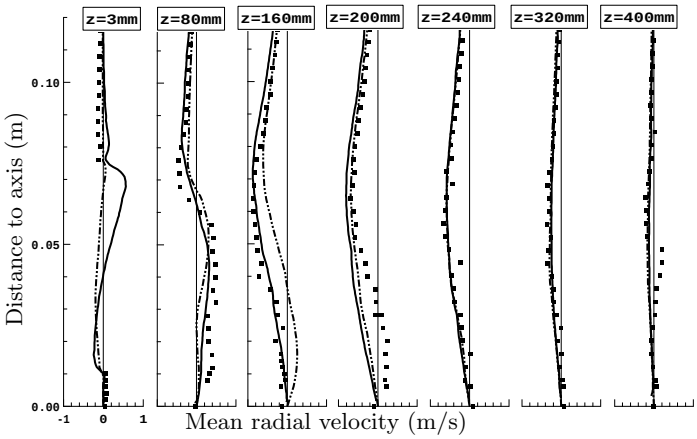

FIGURE 6. Radial profiles of mean radial gas velocities at 7 stations along z axis. Symbols: experiment; solid line: AVBP; dot-dashed line: CDP.

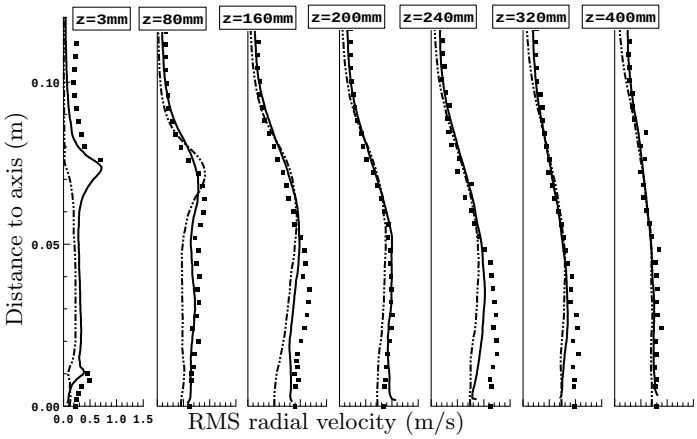

FIGURE 7. Radial profiles of RMS radial gas velocities at 7 stations along z axis. Symbols: experiment; solid line: AVBP; dot-dashed line: CDP.

used in AVBP and CDP are the same as in Table 1†. In all computations presented here, the injected particles have a size of 60 microns. Separated studies which are not reported here, using the Lagrangian solver and multidisperse particles or 60 microns particles only have shown that using a monodisperse distribution of size was very close to the 22 percent case of Borée *et al.* (2001) and was sufficient to capture both the mean flow effects on the gas (through two-way coupling) and the dynamics of the 60 microns class.

An essential part of these LES is the introduction of the particles in terms of position and velocity (Fig. 8). The injection planes are not the same for all codes. The methodologies used to inject the particles are also different to evaluate their impact on results. In AVBP-EE, both the mass loading and the mean velocity imposed in the injection plane

† For these runs, the RUM model is not used and the $\widehat{\delta\theta}_p$ term in Eq. (3.6) is set to zero.

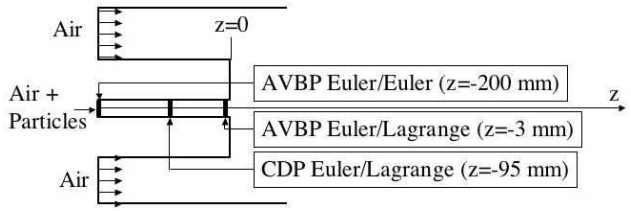

FIGURE 8. Injection position for particles.

	CDP Euler/Lagrange	AVBP Euler/Lagrange	AVBP Euler/Euler
Averaging time (s)	4	0.43	0.64
Particle mean speed	Exp. profile	Exp. profile	Exp. profile
Turbulent fluctuations	White noise (10 %)	White noise (12 %)	Zero
Particle distribution	Homogeneous	Homogeneous	Exp. profile

TABLE 2. Summary of parameters and models used for the particle injection (22 percent mass loading computation). The particles are injected in the central tube.

($z = -200$ mm) are the ones measured experimentally at $z = 3$ mm. No turbulent fluctuations are introduced. In AVBP-EL and in CDP, the mass loading is homogeneous over the injection section and the injection speed profile is also the experimental one measured at $z = 3$ mm. In AVBP-EL and in CDP, a white noise (amplitude of the order of 10 percent of the mean velocity) is added to the particle mean velocity profiles to match experimental measurements at $z = 3$ mm.

The velocity fields for the gas phase change when the particles are injected but these effects are limited and are not discussed here. Figures 9 to 12 show velocity fields for particles obtained with the three codes along with the measurements of Borée. The agreement between the experiments and the three LES sets of data is good. An interesting result is that AVBP-EL (dashed line) and AVBP-EE (solid line) provide extremely similar results showing that the EE approach is able to compute such a flow and to provide results which are equivalent in precision to an EL computation.

The best results are obtained with CDP and injection of turbulence on the gas phase. A convenient way to look at the results is to consider the central z axis of the configuration: a critical zone is located around $z = 160$ mm where the stagnation point for the gas is. This is also a zone where particles accumulate and must stop before turning around to escape from the recirculating flows by the sides. Figure 13 shows fields of gas velocity and of local volume fraction of solid particles for AVBP-EE on the left and CDP on the right side. Both solvers capture the zone where the solid particles accumulate. Local droplet accumulation is also observed upstream of the stagnation point within the central jet. However, the EE computation presented in Fig. 13 shows a droplet flow which stops slightly before the EL computation.

This can be quantified by plotting mean velocities along the axis for the gas (Fig. 14) and for the solid particles (Fig. 15). On this axis, the results provided by CDP are excellent while the two AVBP results match but are slightly off the experimental results.

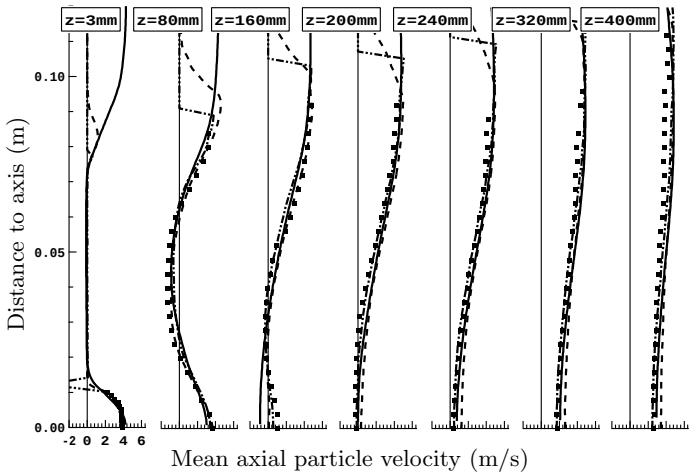

FIGURE 9. Radial profiles of mean axial particle velocities at 7 stations along z axis. Symbols: experiment; solid line: AVBP-EE; dashed line: AVBP-EL; dot-dashed line: CDP.

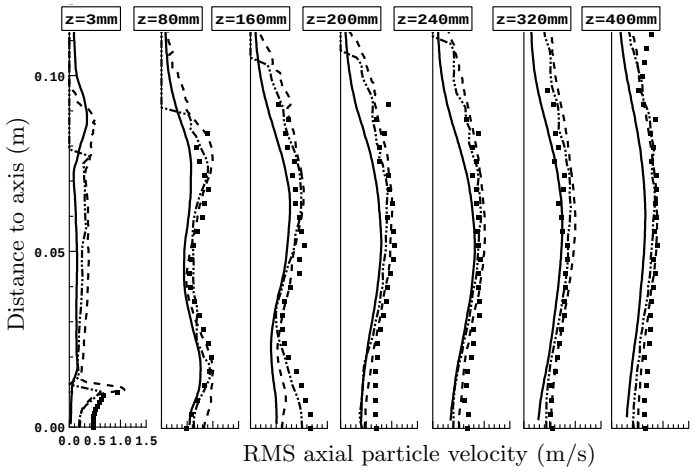

FIGURE 10. Radial profiles of RMS axial particle velocities at 7 stations along z axis. Symbols: experiment; solid line: AVBP-EE; dashed line: AVBP-EL; dot-dashed line: CDP.

The cause of this discrepancy was investigated through various tests during the project and was identified as the absence of turbulence injected on the gas phase in the central duct in AVBP: a direct verification of this effect is that in the two AVBP computations (solid and dashed lines), the gas and the particle velocities in the central duct increase between $z = -200$ and $z = 0$ mm, indicating that the flow is relaminarizing. This also demonstrates the importance of injecting not only the proper mean profile for the gas velocity but also fluctuations with a reasonably well-defined turbulent spectrum as done in CDP. Additional tests also reveal that the injection of white noise on the particle velocities has a very limited effect on the results.

Figures 16 and 17 display axial profiles of RMS velocities for the gas and the particles.

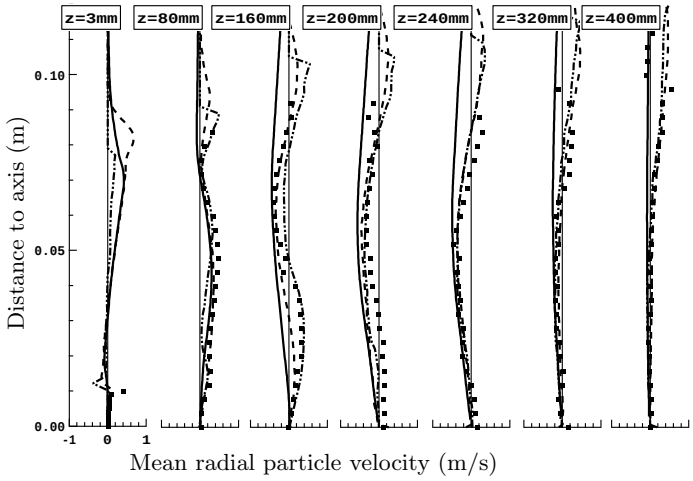

FIGURE 11. Radial profiles of mean radial particle velocities at 7 stations along z axis. Symbols: experiment; solid line: AVBP-EE; dashed line: AVBP-EL; dot-dashed line: CDP.

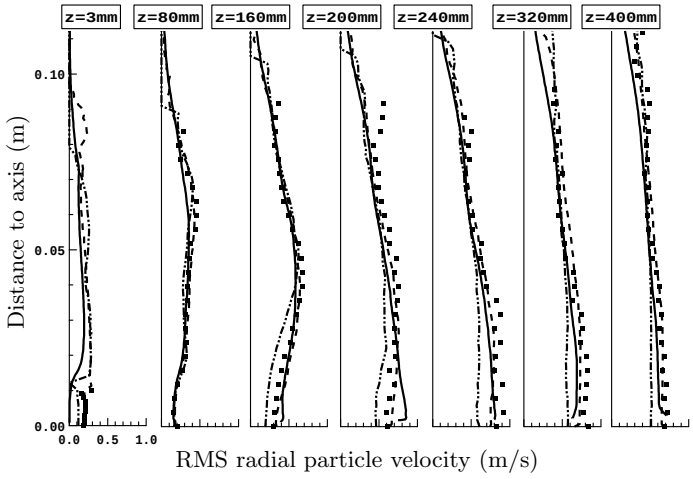

FIGURE 12. Radial profiles of RMS radial particle velocities at 7 stations along z axis. Symbols: experiment; solid line: AVBP-EE; dashed line: AVBP-EL; dot-dashed line: CDP.

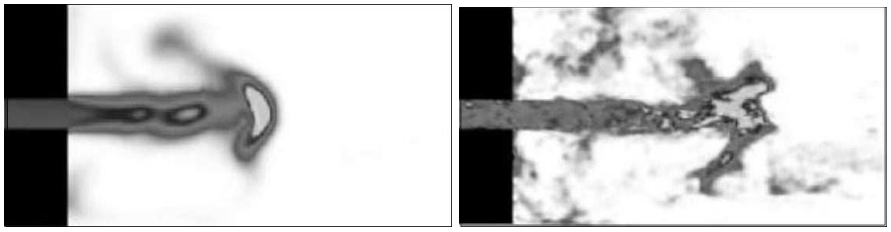

FIGURE 13. Instantaneous volume fraction in the central plane. Maximum value (black): 0.0002. Minimum value (white): 0. Right: values obtained from averaging the Lagrangian simulation in CDP. Left: output from AVBP-EE.

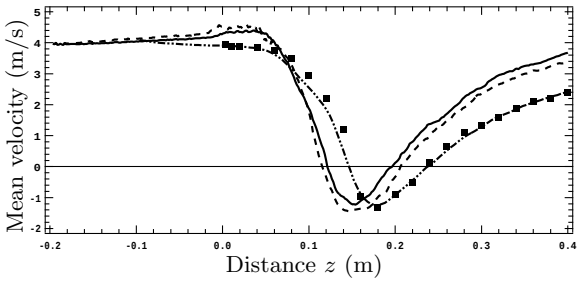

FIGURE 14. Axial profiles of mean gas velocities. Symbols: experiment; solid line: AVBP-EE; dashed line: AVBP-EL; dot-dashed line: CDP.

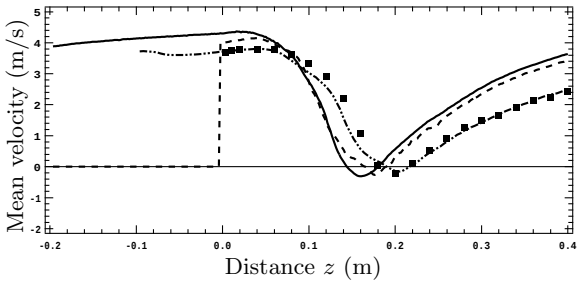

FIGURE 15. Axial profiles of mean particle velocities. Symbols: experiment; solid line: AVBP-EE; dashed line: AVBP-EL; dot-dashed line: CDP.

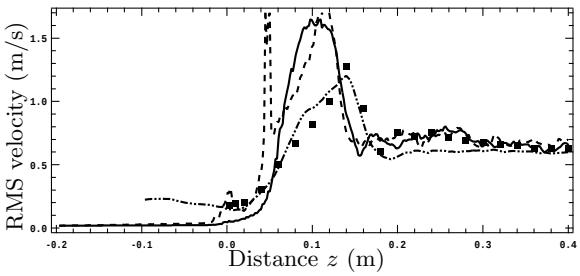

FIGURE 16. Axial profiles of RMS gas axial velocities. Symbols: experiment; solid line: AVBP-EE; dashed line: AVBP-EL; dot-dashed line: CDP.

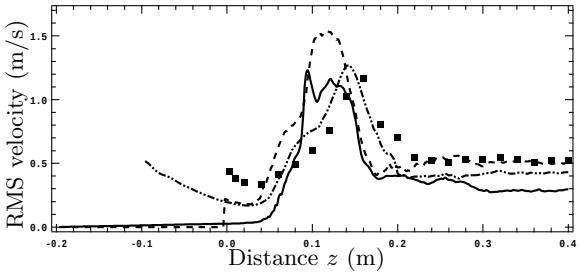

FIGURE 17. Axial profiles of RMS particle axial velocities. Symbols: experiment; solid line: AVBP-EE; dashed line: AVBP-EL; dot-dashed line: CDP.

These plots confirm that the position where the maximum levels of gas and particle turbulence are found on the axis is shifted towards the jet inlet and is too intense for both AVBP computations.

6. Performances and conclusions

For the present test case (mass loading of 22 percent), the total number of particles present in the domain for the Lagrange codes is of the order of 600000. For such a small number of particles, the computing power required by the Lagrangian solvers compared to the power required for the gas flow remains low: the added cost due to the particles is small and no load balancing problem is observed. The EE formulation added cost (of the order of 80 percent) is independent of the mass loading so that, for the present problem, the EL formulations proved to be faster.

In terms of results quality, the EL and the EE results with AVBP are very close showing that both formulations lead to equivalent results in this situation. An important factor controlling the quality of the results is the introduction of turbulence on the gas flow in the injection duct: without these turbulent fluctuations, the results are not as good on the axis in terms of positions of the recirculation zones.

Acknowledgment

The help of J. Borée in providing the experimental data and analyzing the results is gratefully acknowledged.

REFERENCES

Boivin, M., Simonin, O. & Squires, K. 2000 On the prediction of gas-solid flows with two-way coupling using large eddy simulation. *Phys. Fluids* **12** (8).

Boivin, M., Simonin, O. & Squires, K. 1998 Direct numerical simulation of turbulence modulation by particles in isotropic turbulence. *J. Fluid. Mech.* **375**, 235-263.

Borée, J., Ishima, T. & Flour, I. 2001 The effect of mass loading and inter-particle collisions on the development of the polydispersed two-phase flow downstream of a confined bluff body. *J. Fluid Mech.* **443**, 129-165.

Caraeni, D., Bergstrom, C. & Fuchs, L. 2000 Modeling of liquid fuel injection, evaporation and mixing in a gas turbine burner using large eddy simulation. *Flow Turb. and Combustion* **65**, 223-244.

Chakravarthy, V. & Menon, S. 2000 Subgrid modeling of turbulent premixed flames in the flamelet regime. *Flow Turb. and Combustion* **65**, 133-161.

Chapman, S. & Cowling, T. 1939 (digital reprint 1999) *The Mathematical Theory of Non-Uniform Gases*. Cambridge Mathematical Library Edn. Cambridge University Press.

Colin, O., Ducros, F., Veynante, D. & Poinsot, T. 2000 A thickened flame model for large eddy simulations of turbulent premixed combustion. *Phys. Fluids* **12** (7), 1843-1863.

Colin, O. & Rudgyard, M. 2000 Development of high-order Taylor-Galerkin schemes for unsteady calculations. *J. Comp. Phys.* **162** (2), 338-371.

Druzhinin, O.A. & Elghobashi, S. 1999 On the decay rate of isotropic turbulence laden with microparticles. *Phys. Fluids* **11** (3), 602-610.

Fede, P., Villedieu, P., Simonin, O. & Squires, K. 2006 Stochastic modeling of the subgrid fluid velocity fluctuations seen by inertial particles. In *Proc of the Summer Program*. Center for Turbulence Research, NASA Ames/Stanford Univ.

Février, P., Simonin, O. & Squires, K. 2005 Partitioning of particle velocities in gas-solid turbulent flows into a continuous field and a spatially uncorrelated random distribution: Theoretical formalism and numerical study. *J. Fluid Mech.* **533**, 1-46.

Forkel, H. & Janicka, J. 2000 Large-eddy simulation of a turbulent hydrogen diffusion flame. *Flow Turb. and Combustion* **65** (2), 163-175.

Gatignol, R. 1983 The Faxén formulae for a rigid particle in an unsteady non-uniform Stokes flow. *Journal de mécanique théorique et appliquée*, **1** (2), 143-160.

Germano, M., Piomelli, U., Moin, P. & Cabot, W. 1991 A dynamic subgrid-scale eddy viscosity model. *Phys. Fluids* **3** (7), 1760-1765.

Ham, F. & Iaccarino, G. 2004 Energy conservation in collocated discretization schemes on unstructured meshes. In *Annual Research Briefs*, pp. 3-14. Center for Turbulence Research, NASA Ames/Stanford Univ.

Kaufmann, A. 2004 Vers la simulation des grandes échelles en formulation Euler/Euler des écoulements réactifs diphasiques. PhD thesis.

Kaufmann, A., Simonin, O., Cuenot, B., Poinsot, T. & Helie, J. 2003 Dynamics and dispersion in 3D unsteady simulations of two phase flows. In *Supercomputing in Nuclear Applications*. Paris: CEA.

Kim, J. & Moin, P. 1985 Application of a fractional-step method to incompressible Navier-Stokes equations. *J. Comp. Phys.* **59** (2), 308-323.

Mahesh, K., Constantinescu, G. & Moin, P. 2004 A numerical method for large-eddy simulation in complex geometries. *J. Comp. Phys.* **197** (1), 215-240.

Maxey, M. & Riley, J. 1983 Equation of motion for a small rigid sphere in a nonuniform flow. *Phys. Fluids* **26** (4).

Moin, P., Squires, K., Cabot, W. & Lee, S. 1991 A dynamic subgrid-scale model for compressible turbulence and scalar transport. *Phys. Fluids* **A 3** (11), 2746-2757.

Moreau, M., Bédat, B. & Simonin, O. 2005 A priori testing of subgrid stress models for euler-euler two-phase LES from euler-lagrange simulations of gas-particle turbulent flow. In *18th Ann. Conf. on Liquid Atomization and Spray Systems*. ILASS Americas.

Moureau, V., Lartigue, G., Sommerer, Y., Angelberger, C., Colin, O. & Poinsot, T. 2005 High-order methods for dns and les of compressible multicomponent reacting flows on fixed and moving grids. *J. Comp. Phys.* **202** (2), 710-736.

Pitsch, M. & Duchamp de la Geneste, L. 2002 Large eddy simulation of premixed turbulent combustion using a level-set approach. *Proc. of the Comb. Institute* **29**, 2001-2005.

Poinsot, T. & Veynante, D. 2005 *Theoretical and numerical combustion* R.T. Edwards, 2nd edition.

Riber, E., Moreau, M., Simonin, O. & Cuenot, B. 2005 Towards large eddy simulations of non-homogeneous particle laden turbulent gas flows using euler-euler approach. In *11th Workshop on Two-Phase Flow Predictions*. Merseburg, Germany.

Riber, E., Moreau, M., Simonin, O. & Cuenot, B. 2006 Development of Euler-Euler LES Approach for Gas-Particle Turbulent Jet Flow. In *Proc. Symposium Fluid-Particle Interactions in Turbulence*. 2006 ASME Joint U.S. European Fluids Engineering Summer Meeting. Miami, FEDSM2006-98110.

Roux, S., Lartigue, G., Poinsot, T., Meier, U. & Bérat, C. 2005 Studies of mean and unsteady flow in a swirled combustor using experiments, acoustics analysis and large eddy simulations. *Combust. Flame* **141**, 40-54.

Schiller, L. & Nauman, A. 1935 A drag coefficient correlation. *V.D.I. Zeitung* **77**, 318-320.

Schmitt, P., Poinsot, T., Schuermans, B. & Geigle, K. 2006 Large-eddy simulation and experimental study of heat transfer, nitric oxide emissions and combustion instability in a swirled turbulent high pressure burner. *J. Fluid Mech.* **in print**.

Selle, L., Lartigue, G., Poinsot, T., Koch, R., Schildmacher, K.-U., Krebs, W., Prade, B., Kaufmann, P. & Veynante, D. 2004 Compressible large-eddy simulation of turbulent combustion in complex geometry on unstructured meshes. *Combust. Flame* **137** (4), 489-505.

Sommerer, Y., Galley, D., Poinsot, T., Ducruix, S., Lacas, F. & Veynante, D. 2004 Large eddy simulations and experimental study of flashback and blow-off in a lean partially premixed swirled burner. *J. Turb.* **5**.

Vermorel, O., Bédat, B., Simonin, O. & Poinsot, T. 2003 Numerical study and modelling of turbulence modulation in a particle laden slab flow. *J. Turb.* **4, 025**.

Vreman, B., Geurts, B. & Kuerten, H. 1995 Subgrid modeling in les of compressible flow. *Appl. Sci. Res.* **54**, 191-203.

Yoshizawa, A. 1986 Statistical theory for compressible turbulent shear flows, with the application to subgrid modeling. *Phys. Fluids.* **29** (7), 2152-2164.

Appendix C

6^{th} Int. Conference on Multiphase Flow, Leipzig, S3_Fri_A_62 (2007)

Comparaison des deux approches LES Euler/Euler et Euler/Lagrange pour la prédiction d'un écoulement confiné gaz-solide du type " bluff-body "

Aujourd'hui, l'approche numérique par résolution des équations de Navier-Stokes moyennées (RANS pour Reynolds-averaged Navier-Stokes) est régulièrement utilisée comme outil de conception de chambres de combustion, fonctionnant aussi bien avec des combustibles gazeux que des combustibles liquides. Avec le RANS, l'écoulement moyen est résolu alors que les structures turbulentes sont toutes modélisées. Récemment, afin d'offrir une meilleure prédiction des valeurs moyennes de l'écoulement mais également afin de donner accès à des phénomènes instables qui se produisent a l'intérieur des chambres de combustion, la simulation aux grandes échelles (LES pour Large-Eddy Simulation) a été étendue aux écoulements réactifs. Le succès de ces approches pour les flammes monophasiques dans les dernières années est une illustration claire de leur potentiel. La LES donne accès aux grandes structures de l'écoulement en réduisant l'importance de la modélisation et capture ainsi une partie importante de la physique qui contrôle ces flammes. Même si la LES a déjà démontré son potentiel sur des flammes monophasiques, son extension aux flammes diphasiques reste à explorer. Tout d'abord, la physique utilisée pour décrire l'atomisation d'un jet liquide, la dispersion des particules solides, leur interaction avec les parois, leur évaporation et combustion est aussi difficile à modéliser pour la LES que pour le RANS car il s'agit essentiellement de phénomènes de sous-maille. Deuxièmement, l'implantation numérique des écoulements diphasiques pour la LES reste un défi. Les équations pour la phase gazeuse et la phase dispersée doivent être résolues ensemble à chaque pas de temps d'une manière fortement couplée. Par ailleurs, dans le contexte des supercalculateurs parallèles, l'efficacité numérique est une contrainte supplémentaire et le maintien d'une efficacité du parallélisme comparable à celle des calculs gazeux n'est pas si évident pour un calcul diphasique.

Dans cette étude, les résultats des simulations numériques LES des écoulements turbulents chargés en particules sont comparés aux résultats expérimentaux de la configuration étudiée par Borée *et al.* [22] où des particules de verre sont injectées dans un écoulement turbulent comportant une zone de recirculation. Ces tests sont effectués sans combustion ni évaporation, mais sont obligatoires avant de réaliser ce type de calculs dans des géométries complexes proches de celles des chambres de combustion. L'ensemble complet de mesures expérimentales est disponible

en ligne à l'adresse suivante : http://www-mvt.iw.uni-halle.de/english/index.php?bluff_body_flow. Ces données ont été utilisés pour le test de performance du '9$^{\text{ième}}$ workshop pour la prédiction des écoulements diphasiques' (Ishima *et al.* [92]). Dans cette configuration, un jet d'air avec des particules de verre est injecté dans la chambre par le biais d'un tube d'injection entouré d'un co-courant d'air. Le rapport de vitesse entre le tube d'injection et le co-courant a été choisi afin de créer une large zone centrale de recirculation entre le jet central et le co-courant. Le diamètre des particules de verre est compris entre 20 et 100 microns et leur masse volumique est de 2470 kg/m^3. Cette configuration dispose de deux bases de données complètes pour un cas faiblement chargé en masse ($M_j = 22\%$) et un autre fortement chargé en masse ($M_j = 110\%$). Les comparaisons présentées dans cet article se limitent au calcul faiblement chargé où l'écoulement diphasique considéré est suffisamment dilué pour négliger les collisions interparticulaires. Les simulations numériques ont été réalisées uniquement avec des particules de 60 microns. Des études non rapportées ici ont montré qu'un calcul monodisperse avec la taille moyenne en masse de particules est suffisant pour capturer l'effet moyen de la phase gazeuse et la dynamique des particules.

Les méthodes les plus classiques pour la description de la phase dispersée dans ces écoulements sont les approches Euler/Euler (EE) et Euler/Lagrange (EL). Dans la première approche, un même maillage et utilisé pour résoudre l'ensemble des équations différentielles partielles qui decrivent la phase gazeuse et la phase liquide. Dans la seconde approche, le gaz est résolu sur un maillage Eulérien alors que la phase liquide est simulée au moyen de particules Lagrangiennes. Dans les deux cas, le couplage est nécessaire et intervient au travers d'échanges d'information entre le système fluide et liquide. Le solveur utilisé pour cette étude, AVBP, est un code parallèle explicite qui résout les équations de Navier-Stokes en 3D de façon compressible sur de maillages non-structurés et hybrides. Ce solveur contient à la fois les approches Eulérienne et Lagrangienne pour la description de la phase dispersée. Le schéma utilisé dans cette étude est d'ordre 3 en espace avec un avancement en temps de type Runge-Kutta. Le modèle de sous-maille est celui de Smagorinsky [204] et les conditions limites sont du type NSCBC (Poinsot & Veynante [165], Moureau *et al.* [138]).

Cet article est organisé de la façon suivante : d'abord une description de la configuration et des objectifs du travail est présentée. Ensuite, le solveur utilisé pour les simulations numériques est décrit, suivi d'une présentation détaillée des équations de la phase gazeuse et de la phase dispersée (pour les deux approches). Les résultats des calculs gazeux et diphasique sont présentés en comparaison avec les résultats expérimentaux sur sept profils radiaux de vitesses moyenne et fluctuante. Les résultats montrent que l'écoulement est bien prédit. La phase dispersée est bien prédite avec les deux approches, mais la formulation Lagrangienne prédit les valeurs fluctuantes (RMS) plus précisément. La dernière section de l'article contient une analyse des performances (speedup et temps CPU) de calcul gazeux et diphasique. Le coût supplémentaire du calcul diphasique avec l'approche Eulérienne par rapport a un calcul gazeux est invariablement estimé autour de 80% et ne dépend pas de la charge en masse. Par rapport au calcul diphasique Eulérien, dans le cas où le nombre de particules reste faible par rapport au nombre de cellules du maillage, l'approche EL se révéle plus rapide jusqu'à 64 processeurs. Les principales raisons de la chute des performances au-delà de 64 processeurs sont liées à l'anisotropie du maillage tétraédrique utilisé et à l'absence de prise en compte des particules au moment du découpage du maillage. Ces deux faits ensemble vont générer dans ce cas un grand déséquilibrage de charges entre les processeurs qui peuvent arriver à des situations où un seul processeur contient la moitie de particules du domaine.

6th International Conference on Multiphase Flow,
ICMF 2007, Leipzig, Germany, July 9 – 13, 2007

Comparison between Euler/Euler and Euler/Lagrange LES approaches for confined bluff-body gas-solid flow prediction

Marta García[1], Eleonore Riber[1,2], Olivier Simonin[2] and Thierry Poinsot[2]

[1] CERFACS, 42, av. Gaspard Coriolis, Toulouse, 31057, France

[2] IMF Toulouse, UMR CNRS/INPT/UPS, Allée du Professeur Camille Soula, Toulouse, 31400, France

garcia@cerfacs.fr, riber@cerfacs.fr, simonin@imft.fr, poinsot@imft.fr

Keywords: Large-eddy simulation, gas-solid flows, bluff-body flow, Eulerian and Lagrangian approaches

Abstract

In this study, Euler/Euler and Euler/Lagrange LES predictions of particle-laden turbulent flows are compared for the bluff-body configuration from Borée *et al.* (2001) where glass beads are injected into a complex recirculating flow. These tests are performed for non-reacting, non-evaporating sprays but are mandatory validations before computing realistic combustion chambers. The numerical code used for this study is a parallel explicit CFD code that solves the 3D compressible Navier-Stokes equations on unstructured and hybrid grids. This solver contains both Euler/Euler and Euler/Lagrange formulations. Results show that the gas flow and the dispersed phase are well predicted but the Lagrangian approach predicts RMS values more precisely. The importance of inlet boundary conditions for the gas is revealed.

Introduction

Today, RANS (Reynolds-averaged Navier-Stokes) equations are routinely solved to design combustion chambers, for both gaseous and liquid fuels. Recently, in order to provide better accuracy for the prediction of mean flows but also to give access to unsteady phenomena occurring in combustion devices (such as instabilities, flashback or quenching), Large-Eddy Simulation (LES) has been extended to reacting flows. The success of these approaches for gaseous flames in the last years (Caraeni *et al.* 2000; Colin *et al.* 2000; Selle *et al.* 2004; Roux *et al.* 2005; Poinsot & Veynante 2005) is a clear illustration of their potential. LES gives access to the large scales structures of the flow reducing the importance of modelling, and naturally capturing a significant part of the physics controlling these flames. Even though LES has already demonstrated its potential for gaseous flames, its extension to two-phase flames is still largely to be done. First, the physical submodels required to describe the atomization of a liquid fuel jet, the dispersion of solid particles, their interaction with walls, evaporation and combustion are as difficult to build in LES as in RANS because they are essentially subgrid phenomena. Second, the numerical implementation of two-phase flow LES remains a challenge. The equations for both the gaseous and the dispersed phases must be solved together at each time step in a strongly coupled manner. This differs from classical RANS where the resolution of the two phases can be done in a weak procedure, bringing first the gas flow to convergence, then the solid particles and finally iterating until convergence of both phases. Finally, in the context of parallel super-computing, numerical efficiency is an additional constraint. For single-phase flows, efficient and accurate solvers have been developed and speedups of the order of 5000 are not uncommon (http://www.cerfacs.fr/cfd/parallel.html). Maintaining a similar parallel efficiency for a two-phase flow solver while representing the main physics of the flow raises additional questions.

In LES of two-phase flows, physics and numerics interact strongly: the first question is to choose a paradigm to describe the two-phase flow. Most RANS codes use Euler/Lagrange (EL) methods in which the flow is solved using an Eulerian method and the particles are tracked using a Lagrangian approach. An alternative technique is to use two-fluid models in which both the gas and the dispersed phases are solved using an Eulerian method (Euler/Euler or EE) (Reeks 1991; Février & Simonin 1999). The history of RANS development has shown that both EE and EL are useful and either is found today in most commercial codes. For LES, both EE and EL formulations are being developed and the focus of this study is to test them in a reference case where complete sets of solutions for gas and dispersed phase are available. This exercice is performed here without evaporation or combustion.

Nomenclature

C_D	drag coefficient
C_I, C_S	model constants
C_v	specific heat at constant volume ($J\ kg^{-1}\ K^{-1}$)
d_p	particle diameter (m)
e_g	internal energy ($m^2\ s^{-2}$)
E_g	total energy ($m^2\ s^{-2}$)
$f_{c,i}$	coupling force ($kg\ m^{-2}\ s^{-2}$)

$\breve{f}_p$	probability density function ($s^3\ m^{-6}$)
g	gravitational constant ($m\ s^{-2}$)
n_p	particle number density (m^{-3})
N_{procs}	number of processors
p	pressure ($N\ m^{-2}$)
Pr	Prandtl number
$q_{g,j}$	heat tranfer vector ($J\ m^{-2}\ s^{-1}$)
$q_{gp,SGS}$	subgrid covariance ($m^{-2}\ s^{-2}$)
Q	diffusion term ($J\ m^{-2}\ s^{-1}$)
$\mathcal{R}$	air gas constant ($J\ kg^{-1}\ K^{-1}$)
r	radial direction (m)
Re	Reynolds number
S	strain rate tensor (s^{-1})
t	time (s)
T	temperature (K)
$\mathcal{T}$	stress tensor ($kg\ m^{-1}\ s^{-2}$)
u_i	velocity vector, i=1,2,3 ($m\ s^{-1}$)
v_r	local instantaneous relative velocity ($m\ s^{-1}$)
x_i	position vector, i=1,2,3 (m)
z	axial direction (m)

Greek letters

α	volume fraction
δ_{ij}	Kronecker delta
$\delta\theta_p$	Random Uncorrelated Energy (RUE) ($m^2\ s^{-2}$)
$\delta R_{p,ij}$	Random Uncorrelated Velocity (RUV) tensor ($m^2 s^{-2}$)
$\delta S_{p,iij}$	RUV third correlation tensor ($m^{-3}\ s^{-3}$)
Δ_f	filter characteristic length (m)
η	dynamic viscosity ($kg\ m^{-1}\ s^{-1}$)
κ	diffusion coefficient ($m^2\ s^{-1}$)
ν	kinematic viscosity ($m^2\ s^{-1}$)
$\Pi_{\delta\theta_p}$	production term by subgrid scales ($m^{-1}\ s^{-3}$)
ρ	density ($kg\ m^{-3}$)
τ_p	particle relaxation time (s)
$\tau_{g,ij}$	viscous stress tensor ($kg\ m^{-1}\ s^{-2}$)
ϕ	azimuthal direction (m)

Subscripts

g	gas phase
i,j,k	index of coordinates directions
p	particle (dispersed phase)
RUM	Random Uncorrelated Motion
SGS	subgrid-scale

Symbols

$\bar{\cdot}$	LES-filtered quantity
$\tilde{\cdot}$	gas Favre LES-filtered quantity
$\hat{\cdot}$	particle Favre LES-filtered quantity
$\breve{\cdot}$	mesoscopic quantity

Configuration and work objectives

In the present study, two approaches developed at CERFACS within the same solver are used to investigate some critical issues for LES of two-phase flows on massively parallel computers. The explicit compressible solver AVBP is used with both EE (Kaufmann *et al.* 2003) and EL formulations on the same tetrahedron-based grid.

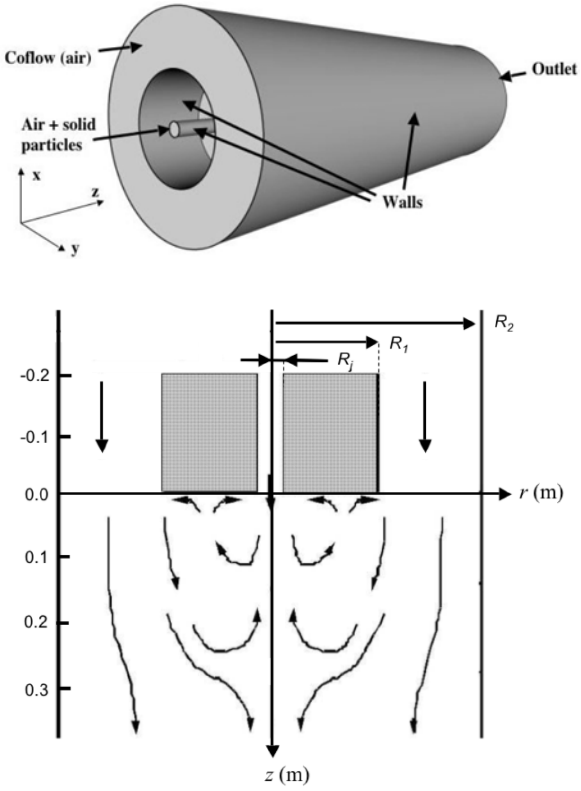

Figure 1: Configuration of Borée *et al.* (2001). The dimensions are : $R_j = 10$ mm, $R_1 = 75$ mm, $R_2 = 150$ mm. The total length of the experiment is 1.5 m.

Both approaches are used to study a bluff-body configuration (Borée *et al.* 2001) where a jet of air and solid particles are injected in a coflow of air (see the sketch in Fig. 1). The jet velocity on the axis is 4 m/s and the maximum coflow velocity is 6 m/s. The experiment is designed to provide large recirculation zones between the central jet and the coflow. The dispersed phase consists of solid particles (glass beads with diameter ranging from 20 to 100 microns with a mean value of 60 microns) so that evaporation, coalescence and break up do not have to be considered. The material density of the glass particle is $\rho_p = 2470$ kg m^{-3}. The mass loading ratio of particles in the inner jet is 0.22 corresponding to a solid volume fraction smaller than 10^{-4}. Thus collision effects are assumed to be negligible in the modelling approaches.

Measurements are performed by a two-component phase-Doppler anemometer (PDA). The origin is set at the edge of the bluff body and at the centre of the inner jet (see Fig. 1). The flow will be described using a cylindrical coordinate system (z, r, ϕ) to indicate the axial (downward), radial and azimuthal directions. Single-phase data are provided in tabulated form at different cross-sections within the jet, in the annular direction and along the z axis. The radial profiles of mean and RMS particle velocities for each size classes are provided in tabulated form at 7 cross-sections of the z axis ($z = 3, 80, 160, 200, 240, 320$ and 400 mm) and along the z axis up to 500 mm. The complete data set, including

accurate boundary conditions, at moderate mass loading (22 percent) has been selected for benchmarking at the 'Ninth workshop on two-phase flow predictions' (Ishima *et al.* 1999) and can be obtained at the following web site: http://www-mvt.iw.uni-halle.de/english/index.php?bluff_body_flow.
Despite of the relative simplicity, this test case contains a number of issues relevant for LES of two-phase flows. These include (i) the comparison of performances and CPU cost for EE and EL approaches and (ii) the analysis of the inlet boundary condition on the dispersed phase solution (turbulent modulation).

Description of the solver

The AVBP solver is a finite volume code based on a cell-vertex formulation. It solves the laminar and turbulent compressible Navier-Stokes equations in two and three space dimensions for hybrid and unstructured grids. Steady state or unsteady flows can be simulated, furthermore it takes into account the variations of molecular weights and heat capacities with temperature and mixture composition. A third-order scheme for spatial differencing and a Runge-Kutta time advancement (Colin & Rudgyard 2000; Moureau *et al.* 2005) is used for the present work. The Smagorinsky model is used to model the subgrid stress tensor. Walls are treated using the law-of-the-wall formulation by Schmitt *et al.* (2007). The boundary conditions are handled with the NSCBC formulation (Poinsot & Veynante 2005; Moureau *et al.* 2005).

The following sections briefly describe the governing equations solved by AVBP for the gaseous and dispersed phases.

Gaseous phase

The filtered conservation equation for gas-phase density, $\bar{\rho}_g$, momentum, $\tilde{u}_{g,i}$, and total energy $\tilde{E}_g = \tilde{e}_g + \frac{1}{2}\tilde{u}^2_{g,j}$ (with $\tilde{e}_g = C_v \tilde{T}_g$, the internal energy, C_v the specific heat at constant volume and $\tilde{T}_g$ the temperature) read:

$$\frac{\partial \bar{\rho}_g}{\partial t} + \frac{\partial (\bar{\rho}_g \tilde{u}_{g,j})}{\partial x_j} = 0 \tag{1}$$

$$\frac{\partial (\bar{\rho}_g \tilde{u}_{g,i})}{\partial t} + \frac{\partial (\bar{\rho}_g \tilde{u}_{g,i} \tilde{u}_{g,j})}{\partial x_j} + \frac{\partial \bar{p}_g}{\partial x_i} - \frac{\partial \bar{\tau}_{g,ij}}{\partial x_j} = \frac{\partial \mathcal{T}_{g,ij}}{\partial x_j} + f_{c,i} \tag{2}$$

$$\frac{\partial (\bar{\rho}_g \tilde{E}_g)}{\partial t} + \frac{\partial (\tilde{u}_{g,j}(\bar{\rho}_g \tilde{E}_g + \bar{p}_g))}{\partial x_j} - \frac{\partial (\bar{\tau}_{g,ij} \tilde{u}_{g,i})}{\partial x_j} + \frac{\partial \bar{q}_{g,j}}{\partial x_j} = \frac{\partial (\mathcal{T}_{g,ij} \tilde{u}_{g,i})}{\partial x_j} + \frac{\partial Q_{g,j}}{\partial x_j} + f_{c,j} \tilde{u}_{g,j}. \tag{3}$$

The left-hand-side (LHS) of Eqs. 1-3 contains all resolved (filtered) variables (being $\bar{\tau}_{g,ij}$ and $\bar{q}_{g,i}$ the viscous stress tensor and the heat transfer vector, while pressure is obtained from the equation of state $\bar{p}_g = \bar{\rho}_g \mathcal{R} \tilde{T}_g$). The right-hand-side (RHS) of Eqs. 2 and 3 contains the SGS terms $\mathcal{T}_{g,ij}$ and $Q_{g,i}$, which are reconstructed using eddy-viscosity concepts (with turbulent viscosity obtained from Smagorinsky model). The last terms in Eqs. 2 and 3, $f_{c,i}$ and $f_{c,j}\tilde{u}_{g,j}$, denote respectively, the coupling force and energy applied to the fluid by all particles.

Dispersed phase: Euler/Lagrange approach

The dispersed phase consists of particles which are assumed to be rigid spheres with diameter comparable or smaller than the Kolmogorov length scale. As the particle density is much larger than the fluid density ($\rho_p/\rho_g = 2470$), the forces acting on particles reduce to drag and gravity. Under these assumptions, the particle equations of motion can then be written for a single particle as:

$$\frac{dx_{p,i}}{dt} = u_{p,i} \tag{4}$$

$$\frac{du_{p,i}}{dt} = -\frac{3}{4}\frac{\rho_g}{\rho_p}\frac{C_D}{d_p}|\mathbf{v}_r|\,\mathrm{v}_{r,i} + g_i = -\frac{u_{p,i} - \tilde{u}_{g,i}}{\tau_p} + g_i \tag{5}$$

with g_i the gravity vector. The local drag coefficient in Eq. (5) is C_D and may be expressed in terms of the particle Reynolds number Re_p following Schiller & Nauman (1935):

$$C_D = \frac{24}{Re_p}\left[1 + 0.15 Re_p^{0.687}\right] \tag{6}$$

$$Re_p = \frac{|\mathbf{v}_r|\, d_p}{\nu_g} \leq 800 \tag{7}$$

where d_p is the particle diameter and ν_g is the kinematic viscosity of the gas phase. The local instantaneous relative velocity between the particle and the surrounding fluid is $\mathrm{v}_{r,i} = u_{p,i} - \tilde{u}_{g,i}$, where $\tilde{u}_{g,i}$ is the fluid velocity at the position of the particle assuming that the flow field is locally undisturbed by the presence of this particle (Gatignol 1983; Maxey & Riley 1983). In first approximation, the velocity is assumed to be equal to the interpolation of the filtered velocity at the position of the particle (Wang & Squires 1996; Yamamoto *et al.* 2001; Apte *et al.* 2003). The effect of the subgrid fluid turbulence is assumed to be negligible owing to the large inertia of the solid particles (Fede & Simonin 2006). The particle relaxation time τ_p is defined as the Stokes characteristic time:

$$\tau_p = \frac{4}{3}\frac{\rho_p}{\rho_g}\frac{d_p}{C_D\,|\mathbf{v}_r|}. \tag{8}$$

The influence of the particles on the gas phase is taken into account in the EL simulations by using the point-force approximation in the general framework of the particle-in-cell method (PIC) (Boivin *et al.* 1998; Vermorel *et al.* 2003), with standard single-phase subgrid turbulence modelling approaches. According to Boivin *et al.* (2000), such an assumption is valid for small mass loading ratio of particles (typically, $\alpha_p \rho_p/\rho_g \leq 1$) with response time larger than the subgrid turbulence characteristic time scale. Modification

of the gas subgrid-scale turbulence model by the particles is neglected. A linear interpolation algorithm is used to compute the fluid velocity at the position of the particle. If particle relaxation time is much larger than the time scale of filtered velocity fluctuations (as in the present case of 22 percent mass loading), such a linear interpolation is found to be sufficiently accurate to resolve particle motions (see e.g. Fede & Simonin (2006)).

Dispersed phase: Euler/Euler approach

Eulerian equations for the dispersed phase can be derived using several approaches. A popular and simple way consists in volume filtering of the separate, local, instantaneous phase equations accounting for the inter-facial jump conditions (Druzhinin & Elghobashi 1999). Such an averaging approach is restrictive because particle sizes and particle distances have to be smaller than the smallest length scale of the turbulence. Besides, they do not account for the crossing of particle trajectories or Random Uncorrelated Motion (RUM), shown by Février *et al.* (2005), which may appear when the particle relaxation time is larger than the Kolmogorov time scale. In the present study, a statistical approach analogous to kinetic theory (Chapman & Cowling 1939) is used to construct a probability density function (pdf) $\breve{f}_p(\mathbf{c}_p, \mathbf{x}, t)$ which gives the local instantaneous probable number of particles with the given translation velocity $\mathbf{u}_p = \mathbf{c}_p$. The resulting model (Février *et al.* 2005; Moreau *et al.* 2005) leads to equations for the particle number density $\bar{n}_p$ and the correlated velocity $\hat{\mathbf{u}}_p$:

$$\frac{\partial}{\partial t}\bar{n}_p + \frac{\partial}{\partial x_j}\bar{n}_p\hat{u}_{p,j} = 0 \tag{9}$$

$$\frac{\partial}{\partial t}\bar{n}_p\hat{u}_{p,i} + \frac{\partial}{\partial x_j}\bar{n}_p\hat{u}_{p,i}\hat{u}_{p,j} = -\frac{\bar{n}_p}{\tau_p}\left(\hat{u}_{p,i} - \hat{u}_{g,i}\right)$$
$$+\bar{n}_p g_i - \frac{\partial}{\partial x_j}\mathcal{T}_{p,ij} - \frac{\partial}{\partial x_j}\bar{n}_p\widehat{\delta R}^*_{p,ij} - \frac{\partial}{\partial x_i}\frac{2}{3}\bar{n}_p\widehat{\delta\theta}_p \tag{10}$$

where $\bar{n}_p$, $\hat{\mathbf{u}}_p$ and $\widehat{\delta\theta}_p$ are respectively the filtered particle number density, correlated velocity and Random Uncorrelated Energy (RUE). The two first terms of the RHS of Eq. (10) are the drag force and gravity effects on large scales, the third one accounts for the subgrid-scale (SGS) effects, the fourth one takes into account the dissipation effects induced by the RUM and the last one is a particle-pressure term proportional to the RUE. $\mathcal{T}_{p,ij}$ stands for the particle subgrid stress tensor:

$$\mathcal{T}_{p,ij} = \bar{n}_p(\widehat{u_{p,i}u_{p,j}} - \hat{u}_{p,i}\hat{u}_{p,j}). \tag{11}$$

As in fluid non-isotherm turbulence, an additional equation for energy is needed. The transport equation of filtered RUE is:

$$\frac{\partial}{\partial t}\overline{n}_p\widehat{\delta\theta}_p + \frac{\partial}{\partial x_j}\overline{n}_p\hat{u}_{p,j}\widehat{\delta\theta}_p = -2\frac{\overline{n}_p}{\tau_p}\widehat{\delta\theta}_p - \frac{2}{3}\overline{n}_p\widehat{\delta\theta}_p\frac{\partial\hat{u}_{p,j}}{\partial x_j}$$
$$-\overline{n}_p\widehat{\delta R}^*_{p,ij}\frac{\partial\hat{u}_{p,i}}{\partial x_j} - \frac{1}{2}\frac{\partial}{\partial x_j}\overline{n}_p\widehat{\delta S}_{p,iij} + \Pi_{\delta\theta_p} - \frac{\partial}{\partial x_j}Q_{p,j}. \tag{12}$$

The first RHS term is the RUE destruction by drag force, the second one is a RUE-dilatation term, the third one is a production term by filtered Random Uncorrelated Velocity (RUV) tensor, the next one is the diffusion by filtered RUV third correlation tensor. $\Pi_{\delta\theta_p}$ and $Q_{p,j}$ are respectively production and diffusion terms by subgrid scales:

$$\Pi_{\delta\theta_p} = \left(\overline{\breve{n}_p\delta R_{p,ij}\frac{\partial\breve{u}_{p,i}}{\partial x_j}} - \bar{n}_p\widehat{\delta R}_{p,ij}\frac{\partial\hat{u}_{p,i}}{\partial x_j}\right) \tag{13}$$

$$Q_{p,j} = \bar{n}_p\left(\widehat{u_{p,j}\delta\theta_p} - \hat{u}_{p,j}\widehat{\delta\theta}_p\right). \tag{14}$$

The particle source term in the gas phase momentum Eq. 2 is equal to minus the drag term in the particle phase Eq. 10.

Closure of filtered RUV terms

Assuming small anisotropy of the RUM, Simonin *et al.* (2002) model $\delta R^*_{p,ij}$ by a viscous term and Kaufmann *et al.* (2005) model $\delta S_{p,iij}$ by a diffusive term similar to Fick's law. For LES approach these models are adapted by replacing non filtered quantities by filtered ones leading to (Moreau *et al.* 2005):

$$\widehat{\delta R}^*_{p,ij} = -\hat{\nu}_{RUM}\left(\frac{\partial\hat{u}_{p,i}}{\partial x_j} + \frac{\partial\hat{u}_{p,j}}{\partial x_i} - \frac{\partial\hat{u}_{p,k}}{\partial x_k}\frac{\delta_{ij}}{3}\right) \tag{15}$$

$$\frac{1}{2}\widehat{\delta S}_{p,iij} = -\hat{\kappa}_{RUM}\frac{\partial\widehat{\delta\theta}_p}{\partial x_j} \tag{16}$$

where the RUM viscosity, $\hat{\nu}_{RUM}$, and the RUM diffusion coefficient, $\hat{\kappa}_{RUM}$, are given by:

$$\hat{\nu}_{RUM} = \frac{\tau_p}{3}\widehat{\delta\theta}_p \quad \text{and} \quad \hat{\kappa}_{RUM} = \frac{10}{27}\tau_p\widehat{\delta\theta}_p. \tag{17}$$

Subgrid terms modeling

By analogy to single phase flows (Moin *et al.* 1991; Vreman *et al.* 1995), Riber *et al.* (2005) propose a viscosity model for the SGS tensor $\mathcal{T}_{p,ij}$. The trace-free SGS tensor is modeled using a viscosity assumption (compressible Smagorinsky model), while the subgrid energy is parametrized by a Yoshizawa model (Yoshizawa 1986):

$$\mathcal{T}_{p,ij} = -C_S 2\Delta_f^2\bar{n}_p|\hat{S}_p|(\hat{S}_{p,ij} - \frac{\delta_{ij}}{3}\hat{S}_{p,kk})$$
$$+ C_I 2\Delta_f^2\bar{n}_p|\hat{S}_p|^2\delta_{ij} \tag{18}$$

where $\hat{S}_p$ is the filtered particle strain rate tensor, $|\hat{S}_p|^2 = 2S_{p,ij}S_{p,ij}$ and Δ_f the filter characteristic length. The model constants have been evaluated in a priori tests (Riber *et al.* 2006) leading to the values $C_S = 0.02$, $C_I = 0.012$.
The subgrid diffusion term in the filtered RUE is modeled by an eddy-diffusivity model:

$$Q_{p,j} = -\frac{\bar{n}_p C_S 2\Delta_f^2|\hat{S}_p|}{Pr_{p,SGS}}\frac{\partial\widehat{\delta\theta}_p}{\partial x_j} \tag{19}$$

with the particle turbulent Prandtl number $Pr_{p,SGS} = 0.8$. The subgrid production of filtered RUE term $\Pi_{\delta\theta_p}$ acts like a dissipation term in the subgrid energy equation. Using an

equilibrium assumption on the particle correlated subgrid energy and neglecting diffusion terms leads to:

$$-\frac{\bar{n}_p}{\tau_p}\left(\frac{\mathcal{T}_{p,kk}}{\bar{n}_p} - q_{gp,SGS}\right) + \Pi_{\delta\theta_p} - \mathcal{T}_{p,ij}\frac{\partial \hat{u}_{p,i}}{\partial x_j} = 0 \quad (20)$$

where the subgrid covariance is $q_{gp,SGS} = \widehat{u_{p,k}u_{g,k}} - \hat{u}_{p,k}\hat{u}_{g,k}$. To first order, the drag force term can be neglected and $\Pi_{\delta\theta_p}$ can be modeled by: $\Pi_{\delta\theta_p} \approx \mathcal{T}_{p,ij}\partial\hat{u}_{p,i}/\partial x_j$ with the SGS tensor modeled by Eq. (18). This model ensures that the correlated energy dissipated by subgrid effects is fully transfered into RUE to be finally dissipated by friction with the fluid.

Comparison of gas flow without particles

Before discussing results for the dispersed phase, the accuracy of the LES solver for the gas phase is evaluated by computing the flow without particles and comparing it to the same data provided in Borée *et al.* (2001). The grid used with the code AVBP is presented in Fig. 2 and some parameters of the simulation are summarized in Table 1.

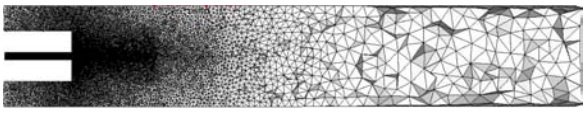

Figure 2: Geometry of the computational domain. Grid elements used: tetrahedra.

Grid type	Tetrahedra
Number of cells / nodes	2,058,883 / 367,313
Time step (μs) / CFL	3.2 / 0.7
Averaging time (s) / Iterations	1.03 / 320,000
LES model	Smagorinsky
Wall model	Law-of-the-wall

Table 1: Summary of parameters and models used in AVBP for the gas-flow computation without particles.

A typical snapshot of the velocity field (modulus) in the central plane is displayed in Fig. 3. The figure shows the complex structure of the recirculating flow: on the axis, the flow is recirculating down to $z = 200$ mm. On the sides of the channel, the flow also separates from $z \approx 50$ mm to $z \approx 400$ mm.

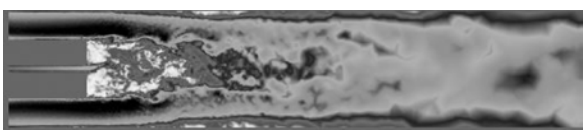

Figure 3: Instantaneous field of velocity modulus. Maximum value (black): 6 m/s. Minimum value (white): 0 m/s.

In Figs 4 to 7, the radial profiles (averaged in the azimuthal direction) of mean and RMS velocities obtained by AVBP are compared with the experimental values at 7 stations of the z axis ($z = 3, 80, 160, 200, 240, 320$ and 400 mm). The LES solver captures most of the flow physics: the axial mean and RMS velocities (Fig. 4 and 5) agree with the measurements. The length of the recirculation zone (evidenced by the negative values of axial velocities on the axis) is well predicted. In the coflow, the RMS values predicted by LES are too low because no turbulence is injected at the inlet of the domain for these computations.

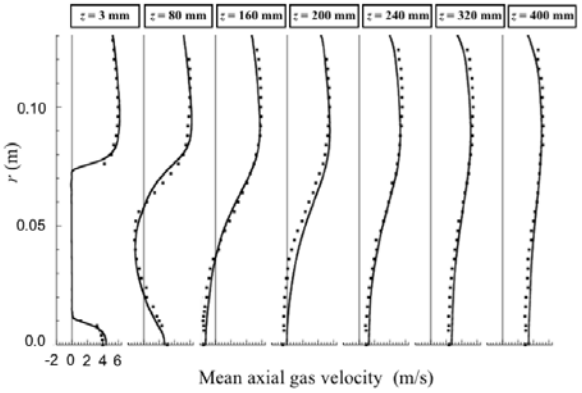

Figure 4: Radial profiles of mean axial gas velocities at 7 stations along z axis. Symbols: experiment; solid line: AVBP.

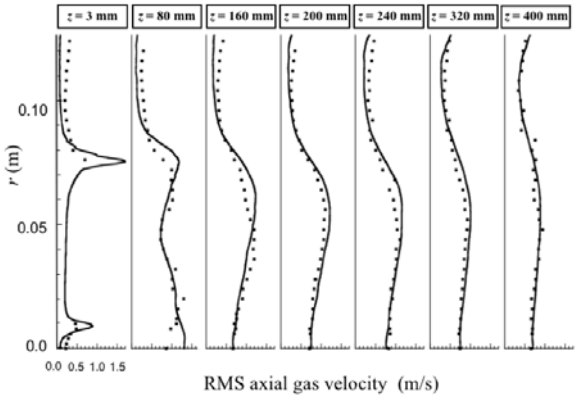

Figure 5: Radial profiles of RMS axial gas velocities at 7 stations along z axis. Symbols: experiment; solid line: AVBP.

The mean radial velocity levels (Fig. 6) remain small (less than 1 m/s) and the LES code captures the radial velocity fields correctly (Fig. 7). The particle mean stagnation point (around $z = 160$ mm) is a delicate zone where the AVBP solver has some difficulties. The source of this problem is the exact position of the stagnation point: any small mismatch in this position leads to large changes in profiles measured around this point. Upstream and downstream of this point, the agreement is very good.

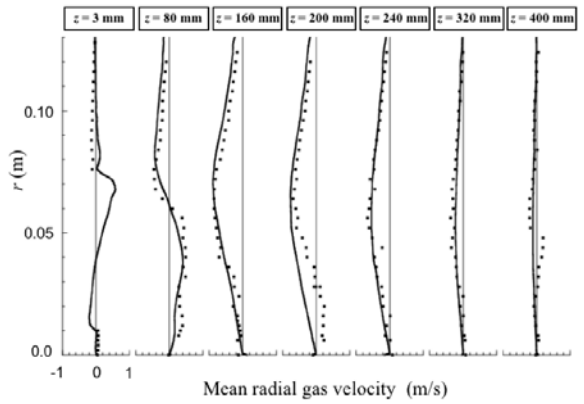

Figure 6: Radial profiles of mean radial gas velocities at 7 stations along z axis. Symbols: experiment; solid line: AVBP.

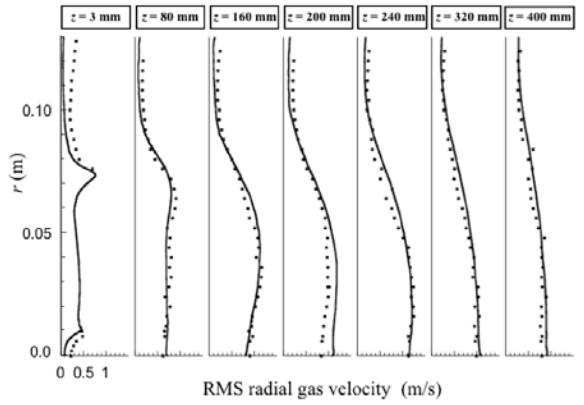

Figure 7: Radial profiles of RMS radial gas velocities at 7 stations along z axis. Symbols: experiment; solid line: AVBP.

The code exhibits an overall good agreement with experimental results. This indicates that tests for the dispersed phase can be performed with reasonable confidence.

Results for two-phase flow cases

This section presents the results for the 22 percent mass loading of the central jet, obtained with two different computations summarized in Table 2[1]. The grid and the time step used are presented in Table 1. In all computations presented here, the injected particles have a size of 60 microns. Separated studies which are not reported here, using another Lagrangian solver and multidisperse particles or 60 microns particles have shown that using a monodisperse distribution of size was very close to the 22 percent case of Borée *et al.* (2001) and was sufficient to capture both the mean flow effects on the gas (through two-way coupling) and the dynamics of the 60 microns class.

[1]For these runs, the RUM model is not used and the $\widehat{\delta\theta}_p$ term in Eq. (10) is set to zero.

	EE	EL
Averaging time (s)	0.64	0.80
Particle mean speed	Exp. profile	Exp. profile
Turbulent fluctuations	Zero	White noise (12%)
Particle distribution	Exp. profile	Homogeneous

Table 2: Summary of parameters and models used for the particle injection (22 percent mass loading computation). The particles are injected in the central tube.

An essential part of these LES is the introduction of the particles in terms of position and velocity. The injection planes are not the same for both approaches (Fig. 8). The methodologies used to inject the particles are also different to evaluate their impact on results. In EE, both the mass loading and the mean velocity imposed in the injection plane ($z = -200$ mm) are the ones measured experimentally at $z = 3$ mm. No turbulent fluctuations are introduced. In the EL formulation, the mass loading is homogeneous over the injection section and the injection speed profile is also the experimental one measured at $z = 3$ mm. In the EL formulation, a white noise (amplitude of the order of 12 percent of the mean velocity) is added to the particle mean velocity profiles to match experimental measurements at $z = 3$ mm.

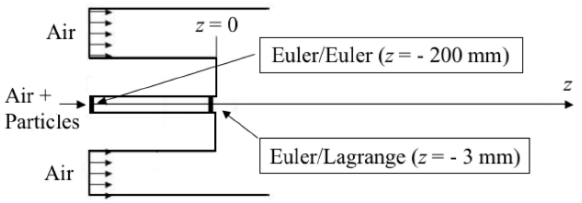

Figure 8: Injection position for particles.

The velocity fields for the gas phase change when the particles are injected but these effects are limited and are not discussed here. Figures 9 to 12 show velocity fields for particles obtained with both approaches along with the measurements of Borée. The agreement between the experiments and the two LES sets of data is good. An interesting result is that EE (solid line) and EL (dashed line) provide similar results showing that the EE approach is able to reproduce the mean-flow properties predicted by the EL computation. On the other hand, Figs. 10 and 12 show that EL formulation predicts particle RMS velocity more precisely. This is consistent with the fact that, when no RUM model is used, the EE approach underestimates turbulent fluctuations of particle velocity. Recent studies by Riber *et al.* (2006) have shown that when these contributions are considered, particle velocity fluctuations are correctly predicted.
A convenient way to look at the results is to consider the central z axis of the configuration: a critical zone is the stagnation point for the gas located around $z = 160$ mm. This is also a zone where particles accumulate and must stop before

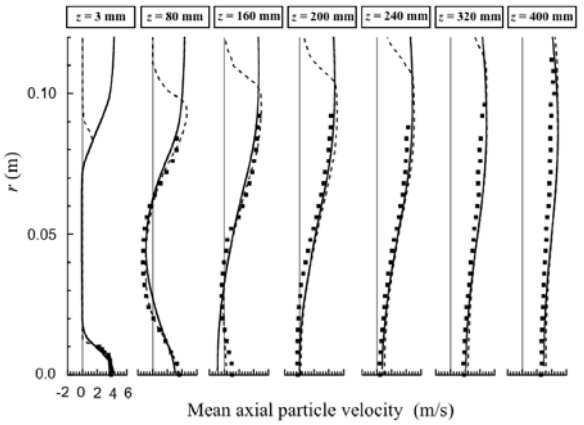

Figure 9: Radial profiles of mean axial particle velocities at 7 stations along z axis. Symbols: experiment; solid line: EE; dashed line: EL.

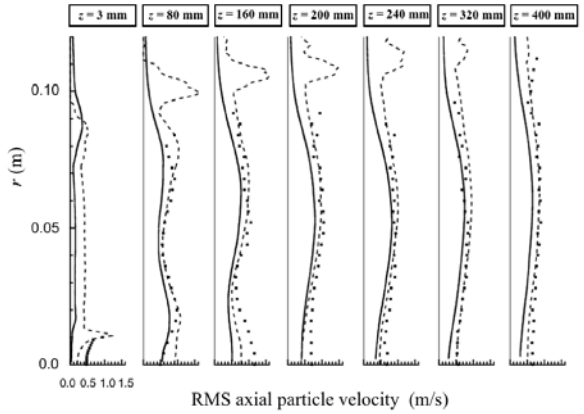

Figure 10: Radial profiles of RMS axial particle velocities at 7 stations along z axis. Symbols: experiment; solid line: EE; dashed line: EL.

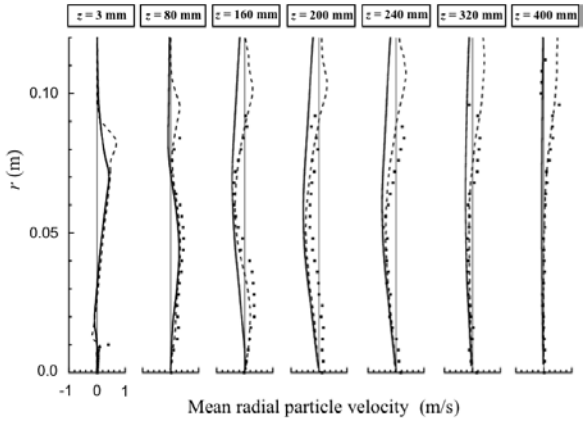

Figure 11: Radial profiles of mean radial particle velocities at 7 stations along z axis. Symbols: experiment; solid line: EE; dashed line: EL.

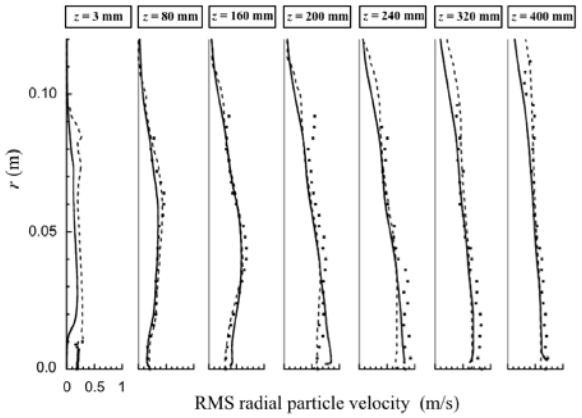

Figure 12: Radial profiles of RMS radial particle velocities at 7 stations along z axis. Symbols: experiment; solid line: EE; dashed line: EL.

turning around to escape from the recirculating flows by the sides. Figure 13 shows field of local volume fraction of solid particles for the EE computation. Local droplet accumulation is also observed upstream of the stagnation point within the central jet.

Figure 13: Instantaneous volume fraction in the central plane from Euler-Euler simulation.

This can be quantified by plotting mean velocities along the axis for the gas (Fig. 14) and for the solid particles (Fig. 15). On this axis, both AVBP results match but are slightly off the experimental results. The cause of this discrepancy was investigated through various tests and was identified as the absence of turbulence injected on the gas phase in the inner jet: a direct verification of this effect is that in both computations (EE: solid and EL: dashed lines), the gas and the particle velocities in the central duct increase between $z = -200$ and $z = 0$ mm, indicating that the flow is relaminarizing. This also demonstrates the importance of injecting not only the proper mean profile for the gas velocity but also fluctuations with a reasonably well-defined turbulent spectrum. Additional tests also reveal that the injection of white noise on the particle velocities has a very limited effect on the results.

Figures 16 and 17 display axial profiles of RMS velocities for the gas and the particles. These plots confirm that the position where the maximum levels of gas and particle turbulence are found on the axis is shifted towards the jet inlet and is too intense for both computations.

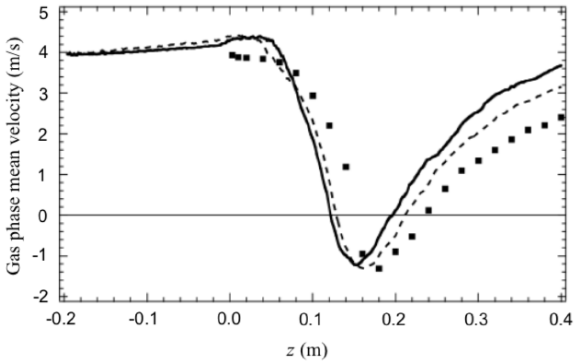

Figure 14: Axial profiles of mean gas velocities. Symbols: experiment; solid line: EE; dashed line: EL.

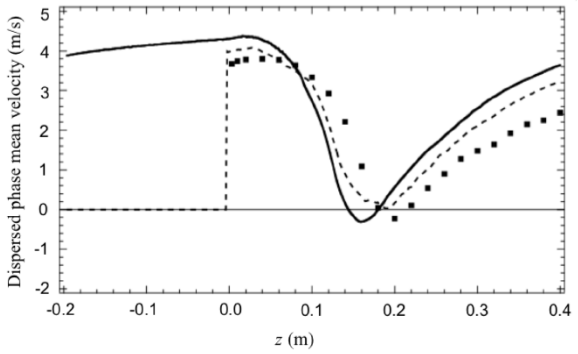

Figure 15: Axial profiles of mean particle velocities. Symbols: experiment; solid line: EE; dashed line: EL.

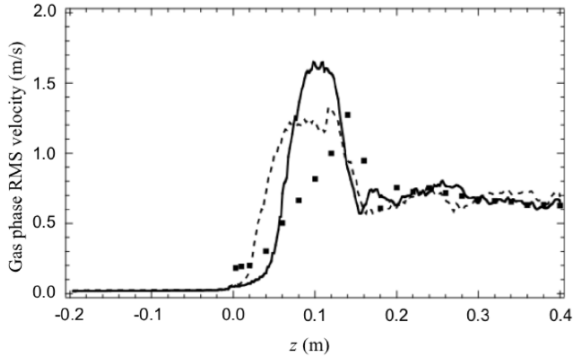

Figure 16: Axial profiles of RMS gas axial velocities. Symbols: experiment; solid line: EE; dashed line: EL.

Analysis of code scalability

In terms of code implementation EE techniques are naturally parallel because the flow and the droplets are solved using the same solver (Kaufmann 2004). On the other hand, the EL approach is not well-suited to parallel computers since two different solvers must be coupled, which increases the complexity of the implementation on a parallel computer. In this case, two methods can be used for LES:

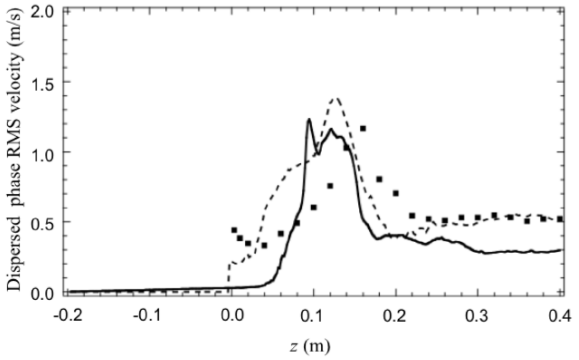

Figure 17: Axial profiles of RMS particle axial velocities. Symbols: experiment; solid line: EE; dashed line: EL.

1. Task parallelization in which some processors compute the gas flow and others compute the droplets flow.

2. Domain partitioning in which droplets are computed together with the gas flow on geometrical subdomains mapped on parallel processors. Droplets must then be exchanged between processors when leaving a subdomain to enter an adjacent domain.

For LES, it is easy to show that only domain partitioning is efficient on large grids because task parallelization would require the communication of very large three-dimensional data sets at each iteration between all processors. However, codes based on domain partitioning are difficult to optimize on massively parallel architectures when droplets are clustered in one part of the domain (typically, near the fuel injectors). Moreover, the distribution of droplets may change during the computation: for a gas turbine reignition sequence, for example, the chamber is filled with droplets when the ignition begins thus ensuring an almost uniform droplet distribution; these droplets then evaporate rapidly during the computation, leaving droplets only in the near injector regions. This leads to a poor speedup on a parallel machine if the domain is decomposed in the same way for the entire computation. As a result, dynamic load balancing strategies are required to redecompose the domain during the computation itself to preserve a high parallel efficiency (Ham *et al.* 2003).

In this section, the scalability of the EL model is analyzed by means of two basic parameters used to measure the efficiency of parallel implementation: the speedup and the reference single-phase CPU time ratio. The former is defined as the ratio between the CPU time of a simulation with 1 processor and the CPU time of a simulation with a given number of processors, N_{procs}:

$$Speedup = \frac{T_{run}(1)}{T_{run}(N_{procs})} \ . \tag{21}$$

The latter is defined as the ratio between the CPU time of a simulation with a given number of procs and the CPU time of the reference single-phase simulation with 1 processor:

$$CPU\ time\ ratio = \frac{T_{run}(N_{procs})}{T_{single-phase}(1)}\ . \qquad (22)$$

Note that the speedup of the EE model can be considered as good as the single-phase computation since the dispersed phase uses the same parallelization applied to the gaseous phase. The EE formulation additional cost is of the order of 80 percent for this test case since the computational cost does not depend on the number of particles.

A scalability study of the EL simulation has been performed in a CRAY XD1 supercomputer at CERFACS for a number of processors up to 64. Table 3-4 and Figs. 18-19 summarize these results for this case (inner jet mass loading of 22 percent) with a total number of particles present in the domain of the order of $600{,}000$.

N_{procs}	1	2	4	8	16	32	64
Ideal scaling	1	2	4	8	16	32	64
Single-phase	1	2.01	4.06	8.2	16.2	32.7	62.5
Two-phase EL	1	1.92	3.85	7.4	13.3	22.9	34.9

Table 3: Summary of the speedup of the EL approach. Supercomputer: CRAY XD1.

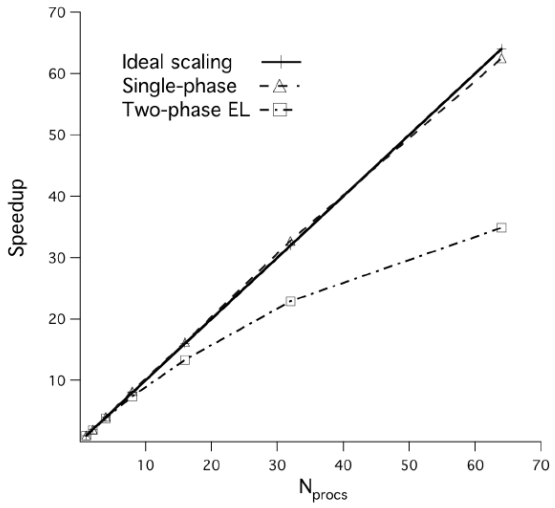

Figure 18: Speedup of the single-phase and the two-phase EL simulation. Supercomputer: CRAY XD1.

The drop of performances shown in Fig 18 is not related to large communications costs between processors as it might be thought at first sight but merely to the parallel load imbalance generated by the partitioning algorithm (Garcia *et al.* 2005). This effect can be observed by plotting the number of nodes, cells and particles presented in each processor. Figure 20 reports the number of nodes and cells presented per processor for a 32-partition simulation by using a recursive inertial bisection (RIB) partitioning algorithm. It shows an excellent load-balancing for the gaseous phase: all processors contains about the same number of cells ($\approx 64{,}500/$processor) and nodes ($\approx 13{,}000/$processor). On the other hand, Fig. 21 shows a huge particle load imbalance where one single processor contains almost half the total number of particles of the simulation. This increases significantly the memory requirements ($\approx$ 20 times the number of nodes) and the floating-point operations for this processor. This points out the need of dynamic load balancing for two-phase flow simulations with a Lagrangian approach, for example, by using multi-constraint partitioning algorithms which take into account particle loading on each processor (Ham *et al.* 2003).

N_{procs}	1	2	4	8	16	32	64
Single-phase	1	0.50	0.25	0.12	0.06	0.030	0.016
Two-phase EL	1.05	0.54	0.27	0.14	0.08	0.046	0.030

Table 4: Summary of the CPU time ratios of the EL approach. Supercomputer: CRAY XD1.

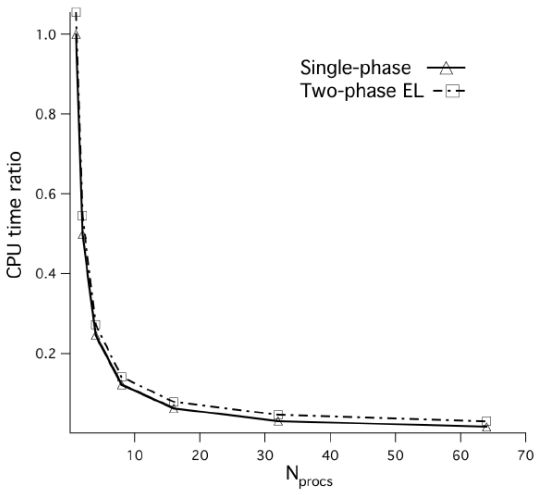

Figure 19: CPU Time ratio of the single-phase and the two-phase EL simulation. Supercomputer: CRAY XD1

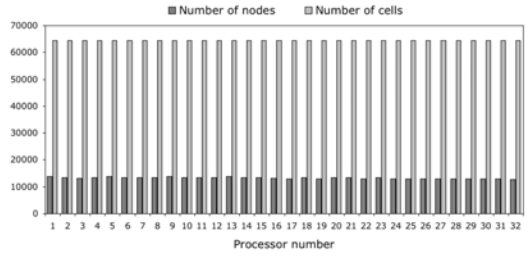

Figure 20: Number of cells and nodes per processor for a 32-partition by using a recursive inertial bisection (RIB) partitioning algorithm.

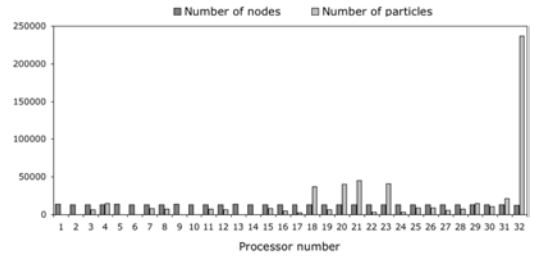

Figure 21: Number of nodes and particles per processor for a 32-partition by using a recursive inertial bisection (RIB) partitioning algorithm.

Conclusions and perspectives

For the present test case (mass loading of 22 percent), the total number of particles present in the domain for the Lagrange codes is of the order of 600,000. For such a small number of particles, the computing power required by the Lagrangian solvers compared to the power required for the gas flow remains low: the additional cost due to the particles is small even with the load balancing problem observed when increasing the number of parallel processors. The EE formulation additional cost (of the order of 80 percent) is independent of the mass loading, so that, for such a dilute case, the EL formulations proved to be faster up to 64 processors. In terms of results quality, the EL and the EE results implemented into the AVBP solver are very close showing that both formulations lead to equivalent results in this situation. An important factor controlling the quality of the results is the introduction of turbulence on the gas flow in the injection duct: without these turbulent fluctuations, the results are not as good on the axis in terms of positions of the recirculation zones. In addition, the absence of RUV contribution considered in the present case evidences an underestimation of turbulent fluctuations for the EE results to be taken into account in future works. Future developments of the Lagrangian module of the AVBP solver will be devoted to the integration of a particle/mesh load balancing capabilities to improve scalability of the EL simulations.

Acknowledgements

The help of Pr J. Borée in providing the experimental data and analyzing the results is gratefully acknowledged.

References

Apte, S.V., Mahesh, K., Moin, P. & Oefelein, J.C. Large-eddy simulation of swirling particle-laden flows in a coaxial-jet combustor. International Journal of Multiphase Flow, Volume 29, 1311 – 1331 (2003).

Boivin, M., Simonin, O. & Squires, K. Direct numerical simulation of turbulence modulation by particles in isotropic turbulence. Journal of Fluid Mechanics, Volume 375, 235 – 263 (1998)

Boivin, M., Simonin, O. & Squires, K. On the prediction of gas-solid flows with two-way coupling using large eddy simulation. Physics of Fluids, Volume 12, Number 8, 2080 – 2090 (2000).

Borée, J., Ishima, T. & Flour, I. The effect of mass loading and inter-particle collisions on the development of the polydispersed two-phase flow downstream of a confined bluff body. Journal of Fluid Mechanics, Volume 443, 129 – 165 (2001)

Caraeni, D., Bergstrom, C. & Fuchs, L. Modeling of liquid fuel injection, evaporation and mixing in a gas turbine burner using large eddy simulation. Flow, Turbulence and Combustion, Volume 65, 223 – 244 (2000)

Chapman, S. & Cowling, T. The Mathematical Theory of Non-Uniform Gases. Cambridge Mathematical Library Edition. Cambridge University Press (1939) (digital reprint 1999)

Colin, O., Ducros, F., Veynante, D. & Poinsot, T. A thickened flame model for large eddy simulations of turbulent premixed combustion. Physics of Fluids, Volume 12, Number 7, 1843 – 1863 (2000)

Colin, O. & Rudgyard, M. Development of high-order Taylor-Galerkin schemes for unsteady calculations. Journal of Computational Physics, Volume 162, Number 2, 338 – 371 (2000)

Druzhinin, O.A. & Elghobashi, S. On the decay rate of isotropic turbulence laden with microparticles. Physics of Fluids, Volume 11, Number 3, 602 – 610 (1999)

Fede, P. & Simonin, O. Numerical Study of Subgrid Fluid Turbulence Effects on the Statistics of Heavy Colliding Particles. Physics of Fluids, Volume 18, 045103 (17 pages) (2006)

Février, P. & Simonin, O. Development and Validation of a Fluid and Particle Turbulent Stress Transport Model in Gas-Solid Flows. Proc. 9th Workshop on Two-Phase Flow Predictions, Merseburg, M. Sommerfeld (Editor), 77 – 85 (1999)

Février, P., Simonin, O. & Squires, K. Partitioning of particle velocities in gas-solid turbulent flows into a continuous field and a spatially uncorrelated random distribution: Theoretical formalism and numerical study. Journal of Fluid Mechanics, Volume 533, 1 – 46 (2005)

García, M., Sommerer, Y., Schönfeld T. & Poinsot, T. Evaluation of Euler-Euler and Euler-Lagrange strategies for Large-Eddy Simulations of turbulent reacting flows. ECCOMAS thematic conference on computational combustion, Lisbon, Portugal (2005)

Gatignol, R. The Faxén formulae for a rigid particle in an unsteady non-uniform Stokes flow. Journal de mécanique théorique et appliquée, Volume 1, Number 2, 143 – 160 (1983)

Ham, F., Apte, S., Iaccarino, G., Wu, X., Herrmann, M., Constantinescu, G., Mahesh, K. & Moin, P. Unstructured LES of reacting multiphase flows in realistic gas turbine combustors.

In Annual Research Briefs. Center for Turbulence Research, NASA Ames/Stanford Univ, 139 – 160 (2003)

Ishima, T., Borée, J., Fanouillère, P. & Flour, I., Presentation of a two phase flow data based obtained on the flow loop Hercule. Proc. 9th Workshop on Two-Phase Flow Predictions, Merseburg, M. Sommerfeld (Editor), 3 – 18 (1999)

Kaufmann, A., Simonin, O., Cuenot, B., Poinsot, T. & Helie, J. Dynamics and dispersion in 3D unsteady simulations of two phase flows. In Supercomputing in Nuclear Applications. Paris: CEA. (2003)

Kaufmann, A. Vers la simulation des grandes échelles en formulation Euler/Euler des écoulements réactifs diphasiques. PhD thesis (2004)

Kaufmann, A., Hélie, J., Simonin, O., & Poinsot, T. Comparison between Lagrangian and Eulerian Particle Simulations Coupled with DNS of Homogeneous Isotropic Decaying Turbulence. Proceedings of the Estonian Academy of Sciences. Engineering, Volume 11, Number 2, 91 – 105 (2005)

Maxey, M. & Riley, J. Equation of motion for a small rigid sphere in a nonuniform flow. Physics of Fluids, Volume 26, Number 4, 883 – 889 (1983)

Moin, P., Squires, K., Cabot, W. & Lee, S. A dynamic subgrid-scale model for compressible turbulence and scalar transport. Physics of Fluids A, Volume 3, Number 11, 2746 – 2757 (1991)

Moreau, M., Bédat, B. & Simonin, O. A priori testing of subgrid stress models for euler-euler two-phase LES from euler-lagrange simulations of gas-particle turbulent flow. In 18th Annual Conference on Liquid Atomization and Spray Systems. ILASS Americas. (2005)

Moureau, V., Lartigue, G., Sommerer, Y., Angelberger, C., Colin, O. & Poinsot, T. High-order methods for dns and les of compressible multicomponent reacting flows on fixed and moving grids. Journal of Computational Physics, Volume 202, Number 2, 710 – 736 (2005)

Poinsot, T. & Veynante, D. Theoretical and numerical combustion. R.T. Edwards, 2nd edition (2005)

Reeks, M. W. On a kinetic equation for the transport of particles in turbulent flows. Physics of Fluids A, Volume 3, 446 – 456 (1991)

Riber, E., Moreau, M., Simonin, O. & Cuenot, B. Towards large eddy simulations of non-homogeneous particle laden turbulent gas flows using euler-euler approach. In 11th Workshop on Two-Phase Flow Predictions. Merseburg, Germany. (2005)

Riber, E., Moreau, M., Simonin, O. & Cuenot, B. Development of Euler-Euler LES Approach for Gas-Particle Turbulent Jet Flow. In Proceedings of Symposium Fluid-Particle Interactions in Turbulence. ASME Joint U.S. European Fluids Engineering Summer Meeting. Miami, FEDSM2006-98110 (2006)

Roux, S., Lartigue, G., Poinsot, T., Meier, U. & Bérat, C. Studies of mean and unsteady flow in a swirled combustor using experiments, acoustics analysis and large eddy simulations. Combustion and Flame, Volume 141, 40 – 54 (2005)

Schiller, L. & Nauman, A. A drag coefficient correlation. V.D.I. Zeitung, Volume 77, 318 – 320 (1935)

Schmitt, P., Poinsot, T., Schuermans, B. & Geigle, K. Large-eddy simulation and experimental study of heat transfer, nitric oxide emissions and combustion instability in a swirled turbulent high pressure burner. Journal of Fluid Mechanics, Volume 570, 17 – 46 (2007)

Selle, L., Lartigue, G., Poinsot, T., Koch, R., Schildmacher, K.-U., Krebs, W., Prade, B., Kaufmann, P. & Veynante, D. Compressible large-eddy simulation of turbulent combustion in complex geometry on unstructured meshes. Combustion and Flame, Volume 137, Number 4, 489 – 505 (2004)

Simonin, O., Février, P., & Laviéville, J. On the Spatial Distribution of Heavy-Particle Velocities in Turbulent Flow : from Continuous Field to Particulate Chaos Journal of Turbulence, Volume 3, 040 (2002)

Vermorel, O., Bédat, B., Simonin, O. & Poinsot, T. Numerical study and modelling of turbulence modulation in a particle laden slab flow. Journal of Turbulence, Volume 4, Number 025, 1 – 39 (2003)

Vreman, B., Geurts, B. & Squires, K. Subgrid modeling in les of compressible flow. Applications Scientific Research, Volume 54, 191 – 203 (1995)

Wang, Q. & Squires, K. Large eddy simulation of particle-laden turbulent channel flow . Physics of Fluids, Volume 8, Number 5, 1207 – 1223 (1996)

Yamamoto, Y., Potthoff, M., Tanaka, T., Kajishima, T. & Tsuji, Y. Large-eddy simulation of turbulent gas-particle flow in a vertical channel: effect of considering inter-particle collisions. Journal of Fluid Mechanics, Volume 442, 303 – 334 (2001)

Yoshizawa, A. Statistical theory for compressible turbulent shear flows, with the application to subgrid modeling. Physics of Fluids, Volume 29, Number 7, 2152 – 2164 (1986)

Appendix D

AIAA Journal, Vol. 46, N^o 7, pp. 1773-1781 (July 2008)

Croissance des erreurs d'arrondi et reproductibilité de la Simulation aux Grandes Échelles

La Simulation aux Grandes Échelles (LES) est devenue un outil très efficace pour la prédiction des écoulements turbulents réactifs et non-réactifs. La grande force de la LES par rapport à la méthode classique par résolution des équations de Navier-Stokes moyennées (RANS) est que, comme dans le cas de la Simulation Numérique Directe (DNS), la LES résout les grandes structures de la turbulence au lieu de les modéliser. Cette caractéristique implique que, comme pour la DNS, la LES est sujette au phénomène de séparation des trajectoires : la solution de l'écoulement obtenue par la LES est très sensible à des petites perturbations de l'état de référence. Cela a pour conséquence de limiter le temps de prédictibilité (temps pour qu'une perturbation appliquée sur les petites échelles de la turbulence ait un effet sur les grandes échelles) de la LES/DNS puisque les conditions initiales d'une simulation visant à reproduire un phénomène naturel sont toujours affectées par les incertitudes de mesure.

Un aspect souvent ignoré est que les perturbations numériques qui se produisent en LES conduisent à un autre problème de prédictibilité : des simulations faites avec des conditions initiales strictement identiques peuvent pourtant produire des résultats différents au bout d'un certain temps. Ces perturbations numériques ont différentes sources :

- Les erreurs d'arrondi sont la première source de bruit aléatoire dans n'importe quel calcul en précision finie dans le sens où ils constituent un élément de forçage inévitable pour les équations de Navier-Stokes et peuvent conduire à une variabilité importante des résultats. L'étude de la croissance d'erreur dans les calculs en précision finie est un sujet important en mathématiques appliquées, mais n'a trouvé que peu d'applications dans la mécanique des fluides multidimensionnelle en raison de la complexité des solveurs utilisés en dynamique des fluides numérique (CFD).
- En raison des grandes ressources informatiques qu'ils requièrent, les calculs LES modernes reposent en grande partie sur le calcul parallèle. Dans la plupart des cas, ces codes parallèles utilisent des techniques de découpage de domaine. Le traitement des interfaces entre

processeurs peut alors être une autre source de "bruit" dans les équations de Navier-Stokes. En effet, même dans les codes explicites où l'algorithme est indépendant du nombre de processeurs, un ordre de sommation différent lors de la reconstruction d'une valeur nodale aux interfaces des partitions peut induire des erreurs de non-associativité. Par exemple, dans les codes explicites cell-vertex utilisant des maillages non-structurés, le résidu au nœud est obtenu par addition des résidus pondérés des cellules voisines. Bien évidemment, en arithmétique exacte le résultat de cette addition est indépendant de l'ordre de l'addition, mais ceci n'est plus vrai en arithmétique finie avec les erreurs d'arrondi. Ainsi, les additions de plus de deux termes peuvent produire des résultats différents à cause de l'arithmétique flottante. Par exemple, les erreurs d'arrondi lors des calculs $(a + b) + c$ et $a + (b + c)$ peuvent être différentes, en particulier s'il existe de grandes différences entre les ordres de grandeur des termes de l'addition. Après quelques dizaines de milliers d'itérations, le résultat LES peut en être sensiblement affecté. Étant donné que la propagation de ces erreurs d'arrondi est induite par la réception non-déterministe des messages aux interfaces des partitions, ce type de comportement peut se produire pour tout code CFD parallèle non-structuré, quel que soit le schéma numérique utilisé. En conséquence, les résultats d'une simulation peuvent varier selon le nombre de processeurs utilisés, voir même entre deux exécutions parallèles consecutives sur un même nombre de processeurs. Le cas des codes implicites en temps ou en espace, comme les schémas compacts, n'est pas considéré ici. En effet, pour de tels schémas, les méthodes utilisées pour résoudre un système linéaire à chaque itération dépendent naturellement du nombre de processeurs. Par conséquent, la propagation des erreurs d'arrondi n'est pas la seule raison pour laquelle les solutions obtenues avec des nombres de processeurs différents varient.

- Même sur un calcul séquentiel, les paramètres internes de l'algorithme de découpage peuvent se coupler avec des erreurs d'arrondi pour forcer la solution LES. Par exemple, l'utilisation de l'algorithme Cuthill-McKee (CM) ou de son inverse (RCM) peut mener à une réorganisation différente des nœuds et donc potentiellement produire le même effet qu'une simple perturbation initiale, c'est-à-dire provoquer la divergence de la solution.

- Enfin, les options de compilation, en particulier celles qui touchent à l'optimisation du code et, de toute évidence celles qui affectent les opérations de troncature, sont une quatrième source de variabilité pour la LES. Les tests des options d'optimisation n'ont pas été effectués dans ce travail. Ces tests présenteraient un intérêt certain mais devraient être fait avec précaution car des options trop agressives peuvent directement influer sur l'ordre des opérations et modifier la physique même du calcul, conduisant ainsi à des résultats erronés.

La solution d'un calcul LES/DNS à un instant donné change inévitablement lorsque les erreurs d'arrondi ne sont pas exactement identiques et les solutions LES/DNS sont connues pour n'avoir de sens que d'un point de vue statistique. Pour une utilisation pratique de la LES/DNS, cela n'est pas sans difficulté car cela signifie que l'exécution de la même simulation sur deux machines différentes ou sur la même machine mais avec un nombre différent de processeurs est équivalent à l'introduction d'une perturbation des conditions initiales et peut donc conduire après un certain temps à des résultats instantanés différents. Dans le cas d'écoulements stationnaires en moyenne, les statistiques ne devraient pas dépendre de ces changements et les profils moyens devraient être identiques. Cependant, lorsque l'objectif de la LES est l'étude de phénomènes instationnaires tel que l'allumage dans une chambre de combustion, savoir que les résultats dépendent de ces paramètres est non seulement troublant mais également un inconvénient en terme d'exploitation industrielle.

Cet article traite de ces problématiques et tente de répondre à plusieurs questions simples d'intérêt pour tout utilisateur de la LES : comment la solution instantanée d'un calcul LES dépend-elle du nombre de processeurs utilisés ? Et de la condition initiale ? Et des détails de l'algorithme ?

La première section donne un exemple des effets du nombre de processeurs dans un cas simple : un écoulement turbulent dans un canal rectangulaire calculé avec un code explicite de LES. Cet exemple montre que même dans un code explicite, faire deux fois le même calcul sur une même machine, avec un nombre de processeurs différent peut conduire à l'obtention de solutions instantanées totalement différentes. La deuxième section donne une description systématique des effets des erreurs d'arrondi pour trois types d'écoulements : un écoulement de Poiseuille laminaire, un canal turbulent et une chambre de combustion à géométrie complexe. Dans tous les cas, la différence entre deux solutions instantanées obtenues en changeant le nombre de processeurs, la condition initiale ou la réorganisation des nœuds est quantifiée en terme de normes entre les deux solutions. Les effets du pas de temps et de la précision de la machine (simple, double et quadruple) sont également étudiés dans cette section. Ces résultats montrent que seuls les écoulements turbulents sont caractérisés par une forte sensibilité à ces paramètres. Ces résultats confirment que la LES reflète la véritable nature de la turbulence dans la mesure où elle peut amplifier exponentiellement dans le temps des perturbations infinitésimales des conditions initiales. Ils révèlent également une limitation de la LES en termes de validation et de prédiction des phénomènes instationnaires.

AIAA JOURNAL
Vol. 46, No. 7, July 2008

Growth of Rounding Errors and Repetitivity of Large-Eddy Simulations

Jean-Mathieu Senoner,* Marta García,* Simon Mendez,* Gabriel Staffelbach,† and Olivier Vermorel†
Centre Européen de Recherche et de Formation Avancée en Calcul Scientifique, 31057 Toulouse Cedex 01, France
and
Thierry Poinsot‡
Institut de Mécanique des Fluides, 31400 Toulouse, France

DOI: 10.2514/1.34862

This paper studies the propagation of rounding errors in large-eddy simulation and shows that instantaneous flowfields produced by large-eddy simulation are partially controlled by these rounding errors and depend on multiple parameters: number of processors used for parallel simulation (even in an explicit code), changes in initial conditions (even of the order of machine accuracy), machine precision (simple, double, or quadruple), etc. Using a laminar Poiseuille pipe flow, a fully developed turbulent channel flow, and a complex burner geometry as test cases, results show that only turbulent flows exhibit a high sensitivity to these parameters. These results confirm that large-eddy simulation reflects the true nature of turbulence insofar as it may exponentially amplify infinitely small perturbations on initial conditions in time. However, they highlight an often overlooked limitation of large-eddy simulation in terms of validation and prediction of unsteady phenomena.

Introduction

LARGE-EDDY simulation (LES) has become the most efficient tool to predict nonreacting [1,2], as well as reacting, turbulent flows [3–8]. The main strength of LES compared with classical Reynolds-averaged methods is that, like direct numerical simulation (DNS) [9–11], LES explicitly captures large-scale unsteady motions due to turbulence, instead of modeling them. This feature implies that like DNS, LES is also subject to the separation of trajectories [12,13]: the flow solution exhibited by LES is very sensitive to any small perturbations of a given reference state. This limits the predictability time of LES/DNS because the initial conditions of a simulation aiming to reproduce a natural phenomenon are always affected by measurement uncertainties, and the determination of predictability times of numerical simulations has been an important field of investigation [14,15]. An often ignored aspect is that the numerical perturbations occurring in LES lead to another predictability issue: simulations started with strictly identical initial conditions may yield different results after a certain time. These numerical perturbations have different sources:

1) Rounding errors are the first source of random noise in any finite precision computation; they constitute an unavoidable forcing for the Navier–Stokes equations and may lead to LES variability. The study of error growth in finite precision computations is an important topic in applied numerical mathematics [16–19] but has found few applications in multidimensional fluid mechanics because of the complexity of the codes used in computational fluid dynamics (CFD).

2) Because of its large computational resource requirements, modern LES heavily relies on parallel computing. Therefore, in codes using domain partitioning, i.e., most of them, the treatment of interfaces is an additional "noise" source in the Navier–Stokes equations. Even in explicit codes, where the algorithm is independent of the number of processors, the different summation orders with which a nodal value is reconstructed at partition interfaces may induce nonassociativity errors. For example, in explicit codes on unstructured meshes using cell vertex methods [20], the residual at one node is obtained by adding the weighted residuals of the surrounding cells. Of course, the exact result of this addition is independent of the addition ordering but this is not true for rounding errors. Therefore, additions of more than two summands may yield distinct results for floating-point accumulation. For example, the rounding errors in $(a + b) + c$ and in $a + (b + c)$ may be different, in particular if there are large differences in orders of magnitude between the summands [21] and, after a few tens of thousands time steps, the LES result may be affected. Because the propagation of these rounding errors is induced by nondeterministic message arrival at partition interfaces, such behavior may occur for any unstructured parallel CFD code, regardless of the numerical schemes used. As a consequence, the simulation output might change when run on a different number of processors. The case of implicit codes in time [2,3,22] or in space, such as compact schemes [23–25], is not considered here; for such schemes, the methods [26,27] used to solve the linear system appearing at each time step depend on the number of processors. Therefore, the propagation of rounding errors is not the only reason why solutions obtained with different numbers of processors vary.

3) Even on a single processor computation, internal parameters of the partitioning algorithm may couple with rounding errors to force the LES solution. For example, a different reordering of nodes using the Cuthill–McKee (CM) or the reverse Cuthill–McKee (RCM) algorithm [28,29] may produce the same effect as a simple perturbation and can be the source of solution divergence.

4) Finally, compilation options, in particular those affecting code optimization, and obviously those affecting truncation operations, are a fourth source of LES variability. Different optimization options of the compiler are not tested in the following. Such tests would certainly be of interest, although care must be taken because too

Received 28 September 2007; revision received 21 February 2008; accepted for publication 25 February 2008.

*Ph.D. Student, Computational Fluid Dynamics Team.
†Senior Research Fellow, Computational Fluid Dynamics Team.
‡Research Director, Institut National Polytechnique de Toulouse and Centre National de la Recherche Scientifique. Associate Fellow AIAA.

aggressive optimization options can affect scheduling of operations in a physically wrong manner and lead to erroneous results.

The solution of a given LES/DNS at a certain instant unavoidably changes when the rounding errors are not exactly identical, and LES/DNS solutions are known to have a meaning only in a statistical manner [30]. It is, however, a real difficulty in the practical use of LES/DNS because it means that running the same simulation on two different machines or one machine with a different number of processors is equivalent to a perturbation of initial conditions and can lead to different instantaneous results after a certain time. For steady flows in the mean, statistics should not depend on these changes and mean profiles should be identical. However, when the objective of the LES is the study of unsteady phenomena, such as ignition or quenching in a combustor [31,32], knowing that results depend on these parameters is certainly a sobering thought and a drawback in terms of industrial exploitation. This paper tries to address these issues and answer a simple question which is of interest for all practitioners of LES: How does the instantaneous solution produced by LES depend on the number of processors used to run the simulation? On the initial condition? On internal details of the algorithm?

The first section gives an example of the effects of the number of processors in a simple case: a rectangular turbulent channel flow computed with a fully explicit LES code [33]. This example shows that even in an explicit code, running a simulation twice on a different number of processors can lead to totally different instantaneous solutions. The second section then gives a systematic description of the effects of rounding errors in three flows: a turbulent channel flow, a laminar Poiseuille flow, and a complex burner flow. For all cases, the difference between two instantaneous solutions obtained by changing either the number of processors, the initial condition, or the node ordering is quantified in terms of norms between the two solutions. The effects of time step and machine precision (simple, double, and quadruple) are also investigated in this section. All simulations have been performed on an IBM JS21 supercomputer.

The numerical solver uses a cell vertex formulation, i.e., the discrete values of the conserved variables are stored at the cell vertices, whereas fluxes are obtained by averaging along the cell edges [20]. A compact conservative formulation of the compressible Navier–Stokes equations is considered:

$$\frac{\partial \mathbf{w}}{\partial t} + \nabla \cdot \mathcal{F} = \mathbf{0} \tag{1}$$

where $\mathbf{w}$ represents the vector of conservative variables, and $\mathcal{F}$ is the tensor of both viscous and inviscid fluxes. The Green–Gauss theorem is used to compute the numerical residual in each computational cell K_e:

$$\mathbf{r}_e := \frac{1}{V_e} \oint_{\partial K_e} \mathcal{F}_h \cdot \mathbf{n} \, \mathrm{d}S \tag{2}$$

where $\mathcal{F}_h$ and V_e, respectively, denote a suitable numerical approximation of the flux $\mathcal{F}$ and the volume of the computational cell K_e.

In the semidiscrete form, the scheme then writes:

$$\frac{\partial \mathbf{w}_j}{\partial t} = \frac{1}{V_j} \sum_{e \in D_j} \mathbf{D}_{j,e} V_e \mathbf{r}_e \tag{3}$$

where $\mathbf{D}_{j,e}$ is the distribution matrix that weighs the residual of cell K_e to the node j, and thus depends on the numerical scheme. V_j is the volume of the dual cell associated with the node j. The spatial discretization described here can be combined to explicit time-stepping approaches, such as Runge–Kutta, to obtain a fully discretized scheme. The scheme used here for all simulations is the Lax–Wendroff scheme [33,34]. The fully discretized scheme writes

$$\frac{\mathbf{w}_j^{n+1} - \mathbf{w}_j^n}{\Delta t} = \frac{1}{V_j} \sum_{e \in D_j} \left(\frac{1}{n_v^e} \mathbf{I} + \frac{\Delta t}{2V_e} \mathcal{A}_e^n \cdot \mathbf{n}_{j,e} \right) V_e \mathbf{r}_e \tag{4}$$

where n_v^e, $\mathcal{A}_e^n$, and $\mathbf{n}_{j,e}$, respectively, denote the number of vertices of the cell K_e, the Jacobian matrices of the cell K_e, and the normal vector associated with the dual cell of the node j on the cell K_e. Additional tests were performed using a third-order scheme in space and time [35], resulting in the same conclusions.

Effects of Number of Processors on Fully Developed Turbulent Channel Flow LES

The first example is the LES of a rectangular fully developed turbulent channel flow with channel dimensions $75 \times 25 \times 50$ mm (Fig. 1). A pressure gradient is applied to a periodic channel flow and random disturbances are added to pass transition to turbulence. There are no boundary conditions except for the walls. The Reynolds number is $Re_\tau = \delta u_\tau / \nu = 1500$, where δ is half the channel height and u_τ the friction velocity at the wall, $u_\tau = (\tau_{\text{wall}}/\rho)^{1/2}$ with τ_{wall} being the wall stress. The mesh contains 30^3 hexahedral elements, and it is not refined at walls where a law-of-the-wall [8] is used. The first grid point is at a reduced distance $y^+ = y u_\tau / \nu \approx 100$ from the wall. The subgrid model is the Smagorinsky model, the value of the constant is $C_S = 0.18$. The Courant–Friedrichs–Lewy (CFL) number λ controlling the time step Δt is $\lambda = \max[(u + c)\Delta t/\Delta]$, where u is the local convective velocity, c the speed of sound, and Δ the mesh size. The chosen value of the CFL number is $\lambda = 0.7$. For all simulations discussed next, the initial condition corresponds to a snapshot of the flow at a given instant, long after turbulence was initialized, so that it is fully established. The domain partitioning method is perfectly equivalent on any number of processors. The recursive inertial bisection [36,37] algorithm has been used to partition the grid, and the Cuthill-McKee algorithm is considered as the default node reordering strategy on subdomains.

Figures 2–4 show fields of axial velocity in the central plane of the channel at three instants after the run initialization. Two simulations performed on, respectively, four (TC1) and eight processors (TC2) with identical initial conditions are compared. The characteristics of all presented simulations are displayed in Tables 1 and 2. The specific times correspond to (in wall units) $t^+ = 7.68$, $t^+ = 18.43$, and $t^+ = 26.11$, respectively, where $t^+ = u_\tau t/\delta$. Obviously, the two flowfields observed at $t^+ = 7.68$ are identical. However, at $t^+ = 18.43$, differences start to become visible. Finally, at $t^+ = 26.11$, the instantaneous flowfields obtained in TC1 and TC2 are totally different. Even though the instantaneous flowfields are different, statistics remain the same: mean and root mean square axial velocity profiles averaged over $t^+ \approx 60$ are identical for both simulations, as can be seen in Figs. 5 and 6.

This very simple example illustrates the main question of the present work: Is the result of Figs. 2–4 reasonable? If it is not a simple programming error (the next section will show that it is not), can other parameters produce similar effects?

Sensitivity of Laminar and Turbulent Flows to Small Perturbations

To understand how LES can produce diverging instantaneous results such as those shown in the previous section, simple tests were performed to investigate the effects of various aspects of the methodology: 1) laminar/turbulent baseline flow, 2) number of processors, 3) initial condition, 4) node ordering, 5) time step,

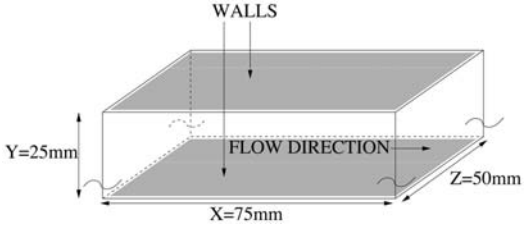

Fig. 1 Schematic of periodic channel. Upper and lower boundaries consist of walls, all other boundaries are pairwise periodic.

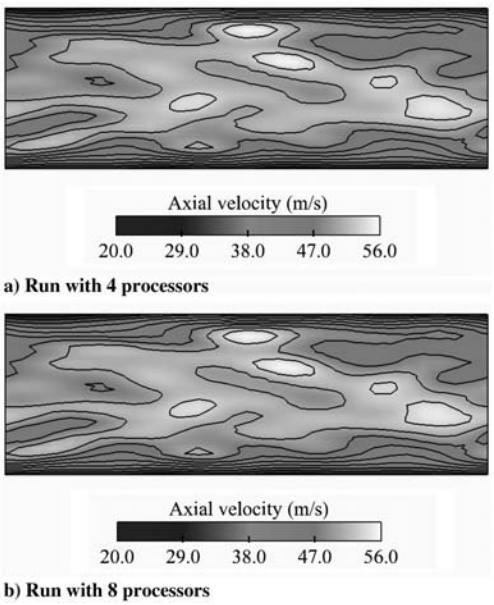

Fig. 2 Instantaneous field of axial velocity in the central plane of the channel at $t^+ = 7.68$: a) run TC1, b) run TC2.

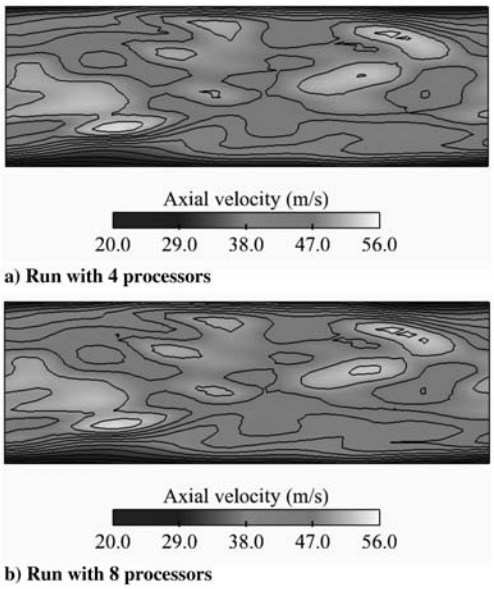

Fig. 3 Instantaneous field of axial velocity in the central plane of the channel at $t^+ = 18.43$: a) run TC1, b) run TC2.

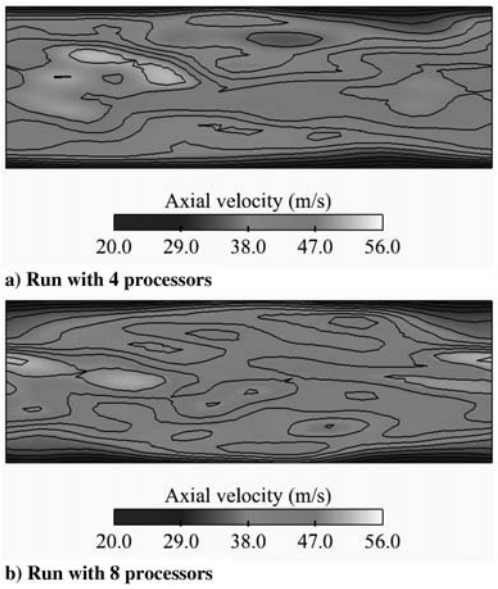

Fig. 4 Instantaneous field of axial velocity in the central plane of the channel at $t^+ = 26.11$: a) run TC1, b) run TC2.

6) floating-point representation according to the Institute of Electrical and Electronics Engineers (IEEE) standard, and 7) investigation of a more realistic configuration with nonperiodic boundary conditions.

For these tests, the objective is to quantify the differences between two LES solutions produced by a couple of simulations in Tables 1 and 2. Let u_1 and u_2 be the axial velocity components of two given instantaneous solutions at the same instant after initialization. A proper method to compare the latter is to use the following norms:

$$N_{\max} = \max(|u_1(\mathbf{x}) - u_2(\mathbf{x})|) \quad \text{for } \mathbf{x} \in \Omega \tag{5}$$

$$N_{\text{mean}} = \left(\frac{1}{V_\Omega}\int_\Omega [u_1(\mathbf{x}) - u_2(\mathbf{x})]^2 \, \mathrm{d}\Omega\right)^{\frac{1}{2}} \quad \text{for } \mathbf{x} \in \Omega \tag{6}$$

where Ω and V_Ω, respectively, denote the computational domain and its volume. Both norms are expressed in meters per second. $N_{\max}$ provides the maximum local axial velocity difference in the field between two solutions, whereas N_{mean} yields a volumetrically averaged axial velocity difference between the two solutions. The growth of $N_{\max}$ and N_{mean} vs the number of time steps will be used as a direct indicator for the divergence of the solutions.

Fully Deterministic LES?

First, it is useful to indicate that performing any of the LES of Table 1 twice on the same machine with the same number of

Table 1 Summary of LES runs (fully developed turbulent channel flow)

Run ID	No. processors	Initial conditions	Precision	Graph ordering	CFL λ
TC1	4	Fixed	Double	CM	0.7
TC2	8	Fixed	Double	CM	0.7
TC3	1	Fixed	Double	CM	0.7
TC4	1	Modif.	Double	CM	0.7
TC5	1	Fixed	Double	RCM	0.7
TC6	4	Fixed	Double	CM	0.35
TC7	8	Fixed	Double	CM	0.35
TC8	4	Fixed	Simple	CM	0.7
TC9	8	Fixed	Simple	CM	0.7
TC10	28	Fixed	Quadr.	CM	0.7
TC11	32	Fixed	Quadr.	CM	0.7

Table 2 Summary of laminar runs (Poiseuille flow)

Run ID	No. processors	Initial conditions	Precision	Graph ordering	CFL λ
LP1	4	Fixed	Double	CM	0.7
LP2	8	Fixed	Double	CM	0.7

processors, the same initial conditions, and the same partition algorithm, leads to exactly the same solution: N_{max} and N_{mean} being zero to machine accuracy. In that sense, the LES remains fully deterministic. However, this is true only if the order of operations at interfaces is not determined by the order of message arrival so that summations are always carried out in the same order. Otherwise, the randomness induced by the nondeterministic order of message arrival is enough to induce diverging solutions. Note that nondeterministic message arrival is usually implemented in parallel codes to improve performance, and that blocking messages order can severely affect the overall simulation cost.

Influence of Turbulence

The first test is to compare a turbulent channel flow studied in the previous section and a laminar flow. A three-dimensional Poiseuille flow was used as a test case. The Poiseuille computation is performed on a pipe geometry with 361×26 points. The flow is laminar and the Reynolds number based on the bulk velocity and diameter is approximately 500. The boundary conditions are set periodic at the inlet/outlet and no slip at the duct wall; a constant axial pressure gradient is imposed in the entire domain. Run parameters of the laminar Poiseuille flow are displayed in Table 2.

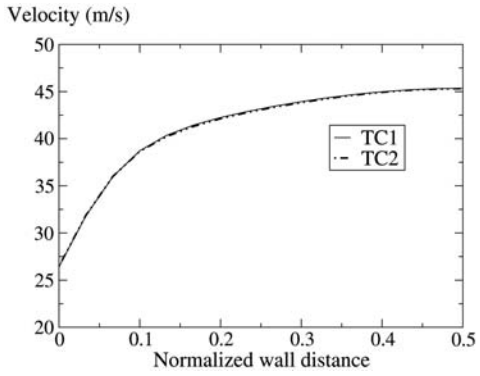

Fig. 5 Comparison of the mean velocity profiles for TC1 (4 processors) and TC2 (8 processors) over half-channel height.

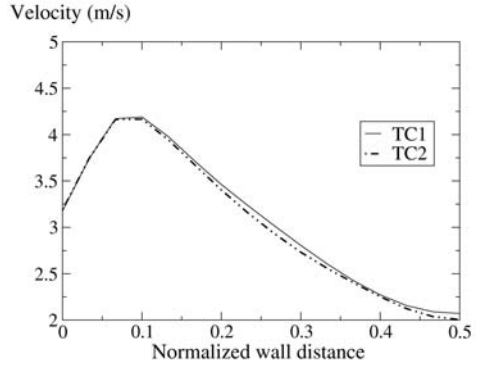

Fig. 6 Comparison of the root mean square velocity profiles for TC1 (4 processors) and TC2 (8 processors) over half channel height.

Figure 7 shows the evolutions of N_{max} and N_{mean} vs time step for runs TC1/TC2 and LP1/LP2. Note that the first point of the graph is the evaluation of the difference after one time step. The only parameter tested here is a change of the number of processors. As expected from the snapshots of Figs. 2–4, the turbulent channel flow simulations are very sensitive to a change in the number of processors, and the solutions of TC1 and TC2 diverge rapidly, leading to a maximum difference of 20 m/s and a mean difference of 3–4 m/s after 90,000 time steps. On the other hand, the difference between LP1 and LP2 hardly increases and levels off when reaching values on the order of 10^{-12} m/s, despite the periodic boundary conditions. This is expected because there is only one stable solution for the Poiseuille flow for infinite times and, accordingly, laminar flows do not induce exponential divergence of trajectories. However, this simple test case confirms that the turbulent character of the flow is the source of the divergence of solutions. This phenomenon must not be confused with the growth of a hydrodynamic mode, which is induced by the bifurcation in phase space of an equilibrium state of a given physical system. Obviously, such an equilibrium state does not exist for a fully developed turbulent channel flow. Moreover, the stagnation of absolute and mean differences between TC1/TC2 simply implies that after 90,000 time steps solutions have become fully uncorrelated and should not be misinterpreted as the saturation of an exponentially growing mode.

The basic mechanism leading to Figs. 2–4 is that the turbulent flow acts as an amplifier for rounding errors generated by the fact that the mesh is decomposed differently in TC1 and TC2. The source of this difference is the new node reordering obtained for both decompositions. This implies a different ordering when adding the contributions to a cell residual for nodes inside the subdomains, but mainly at partition interfaces. This random noise roughly starts at machine accuracy (Fig. 7) at a few points in the flow and grows continuously if the flow is turbulent.

The growth rate of the differences between solutions in simulations TC1 and TC2 cannot be estimated in a simple manner. A description for the determination of growth rates of trajectory separation in two-dimensional vortical flows is given by Leith [14], and is briefly summarized in the following. A description of vortices as points with associated circulations and negligible viscosity is assumed. Under these hypotheses, a set of linearized ordinary differential equations can be derived to evaluate the time evolution of the distance between two neighboring flowfield trajectories differing by an arbitrary infinitesimal perturbation $\delta(t)$. This system admits

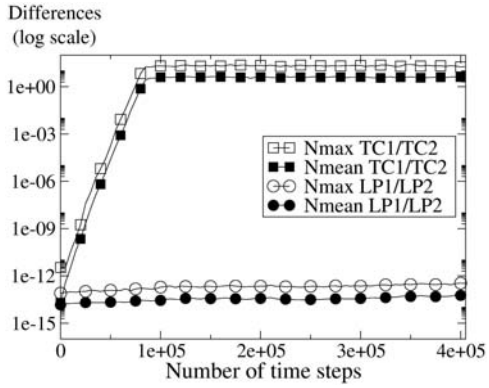

Fig. 7 Differences between solutions vs time step. Squares: turbulent channel flow. Circles: laminar Poiseuille flow.

exponential solutions, the growth rates of which are determined by the real part of the eigenvalues. The evolution of inviscid/conservative systems conserves volume in phase space. As the real part of the eigenvalues describes the separation of trajectories in time, it represents a measure of the evolution of the volume in phase space. Thus, the sum of the real parts vanishes and at least one of them has to be positive. At this stage, the number of degrees of freedom of the system imposes topological constraints on the trajectories and can prevent their separation, but a few degrees of freedom suffice for such systems to exhibit chaotic behavior, as demonstrated by the famous Lorenz attractor [38]. When considering dissipative two- or three-dimensional turbulent flows, a well-defined phase space does not exist. Therefore, predictability analysis is based on the evolution of the energy spectrum of two realizations of a given velocity field differing by a perturbation $\delta(\mathbf{u})$ but having the same statistics. It is possible to derive equations for the evolution of the error energy spectrum and define predictability times using simulations of decaying turbulence [15].

Therefore, a simple estimate of the growth rate from flow parameters a priori does not seem possible. However, one may suppose that, independently of the spatial distribution and amplitude of perturbations applied to a given turbulent flowfield, the separation of trajectories for various simulations yields similar exponential growth rates, which is confirmed in the following. Moreover, it is a purely physical phenomenon and, though induced by rounding errors, the growth rate should not depend on numerical parameters such as machine precision or time step. These aspects are addressed in forthcoming sections.

Influence of Initial Conditions

The previous section has shown that turbulence combined with a different domain partitioning (i.e., a different number of processors) is sufficient to lead to totally different instantaneous flow realizations. It is expected that a perturbation in initial conditions will have a similar effect as domain partitioning. This is verified in runs TC3 and TC4 which are run on a single processor, thereby eliminating issues linked to parallel implementation. The only difference between TC3 and TC4 is that, in TC4, the initial solution is identical to TC3, except at one random point where a single 10^{-16} m/s perturbation is applied to the streamwise velocity component. Simulations with different locations of the perturbation were run to ensure that the position did not affect results.

Figure 8 shows that the growth rate of the difference between TC3 and TC4 is exactly the same as the one observed between TC1 and TC2 (also displayed in Fig. 8): two solutions starting from a very slightly perturbed initial condition diverge as fast as two solutions starting from the same solution but running on different numbers of processors. Note that the difference between runs TC1 and TC2 comes from the accumulation of rounding errors along the interface between subdomains at each time step, whereas TC3 and TC4 differ only through the initial condition: the sequence of floating-point operations is exactly the same in TC3 and TC4. Still, the differences between TC3 and TC4 increase as fast as those between TC1 and TC2; this confirms that a turbulent flow amplifies any difference in the same manner, whether it is due to different sequences of rounding errors or to a perturbation of the initial conditions.

Effects of Node Ordering in Mesh

It has already been indicated that performing the same simulation twice (with the same number of processors and same initial conditions) leads to exactly the same result. However, this is only true as long as exactly the same code is used. It is not verified anymore as soon as a modification affecting rounding errors is done in the code. At this point, so many factors affecting rounding errors can be cited that a general discussion is pointless. This paper focuses on fully explicit codes and on one example only: the order used to add residuals at nodes in a cell vertex scheme. This order is controlled by the developer. For simulation TC5, the ordering of this addition was changed (reverse Cuthill-McKee algorithm); the residual at a given mesh node was assembled by adding the contributions to a cell residual in a different order. This change does not affect the flow data. In TC5, the node residual in a regular tetrahedral mesh is obtained by $1/4\{R_1 + [R_2 + (R_3 + R_4)]\}$ where R_i are the residuals of the cells surrounding the node and by $1/4\{R_4 + [R_3 + (R_2 + R_1)]\}$ in TC3. It has an effect, however, on rounding errors, and the cumulated effects of this nonassociativity error are what this test tries to demonstrate. TC5 and TC3 are performed with the same initial condition and run on one processor only. The only difference is the node reordering strategy.

As shown by Fig. 9, the differences between TC5 and TC3 are again similar to those observed between TC1 and TC2 (obtained by changing the number of processors). This confirms that rounding errors (and not the parallel character of the code) are the source of the solution divergence. It also shows that any modification of the code could lead to such a divergence, suggesting that repeating an LES simulation with a modified code will probably never yield the same instantaneous flowfields, potentially leading to discussions on the validity of the modifications.

Effects of Time Step

It is interesting to verify that numerical aspects do not influence the growth rate of the solutions difference and that the growth rate is only determined by the physical and geometrical parameters of the configuration. On that account, simulations TC6 and TC7 are performed with a time step reduced by a factor of two compared with simulations TC1 and TC2. TC6 and TC7 are carried out on, respectively, four and eight processors. The norms between TC6 and TC7 are displayed in Fig. 10 and compared with the norms between TC1 and TC2. From the preceding explanations, similar growth rates are expected when comparing the growth rates over physical time.

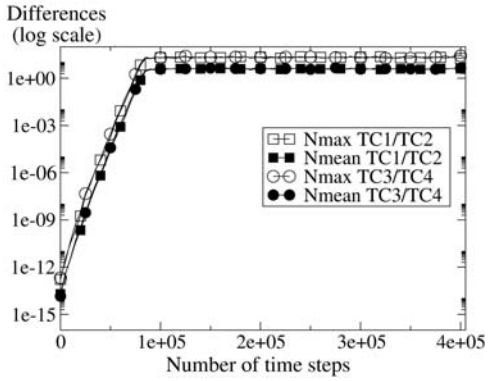

Fig. 8 Differences between solutions vs time step. Squares: different number of processors. Circles: different initial conditions.

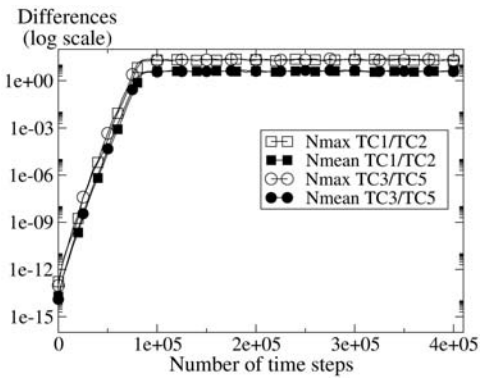

Fig. 9 Differences between solutions vs time step. Squares: different number of processors. Circles: different addition order.

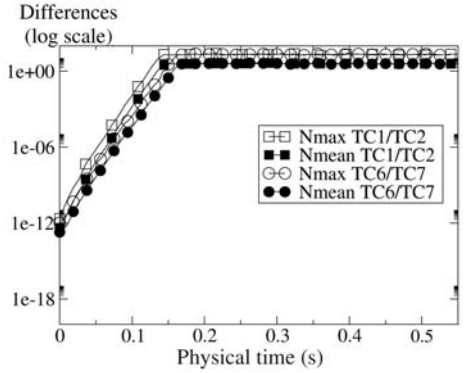

Fig. 10 Differences between solutions vs physical time. Squares: time step Δt. Circles: time step $\Delta t/2$.

The growth rates observed in Fig. 10 are indeed very similar. The slight difference is probably due to the variation of the numerical dispersion and dissipation properties of the scheme with the CFL number [39].

Effects of Machine Precision

A last test to verify that the divergence between solutions is not due to a programming error, but depends primarily on rounding errors, is to perform the same computation with simple/quadruple precision instead of double precision. Simulations TC1 and TC2 were repeated using simple precision in runs TC8 and TC9 (Table 1) and quadruple precision in TC10 and TC11. To compensate for the increase in computational time for quadruple precision simulations, roughly a factor of 10 compared with double precision, TC10 and TC11 are carried out on, respectively, 28 and 32 processors to yield a reasonable computing time. Results are displayed in Fig. 11 and compared with the difference between TC1 and TC2.

Figure 11 shows that the solutions differences for TC8/TC9 and TC10/TC11 roughly start from the respective machine accuracies (differences of 10^{-6} for simple precision after one time step, differences of 10^{-30} for quadruple precision after one time step) and increase exponentially with the same growth rate, before reaching identical difference levels for all three cases. This shows that higher precision computations cannot prevent the exponential divergence of trajectories but only delay it.

Propagation of Rounding Errors on More Realistic Configuration

The previous example corresponds to a periodic turbulent channel flow where perturbations cannot leave the computational domain.

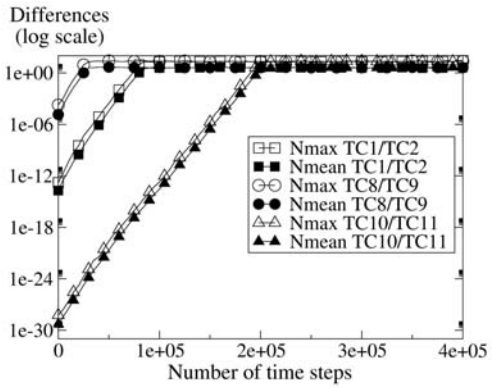

Fig. 11 Differences between solutions vs time step. Squares: double precision. Circles: simple precision. Triangles: quadruple precision.

They can therefore be amplified indefinitely and this might explain the divergence of solutions observed in Figs. 2–11. To verify whether the previously discussed divergence phenomena are independent of the configuration and can also occur in nonperiodic flows, a more realistic configuration is tested.

The chosen configuration is the nonreacting flow in a complex swirled combustor including a plenum, a swirler, and a combustion chamber. The Reynolds number at the inlet of the combustion chamber (based on an equivalent radius of the swirler) is approximately 5200. To avoid the specification of the boundary condition at the outlet of the combustion chamber for further acoustic analysis, the atmosphere around the outlet has also been meshed (Fig. 12). Boundary conditions are summarized in Fig. 13. All solid boundaries are modeled using adiabatic wall laws. The inlet, coflow, and outlet boundary conditions rely on characteristic decomposition according to Moureau et al. [33] and Poinsot and Lele [40]. The inlet injects an air mixture (N_2, O_2) with 15 g/s at $T = 298$ K. The coflow imposed on the left sidewall aims to mimic air entrainment due to the outgoing flow of the combustion chamber. The coflow velocity is set to $u_z = 0.1$ m/s and $T = 298$ K.

The only parameter changing in the two simulations is the number of processors, and the parameters of the run are specified in Table 3.

A divergence of solutions similar to the periodic turbulent channel flow can be observed in Fig. 14.

Instantaneous fields of axial velocity for both runs in the central plane at $t = 32.4$ ms (80,000 time steps) after initialization show that instantaneous flowfields are uncorrelated (Fig. 15). The differences remain mostly confined to the highly turbulent zone at the inlet of the combustion chamber. This region is volumetrically small compared with the entire computed geometry, in particular the atmospheric region, which is why the mean difference curve remains low compared with the turbulent channel flow. The maximal local difference reaches values of 45 m/s.

Figure 16 displays the evolution of axial velocity for the two simulations for a point located at 20 cm of the chamber inlet plane, on the chamber axis. As expected, the signals diverge suddenly due to the exponential amplification of rounding errors, leading to uncorrelated signals after approximately 30 ms ($t = 0$ s corresponds to initialization).

These results clearly demonstrate that rounding errors may propagate until full uncorrelation, even for configurations with inlet/

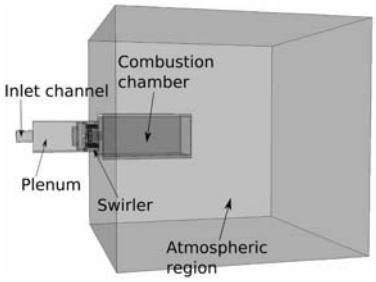

Fig. 12 Schematic of the complex burner geometry.

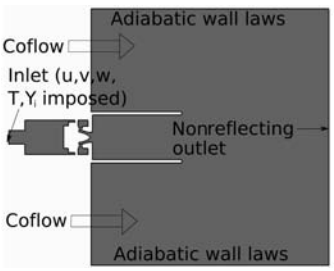

Fig. 13 Midplane cut with boundary-condition specification.

Table 3 Summary of complex burner geometry runs

Run ID	No. processors	Initial conditions	Precision	Graph ordering	CFL λ
CB1	28	Fixed	Double	CM	0.7
CB2	32	Fixed	Double	CM	0.7

outlet boundary conditions, and that it is not an artifact due to the periodicity of the turbulent channel flow (Fig. 1). The presence of recirculation zones in the complex burner geometry, where part of the fluid constantly remains in the computational domain, may be an explanation for this behavior, but this aspect requires further investigation.

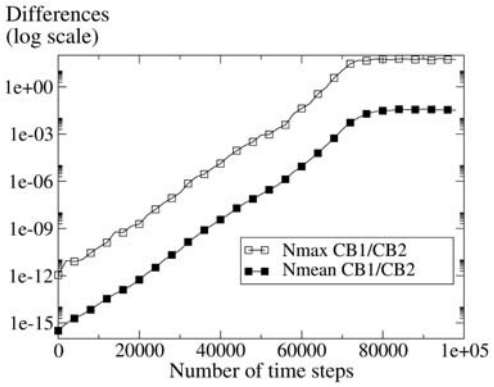

Fig. 14 Differences between CB1 and CB2 (different number of processors) vs time step.

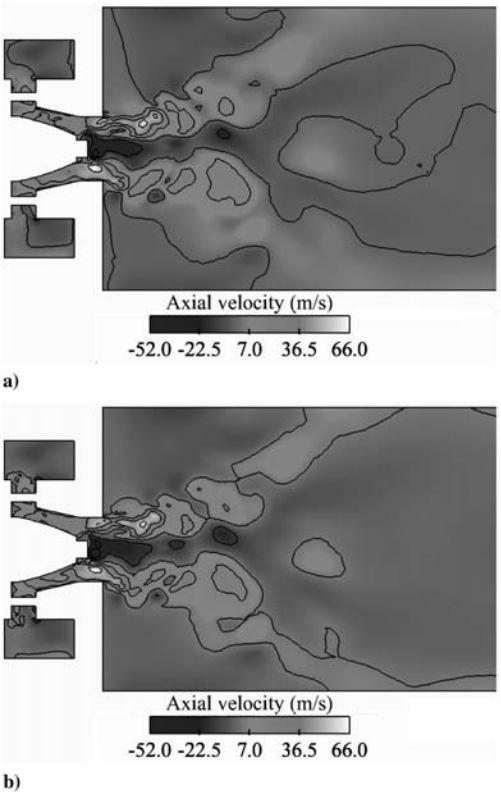

Fig. 15 Instantaneous field of axial velocity in the central plane of the burner at $t = 32.4$ ms: a) run CB1, b) run CB2.

Conclusions

This work focused on the sensitivity of instantaneous large-eddy simulation fields to different rounding error propagation due to situations where various parameters of the run, such as number of processors, initial condition, time step, and changes in addition ordering of cell residuals for cell vertex methods, are modified. The baseline simulation used for the tests was a fully developed periodic turbulent channel flow, but a complex burner geometry displayed a similar behavior. The conclusions are as follows:

1) Any sufficiently turbulent flow computed in LES exhibits significant sensitivity to these parameters, leading to instantaneous solutions which can be totally different. As expected, laminar flows are almost insensitive to these parameters even for periodic simulations.

2) The divergence of solutions is due to two combined facts: 1) the exponential separation of trajectories in turbulent flows, and 2) the different propagation of rounding errors induced by domain partitioning and scheduling of operations. More generally, any change in the code lines affecting the propagation of rounding errors will have a similar effect. This implies that the validation of an LES code after modifications may only be based on statistical fields. This makes error detection in LES codes much more difficult than in classical codes; comparing instantaneous solutions is not a proper validation method for LES.

3) Small changes in initial conditions (of the order of machine accuracy at one point of the flow only) produce similar divergence of solutions.

4) Working with higher precision machines does not suppress the divergence of solutions, but delays it.

Converged statistics reflect the fact that most possible realizations of a turbulent flow have been taken. It is therefore clear that the propagation of rounding errors does not affect statistics of large-eddy and direct numerical simulations. However, instantaneous values may a priori only be used for times during which the differences between two runs with identical initial solution remain negligible with respect to a suitable error norm. The increase in floating-point representation delays the divergence of solutions, but the increase in computational costs appears too severe for practical applications. Another option consists of the use of software which inhibits the

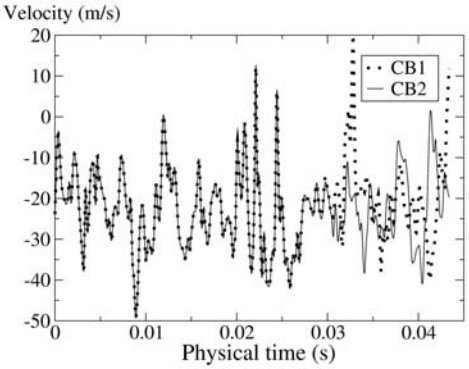

Fig. 16 Evolution of axial velocity at a point located on the chamber axis for CB1 and CB2 over time.

propagation of rounding errors. This would allow the increase of the computational predictability time of a given simulation. The ability to include such software in complex computational fluid dynamics codes must be investigated and the increase in computational expense is again a crucial aspect. More generally, these results demonstrate that the concept of numerical quality in LES will require much more detailed studies and tools than what has been used up to now for Reynolds-averaged simulations.

Acknowledgments

We thank F. Chaitin-Chatelin for helpful discussions. The first author gratefully acknowledges the funding by the European Community in the framework of the Marie Curie Early Stage Research Training Fellowship (contract number MEST-CT-2005-020426).

References

[1] Sagaut, P., *Large Eddy Simulation for Incompressible Flows*, 1st ed., Springer, Berlin, 2002.

[2] Mahesh, K., Constantinescu, G., and Moin, P., "Numerical Method for Large-Eddy Simulation In Complex Geometries," *Journal of Computational Physics*, Vol. 197, No. 1, 2004, pp. 215–240. doi:10.1016/j.jcp.2003.11.031

[3] Di Mare, F., Jones, W. P., and Menzies, K., "Large Eddy Simulation of a Model Gas Turbine Combustor," *Combustion and Flame*, Vol. 137, No. 3, 2004, pp. 278–295. doi:10.1016/j.combustflame.2004.01.008

[4] Poinsot, T., and Veynante, D., *Theoretical and Numerical Combustion*, 2nd ed., R. T. Edwards, Philadelphia, 2005.

[5] Pitsch, H., "Large Eddy Simulation of Turbulent Combustion," *Annual Review of Fluid Mechanics*, Vol. 38, Jan. 2006, pp. 453–482. doi:10.1146/annurev.fluid.38.050304.092133

[6] El-Asrag, H., and Menon, S., "Large Eddy Simulation of Bluff-Body Stabilized Swirling Non-Premixed Flames," *Proceedings of the Combustion Institute*, Vol. 31, No. 2, 2007, pp. 1747–1754. doi:10.1016/j.proci.2006.07.251

[7] Duwig, C., Fuchs, L., Griebel, P., Siewert, P., and Boschek, E., "Study of a Confined Turbulent Jet: Influence of Combustion and Pressure," *AIAA Journal*, Vol. 45, No. 3, 2007, pp. 624–661. doi:10.2514/1.26352

[8] Schmitt, P., Poinsot, T. J., Schuermans, B., and Geigle, K., "Large-Eddy Simulation and Experimental Study of Heat Transfer, Nitric Oxide Emissions and Combustion Instability in a Swirled Turbulent High Pressure Burner," *Journal of Fluid Mechanics*, Vol. 570, 2007, pp. 17–46. doi:10.1017/S0022112006003156

[9] Poinsot, T., Candel, S., and Trouvé, A., "Application of Direct Numerical Simulation to Premixed Turbulent Combustion," *Progress in Energy and Combustion Science*, Vol. 21, No. 6, 1995, pp. 531–576. doi:10.1016/0360-1285(95)00011-9

[10] Moin, P., and Mahesh, K., "DNS: A Tool in Turbulence Research," *Annual Review of Fluid Mechanics*, Vol. 30, Jan. 1998, pp. 539–578. doi:10.1146/annurev.fluid.30.1.539

[11] Vervisch, L., and Poinsot, T., "Direct Numerical Simulation of Non Premixed Turbulent Flames," *Annual Review of Fluid Mechanics*, Vol. 30, Jan. 1998, pp. 655–692. doi:10.1146/annurev.fluid.30.1.655

[12] Tennekes, H., and Lumley, J. L., *First Course in Turbulence*, 1st ed., MIT Press, Cambridge, MA, 1972.

[13] Lesieur, M., *Turbulence in Fluids*, 1st ed., Martinus–Nijhoff, Dordrecht, The Netherlands, 1987, pp. 230–231.

[14] Leith, C., "Atmospheric Predictability and Two-Dimensional Turbulence," *Journal of the Atmospheric Sciences*, Vol. 28, No. 2, 1971, pp. 145–161. doi:10.1175/1520-0469(1971)028<0145:APATDT>2.0.CO;2

[15] Métais, O., and Lesieur, M., "Statistical Predictability of Decaying Turbulence," *Journal of the Atmospheric Sciences*, Vol. 43, No. 9, 1986, pp. 857–870. doi:10.1175/1520-0469(1986)043<0857:SPODT>2.0.CO;2

[16] Stoer, J. S., and Bulirsch, R., *Introduction to Numerical Analysis*, 1st ed., Springer, Berlin, 1980.

[17] Chaitin-Chatelin, F., and Frayssé, V., *Lectures on Finite Precision Computations*, 1st ed., Society for Industrial and Applied Mathematics, Philadelphia, 1996.

[18] Overton, M. L., *Numerical Computing with IEEE Floating Point Arithmetic*, 1st ed., Society for Industrial and Applied Mathematics, Philadelphia, 2001.

[19] Vignes, J., "Discrete Stochastic Arithmetic for Validating Results of Numerical Software," *Numerical Algorithms*, Vol. 37, Nos. 1–4, Dec. 2004, pp. 377–390. doi:10.1023/B:NUMA.0000049483.75679.ce

[20] Schönfeld, T., and Rudgyard, M., "Steady and Unsteady Flow Simulations Using the Hybrid Flow Solver AVBP," *AIAA Journal*, Vol. 37, No. 11, 1999, pp. 1378–1385.

[21] Hanrot, G., Lefévre, V., Stehlé, D., and Zimmermann, P., "Worst Cases for a Periodic Function with Large Arguments," *Proceedings of the 18th IEEE Symposium on Computer Arithmetic*, edited by P. Kornerup, and J.-M. Muller, IEEE Computer Society Press, Los Alamitos, CA, 2007, pp. 133–140.

[22] Freitag, M., and Janicka, J., "Investigation of a Strongly Swirled Premixed Flame Using LES," *Proceedings of the Combustion Institute*, Vol. 31, No. 1, 2007, pp. 1477–1485. doi:10.1016/j.proci.2006.07.225

[23] Lele, S., "Compact Finite Difference Schemes with Spectral-Like Resolution," *Journal of Computational Physics*, Vol. 103, No. 1, 1992, pp. 16–42. doi:10.1016/0021-9991(92)90324-R

[24] Abarbanel, S. S., and Chertock, A. E., "Strict Stability of High-Order Compact Implicit Finite-Difference Schemes: The Role of Boundary Conditions for Hyperbolic PDEs, 1," *Journal of Computational Physics*, Vol. 160, No. 1, 2000, pp. 42–66. doi:10.1006/jcph.2000.6420

[25] Sengupta, T. K., Ganerwal, G., and Dipankar, A., "High Accuracy Compact Schemes and Gibbs' Phenomenon," *Journal of Scientific Computing*, Vol. 21, No. 3, 2004, pp. 253–268. doi:10.1007/s10915-004-1317-2

[26] Saad, Y., "Flexible Inner-Outer Preconditioned GMRES Algorithm," *Journal of Scientific Computing*, Vol. 14, No. 2, 1993, pp. 461–469. doi:10.1137/0914028

[27] Fraysse, V., Giraud, L., and Gratton, S., "Set of Flexible-GMRES Routines for Real and Complex Arithmetics," Centre Européen de Recherche et de Formation Avancée en Calcul Scientifique TR/PA/98/20, 1998.

[28] Cuthill, E., and McKee, J., "Reducing the Bandwidth of Sparse Symmetric Matrices," *Proceedings of the 24th National Conference of the ACM*, Vol. 1, Assoc. for Computing Machinery, New York, 1969, pp. 157–172.

[29] Liu, W.-H., and Sherman, A. H., "Comparative Analysis of the Cuthill-Mckee and the Reverse Cuthill-Mckee Ordering Algorithms for Sparse Matrices," *SIAM Journal on Numerical Analysis*, Vol. 13, No. 2, 1976, pp. 198–213. doi:10.1137/0713020

[30] Pope, S. B., "Ten Questions Concerning the Large-Eddy Simulation of Turbulent Flows," *New Journal of Physics*, Vol. 6, No. 1, 2004, p. 35. doi:10.1088/1367-2630/6/1/035

[31] Sommerer, Y., Galley, D., Poinsot, T., Ducruix, S., Lacas, F., and Veynante, D., "Large Eddy Simulation and Experimental Study of Flashback and Blow-Off in a Lean Partially Premixed Swirled Burner," *Journal of Turbulence*, Vol. 5, No. 1, Article 37, 2004. doi:10.1088/1468-5248/5/1/037

[32] Boileau, M., Staffelbach, G., Cuenot, B., Poinsot, T., and Bérat, C., "LES of an Ignition Sequence in a Gas Turbine Engine," *Combustion and Flame*, 2008 (to be published).

[33] Moureau, V., Lartigue, G., Sommerer, Y., Angelberger, C., Colin, O., and Poinsot, T., "High-Order Methods for DNS and LES of Compressible Multi-Component Reacting Flows on Fixed and Moving Grids," *Journal of Computational Physics*, Vol. 202, No. 2, 2005, pp. 710–736. doi:10.1016/j.jcp.2004.08.003

[34] Hirsch, C., *Numerical Computation of Internal and External Flows: Computational Methods for Inviscid and Viscous Flows*, 1st ed., Vol. 2, Wiley, New York, 1988, pp. 224–306.

[35] Colin, O., and Rudgyard, M., "Development of High-Order Taylor-Galerkin Schemes for Unsteady Calculations," *Journal of Computational Physics*, Vol. 162, No. 2, 2000, pp. 338–371. doi:10.1006/jcph.2000.6538

[36] Williams, R. D., "Performance of Dynamic Load Balancing Algorithms for Unstructured Mesh Calculations," *Concurrency, Practice and Experience*, Vol. 3, No. 5, 1991, pp. 457–481. doi:10.1002/cpe.4330030502

[37] Taylor, V. E., and Nour-Omid, B., "Study of the Factorization Fill-In for a Parallel Implementation of the Finite Element Method," *International Journal for Numerical Methods in Engineering*, Vol. 37, No. 22, 1994,

pp. 3809–3823.
doi:10.1002/nme.1620372205

[38] Lorenz, E. N., "Deterministic Nonperiodic Flow," *Journal of the Atmospheric Sciences*, Vol. 20, No. 2, 1963, pp. 130–141.
doi:10.1175/1520-0469(1963)020<0130:DNF>2.0.CO;2

[39] Hirsch, C., *Numerical Computation of Internal and External Flows: Fundamentals of Numerical Discretization*, 1st ed., Vol. 1, Wiley, New York, 1988, pp. 307–319.

[40] Poinsot, T., and Lele, S., "Boundary Conditions for Direct Simulations of Compressible Viscous Flows," *Journal of Computational Physics*, Vol. 101, No. 1, 1992, pp. 104–129.
doi:10.1016/0021-9991(92)90046-2

P. Givi
Associate Editor

Appendix E

Journal of Computational Physics, Vol. 228, N^o 2, pp. 539-564 (2009)

Évaluation des méthodes numériques pour la Simulation aux Grandes Échelles des écoulements diphasiques particulaires réactifs turbulents

La prédiction de la dispersion du carburant dans les écoulements diphasiques turbulents est une partie importante des écoulements réactifs car le carburant est en général injecté sous forme liquide avant d'être brûlé. Même si la simulation aux grandes échelles (LES) a déjà démontré son potentiel sur des flammes monophasiques dans les dernières années, son extension aux flammes diphasiques reste à explorer. Tout d'abord, la physique utilisée pour décrire l'atomisation d'un jet liquide, la dispersion des particules solides, leur interaction avec les parois, leur évaporation et combustion est difficile à modéliser car il s'agit essentiellement de phénomènes de sous-maille. Deuxièmement, l'implantation numérique des écoulements diphasiques pour la LES reste un défi. Enfin, dans le contexte du calcul massivement parallèle, l'efficacité numérique représente une contrainte supplémentaire et le maintien d'une efficacité du parallélisme comparable à celle des calculs gazeux n'est pas si évident pour un calcul diphasique.

Cet article est une compilation d'une partie des résultats de la thèse de Riber [179] concernant le chapitre d'analyses et validation des résultats du calcul gazeux et diphasique monodispersé sur la configuration de Borée *et al.* [22] où des particules de verre sont injectées dans un écoulement turbulent comportant une zone de recirculation. Les résultats des simulations numériques LES avec l'approche Euler/Euler (EE) sont comparés avec les résultats expérimentaux et aussi avec les résultats numériques de deux codes de calculs avec une formulation Lagrangienne. Un de ces codes de calculs contient la version Lagrangienne développée pendant cette thèse.

Cet article est organisé de la façon suivante : d'abord la sélection de la configuration est présentée. L'objectif à court terme est de faire des simulations LES diphasiques sur des géométries complexes avec évaporation et combustion. La validation de la dispersion des particules dans un écoulement dont les caractéristiques sont similaires mais avec une complexité moindre est donc nécessaire. De ce point de vue et avec des applications aéronautiques en perspective, la configuration étudiée par Borée *et al.* [22] est très intéressante. Par ailleurs, elle dispose d'une grande quantité de données de calculs gazeux et diphasiques. Une description du banc expérimental est présentée au début de la section. Elle inclut en même temps de l'information sur les caractéristiques

des écoulements de type bluff body. Le rapport de vitesse entre le tube d'injection et le co-courant va donner lieu à des écoulements très différents. Dans ce cas, l'écoulement a deux points de stagnation dans l'axe avec une large zone centrale de recirculation entre le jet central et le co-courant. Le diamètre des particules de verre est compris entre 20 et 100 microns et leur masse volumique est de 2470 kg/m^3. Les comparaisons présentées dans cet article se limitent au cas faiblement chargé en masse ($M_j = 22\%$) où l'écoulement diphasique considéré est suffisamment dilué pour négliger les collisions interparticulaires. Les principaux objectifs de cet article sont résumés dans cette section :

- étude de l'influence du type des cellules du maillage (hexaèdres vs tétraèdres),
- évaluation de l'influence du schéma numérique,
- comparaison des formulations implicite et explicite pour l'avancement en temps,
- comparaison de la précision des approches Euler/Euler et Euler/Lagrange.

La section 3 commence par une description des deux solveurs de calcul utilisés dans cette étude : le solveur explicite AVBP qui contient les formulations Eulérienne et Lagrangienne pour le traitement de la phase dispersée développé au centre de recherche CERFACS, en France; et le solveur implicite CDP qui traite la phase dispersée avec l'approche Lagrangienne, développé au Centre de Recherche de la Turbulence (CTR) de l'Université de Stanford. Une description détaillée des équations utilisées pour les formulations EE et EL est incluse dans cette section.

La section 4 commence avec la présentation des dimensions du domaine de calcul et détaille les principales caractéristiques des deux maillages sur lesquels ont été effectués les tests de l'influence du type de cellule. Ensuite, les conditions aux limites pour les entrées, les sorties et le traitement aux parois sont présentées. La principale différence étant dans l'injection de turbulence du tube d'amenée. Une fois la présentation des cas tests faite, les résultats des différentes simulations sont analysés en comparant sur sept profils axiaux et radiaux les vitesses moyenne et fluctuante.

La section 5 présente les différentes coupes d'injection de particules dans le tube centrale. Les résultats des calculs diphasiques avec les approches EE et EL sont montrés en comparaison avec les résultats expérimentaux sur sept profils radiaux de vitesses moyenne et fluctuante. Des comparaisons entre les deux codes, avec la même approche (EL), sont ainsi incluses dans cette partie.

Les conclusions sont incluses dans la section 6.

Journal of Computational Physics 228 (2009) 539–564

Contents lists available at ScienceDirect

Journal of Computational Physics

journal homepage: www.elsevier.com/locate/jcp

Evaluation of numerical strategies for large eddy simulation of particulate two-phase recirculating flows

E. Riber [a,b,*], V. Moureau [c], M. García [b], T. Poinsot [a], O. Simonin [a]

[a] IMFT-UMR 5502, allée du Professeur Camille Soula, 31400 Toulouse, France
[b] CERFACS, 42, avenue Gaspard Coriolis, 31057 Toulouse Cedex 01, France
[c] CTR, Stanford University, Stanford, CA 94305-3030, USA

ARTICLE INFO

Article history:
Received 18 December 2007
Received in revised form 5 June 2008
Accepted 1 October 2008
Available online 10 October 2008

Keywords:
LES
Two-phase recirculating flows
Particles
Euler/Lagrange
Euler/Euler

ABSTRACT

Predicting particle dispersion in recirculating two-phase flows is a key issue for reacting flows and a potential application of large eddy simulation (LES) methods. In this study, Euler/Euler and Euler/Lagrange LES approaches are compared in the bluff body configuration from Borée et al. [J. Borée, T. Ishima, I. Flour, The effect of mass loading and inter-particle collisions on the development of the polydispersed two-phase flow downstream of a confined bluff body, J. Fluid Mech. 443 (2001) 129–165] where glass beads are injected into a complex recirculating flow. These tests are performed for non-reacting, non-evaporating sprays but are mandatory validations before computing realistic combustion chambers. Two different codes (one explicit and compressible and the other implicit and incompressible) are also tested on the same configuration. Results show that the gas flow is well predicted by both codes. The dispersed phase is also well predicted by both codes but the Lagrangian approach predicts root-mean-square values more accurately than the Eulerian approach. The effects of mesh, solvers and numerical schemes are discussed for each method.

1. Introduction

Today, RANS (Reynolds-averaged Navier–Stokes) equations are routinely solved to design combustion chambers, for both gaseous and liquid fuels. Recently, large eddy simulation (LES) has been extended to reacting gaseous flows in order to give access to unsteady phenomena occurring in combustion devices (such as instabilities, flashback or quenching), and to provide better accuracy for the prediction of mean flows. The success of these approaches for gaseous flames in the last years [2–12] is a clear illustration of their potential. LES gives access to the large scales structures of the flow, reducing the importance of modeling, and capturing a significant part of the physics controlling these flames.

Even though LES has already demonstrated its potential for gaseous flames, its extension to two-phase flames is still largely to be done. First, the physical submodels required to describe the atomization of a liquid fuel jet, the dispersion of fuel droplets, their interaction with walls, evaporation and combustion are as difficult to build in LES as in RANS because they are essentially subgrid phenomena. Second, the numerical implementation of two-phase flow LES remains a challenge: the equations for both the gaseous and the dispersed phases must be solved together at each time step in a strongly coupled manner. This differs from classical RANS where the resolution of the two phases can be done in a weak procedure, bringing first the gas flow to convergence, then the solid particles and iterating until convergence of both phases. Finally, in the

* Corresponding author. Address: CERFACS, 42, avenue Gaspard Coriolis, 31057 Toulouse Cedex 01, France. Tel.: +33 561 19 3115; fax: +33 561 19 3000.
E-mail address: riber@cerface.fr (E. Riber).

0021-9991/$ - see front matter © 2008 Elsevier Inc. All rights reserved.
doi:10.1016/j.jcp.2008.10.001

context of parallel supercomputing, numerical efficiency is an additional constraint. For single-phase flows, efficient and accurate solvers have been developed and speedups of the order of 5000 are not uncommon [13]. Representing the main physics of two-phase flows while maintaining a similar parallel efficiency for two-phase flow solvers raises additional questions: particle/mesh load imbalance is a crucial issue in Euler/Lagrange simulations, as discussed for instance in [14,15].

In LES of reacting two-phase flows, physics and numerics interact strongly: the first question is to choose a paradigm to describe the two-phase flow. In dilute particle-laden flows, most RANS codes use Euler/Lagrange (EL) methods in which the gas flow is solved using an Eulerian method and the particles are tracked using a Lagrangian approach. An alternative technique is to use Euler/Euler (EE) methods in which both phases are solved using an Eulerian approach. The history of RANS development has shown that the EL and EE methods both show advantages and disadvantages depending on the application. Consequently, both approaches are found today in most commercial codes. For LES, both EE and EL approaches are being developed and the focus of this study is to test and compare them in a reference case where complete sets of experimental results for gas and dispersed phase are available. This exercise is performed here without evaporation or combustion: the droplets are replaced by solid particles.

2. Flow configuration and work objectives

2.1. Choice of the configuration

In combustion chambers, the flame resulting from a free jet flow would be too long compared to the dimensions of the chamber, and also very difficult to stabilise. Therefore, most combustion devices are designed so as to anchor the flame at a specific location. The use of a flame holder is often difficult due to the very high temperatures that may damage the device itself. Another possibility is to stabilise the flame behind a sudden expansion like a backward-facing step: the flow is strongly decelerated forming a corner recirculation zone, and the recirculating hot gases then provoke the ignition of the incoming fresh gases. As far as aeronautical combustion chambers are concerned, highly swirling flows that pass through a sudden expansion are preferred since they provide a more compact stabilised flame. A central toroidal recirculation zone is created, acting as a flame holder in the center of the flow, close to the injector tip. In such devices, the recirculation zones induce high turbulence levels and high mixing rates, stabilising the flame and reducing pollutant emissions.

Before computing reactive two-phase flows in such devices, a validation of the turbulent dispersion of the particles in similar flows is needed. Indeed, the accurate description of the fuel droplet motion is crucial to determine first the resulting fuel vapor distribution, and then the combustion mode and the pollutant emissions among others. With aeronautical applications in prospect, the bluff body flow from Borée et al. [1] is a very interesting configuration. First, it exhibits the same flow structures as combustion chambers, with corner recirculation zones and stagnation points. To predict their location, a precise description of the large structures and the intermittency of the fluid flow is required [16–18]. Second, the particle motion is complex: depending on their inertia, the fuel droplets are captured in the recirculation zones or cross them. Since they are then vaporised, they directly determine the gaseous fuel field, and consequently, the burner efficiency as well as the pollutant emissions [19,20]. Then, as very few particles reach the external walls of the chamber, the particle–wall interactions can be neglected in this configuration, which simplifies the comparison between both methods. Indeed, modeling particle motion in wall-bounded flows is still a challenge despite multiple studies using either the EL approach [21–24] or the EE approach [25–27]. Furthermore, in a hot combustion chamber where liquid fuel is injected, the fuel droplets often evaporate rapidly and the interaction between particles and solid walls is not a crucial mechanism. If not, a liquid film develops on the walls, which requires specific modeling [28]. Finally, a large amount of data is provided by Borée et al. [1], including mean and fluctuating quantities for both phases, which allows to validate not only the gas LES models, but also the dispersed phase modeling.

2.2. Description of the experimental setup

The configuration of Borée et al. [1] consists of a vertical axisymmetrical particle-laden confined bluff body flow (see Fig. 1) on the flow loop Hercule of EDF – R&D.[1] Air blowers are used to generate the coflow whereas both air and glass beads are injected in the inner pipe. The measurement zone is located at $z = 0$ downstream of the inner and annular ducts, where large recirculation zones are created between the central jet and the coflow. Thus, the resulting flow is very similar to the ones obtained in industrial combustion devices, where fuel droplets are injected together with air. Hereafter, the symbols $\cdot_f$ and $\cdot_p$ denote the fluid and the particles.

2.2.1. The gas phase

Schefer et al. [17] show that the topology of a turbulent bluff body flow strongly depends on the ratio $\overline{U}_{f,I}/\overline{U}_{f,C}$, where $\overline{U}$ is a bulk velocity and the subscripts I and C denote the inner pipe and the coflow, respectively. Depending on the velocity ratio $\overline{U}_{f,I}/\overline{U}_{f,C}$, there are three possible flow topologies [17]. In Fig. 2, sketches of mean gas velocity vectors are drawn for three

[1] Électricité de France – Recherche & Développement.

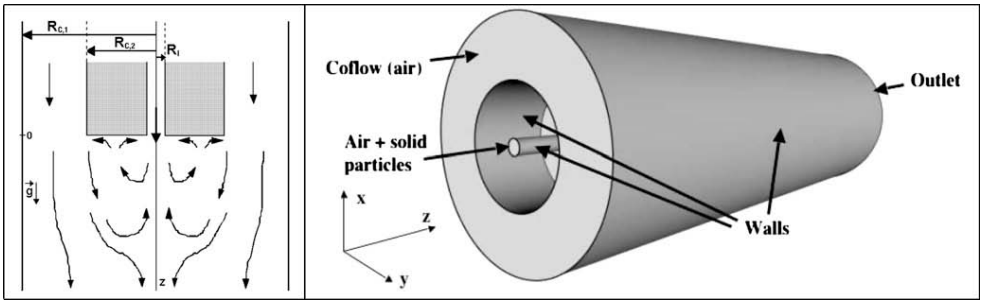

Fig. 1. Configuration of Borée et al. [1]. The dimensions are: R_I = 0.010 m, $R_{C,1}$ = 0.075 m, $R_{C,2}$ = 0.150 m. The ducts and the chamber are respectively 2 m and 1.5 m long.

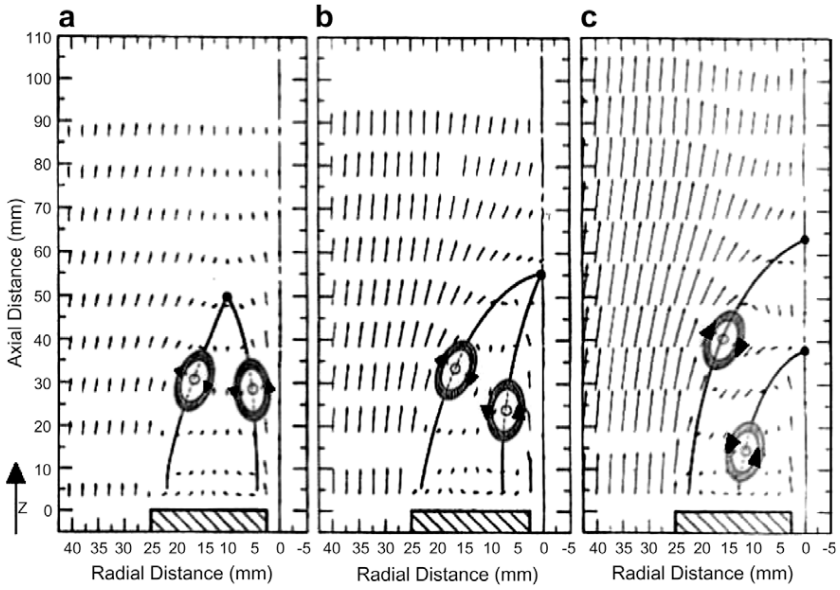

Fig. 2. Plots of the measured mean velocity vectors in a bluff body stabilised methane jet for $\overline{U}_{f,1}/\overline{U}_{f,C} = 2.8$ (a), $\overline{U}_{f,1}/\overline{U}_{f,C} = 1.4$ (b), and $\overline{U}_{f,1}/\overline{U}_{f,C} = 0.84$ (c). Black dots show the location of the stagnation points and round arrays give the direction of rotation of the shear layer vortices. From Schefer et al. [17].

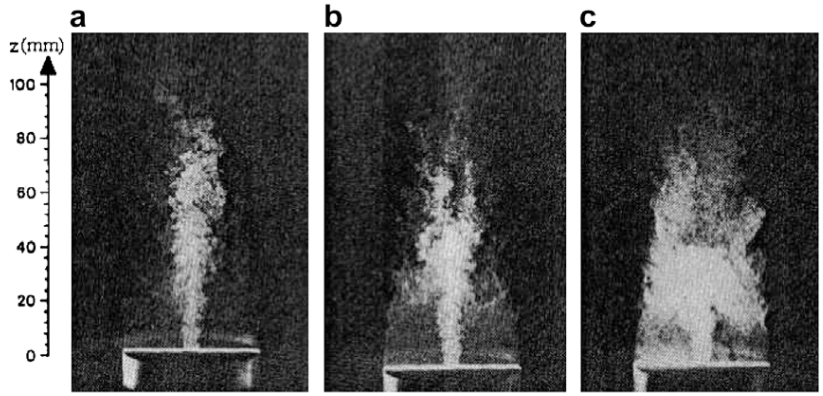

Fig. 3. Mie scattering measurements of the instantaneous particle distribution in a bluff body stabilised methane jet for $\overline{U}_{f,1}/\overline{U}_{f,C} = 2.8$ (a), $\overline{U}_{f,1}/\overline{U}_{f,C} = 1.4$ (b), and $\overline{U}_{f,1}/\overline{U}_{f,C} = 0.84$ (c). From Schefer et al. [17].

decreasing velocity ratios ($\overline{U}_{f,I}/\overline{U}_{f,C} = 2.8, 1.4$ and 0.84) whereas in Fig. 3, the gas flow is seeded with small particles to give access to the flow topology for the same three velocity ratios:

(1) For the highest velocity ratio ($\overline{U}_{f,I}/\overline{U}_{f,C} = 2.8$), the flow along the axis is similar to a free jet flow. The air flows coming from the inner and annular pipes converge far from the outlet of the inner duct. Two counter-rotative eddies separate the two flows before they converge. There are two stagnation points on both sides of the central jet.
(2) At lower velocity ratio ($\overline{U}_{f,I}/\overline{U}_{f,C} = 1.4$), a single stagnation point is formed along the centerline and the flow looks like a non-penetrating jet.
(3) Finally, for the smallest velocity ratio ($\overline{U}_{f,I}/\overline{U}_{f,C} = 0.84$), a second stagnation point appears on the axis whose location is linked to the geometry global parameter. The second stagnation point remains close to the chamber inlet and does not move any longer when the ratio $\overline{U}_{f,I}/\overline{U}_{f,C}$ becomes lower.

The experiments of Borée et al. [1] are conducted at ambient temperature and standard pressure: $T_f = 293$ K and $P_f = 10^5$ Pa. The radius of the inner pipe is $R_I = 10$ mm. The air volume flux of the inner pipe is $Q_{f,I} = 3.4$ m^3 h^{-1}, which corresponds to a mean velocity $\overline{U}_{f,I} = 3.4$ m s^{-1}, whereas the maximum velocity in the inner duct reaches $U^{\max}_{f,I} = 4$ m s^{-1}. Although the Reynolds number is rather moderate ($Re_I = 2R_I\overline{U}_{f,I}/\nu_f \approx 4500$, where ν_f is the kinematic viscosity of the fluid), the ratio $U^{\max}_{f,I}/\overline{U}_{f,I} = 1.18$ at the outlet of the inner pipe is however consistent with developed turbulent pipe flow.

The dimensions of the annular outer region are: $R_{C,1} = 75$ mm, $R_{C,2} = 150$ mm. The air volume flux in the coflow is $Q_{f,C} = 780$ m^3 h^{-1}, which corresponds to mean and maximum velocities equal to: $\overline{U}_{f,C} = 4.1$ m s^{-1} and $U^{\max}_{f,C} = 6$ m s^{-1}. The associated Reynolds number of the annular jet is $Re_C = 2(R_{C,2} - R_{C,1})\overline{U}_{f,C}/\nu_f \approx 40,000$. The main characteristics of the configuration are summarised in Table 1.

The velocity ratio $\overline{U}_{f,I}/\overline{U}_{f,C}$ considered by Borée et al. [1] is 0.83. Following Schefer et al. [17], there are two stagnation points along the centerline. Choosing a ratio lower than one creates a complex gas flow behavior when modeling particle dispersion: depending on their inertia, the particles remain in the recirculation zone delimited by the two stagnation points or leave it.

2.2.2. The dispersed phase

In Borée et al. [1], polydisperse glass particles with material density $\rho_p = 2470$ kg m^{-3}, are injected in the inner pipe only through a particle feeder. Two mass fluxes of glass beads, $Q^1_{p,I} = 1$ kg h^{-1} and $Q^2_{p,I} = 5$ kg h^{-1}, have been used experimentally to study the influence of particle inertia on the two-phase flow as well as the role of inter-particle interactions. The corresponding mass loading in the inner duct then varies from $M^1_{p,I} = 22\%$ to $M^2_{p,I} = 110\%$. In this study, only the lowest mass loading case is considered.

Particle diameter covers a wide range of size classes from $d_p = 20$ μm to $d_p = 100$ μm. Fig. 4 shows the initial particle distribution, in mass (M) and in number (N). The resulting mean diameters are respectively $d_{p,M} = 63$ μm and $d_{p,N} = 50$ μm. Char-

Table 1
Characteristics of the gas phase at the outlet of the inner and annular pipes.

Gas phase	Inner pipe	Annular pipe
Radius (m)	0.010	0.075
Volume flux (m^3 h^{-1})	3.4	780
Mean velocity (m s^{-1})	3.4	4.1
Max velocity (m s^{-1})	4.	6.
Reynolds number (–)	4500	40,000

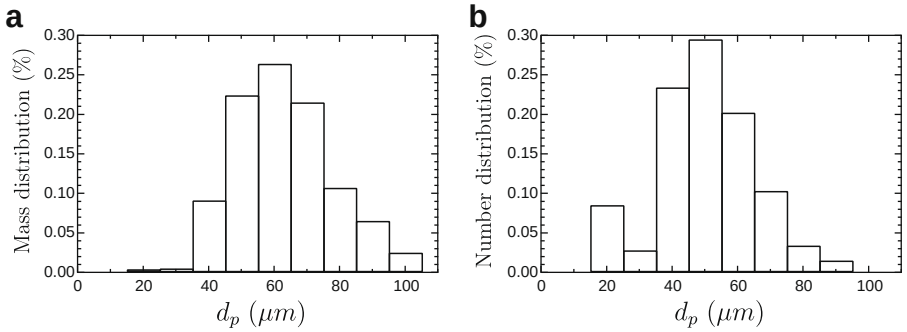

Fig. 4. Experimental initial mass (a), and number (b) distribution of the particle size.

acterising the particle distribution using a particle Doppler anemometry (PDA) method [29] requires special care: the glass beads should remain spherical and the inter-particle collision should not induce any particle break-up. Therefore, Borée et al. [1] repeated the measurements and used a microscope to verify the shape and size of particles.

2.2.3. Characteristic time scales of the two-phase flow

Table 2 gives the particle relaxation time τ_p depending on the particle diameter d_p. In a first approximation, Stokes flow around the particles is assumed so that τ_p reads

$$\tau_p = \frac{\rho_p d_p^2}{18\mu_f}, \tag{1}$$

where μ_f is the dynamic viscosity of the fluid.

The comparison of the particle relaxation time with a characteristic time scale of the fluid most energetic eddies $\tau_{f,t}$, yields the Stokes number St. To evaluate $\tau_{f,t}$ at the outlet of the inner pipe, the length of the most energetic eddies is estimated as a third of the pipe diameter and their velocity as the maximum fluctuating velocity in the pipe:

$$St = \frac{\tau_p}{\tau_{f,t}}, \quad \text{where } \tau_{f,t} = \frac{\frac{2R_I}{3}}{u_{f,I}^{\max}} \approx 7 \text{ ms}. \tag{2}$$

Table 2 presents the characteristic Stokes number of the particles depending on their diameter: the smallest particles with diameter $d_p = 20$ μm almost follow the gas flow while the inertia of the biggest ones with diameter $d_p = 100$ μm makes them much more independent of the fluid flow.

As underlined by Schefer et al. [30], the recirculation zones and the stagnation points are related to the inner and outer pipe flow characteristics. However, in the inner pipe (whose diameter is small), the motion of the particles is complex, due to interactions with the fluid and the walls as well as inter-particle collisions. To quantify whether particles have time to adapt to changes in gas mean velocity within the inner duct, the particle relaxation time is compared to their transit time T_p^T in the pipe:

$$T_p^T = \frac{L_I}{U_{f,I}^{\max}} = 500 \text{ ms}, \tag{3}$$

where $L_I = 2$ m is the length of the inner duct that particles travel across and $U_{f,I}^{\max}$ is the inner maximum gas velocity. Compared to the particle relaxation time, the particle transit time of all particles in the inner pipe remains large. Thus, the particles have time to adapt to fluid turbulence before they reach the outlet of the inner pipe.

2.3. Objectives of the simulations

In this study two unstructured codes developed at CERFACS and CTR are used to investigate the configuration of Borée et al. [1]:

(1) An explicit compressible code (AVBP) using both EL and mesoscopic EE [31–33] approaches. For the present study, AVBP is used on both hexahedron-based and tetrahedron-based grids.
(2) An implicit incompressible code (CDP) using a EL formulation. For this study, hexahedron-based grids are used in CDP.

The dispersed phase consists of solid particles so that evaporation, coalescence and break-up do not have to be considered. Accounting for polydispersion in the bluff body configuration using EL approaches is straightforward: particles with different diameters are injected at the inlet of the chamber. When using EE approaches, there are two main methods. On the one hand, polydispersion can be accounted for by introducing a particle size distribution [34]. On the other hand, EE approaches can be extended to polydispersion using a multi-class method: the set of particulate equations is resolved for a finite number of particle classes depending on their diameter. The main disadvantage of this method is its computational cost which drastically increases with the number of classes to be considered. In the specific case of Borée et al. [1] experiments, separate studies (not reported here) using Lagrangian simulations and polydisperse particles or 60 μm particles only have shown that using a monodisperse distribution of size was very close to the 22% case of Borée et al. [1] and was sufficient to capture both the mean flow effects on the gas (through two-way coupling) and the dynamics of the 60 μm class. Therefore, in this work, particle distribution is assumed monodisperse with particle diameter close to the initial mean diameter in mass: $d_p = 60$ μm. Only the low mass loading case ($M_p = 22\%$) of Borée et al. [1] is studied. Since the particle volume fraction

Table 2
Experimental particle relaxation time and Stokes number depending on particle diameter.

d_p (μm)	20	30	40	50	60	70	80	90	100
τ_p (ms)	3.1	6.9	12.3	19.2	27.6	37.6	49.1	62.2	76.7
St (–)	0.4	1.0	1.8	2.7	3.9	5.4	7.0	8.9	11.0

α_p is about 1% at the inlet, inter-particle collisions are found to play a crucial role in the injection tube [35]. Nevertheless, the dilution effect being very effective, collision effect may be neglected in the modeling approaches for the numerical simulation of the downstream two-phase flow. Furthermore, the two-way coupling is taken into account through drag force. However, its impact on the gas phase has been shown of minor importance in the 22% mass loading case [1]. This case allows to study the following points:

(1) evaluate influence of mesh type (hexahedra vs tetrahedra);
(2) evaluate influence of numerical convective scheme (second and third order);
(3) compare implicit and explicit formulations for time advancement;
(4) compare accuracy of EE and EL approaches.

3. Description of solvers and models

3.1. Gas flow solvers

Numerical methods used in both LES solvers for the gas phase have been extensively described in the literature ([9,7,36] for CDP and [8,12] for AVBP) and will only be summarised here.

The explicit LES solver AVBP solves the compressible Navier–Stokes equations with a second-order finite-volume Lax–Wendroff scheme or a third-order finite-element scheme TTGC [37,9]. The WALE model [38] that predicts the right scaling for the fluid turbulent viscosity when approaching a solid boundary (i.e., $\nu_{f,t} = 0$) is used to model the subgrid stress tensor.

The LES solver CDP solves implicitly the incompressible Navier–Stokes equations. The time integration of CDP is based on the fractional-step method [39] and the space integration relies on a second-order central scheme that conserves the kinetic energy [7,36]. The dynamic Smagorinsky model [40] is used to model the subgrid stress tensor.

The boundary conditions for each solver are detailed in Section 4.3.

3.2. Dispersed phase flow solvers

The particles are assumed to be rigid spheres with diameter comparable or smaller than the Kolmogorov length-scale. If the particle density is much larger than the fluid density, the forces acting on particles reduce to drag and gravity [41,42].

3.2.1. Euler/Lagrange approach

In EL simulations, the influence of the particles on the gas phase momentum and energy equations is taken into account by using the point-force approximation in the general framework of the particle-in-cell method (PIC) [43–47], with standard single-phase subgrid turbulence modeling approaches. According to Boivin et al. [48], such an assumption is valid for small mass loading ratio (typically, $\alpha_p\rho_p/\rho_f \leqslant 1$) with response time larger than the subgrid turbulence characteristic time scale. In particular, the coupling force exerted by each particle on the fluid is projected onto the grid nodes. The weights in the projection operation are inversely proportional to the distances between the particle and the nodes of the containing cell.

With these assumptions, the particle equations of motion can then be written for a single particle as

$$\frac{dx_{p,i}}{dt} = u_{p,i}, \tag{4}$$

$$\frac{du_{p,i}}{dt} = -\frac{3}{4}\frac{\rho_f}{\rho_p}\frac{C_D}{d_p}|\mathbf{v}_r|v_{r,i} + g_i = -\frac{u_{p,i} - \tilde{u}_{f,i}}{\tau_p} + g_i. \tag{5}$$

The local drag coefficient in Eq. (5) is C_D and may be expressed in terms of the particle Reynolds number Re_p following Schiller and Nauman [49]:

$$C_D = \frac{24}{Re_p}[1 + 0.15Re_p^{0.687}], \quad Re_p = \frac{|\mathbf{v}_r|d_p}{\nu_f} \leqslant 800, \tag{6}$$

where τ_p is the particle relaxation time defined as

$$\tau_p = \frac{4}{3}\frac{\rho_p}{\rho_f}\frac{d_p}{C_D|\mathbf{v}_r|}. \tag{7}$$

The local instantaneous relative velocity between the particle and the surrounding fluid is $\mathbf{v}_{r,i} = u_{p,i} - \tilde{u}_{f,i}$, where $\tilde{u}_{f,i}$ is the fluid velocity at the position of the particle assuming that the flow field is locally undisturbed by the presence of this particle [42,50]. In first approximation, the velocity is assumed to be equal to the interpolation of the filtered velocity at the position of the particle [21,51,52]. The effect of the subgrid fluid turbulence is assumed to be negligible owing to the large inertia of the solid particles [53]. A linear interpolation algorithm is used to compute the fluid velocity at the position of the particle.

3.2.2. Euler/Euler approach

Eulerian equations for the dispersed phase may be derived by several means. A popular and simple way consists in volume filtering of the separate, local, instantaneous phase equations accounting for the inter-facial jump conditions [54]. Such

an averaging approach is restrictive because the filter length must be both larger than the inter-particle distance (to define continuous mean fields of particle number density and particle velocity), and smaller than the smallest length-scale in the particle velocity field to ensure unicity of the particle velocity in the filtering volume. Moreover, Druzhinin [54] assumes that all the particles located in this filtering volume have the same velocity, which is untrue when the particle relaxation time is larger than the smallest turbulent time scale [32]. An alternative to the two-fluid approach is the Eulerian equilibrium approach proposed by Ferry and Balachandar [55] that reduces the number of transport equations to be solved: only the transport equation for particle number density is solved while the particle velocity is given by the expansion in τ_p of the local fluid quantities first proposed by Maxey [41] and then extended by Druzhinin [56], and Ferry and Balachandar [55]. Both approaches show good agreement with EL results when focusing on preferential concentration of low-inertia particles in HIT flows [41,57]. However, the errors in the predictions of the particle field increase with the particle response time [58].

Though, the crucial assumption of the above approaches, the particle velocity uniqueness at a given position, fails when the particle relaxation time is larger than the Kolmogorov time scale, due to the crossing of particle trajectories. To overcome this difficulty, Février et al. [32], proposed a probability density function (PDF) approach based on a conditional ensemble average of the particle properties for a given turbulent fluid flow realization. In such an approach, any discrete particle velocity may be separated into two contributions: an Eulerian velocity field, the mesoscopic velocity field shared by all the particle realizations, and a Lagrangian random distribution, the random uncorrelated velocity (RUV), spatially uncorrelated and which accounts for the particle trajectory crossing. The conditional particle velocity PDF $\breve{f}_p(\mathbf{c}_p, \mathbf{x}, t)$ gives the local instantaneous probable number of particles with the given translation velocity $\mathbf{u}_p = \mathbf{c}_p$, and obeys a Boltzmann-type kinetic equation accounting for external forces acting on the particles and inter-particle collisions. The moments of the particle PDF are mesoscopic Eulerian quantities which obey transport equations derived by integration from the kinetic equation, following the same methodology than for the derivation of the Navier–Stokes equations in the frame of kinetic theory [59]. So, Février et al. [32] derived transport equations for particle number density $\bar{n}_p$, mesoscopic velocity $\breve{\mathbf{u}}_p$ and random uncorrelated kinetic energy (RUE) $\delta\breve{\theta}_p$ and Simonin [60] proposed, as a first approximation, a viscosity assumption to model the random uncorrelated kinetic stresses. The mesoscopic approach was evaluated using a priori test from discrete particle simulation (DPS) coupled with DNS or LES of forced homogeneous isotropic turbulence [61] and fully-developed channel flow [22]. Then, by analogy with the gas phase, a LES filter is applied to the equations for the mesoscopic quantities [62,33], which leads to equations for the filtered (in the LES sense) particle number density $\bar{n}_p$ and the filtered correlated velocity $\hat{\mathbf{u}}_p$ using the mass-weighted averaging $\widehat{n_p u_{p,j}} = \bar{n}_p \hat{u}_{p,j}$ [63]:

$$\frac{\partial}{\partial t}\bar{n}_p + \frac{\partial}{\partial x_j}\bar{n}_p \hat{u}_{p,j} = 0, \tag{8}$$

$$\frac{\partial}{\partial t}\bar{n}_p \hat{u}_{p,i} + \frac{\partial}{\partial x_j}\bar{n}_p \hat{u}_{p,i}\hat{u}_{p,j} = -\frac{\bar{n}_p}{\tau_p}(\hat{u}_{p,i} - \hat{u}_{f,i}) + \bar{n}_p g_i - \frac{\partial}{\partial x_j}T_{p,ij} - \frac{\partial}{\partial x_j}\bar{n}_p \widehat{\delta R^*_{p,ij}} - \frac{\partial}{\partial x_i}\frac{2}{3}\bar{n}_p \widehat{\delta\theta}_p, \tag{9}$$

where $\bar{n}_p$, $\hat{\mathbf{u}}_p$, $\widehat{\delta R^*_{p,ij}}$ and $\widehat{\delta\theta}_p$ are respectively the filtered particle number density, the particle correlated velocity, the second-order uncorrelated particle velocity correlation tensor deviatoric, and the particle RUE. The first two terms of the right-hand side (RHS) of Eq. (9) are the drag force and gravity effects on large scales, the third one accounts for the subgrid-scale (SGS) effects, the fourth one is a diffusion term and the last one represents the pressure effect due to RUE. $T_{p,ij}$ stands for the particle subgrid stress tensor:

$$T_{p,ij} = \bar{n}_p(\widehat{u_{p,i}u_{p,j}} - \hat{u}_{p,i}\hat{u}_{p,j}). \tag{10}$$

3.2.3. Filtered RUV and subgrid term modeling

Assuming small anisotropy of the RUM, Simonin et al. [64] model $\delta R^*_{p,ij}$ by a viscous term. For LES approaches this model is adapted by replacing non-filtered quantities by filtered ones leading to [62]:

$$\widehat{\delta R^*_{p,ij}} = -\hat{\nu}_{p,\mathrm{RUM}}\left(\frac{\partial \hat{u}_{p,i}}{\partial x_j} + \frac{\partial \hat{u}_{p,j}}{\partial x_i} - \frac{2}{3}\frac{\partial \hat{u}_{p,k}}{\partial x_k}\delta_{ij}\right), \tag{11}$$

where the RUM viscosity $\hat{\nu}_{p,\mathrm{RUM}}$ is obtained in the framework of the kinetic theory of particulate flows [61]:

$$\hat{\nu}_{p,\mathrm{RUM}} = \frac{\tau_p}{3}\widehat{\delta\theta}_p. \tag{12}$$

For the SGS tensor $T_{p,ij}$, Riber et al. [65] propose a viscosity model by analogy with single-phase flows [66,67]. The trace-free SGS tensor is modeled using a viscosity assumption (compressible Smagorinsky model), while the subgrid energy is parametrized by a Yoshizawa model [68]:

$$T_{p,ij} = -C_S 2\Delta_f^2 \bar{n}_p |\widehat{S}_p|\left(\widehat{S}_{p,ij} - \frac{\delta_{ij}}{3}\widehat{S}_{p,kk}\right) + C_I 2\Delta_f^2 \bar{n}_p |\widehat{S}_p|^2 \delta_{ij}, \tag{13}$$

where $\widehat{S}_p$ is the filtered particle strain rate tensor, $|\widehat{S}_p|^2 = 2S_{p,ij}S_{p,ij}$ and Δ_f the filter characteristic length. The model constants have been evaluated in a priori tests [69] leading to the values $C_S = 0.02$, $C_I = 0.012$.

3.2.4. Simplified Euler/Euler model

The filtered particle RUE is required twice in the transport equation for filtered particle correlated velocity (Eq. (9)): first in the term representing pressure effects due to particle RUE; second when modeling the filtered second-order uncorrelated particle velocity correlation tensor deviatoric (see Eqs. (11) and (12)). To close these two terms, a transport equation for filtered particle RUE can be solved, as proposed by Février et al. [32]. This has been done by Kaufmann et al. [70] when simulating DNS of particle-laden HIT flows, showing good agreement between Lagrangian and Eulerian results. Still, these models proposed for the unclosed terms due to RUM are very recent and the validity of the viscosity model has recently been questioned by Riber [33] when performing LES in a particle-laden turbulent confined jet flow [71]. Indeed, the resolved particle fluctuations were considerably damped and only the RUM contributed to the particle agitation, which is not realistic. An alternative already tested by Boileau et al. [20] and Riber [33], consists in neglecting the RUM contributions in the transport equations for the dispersed phase. Then, the set of equations reduces to

$$\frac{\partial}{\partial t}\bar{n}_p + \frac{\partial}{\partial x_j}\bar{n}_p\hat{u}_{p,j} = 0, \tag{14}$$

$$\frac{\partial}{\partial t}\bar{n}_p\hat{u}_{p,i} + \frac{\partial}{\partial x_j}\bar{n}_p\hat{u}_{p,i}\hat{u}_{p,j} = -\frac{\bar{n}_p}{\tau_p}(\hat{u}_{p,i} - \hat{u}_{f,i}) + \bar{n}_p g_i - \frac{\partial}{\partial x_j}T_{p,ij}. \tag{15}$$

This simplified Euler/Euler model has been chosen to be evaluated in the bluff body configuration. Note that when using this simplified model, the mean particle velocity and mass flux fields are expected to be correctly predicted while the agitation of the particles should be under-estimated since a part, depending on the particle inertia, is the RUM contribution [33].

4. Comparison of single-phase flow simulations

4.1. Choice of the computational domain

The total volume of the configuration is large, due to the length of the ducts (2 m) and the chamber itself (1.5 m), which is far larger than a typical combustion chamber test-rig. Therefore, calculating the whole geometry would be computationally expensive.

Since the location of the second stagnation point mainly depends on the geometry global diameter, the diameters of the inner and annular pipes have been kept: $R_I = 0.010$ m; $R_{C,1} = 0.075$ m; $R_{C,2} = 0.150$ m. In contrast, the pipes have been shortened to 0.1 m for two reasons. On the one hand, it is necessary to decrease the length of the ducts: considering the low Reynolds number and the grid resolution in the inner pipe as well as the accuracy of the numerical scheme, it is impossible to wait for natural destabilisation of the gas flow within the pipe. Specific inlet boundary conditions are therefore used to help the flow destabilisation (see Section 4.3). On the other hand, the pipes cannot be decreased down to 0.1 m: the accurate prediction of particle motion in a pipe (or a channel) is still difficult to obtain, especially because of particle–wall interactions [21] and inter-particle collisions [22]. Since these interactions are not accounted for in this work, one has to ensure that the modified pipe length stays compatible with the particle relaxation time and the particle transit time evaluated in Section 2.2.2.

Note that the length of the chamber (1.5 m) may also be decreased since the second stagnation point is located in the vicinity of $z = 0.4$ m and the flow shows very few structures downstream from this point. In this work, the chamber is shortened for one of the grids tested, as specified in Section 4.2.

These simplifications allow to divide the volume of the computational domain by two, which drastically reduces the computational cost of the LES.

4.2. Grids tested

Two grids have been tested on this bluff body configuration to investigate the effects of both resolution and grid type (tetrahedra or hexahedra). Table 3 details the characteristics of the two grids named *gridtet* and *gridhex*. Figs. 5 and 6 present an overview of the grid resolutions in longitudinal and front cutting planes, respectively.

Table 3
Characteristics of the two grids tested.

Name	*gridtet*	*gridhex*
Grid type	Tetrahedra	Hexahedra
Number of nodes	549,369	3,255,085
Number of cells	3,115,898	3,207,960
Length of the pipes (m)	0.1	0.1
Length of the chamber (m)	1.5	0.8
Total volume of the domain (m^3)	0.111	0.062
y^+ in the inner pipe (–)	15	7.5
y^+ in the coflow (–)	64	15

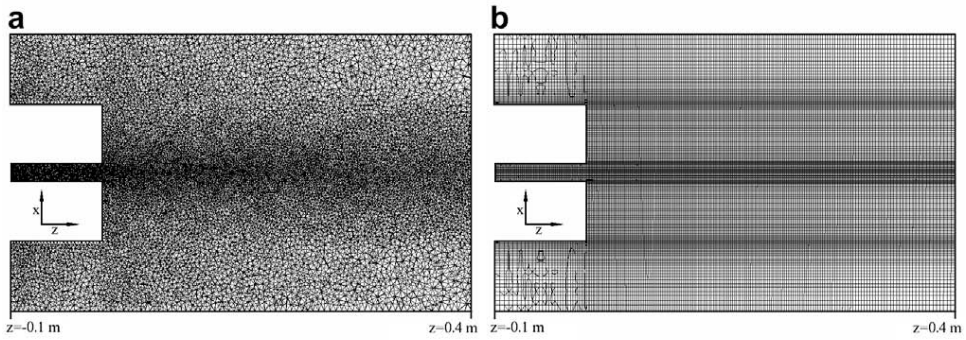

Fig. 5. Longitudinal cutting plane ($y = 0$) of the two grids tested: *gridtet* (a) and *gridhex* (b) detail of the region $z \in [-0.1; 0.4]$ m.

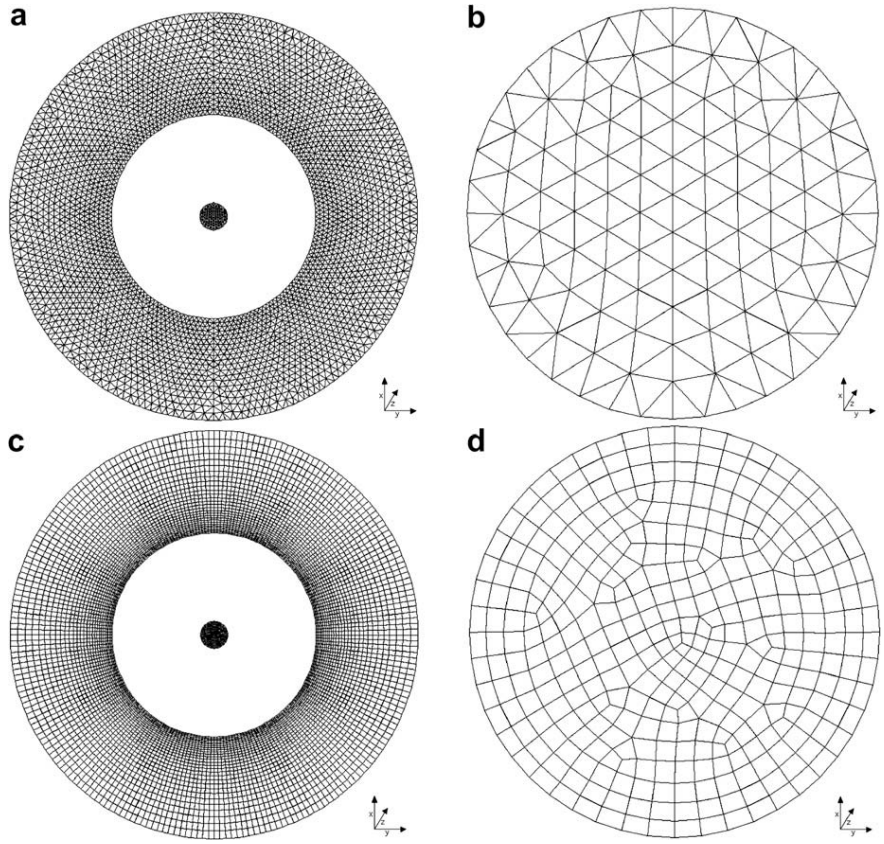

Fig. 6. Global front view (left) and detail of the inner inlet (right) for the two grids tested: *gridtet* (a and b) and *gridhex* (c and d).

There are three main differences between the two grids. First, the length of the chamber is different: according to the experimental setup, the chamber is 1.5 m long for *gridtet* whereas *gridhex* has been shortened down to 0.8 m for two reasons. On the one hand, the second stagnation point is located far upstream from the outlet of the chamber. On the second hand, the grid can be easily coarsened downstream from the second stagnation point to save computational cost when using tetrahedra, which is more difficult with hexahedra. This simplification has been verified to have no influence on the results. Consequently, as summarised in Table 3, the total number of cells is very similar for the two grids, but the total volume is twice larger for *gridtet* than for *gridhex*. The second difference between the two grids deals with the non-dimensional wall distance y^+ in the pipes which is two times smaller in the inner pipe and four times smaller in the coflow in *gridhex* than in *gridtet*. Both grids contain much more cells in the inner pipe than in the outer one. Finally, in the tetrahedron-based grid,

special care has been taken to generate small cells in the recirculation zones, which was unaffordable in the hexahedron-based grid considering the increase in computational cost it would induce.

4.3. Boundary conditions

As the two LES codes use different formulations (see Section 3.1), the boundary conditions shown in Fig. 1 are described separately.

4.3.1. Boundary conditions for the AVBP code

The characteristic boundary conditions developed by Poinsot and Lele [72], and Moureau et al. [9] are used for these simulations.

The outlet is nearly non-reflective at atmospheric pressure: $P_f = 1.013 \times 10^5$ Pa.

The inlet treatment is more complex. Indeed, the first test section where the experimental profiles of mean and fluctuating fluid velocities are known is located at $z = 3$ mm. Then, the main difficulty consists in specifying the boundary conditions at the inlet of the pipes in order to obtain good agreement between the simulations and the experiments at $z = 3$ mm. Considering the Reynolds numbers in both pipes (see Section 2.2.1), typical mean axial velocity profiles of fully-developed turbulent pipes (following the classical 1/7 power-law) are imposed at the inlet of the inner and annular pipes, corresponding to the experimental mass flux. However, the Reynolds numbers in the pipes are too low to expect natural destabilisation of the gas flow, i.e., without any flow forcing. Therefore, a time and space-varying velocity signal at the inlet of both pipes is imposed in order to reproduce the effect of an incoming turbulent field as observed in the experiment. This incoming turbulent signal is constructed using a random flow generation (RFG) algorithm [73,74]. The incoming field consists of a superposition of harmonic functions (50 modes projected in the three directions) with two characteristic length-scales prescribed by user: the most energetic length-scale depends on the pipe diameters while the most dissipative one is directly linked to the grid resolution on the inlet patch. Typical fluctuating profiles of fully-developed pipes are imposed at the inlet of the pipes to match experimental fluctuating profiles at $z = 3$ mm. Forcing the flow in such a way considerably accelerates the establishment of developed turbulent flows. It also ensures the presence of coherent perturbations not warranted with a pure white noise.

Since the WALE subgrid model shows a correct behavior close to the wall [38], no wall modeling is used: non-slip conditions are imposed at the walls that are isothermal at ambient temperature: $T_f = 293$ K.

4.3.2. Boundary conditions for the CDP code

An alternative to the RFG method to generate inlet turbulence in the inner pipe is to compute a well-resolved turbulent pipe separately and to inject it in the bluff body computation. The advantage of this injected turbulence is to be non-synthetic without any parameter to prescribe. This method is used for the inner pipe by computing a periodic pipe with a constant volume forcing in the momentum equations. The forcing is dynamically adjusted to obtain the right mass flux. The computational mesh, which is five diameter long, consists of 2.05 million hexahedra with a y^+ equal to 1.9. Even with this well-resolved mesh, the transition from a laminar to a turbulent regime is achieved by beginning the computation with a Reynolds number of 6000 before decreasing slowly to the target Reynolds number of 4500. Then, instead of recording the velocity on a cut plane, a single instantaneous snapshot of the flow is taken. In this snapshot, the streamwise spatial abscissa is transformed into a time abscissa by dividing it by the mean velocity in the pipe. Finally, the inlet velocity for the bluff body pipe is spatially and temporally interpolated from the transformed snapshot. This method saves CPU time because the stand-alone pipe may be computed during a physical time much shorter than the one needed to converge the bluff body flow. The only drawback is that it deforms the eddies where the mean streamwise velocity is different of the global mean velocity, mainly close to the wall.

For the coflow, no turbulence is injected. Only the mean velocity profile is prescribed by imposing the experimental mean velocity measured at $z = 3$ mm.

Non-slip conditions are imposed at the walls that are isothermal at ambient temperature: $T_f = 293$ K while the outlet is purely convective due to the incompressible equations solved in the CDP code.

4.4. Test cases

In such an industrial-like configuration, the computational cost is often the limiting factor determining the grid resolution and the numerical method to be used. The choice of the numerical scheme (low- or high-order), the grid resolution and type (hexahedra or tetrahedra) and the solver type (implicit or explicit) is not straightforward. Whether results are more accurate with a low-order scheme used on a refined grid or with a high-order scheme coupled with a coarser grid is still an open question, for instance [75]. While Colin and Rudgyard [37] and Vreman [76] for example aim at developing high-order schemes on coarse grids, other authors use second-order schemes on more refined grids [77,7]. Naturally, the computational cost of the simulation is a key point for the final choice. In this section, five cases are analysed to investigate the influence of:

(1) *The* numerical scheme: The TTGC scheme [4], third-order accurate finite-element, is known to provide better results than the second-order finite-volume LW scheme, especially in recirculating flows. The influence of the scheme is shown in Section 4.6 using the same unstructured grid *gridtet*, and the AVBP code.

(2) *The* inlet boundary condition treatment: The relatively low Reynolds number associated with a low grid resolution in the pipes do not allow a natural transition to turbulence. The influence of the inlet forcing using the RFG method described in Section 4.3.1, is analysed in Section 4.7 using the AVBP code with the grid *gridtet* and the TTGC scheme.
(3) *The* grid: Hexahedron-based grids are rarely used to calculate swirled flows since they are said to generate preferential directions. The AVBP code with the TTGC scheme is used to investigate the influence of grid type and grid resolution in Section 4.8.
(4) *The* code: In Section 4.10, the results provided by AVBP and CDP on the hexahedron-based grid *gridhex* are compared with the measurements to evaluate the accuracy of both gas LES solvers.

All cases are summarised in Table 4 for those carried out with AVBP whereas the LES performed with CDP is detailed in Section 4.10. To validate results, the following diagnostics are used:

(1) the Q-criterion of Dubief and Delcayre [78], Hunt et al. [79] and Hussain and Jeong [80] to visualise the flow structures;
(2) the axial variations of mean and root-mean-square (RMS) axial velocities (as plotted in Fig. 3 in Borée et al. [1]) to measure the length of the recirculation zone;
(3) the radial variations of mean and RMS axial velocities at seven stations along the duct axis (z = 3, 80, 160, 200, 240, 320 and 400 mm as represented in Fig. 7) to provide a detailed comparison of LES and experimental fields.

The cylindrical coordinate system (z, r, θ) is used to indicate axial (downward), radial and azimuthal directions. As no mean swirling motion was detected, only the axial and radial velocity components are provided. The mean components resulting from LES-averaging are respectively noted W and U_r whereas the RMS components are w_{rms} and $u_{r,\mathrm{rms}}$.

4.5. Qualitative gas flow analysis

The analysis of the averaged quantities resulting from LES requires a simulation time long enough to ensure convergence, and a sampling time small enough to ensure that the smallest structures can contribute to the averaged solution. In the present configuration, the lowest frequency to be represented is associated to the two counter-rotating structures on each side of the axis as plotted in Fig. 2(c). Considering their size $l_{f,l} \approx 8 \times 10^{-2}$ m, and their mean rotating velocity $U_{f,l} \approx 1$ m s^{-1}, the order of magnitude of the associated time is $\tau_{f,l} \approx 8 \times 10^{-2}$ s. The most energetic eddies in the inner pipe constitute a reasonable choice to determine the order of magnitude of the highest frequencies. Considering their size $l_{f,t} \approx 7 \times 10^{-3}$ m, and their velocity $u'_{f,t} \approx 1.5$ m s^{-1}, the order of magnitude of the associated time scale is $\tau_{f,t} \approx 4.6 \times 10^{-3}$ s. All the LES performed with the explicit solver AVBP have been run for $T_{\mathrm{av,AVBP}} \approx 1$ s while the LES performed with the implicit solver CDP has been run longer: $T_{\mathrm{av,CDP}} \approx 2.5$ s. The time between two samples is $\Delta t_r \approx 1.2 \times 10^{-3}$ s. In both codes, the statistics of the mean fields are then well converged. This is not always the case for the RMS quantities but the overall tendency gives enough information to compare models and solvers.

Table 4
Test cases computed with AVBP and corresponding parameters.

Case	Solver	Grid	Scheme	Inlet treatment
avbp_tet_lw_norfg	AVBP	*gridtet*	LW	None
avbp_tet_ttgc_norfg	AVBP	*gridtet*	TTGC	None
avbp_tet_ttgc_rfg	AVBP	*gridtet*	TTGC	RFG
avbp_hex_ttgc_rfg	AVBP	*gridhex*	TTGC	RFG

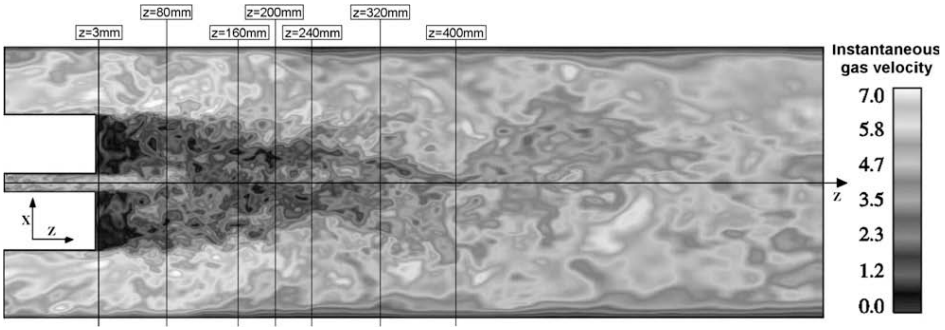

Fig. 7. Instantaneous field of velocity modulus obtained with case *avbp_hex_ttgc_rfg* in the cutting plane $y = 0$. The seven vertical lines represent the experimental stations.

Fig. 7 shows an instantaneous field of the gas velocity modulus in the cutting plane $y = 0$ for the case *avbp_hex_ttgc_rfg*. Many structures of different sizes are visible. The largest ones are linked to the diameter of the coflow, intermediate ones appear in the shear layers and structures coming out of the inner jet are also clearly identified.

The time-averaged fields considerably differ from the instantaneous flow structure. Fig. 8(a)–(c) presents, respectively, the mean field of gas axial velocity, and the RMS fields of gas axial and radial velocities in the cutting plane $y = 0$ for the case *avbp_hex_ttgc_rfg*. The iso-contour line of zero mean axial velocity is added on the three pictures. All fields are rather symmetric, which indicates good convergence of the simulations. As expected, there are two points with zero velocity along the axis, corresponding to distinct inner jet and coflow stagnation points. The peak of axial fluctuations is located at the inner jet stagnation point whereas the radial fluctuations are maximum in the vicinity of the furthest stagnation point. Both axial and radial fluctuations show secondary peaks, respectively in the external shear layer and close to the first stagnation point. At these two specific locations, turbulence is highly anisotropic.

4.6. Influence of the numerical scheme

To evaluate the influence of the numerical scheme on the gas flow, the cases *avbp_tet_lw_norfg* and *avbp_tet_ttgc_norfg* are compared. Both LES are performed with AVBP on the unstructured grid *gridtet*. The RFG method is not used at the inlet of the ducts so that the only difference between the two cases is the numerical scheme.

The qualitative impact of the scheme order on the small structures is clear in Fig. 9 where instantaneous iso-surfaces of Q-criterion are displayed for both LW and TTGC schemes. Both fields exhibit two kinds of coherent structures: some longitudinal vortices come from the inner pipe whereas some others are created in the external shear zone and are rather azimuthal. However, the TTGC scheme provides more numerous and more detailed flow structures than the LW scheme.

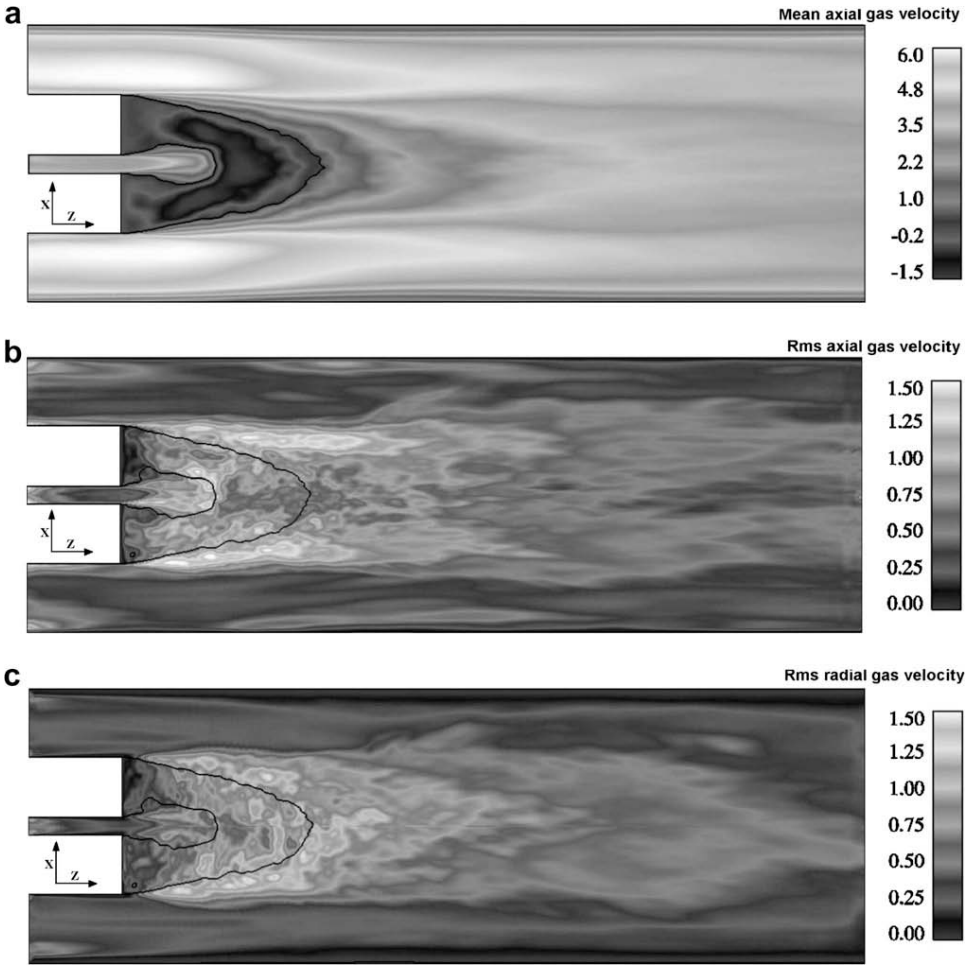

Fig. 8. Mean fields of gas axial velocity (a), and RMS fields of gas axial (b) and radial (c) velocity obtained with case *avbp_hex_ttgc_rfg* in the cutting plane $y = 0$. The black line corresponds to the iso-contour line $\langle W_f \rangle = 0$.

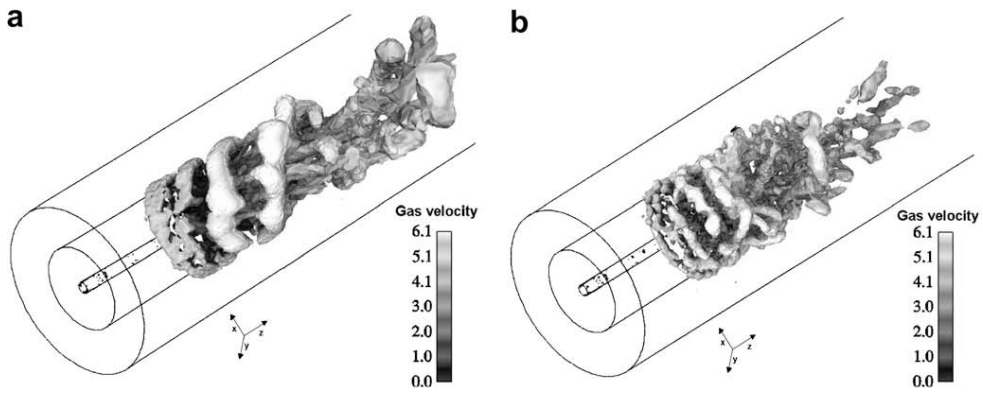

Fig. 9. Instantaneous iso-surfaces of Q-criterion for LW (a), and TTGC (b). The iso-surfaces are colored by instantaneous velocity. (Simulations performed with AVBP.)

These differences are quantified in Fig. 10 where the axial profiles of mean and RMS axial velocities are plotted. When using LW, the two points with zero mean axial velocity that delimit the recirculation zone are located too far downstream from the ducts, and so is the peak of RMS axial velocity. On the contrary, the location of the two stagnation points as well as the peak of RMS axial velocity are well predicted with TTGC. Only the amplitude of this peak is over-estimated. With two-phase flows and even combustion in prospect, delimiting precisely the recirculation zone is of high importance: the particle distribution as well as the flame location and shape greatly depend on the first stagnation point. Consequently, all the LES performed with AVBP and analysed hereafter use the TTGC scheme.

4.7. Influence of the inlet boundary treatment

The runs of Fig. 10 were performed without imposing turbulent velocity fluctuations in the inner pipe and this simplification is questionable. Indeed, the mean axial fluid velocity is shown to increase along the inner pipe ($-0.1 < z < 0$) while there is no fluctuation developing in the duct, showing that the turbulent flow within the central pipe is not correctly captured by the solver. Performing a true LES in the ducts would be computationally expensive because it would require a considerable increase in resolution. Therefore, in this work, the specific inlet boundary treatment described in Section 4.3.1 has been used to feed turbulent fluctuations in the inner pipe.

The direct comparison of the cases *avbp_tet_ttgc_norfg* and *avbp_tet_ttgc_rfg* exhibits the impact of the inlet turbulent forcing method, as shown in Fig. 11. Usually in a pipe flow, the peaks of velocity fluctuations reach almost 10% of the mean velocity on the centerline. Owing to a lack of resolution in the inner pipe, the velocity fluctuations imposed at the inlet of the pipe have deliberately been increased to 15% of the axial mean velocity. The main purpose is to get good agreement between simulations and experiments at the outlet of the duct, i.e., at $z = 3$ mm, which is shown in Fig. 11(b). The consequence of the fluid agitation in the duct itself is a flatter mean axial velocity profile in the pipe: Fig. 11(a) shows that the maximum of mean axial velocity is in better agreement with the experiments at the outlet of the duct when using the RFG method. Note that the accurate prediction of the location of the recirculation zone for the case *avbp_tet_ttgc_norfg* is only due to a fortuitous compensation of errors.

4.8. Influence of the grid

The influence of the grid type as well as the grid resolution is investigated comparing the results provided by the cases *avbp_tet_ttgc_rfg* and *avbp_hex_ttgc_rfg*. As mentioned in Table 4, the only difference between these two LES is the grid.

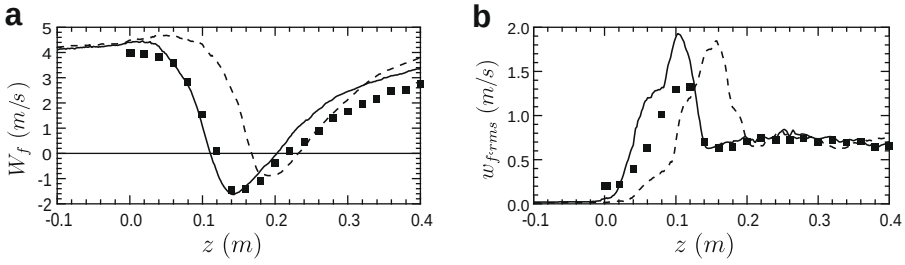

Fig. 10. Axial profiles of mean (a), and RMS (b), axial gas velocity. Symbols: experiment – dashed line: LW – solid line: TTGC. (Simulations performed with AVBP.)

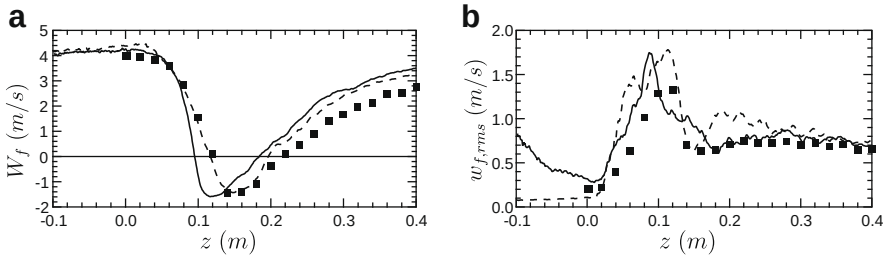

Fig. 11. Axial profiles of mean (a), and RMS (b), axial gas velocity. Symbols: experiment – dashed line: no injected turbulent fluctuations – solid line: turbulent fluctuations injected at inlet. (Simulations performed with AVBP.)

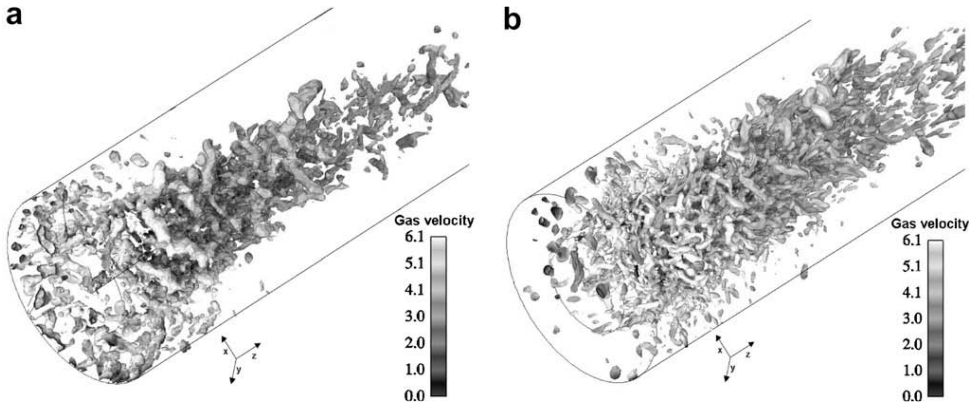

Fig. 12. Instantaneous iso-surfaces of Q-criterion for *gridtet* (a), and *gridhex* (b). The iso-surfaces are colored by instantaneous velocity. (Simulations performed with AVBP.)

The qualitative impact of the grid on the fluid flow topology is shown in Fig. 12 where instantaneous iso-surfaces of Q-criterion are displayed for both cases. Although the two fields exhibit the same kind of longitudinal and azimuthal coherent structures, there are much more, but also much smaller vortices with the hexahedron-based grid. In other words, both grids resolve the large vortices in the same way but the grid *gridhex* resolves much smaller eddies whereas they are dissipated by the grid *gridtet*.

Nevertheless, these differences in flow structures are difficult to quantify when plotting the radial mean and RMS axial velocity at the seven experimental stations as done in Fig. 13. The amplitude of the mean and RMS velocity is very similar for both grids, and in good agreement with the measurements. The most significant discrepancy is located in the central region close to the station $z = 80$ mm where the axial velocity fluctuations are over-estimated with *gridtet*. As a consequence, the inner jet flow penetrates slightly farther in the chamber, improving the prediction of the location of the first stagnation point as well as the length of the recirculation zone.

4.9. Compromise between scheme order and grid

Accounting for the cost efficiency slightly modifies the conclusions drawn in Sections 4.6 and 4.8. Table 5 compares the computational cost of the cases *avbp_tet_lw_norfg*, *avbp_tet_ttgc_rfg* and *avbp_hex_ttgc_rfg* when simulating 0.1 s physical time. Note that the RFG inlet treatment does not notably modify the computational cost so that the case *avbp_tet_ttgc_norfg* is not reported in Table 5. On the one hand, the computational cost of a simulation with TTGC is 2.5 bigger than with LW [4]. On the other hand, using the unstructured grid *gridtet* is about four times cheaper than using the hexahedron-based grid *gridhex*. This figure is to be related to the gain in quality of the predictions choosing the final configuration and grid.

4.10. Influence of the code

The accuracy of both AVBP and CDP codes is finally compared analysing the results provided by the cases *cdp_hex* and *avbp_hex_ttgc_rfg*. For this purpose, the case *avbp_hex_ttgc_rfg* has been chosen, not only because it shows the best agreement with the measurements but also because it is the best candidate for direct comparisons with CDP. Indeed, both codes use here the same hexahedron-based grid. There are however some differences in the parameters used, as summarised in

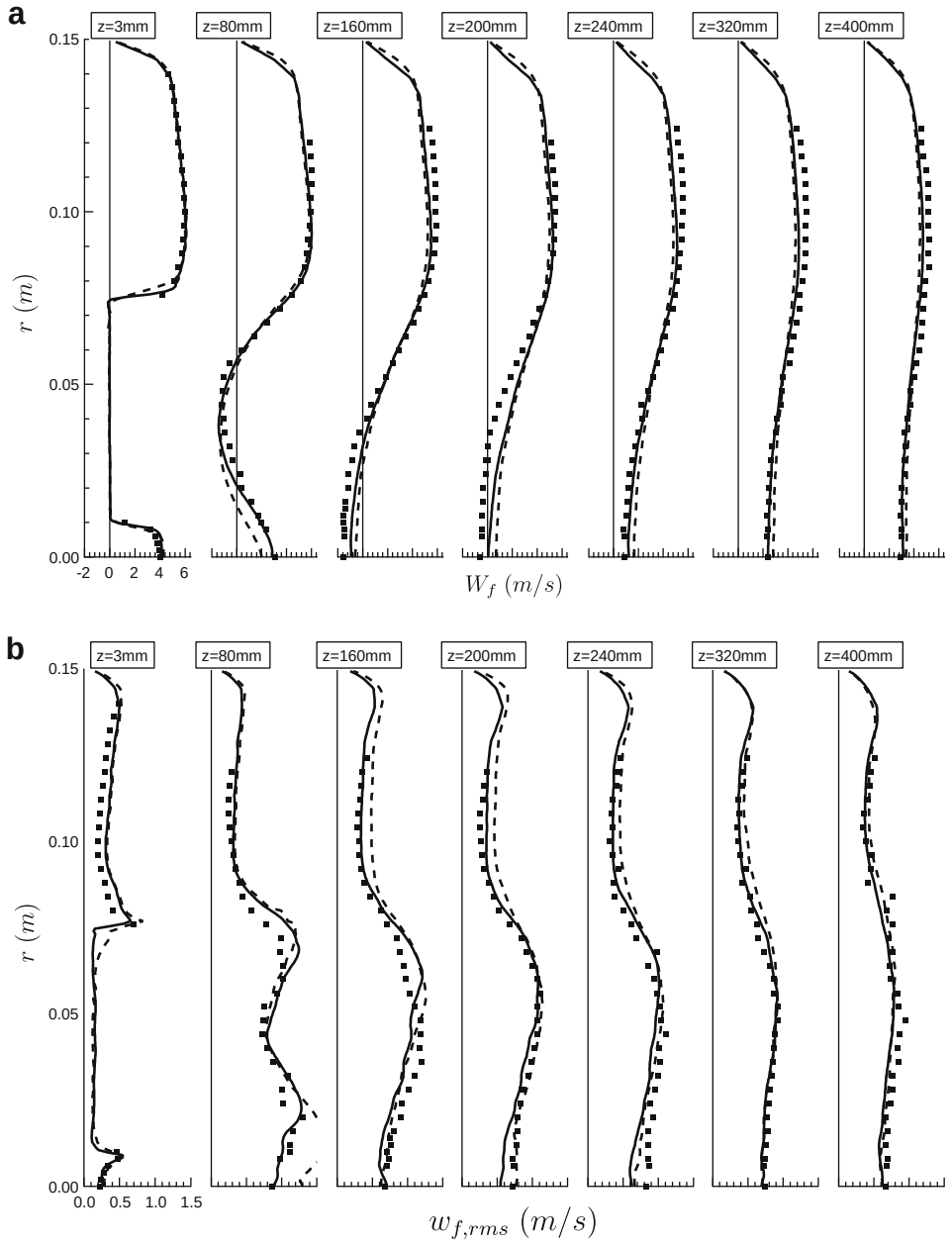

Fig. 13. Radial profiles of mean (a), and RMS (b), axial gas velocity. Symbols: experiment – dashed line: *gridtet* – solid line: *gridhex*. (Simulations performed with AVBP.)

Table 5
Code efficiency for single-phase flow calculations depending on the scheme and the grid. Statistics given for 0.1 s (physical time) computed with TTGC on 16 processors on a CRAY XD1 supercomputer.

Case	Total CPU time (μs)	Efficiency/iteration/node (μs)	Efficiency/iteration/cell (μs)
avbp_tet_lw_norfg	28,527	1.81	0.32
avbp_tet_ttgc_rfg	68,460	4.35	0.77
avbp_hex_ttgc_rfg	235,823	3.06	3.10

Table 6. As already mentioned, CDP solves the incompressible Navier–Stokes equations implicitly whereas AVBP solves the compressible Navier–Stokes equations explicitly. The main consequence is that the time step is 35 times larger for CDP, lead-

Table 6
Comparison of the parameters and models used for the single-phase flow LES performed with AVBP and CDP on the hexahedron-based grid *gridhex*.

Case	avbp_hex_ttgc_rfg	cdp_hex
Solver	AVBP	CDP
Time step (μs)/CFL	4.22/0.7	147/50
Averaging time (s)/iterations	1./192,000	2.65/18,000
Convective	TTGC (third order)	Second-order kinetic energy conserving
Scheme	[4]	[36]
SGS model/wall model	WALE/none	Dynamic Smagorinsky/none
Inner jet/coflow inlet BC	Forcing/forcing	Forcing/no forcing

ing to a reduced computational cost. As a result, the total averaging time is smaller for AVBP, but the convergence has been ensured to be good enough. Another noticeable difference is the treatment of the inlet boundary condition, as detailed in Section 4.3.

Fig. 14 displays mean and RMS gas axial velocities along the axis while Fig. 15 shows the radial profiles of mean and RMS gas axial velocities for the two codes along with the experimental measurements. The global agreement between the two codes and the experiments is very good and most of the flow physics is captured by the two LES codes. The width and the length of the recirculation zone are well predicted (see Fig. 15(a)). As shown in Fig. 14(a), the differences between both codes in predicting the location of the two stagnation points are minor. Focusing on the RMS velocities in Fig. 15(b), the agreement with measurements is also good. The location and the amplitude of the peaks are well predicted, except in the coflow where CDP underpredicts the RMS velocities. The origin of the discrepancy is the treatment of the coflow inlet boundary condition, with no turbulence injected with CDP in the outer duct.

The overall result is that both codes provide very similar results, also close to the measurements, even though they use different numerical methods. This indicates that the accuracy of both codes is good enough to test the dispersed phase with reasonable confidence on this configuration.

5. Comparison of two-phase flow simulations

This section presents the results for the 22% particle mass loading ratio of the central jet. Riber [33] showed that the impact of the dispersed phase on the gas phase is limited at this mass loading ratio: the central jet penetrates slightly further in the chamber, also slightly modifying the location of the recirculation zone. As the differences with the single-phase flow case are minor in the present case, the gas phase results are not discussed and only the results for the dispersed phase are provided hereafter. The validation of the particle dynamics modeling in this recirculating gas flow is done using three different solvers: CDP and AVBP-EL which both calculate the particle motion with the EL approach summarised in Section 3.2.1, and AVBP-EE that uses the simplified mesoscopic EE approach detailed in Section 3.2.2.

An essential part of these two-phase flow LES is the introduction of particles in terms of position and velocity in the central jet. This point is discussed in Section 5.1. Then, the three solvers are compared in two steps in Section 5.2. First, since the gas LES solvers from AVBP and CDP give very similar results on the hexahedron-based grid *gridhex*, the two Lagrangian solvers CDP and AVBP-EL are compared and validated by comparisons with the measurements. Second, the two approaches (EL and mesoscopic EE) are compared using the solvers AVBP-EL and AVBP-EE on *gridhex*. As the gas solver and the grid are exactly the same, a direct comparison of the two methods is proposed.

5.1. Particle injection and test cases

In all cases, the injected particles have a diameter of 60 μm, as justified in Section 2.3. The introduction of these particles in terms of position and velocity is one of the main difficulty in such a two-phase flow configuration. First, the methodology differs depending on the solver used. Second, the injection planes are different for all solvers, as shown in Fig. 16. Thus, the

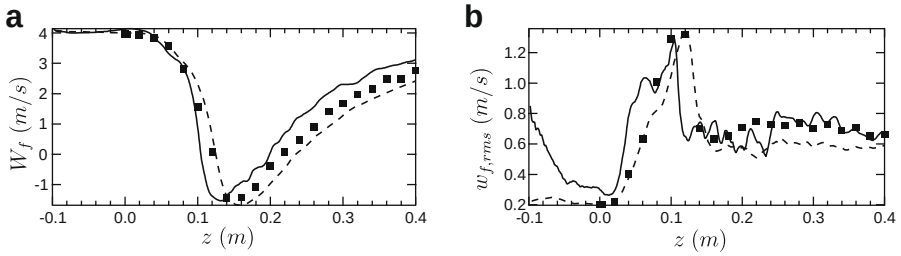

Fig. 14. Axial profiles of mean (a), and RMS (b), axial gas velocity. Symbols: experiment – solid line: AVBP – dashed line: CDP.

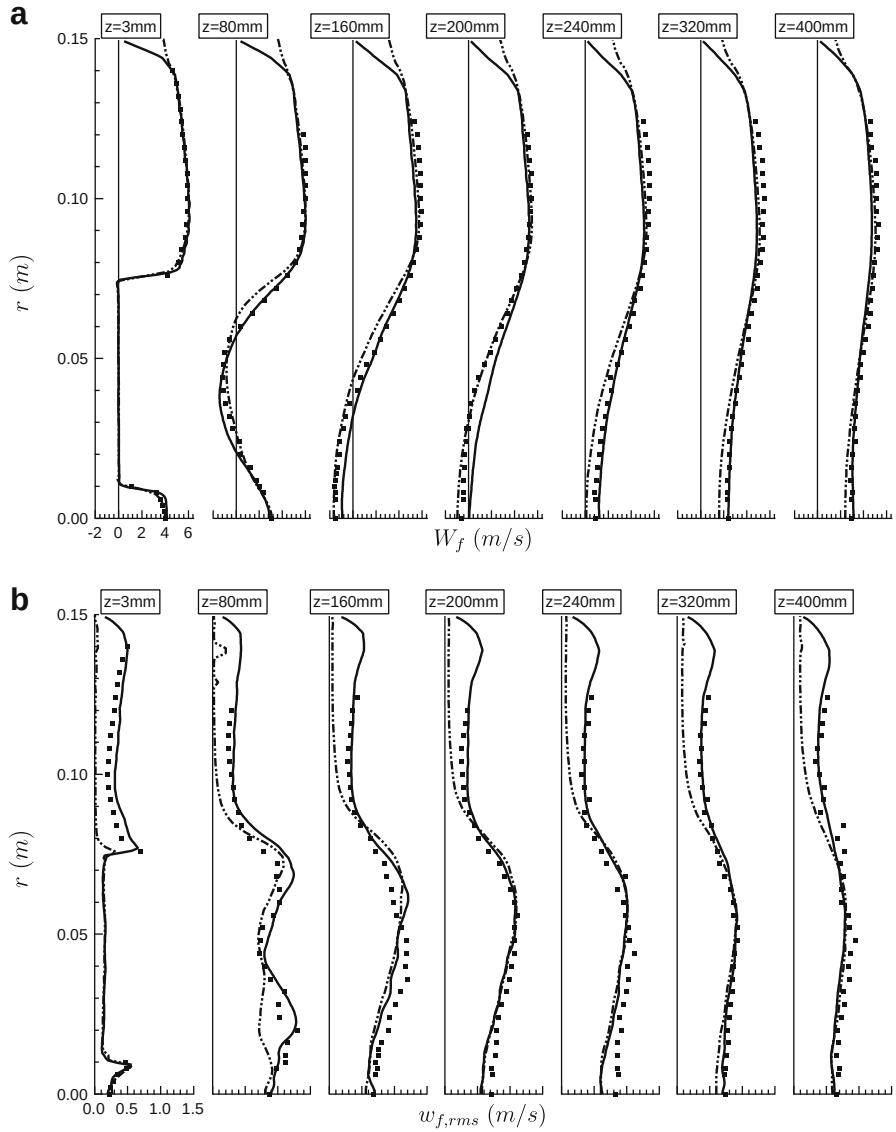

Fig. 15. Radial profiles of mean (a), and RMS (b), axial gas velocity. Symbols: experiment – solid line: AVBP – dot-dashed line: CDP.

impact of the particle injection method on the results can be evaluated. In AVBP-EE, both the particle number density profile and the mean velocity profile are imposed at the inner pipe inlet ($z = -100$ mm) and correspond to the ones measured experimentally at $z = 3$ mm. No turbulent fluctuations are introduced. In AVBP-EL and in CDP, the injection planes are located at $z = -3$ mm and $z = -95$ mm, respectively. The injection speed profile is also the experimental one measured at $z = 3$ mm but the mass loading is homogeneous over the injection section. Furthermore, in AVBP-EL and in CDP, a white noise (amplitude

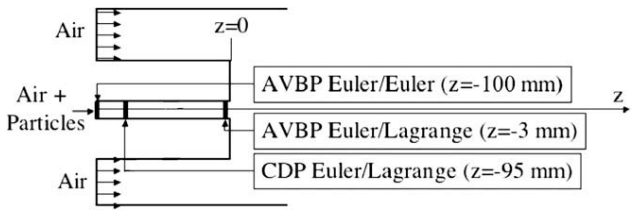

Fig. 16. Location of the particle injection depending on the two-phase flow solver used.

Table 7
Summary of two-phase flow test cases and parameters used for the particle injection.

	cdp_EL_hex	avbp_EL_hex	avbp_EE_hex
Averaging time (s)	4.0	0.5	1.0
Grid	*gridhex*	*gridhex*	*gridhex*
Particle mean axial velocity	Experimental profile	Experimental profile	Experimental profile
Turbulent fluctuations	White noise (10%)	White noise (12%)	Zero
Particle distribution	Homogeneous	Homogeneous	Experimental profile

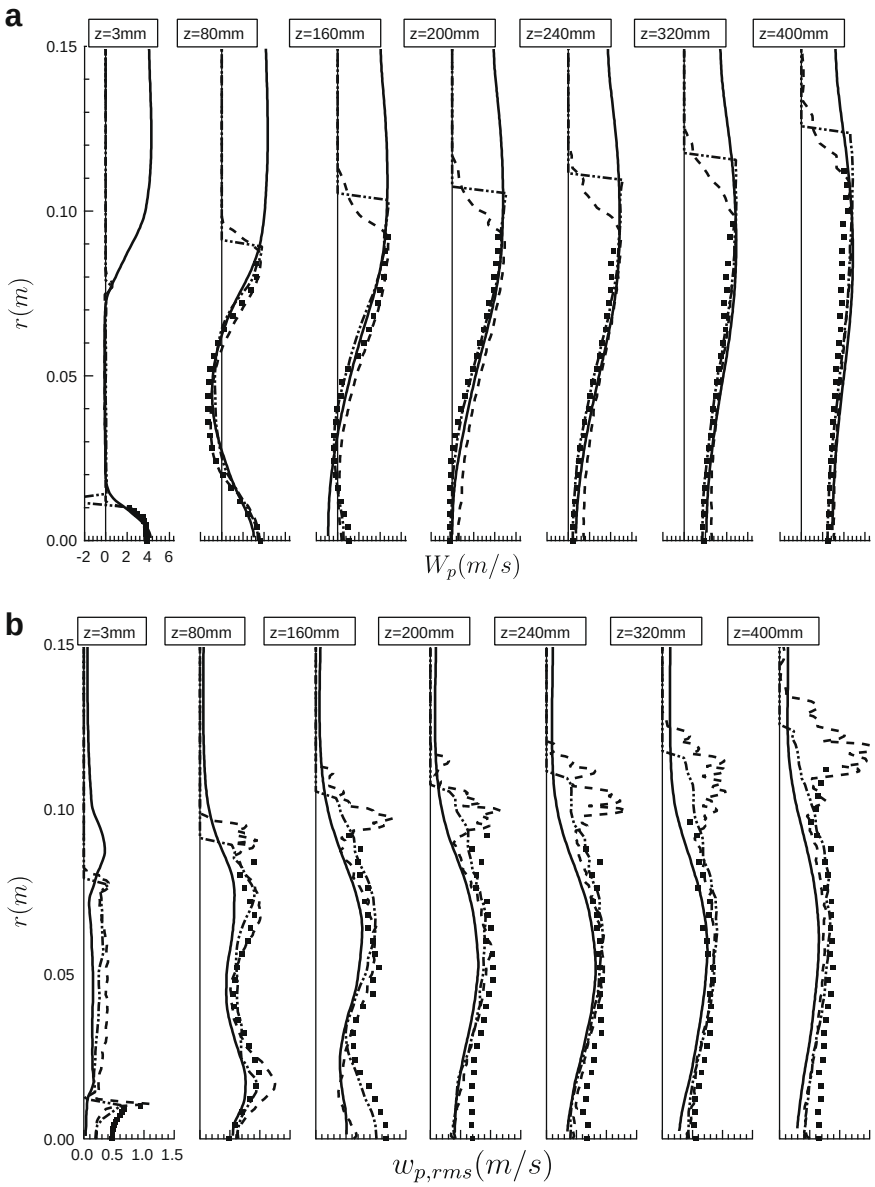

Fig. 17. Radial profiles of mean (a) and RMS (b) axial particle velocity. Symbols: experiment – solid line: AVBP-EE – dashed line: AVBP-EL – dot-dashed line: CDP-EL.

of the order of 10% of the mean velocity) is added to the particle mean velocity profiles to match experimental measurements at z = 3 mm.

These differences in particle injection are summarised in Table 7. Although they must be taken into account when comparing the three solvers AVBP-EL, AVBP-EE and CDP, the comparison of the Lagrangian solvers on the one hand, and the EL and mesoscopic EE approaches on the other hand is still relevant. The three LES performed with the three different solvers are also detailed in Table 7. The case *cdp_EL_hex* uses the same gaseous parameters as the case *cdp_hex* whereas the two cases *avbp_EL_hex* and *avbp_EE_hex* are based on the case *avbp_hex_ttgc_rfg* (see Table 6). Due to the implicit formulation of CDP, the total averaging time affordable with CDP is once again larger than with AVBP.

5.2. Results for two-phase flow simulations

Figs. 17 and 18 display the radial profiles of mean and RMS axial and radial particle velocities at the seven stations along the axis while Fig. 19 shows the axial profiles of mean and RMS axial particle velocities. The results of the three cases defined in Table 7 are directly compared with measurements. For the sake of simplicity, the analysis of the results is divided into two

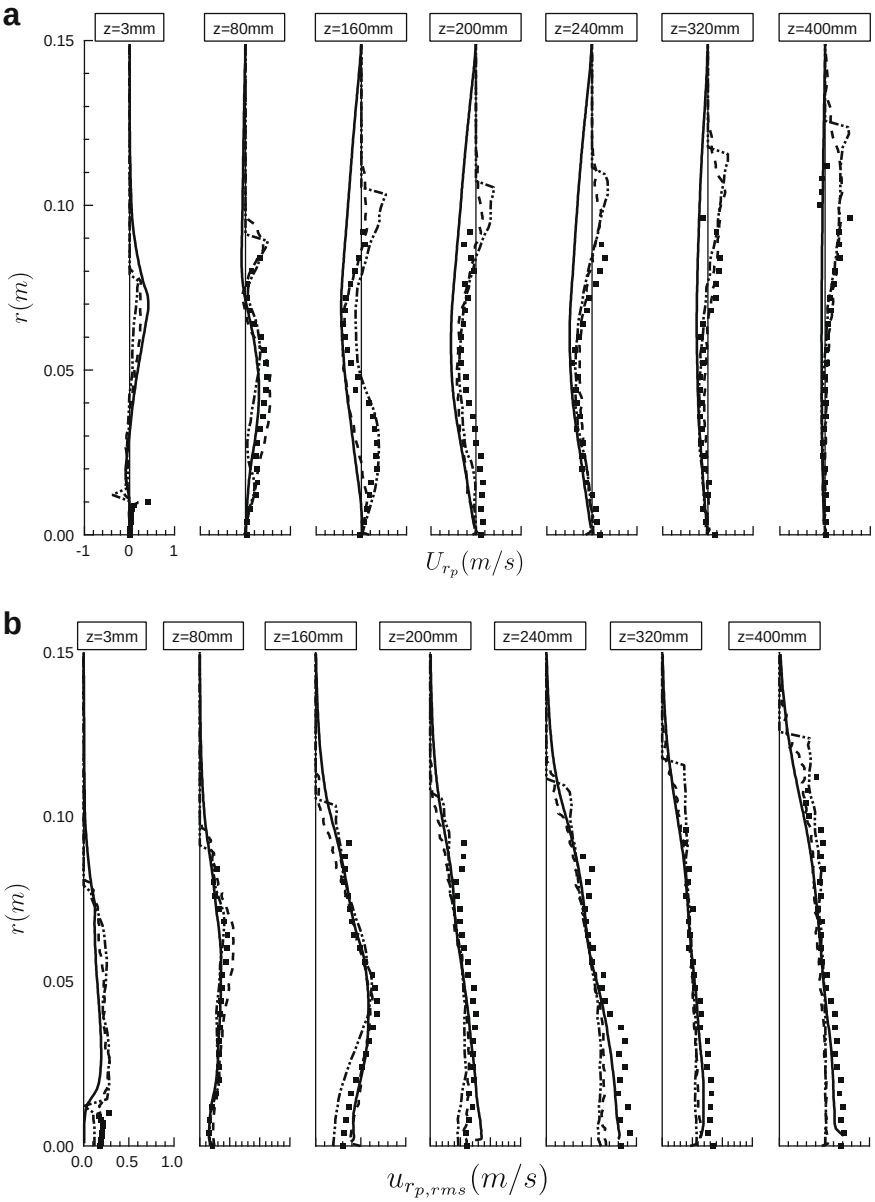

Fig. 18. Radial profiles of mean (a) and RMS (b) radial particle velocity. Symbols: experiment – solid line: AVBP-EE – dashed line: AVBP-EL – dot-dashed line: CDP-EL.

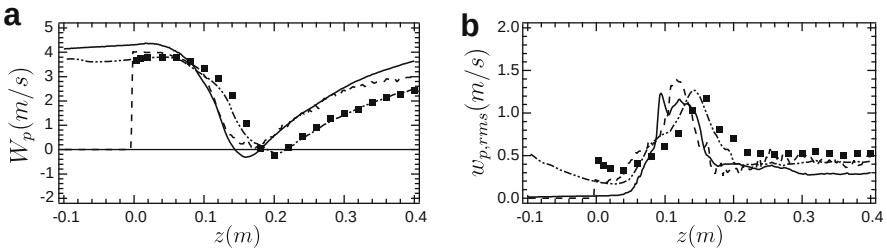

Fig. 19. Axial profiles of mean (a) and RMS (b) axial particle velocity. Symbols: experiment – solid line: AVBP-EE – dashed line: AVBP-EL – dot-dashed line: CDP-EL.

parts: first, the Lagrangian solvers are compared in Section 5.2.1. Second, the EL and mesoscopic EE approaches are directly compared in Section 5.2.2.

5.2.1. Comparison of the two EL solvers

Focusing on the results obtained with the two Lagrangian solvers, Figs. 17–19 show a very good agreement between the two codes, and with the measurements. Better results are generally obtained with CDP but not in all sections. A convenient way to look at the results is to consider the central axis of the configuration: a critical zone is located around z = 160 mm, the stagnation point for the gas phase. This is also a zone where particles accumulate and must stop before turning around to escape from the recirculating zone by the sides. As a consequence, this zone is difficult to predict accurately for the dispersed phase and the slight differences in calculating the turbulence in the inner pipe may induce such discrepancies on the dispersed phase.

5.2.2. Comparison of the EL and the EE approaches

In this section, the cases *avbp_EL_hex* and *avbp_EE_hex* are compared. As the two cases use the same grid and exactly the same gas solver, the EL approach and the mesoscopic EE approach can be directly compared.

First, a qualitative comparison is provided in Fig. 20 which displays instantaneous fields of particle number density for the two cases. Note that this quantity is directly available when using the mesoscopic EE approach but is reconstructed from the Lagrangian simulations using a volumic projection method. The two instantaneous fields of particle number density are similar: both approaches show several of particles along the inner jet and the largest one is located close to the second stagnation point. Most of the particles trapped in this region are then released in the gaseous recirculation zones. The two fields show however differences when focusing on the small structures which are more numerous using the EL approach.

Second, Figs. 17–19 show that the two approaches provide extremely similar results showing that the mesoscopic EE approach is able to compute such a flow and to provide results that are equivalent in precision to an EL computation. There are however at least two discrepancies. First, the mean particle axial velocity profiles at z = 160 mm show that the particles do not go far enough in the chamber with the mesoscopic EE approach. Nevertheless, this point has been shown to be very delicate to predict for the gas phase and very dependent on the inlet conditions in the pipe. In the present EE computation, no particle velocity fluctuations are imposed at the inlet of the inner pipe with the mesoscopic approach but this may not be crucial. The second main difference deals with the particle agitation that is under-estimated by the mesoscopic EE approach both on the radial and the axial profiles of particle RMS velocities. Actually, this is not surprising since the simplified mesoscopic EE model is used in this work: as the total particle agitation is divided into a correlated and an uncorrelated part, neglecting the RUM contribution in this bluff body flow prevents from predicting the experimental level of particle agitation. Nevertheless, the mean quantities are still well predicted with the mesoscopic EE model.

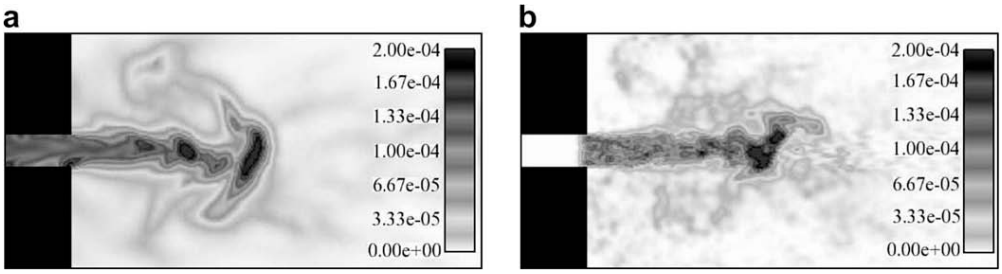

Fig. 20. Instantaneous particle volume fraction field in the central plane obtained with the cases *avbp_EE_hex* (a) and *avbp_EL_hex* (b).

5.2.3. Scalability of the EL approach

One interesting issue in the comparison between Eulerian and Lagrangian methods is the analysis of scalability and computational performance. The implementation on massively parallel machines of the Eulerian approaches is not technically problematic because the flow and the droplets are solved on the same grid using the same spatial discretization scheme. On the other hand, Lagrangian approaches are less well-suited to parallel computers since the two phases must be coupled, which increases the complexity of the implementation. Thus, before implementing a Lagrangian module into a new solver one of these two strategies should be adopted for the dispersed phase treatment:

(1) Task parallelization in which some processors compute the gaseous phase and others compute the droplets.
(2) Domain partitioning in which particles are computed together with the gas flow on geometrical subdomains mapped on parallel processors. Individual particles or parcels are tracked as they cross the computational domain and must be exchanged between processors when leaving a subdomain to enter an adjacent one.

Particle tracking within an unstructured solver reveals an additional constraint since particle coordinates cannot be easily used to locate them inside a cell, and time (and memory) consuming searching algorithm must be used. However, for LES it is easy to show that only the strategy based on domain partitioning is efficient on large grids because task parallelization would require the communication of very large three-dimensional data sets at each iteration between all processors. It is well known that codes based on domain partitioning are difficult to optimize on massively parallel architectures when droplets are clustered in one part of the domain (typically, near the fuel injectors) due to load imbalance. Moreover, the distribution of droplets may change during the computation: for a gas turbine reignition sequence, for example, the chamber is filled with droplets when the ignition begins thus ensuring an almost uniform droplet distribution; these droplets then evaporate rapidly during the computation, leaving droplets only in the near injector regions. This may lead to a poor speedup on a parallel machine if the domain is decomposed in the same way for the entire computation since some processors should compute a high number of particles while other are waiting for this task to finish. As a result, load balancing strategies are required to redecompose the domain by taking into account particles information to preserve a high parallel efficiency [14].

In this section, the scalability of the AVBP-EL solver is analysed using the simulation speedup and the reference single-phase CPU time ratio. The former is defined as the ratio between the CPU time of a simulation with n processors and the CPU time of a simulation with a given number of processors, N_{procs}:

$$\text{Speedup} = \frac{T_{\text{run}}(n)}{T_{\text{run}}(N_{\text{procs}})} * n. \tag{16}$$

The latter is defined as the ratio between the CPU time of a simulation with a given number of processors and the CPU time of the reference single-phase simulation with n processors:

$$\text{CPU time ratio} = \frac{T_{\text{run}}(N_{\text{procs}})}{T_{\text{single-phase}}(n)}. \tag{17}$$

Default value of n is 1 but sometimes it is not possible to run the sequential simulation mainly due to high memory requirements, in which case the speedup and CPU time ratio are reported to a reference parallel simulation. This scalability study has been performed in a CRAY XD1[2] supercomputer for a number of processors up to 64. Results of the moderate mass loading test case for the two grids named *gridtet* and *gridhex* are presented hereafter. The total number of particles presented in the domain is of the order of 560,000 and 430,000, respectively. Variations smaller than 0.5% in the number of particles were observed between the beginning and the end of the simulation, which implies that it is statistically stationary. The lower number of particles used in *gridhex* is due to the difference in the length between the two grids (see Table 3). Even if the length of the chamber is half the dimension of *gridtet*, the number of particles is three-fourths since they are mainly concentrated inside the recirculation zone.

Fig. 21 shows the speedup of the single-phase and the monodisperse test case with *gridtet* (Fig. 21(a)) and *gridhex* (Fig. 21(b)) using AVBP-EL. Scaling of *gridhex* is reported relative to the 8 processor case ($n = 8$), which was the smallest number of CRAY XD1 processors that could run this problem due to high memory requirements. In both cases, the good scalability of the single-phase is unquestionable. The drop of performances observed in Fig. 21(a) for the two-phase flow simulation is not related to large communications costs between processors but merely to the parallel load imbalance generated by the partitioning algorithm [15]. The same simulation with a different grid can lead to a completely different speedup graph, as it can be observed from Fig. 21(b). Note that these graphs do not contain information about the speedup with AVBP-EE. It can be considered as good as the single-phase computation since the dispersed phase uses the same parallelization applied to the gaseous phase.

The differences between the two speedup graphs can be explained by plotting the number of nodes (or cells) and particles presented in each processor. As AVBP is based on a *cell-vertex* formulation, comparing the number of nodes to the number of particles is more representative of the computational loading since almost all arrays are dimensioned as a function of the

[2] This machine has 58 nodes with 2 processors/node and 2 GB/processor.

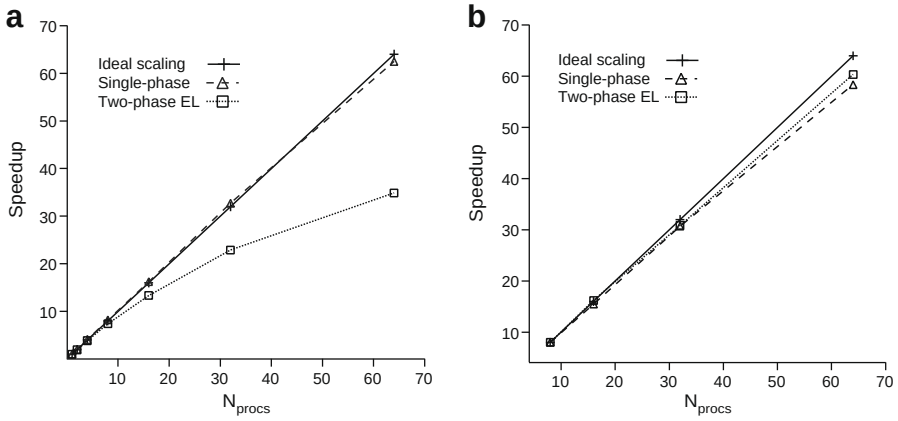

Fig. 21. Speedup of the single-phase and the monodisperse test case with *gridtet* (a) and *gridhex* (b) on a CRAY XD1 supercomputer. (Simulations performed with AVBP-EL.)

number of nodes per processor. Fig. 22 reports the number of nodes and particles per processor for a 32-partition simulation by using a recursive inertial bisection (RIB) [81] partitioning algorithm, with *gridtet* and *gridhex*, respectively. As expected from Fig. 21, Fig. 22 shows an excellent load balancing for the gaseous phase: all processors contain about the same number of nodes. On the contrary, it shows a strong particle load imbalance (Fig. 22(a)) where one single processor contains almost half the total number of particles of the simulation. This fact is related to the grid downstream coarsening which increases significantly the memory requirements and the floating-point operations for this processor. This points out the need of load

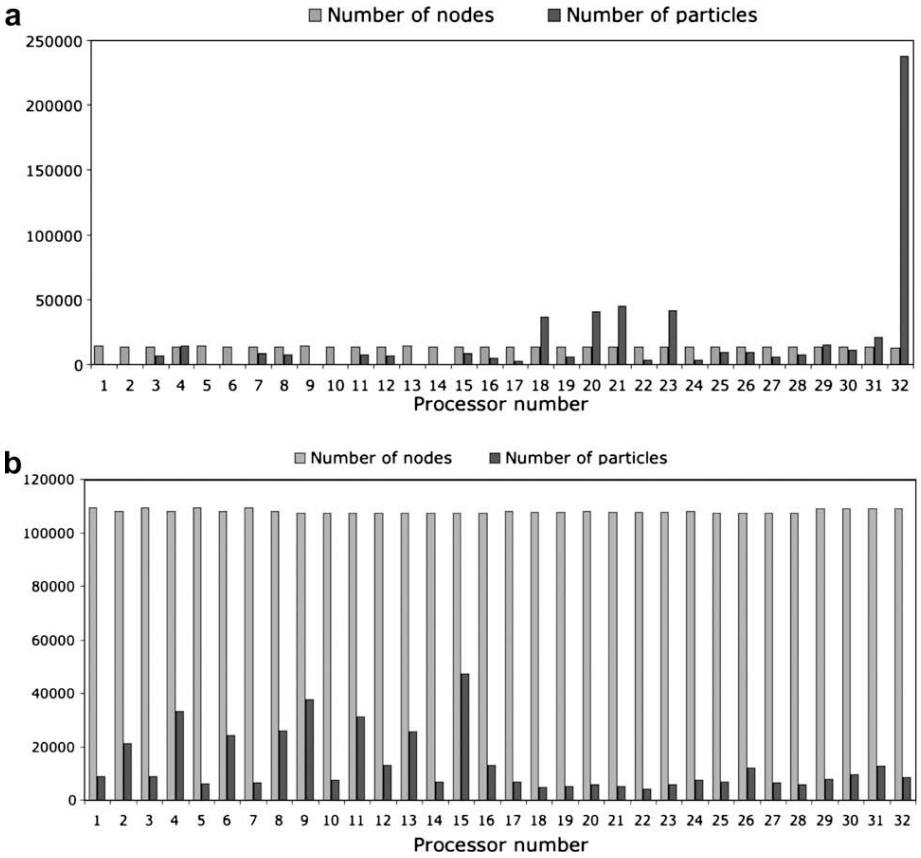

Fig. 22. Number of nodes and particles per processor for a 32-partition by using a recursive inertial bisection (RIB) partitioning algorithm for *gridtet* (a) and *gridhex* (b). (Simulations performed with AVBP-EL.)

Table 8
Summary of the CPU time ratios of AVBP-EL with *gridtet* on a CRAY XD1 supercomputer.

N_{procs}	1	2	4	8	16	32	64
Single-phase	1	0.50	0.25	0.12	0.06	0.030	0.016
Two-phase EL	1.05	0.54	0.27	0.14	0.08	0.046	0.030

Table 9
Summary of the CPU time ratios of AVBP-EL with *gridhex* on a CRAY XD1 supercomputer.

N_{procs}	8	16	32	64
Single-phase	1	0.51	0.26	0.137
Two-phase EL	1.06	0.524	0.275	0.14

balancing strategies for two-phase flow simulations with a Lagrangian approach, for example, by using multi-constraint partitioning algorithms which take into account particle loading on each processor [14]. Even if the dispersed phase presents a small load imbalance in Fig. 22(b), it is hidden by the higher computational loading needed to calculate the gaseous phase. This is the main reason of the good speedup observed in Fig. 21(b).

Tables 8 and 9 summarised the CPU time ratios of AVBP-EL with both grids on a CRAY XD1 supercomputer. Additional time to perform the two-phase flow simulation can vary from 5% up to 87% with the Lagrangian formulation in *gridtet* but it is not higher than 5% with *gridhex* which confirms the tendencies observed with the speedup graphs. All simulations with AVBP-EE has a constant added cost of the order of 80% since this approach is independent of the mass loading. Therefore, at this moderate mass loading the Lagrangian approach proved to be faster than the Eulerian formulation.

5.3. Discussion

The previous results require additional comments:

- The quality of the gas phase prediction is essential for the dispersed phase results.
- The comparison of different solvers and boundary conditions demonstrates the importance of the flow in the central injection pipe: the mean and RMS gas velocity profiles as well as the particle motion directly change the flow field significantly. For example, the location of the stagnation points (see Fig. 14) is extremely sensitive to any change in the inlet pipe boundary conditions. This is a major drawback of this configuration because performing an accurate LES of the two-phase flow within this pipe is still out of reach of present capacities for at least two reasons. First, the gaseous flow within the pipe is difficult to resolve and would require a very fine mesh and sophisticated wall models. Second, the two-phase flow in the pipe is heavily loaded so that computing the motion of the particles within the pipe would require additional models for particle–particle and wall–particle interactions [35]. For the present results, the boundary conditions for the dispersed phase at the tube inlet are approximate solutions and the variety of methods tested for the LES of Table 7 demonstrates that no easy solution was found to model particles injection in the central tube.

Despite these limitations and differences in inlet conditions, results confirm that most of the flow structures are correctly captured and that LES of two-phase flows (using EL or mesoscopic EE approaches) is possible and provides accurate results. To improve on these results, a significant effort will have to be applied to describe the two-phase flow within the injection tube. Note that in a real combustion chamber, the region where such heavily loaded flows are found is very small and limited to the vicinity of the fuel injector.

6. Conclusions

This work has presented a comparison between multiple LES approaches and codes for non-reacting two-phase flows and the experimental results of Borée et al. [1]. This experiment was chosen because it contains multiple complex flow features which are typical of combustion chambers: strong recirculating zones created by a dump geometry, multiple stagnation points, high turbulent Reynolds number. LES and experiments have been compared in terms of radial profiles of mean and RMS axial and radial velocities at seven stations along the axis, and axial profiles of mean and RMS axial velocities on the experiment central axis. LES approaches included both Euler/Euler and Euler/Lagrange models. Two codes (incompressible implicit and compressible explicit) were used to evaluate the effects of the gas solver on the results so that three two-phase flow solvers were used:

- an Euler/Euler explicit compressible solver;
- an Euler/Lagrange explicit compressible solver;
- an Euler/Lagrange implicit incompressible solver.

All computations were performed for monodisperse particle distributions with diameter d_p = 60 μm which corresponds to the initial mean experimental diameter in mass. The effects of subgrid-scale model, numerical scheme accuracy and of grid refinement were also investigated. The main conclusions are the following:

- All LES approaches provide high-quality results compared to the PDA data of the configuration of Borée et al. [1], thereby confirming the potential of these methods and their relative insensitivity to the details of the numerical solver. The variations between LES solvers are mainly due to changes in boundary conditions.
- The quality of the gas flow predictions is critical in order to accurately compute the dispersed phase.
- The most critical parameter controlling accuracy is the grid and the convective scheme: using high-order schemes built for LES provides the best results.
- The most critical zone in the flow is the central injection tube which feeds the experiment with a highly loaded air/particles jet. True two-phase LES is impossible in this duct today. Results show that this element controls the flow, especially the positions of stagnation points on the experiment axis. Even though the quality of the present LES results is high in most of the flow, this work confirms that future LES accuracy in combustion chambers will need to include all feeding ducts which represents a significant challenge.
- Both Euler/Lagrange codes provide very similar results while the Euler/Euler approach gives similar mean velocity fields but slightly under-estimates fields of particle agitation. This corresponds to the expected behavior of the present mesoscopic model in which the uncorrelated motion was not taken into account [32,33].
- For the present case with moderate mass loading, the total number of particles per processor is moderate. The CPU and memory requirements to track particles is lower than for the gaseous phase even with the load balancing problem observed with one of the grids studied. Although the additional cost of Eulerian formulations is independent of the mass loading, for such a dilute case, the Lagrangian approach proved to be faster up to 64 processors.

These results confirm the potential of LES approaches for two-phase flows. Nevertheless, there is still much work to be done concerning:

- the effects of the subgrid fluid turbulence on the particle velocity [53];
- the RUM modeling in order to estimate the particle agitation more precisely with the mesoscopic EE approach;
- the wall–particle interactions as well as the particle–particle interactions to simulate the dispersed phase accurately in pipe and channel flows;
- the extension to two-phase reacting flows which has already been initiated [20].

Acknowledgments

Part of this work was performed during the 2006 CTR Summer Program at Stanford and the support of Pr Pitsch and Moin is gratefully acknowledged. Most simulations were performed on the national computing center CINES in Montpellier and on CTR supercomputers.

References

[1] J. Borée, T. Ishima, I. Flour, The effect of mass loading and inter-particle collisions on the development of the polydispersed two-phase flow downstream of a confined bluff body, J. Fluid Mech. 443 (2001) 129–165.
[2] D. Caraeni, C. Bergstrom, L. Fuchs, Modeling of liquid fuel injection, evaporation and mixing in a gas turbine burner using large Eddy simulation, Flow Turbul. Combust. 65 (2000) 223–244.
[3] V. Chakravarthy, S. Menon, Subgrid modeling of turbulent premixed flames in the flamelet regime, Flow Turbul. Combust. 65 (2000) 133–161.
[4] O. Colin, F. Ducros, D. Veynante, T. Poinsot, A thickened flame model for large Eddy simulations of turbulent premixed combustion, Phys. Fluids 12 (7) (2000) 1843–1863.
[5] H. Forkel, J. Janicka, Large Eddy simulation of a turbulent hydrogen diffusion flame, Flow Turbul. Combust. 65 (2) (2000) 163–175.
[6] H. Pitsch, L. Duchamp de la Geneste, Large Eddy simulation of premixed turbulent combustion using a level-set approach, Proc. Combust. Inst. 29 (2002) 2001–2005.
[7] K. Mahesh, G. Constantinescu, P. Moin, A numerical method for large Eddy simulation in complex geometries, J. Comput. Phys. 197 (1) (2004) 215–240.
[8] L. Selle, G. Lartigue, T. Poinsot, R. Koch, K.-U. Schildmacher, W. Krebs, B. Prade, P. Kaufmann, D. Veynante, Compressible large Eddy simulation of turbulent combustion in complex geometry on unstructured meshes, Combust. Flame 137 (4) (2004) 489–505.
[9] V. Moureau, G. Lartigue, Y. Sommerer, C. Angelberger, O. Colin, T. Poinsot, High-order methods for DNS and LES of compressible multi-component reacting flows on fixed and moving grids, J. Comput. Phys. 202 (2) (2005) 710–736.
[10] S. Roux, G. Lartigue, T. Poinsot, U. Meier, C. Bérat, Studies of mean and unsteady flow in a swirled combustor using experiments, acoustic analysis and large Eddy simulations, Combust. Flame 141 (2005) 40–54.
[11] T. Poinsot, D. Veynante, Theoretical and Numerical Combustion, second ed., R.T. Edwards, 2005.
[12] P. Schmitt, T. Poinsot, B. Schuermans, K. Geigle, Large Eddy simulation and experimental study of heat transfer, nitric oxide emissions and combustion instability in a swirled turbulent high pressure burner, J. Fluid Mech. 570 (2007) 17–46.
[13] G. Staffelbach, L. Gicquel, T. Poinsot, Highly parallel large Eddy simulations of multiburner configurations in industrial gas turbines, Lect. Notes Comput. Sci. Eng. – Complex Effects LES 56 (2006) 326–336.
[14] F. Ham, S. Apte, G. Iaccarino, X. Wu, M. Herrmann, G. Constantinescu, K. Mahesh, P. Moin, Unstructured LES of reacting multiphase flows in realistic gas turbine combustors, in: Annual Research Briefs, Center for Turbulence Research, NASA Ames/Stanford Univ., 2003, pp. 139–160.
[15] M. García, Y. Sommerer, T. Schönfeld, T. Poinsot, Evaluation of Euler–Euler and Euler–Lagrange strategies for large-Eddy simulations of turbulent reacting flows, in: ECCOMAS Thematic Conference on Computational Combustion, Lisbon, Portugal, 2005.

[16] L. Chin, R. Tankin, Vortical structures from a two-dimensional nozzle with a bluff body slot, Phys. Fluids A 4 (8) (1992) 1724–1736.
[17] R. Schefer, M. Namazian, J. Kelly, Velocity measurements in turbulent bluff body stabilized flows, AIAA J. 32 (9) (1994) 1844–1851.
[18] M. Namazian, J. Kelly, R. Schefer, Concentration imaging measurements in turbulent concentric-jet flows, AIAA J. 30 (1992) 384–394.
[19] Y. Hardalupas, C. Liu, J. Whitelaw, Experiments with disk stabilised kerosene-fuelled flames, Combust. Sci. Technol. 97 (1994) 157–191.
[20] M. Boileau, S. Pascaud, E. Riber, B. Cuenot, L. Gicquel, T. Poinsot, Large Eddy simulation of spray combustion in gas turbines, Flow Turbul. Combust. 80 (2008) 351–373.
[21] Q. Wang, K. Squires, Large Eddy simulation of particle-laden turbulent channel flow, Phys. Fluids 8 (5) (1996) 1207–1223.
[22] M. Vance, K. Squires, O. Simonin, Properties of the particle velocity field in gas–solid turbulent channel flow, Phys. Fluids 18 (2006). 063302.
[23] M. Picciotto, C. Marchioli, A. Soldati, Characterization of near-wall accumulation regions for inertial particles in turbulent boundary layers, Phys. Fluids 17 (2005). 098101.
[24] C. Marchioli, M. Picciotto, A. Soldati, Particle dispersion and wall-dependent fluid scales in turbulent bounded flow: implications for local equilibrium models, J. Turbul. 7 (60) (2006) 1–12.
[25] M. Sakiz, O. Simonin, Development and validation of continuum particle wall boundary conditions using Lagrangian simulation of a vertical gas–solid channel flow, in: Proceedings of the Eighth International Symposium on Gas-Particle Flows, ASME Fluids Engineering Division Summer Meeting, vol. FEDSM99-7898, 1999.
[26] V. Alipchenkov, L. Zaichik, O. Simonin, A comparison of two approaches to derivation of boundary conditions for continuous equations of particle motion in turbulent flow, High Temperature, Translated from Teplofizika Vysokikh Temperatur 39 (2001) 108–114.
[27] O. Simonin, J. He, Eulerian prediction of the particle behaviour in a turbulent boundary layer, in: M. Sommerfeld (Ed.), Proceedings of the Sixth Workshop on Two-Phase Flow Predictions, Erlangen 1992, Bilateral Seminars of the International Bureau/Forschungszentrum Juelich GmbH, vol. 14, Erlangen, Germany, 1993, pp. 154–165.
[28] G. Desoutter, B. Cuenot, C. Habchi, T. Poinsot, Interaction of a premixed flame with a liquid fuel film on a wall, Proc. Combust. Inst. 30 (2005) 259–266.
[29] W. Bachalo, M. Houser, Phase/doppler spray analyser for simultaneous measurements of drop size and velocity distributions, Opt. Eng. 23 (1984) 583–590.
[30] R.W. Schefer, M. Namazian, J. Kelly, Stabilization of lifted turbulent-jet flames, Combust. Flame 99 (1994) 75–86.
[31] A. Kaufmann, O. Simonin, B. Cuenot, T. Poinsot, J. Hélie, Dynamics and dispersion in 3D unsteady simulations of two phase flows, in: Supercomputing in Nuclear Applications, CEA, Paris, 2003.
[32] P. Février, O. Simonin, K. Squires, Partitioning of particle velocities in gas–solid turbulent flows into a continuous field and a spatially uncorrelated random distribution: theoretical formalism and numerical study, J. Fluid Mech. 533 (2005) 1–46.
[33] E. Riber, Développement de la méthode de simulation aux grandes échelles pour les écoulements diphasiques turbulents, Ph.D. Thesis, INP Toulouse, 2007.
[34] R. Fan, D.L. Marchisio, R.O. Fox, Application of the direct quadrature method of moments to polydisperse gas–solid fluidized beds, Powder Technol. 139 (7) (2004).
[35] N. Caraman, J. Borée, O. Simonin, Effect of collisions on the dispersed phase fluctuation in a dilute tube flow: experimental and theoretical analysis, Phys. Fluids 15 (12) (2003) 3602–3612.
[36] F. Ham, G. Iaccarino, Energy conservation in collocated discretization schemes on unstructured meshes, in: Annual Research Briefs, Center for Turbulence Research, NASA Ames/Stanford Univ., 2004, pp. 3–14.
[37] O. Colin, M. Rudgyard, Development of high-order Taylor–Galerkin schemes for unsteady calculations, J. Comput. Phys. 162 (2) (2000) 338–371.
[38] F. Nicoud, F. Ducros, Subgrid-scale stress modelling based on the square of the velocity gradient, Flow Turbul. Combust. 62 (3) (1999) 183–200.
[39] J. Kim, P. Moin, Application of a fractional-step method to incompressible Navier–Stokes equations, J. Comput. Phys. 59 (2) (1985) 308–323.
[40] M. Germano, U. Piomelli, P. Moin, W. Cabot, A dynamic subgrid-scale Eddy viscosity model, Phys. Fluids 3 (7) (1991) 1760–1765.
[41] M. Maxey, The gravitational settling of aerosol particles in homogeneous turbulence and random flow fields, J. Fluid Mech. 174 (1987) 441–465.
[42] R. Gatignol, The Faxén formulae for a rigid particle in an unsteady non-uniform Stokes flow, J. Méc. Théor. Appl. 1 (2) (1983) 143–160.
[43] M. Boivin, O. Simonin, K. Squires, Direct numerical simulation of turbulence modulation by particles in isotropic turbulence, J. Fluid Mech. 375 (1998) 235–263.
[44] O. Vermorel, B. Bédat, O. Simonin, T. Poinsot, Numerical study and modelling of turbulence modulation in a particle laden slab flow, J. Turbul. 4 (2003) 025.
[45] S. Elghobashi, G. Truesdell, On the two-way interaction between homogeneous turbulence and dispersed solid particles, Phys. Fluids 5 (7) (1993) 1790–1801.
[46] K. Squires, J. Eaton, Particle response and turbulence modification in isotropic turbulence, Phys. Fluids 2 (7) (1990) 1191–1203.
[47] R. Miller, J. Bellan, Direct numerical simulation and subgrid analysis of a transitional droplet laden mixing layer, Phys. Fluids 12 (3) (1999) 650–671.
[48] M. Boivin, O. Simonin, K. Squires, On the prediction of gas–solid flows with two-way coupling using large Eddy simulation, Phys. Fluids 12 (8) (2000) 2080–2090.
[49] L. Schiller, A. Nauman, A drag coefficient correlation, VDI Zeitung 77 (1935) 318–320.
[50] M. Maxey, J. Riley, Equation of motion for a small rigid sphere in a nonuniform flow, Phys. Fluids 26 (4) (1983) 883–889.
[51] Y. Yamamoto, M. Potthoff, T. Tanaka, T. Kajishima, Y. Tsuji, Large-Eddy simulation of turbulent gas-particle flow in a vertical channel: effect of considering inter-particle collisions, J. Fluid Mech. 442 (2001) 303–334.
[52] S. Apte, K. Mahesh, T. Lundgren, A Eulerian–Lagrangian model to simulate two-phase particulate flows, in: Annual Research Briefs, Center for Turbulence Research, NASA Ames/Stanford Univ., 2003, pp. 161–167.
[53] P. Fede, O. Simonin, Numerical study of the subgrid fluid turbulence effects on the statistics of heavy colliding particles, Phys. Fluids 18 (2006) 045103.
[54] O. Druzhinin, S. Elghobashi, On the decay rate of isotropic turbulence laden with microparticles, Phys. Fluids 11 (3) (1999) 602–610.
[55] J. Ferry, E. Balachandar, A fast Eulerian method for disperse two-phase flow, Int. J. Multiphase Flow 27 (2001) 1199–1226.
[56] O. Druzhinin, On the two-way interaction in two-dimensional particle-laden flows – the accumulation of particles and flow modification, J. Fluid Mech. 297 (1995) 49–76.
[57] S. Rani, E. Balachandar, Evaluation of the equilibrium Eulerian approach for the evolution of particle concentration in isotropic turbulence, Int. J. Multiphase Flow 29 (2003) 1793–1816.
[58] S. Rani, E. Balachandar, Preferential concentration of particles in isotropic turbulence: a comparison of the Lagrangian and the equilibrium Eulerian approaches, Int. J. Multiphase Flow 141 (1–2) (2004) 109–118.
[59] S. Chapman, T. Cowling, The Mathematical Theory of Non-Uniform Gases, Cambridge Mathematical Library ed., Cambridge University Press, 1939.
[60] O. Simonin, Gas particules, Cours d'options, École Nationale Superieure d'Electrotechnique, d'Electronique, d'Informatique, d'Hydraulique et des Télécommunications, 2002.
[61] P. Février, O. Simonin, Statistical and continuum modelling of turbulent reactive particulate flows. Part 2: Application of a two-phase second-moment transport model for prediction of turbulent gas-particle flows, in: Theoretical and Experimental Modeling of Particulate Flows, Lecture Series 2000–2006, von Karman Institute for Fluid Dynamics, Rhode Saint Genese, Belgium, 2000.
[62] M. Moreau, B. Bédat, O. Simonin, A priori testing of subgrid stress models for Euler–Euler two-phase LES from Euler–Lagrange simulations of gas-particle turbulent flow, in: 18th Annual Conference on Liquid Atomization and Spray Systems, ILASS Americas, 2005.
[63] A. Favre, Statistical equations of turbulent gases, in: Problems of Hydrodynamics and Continuum Mechanics, SIAM, Philadelphia, 1969, pp. 231–266.
[64] O. Simonin, P. Février, J. Laviéville, On the spatial distribution of heavy-particle velocities in turbulent flow: from continuous field to particulate chaos, J. Turbul. 3 (2002) 040.

[65] E. Riber, M. Moreau, O. Simonin, B. Cuenot, Towards large Eddy simulation of non-homogeneous particle laden turbulent gas flows using Euler–Euler approach, in: 11th Workshop on Two-Phase Flow Predictions, Merseburg, Germany, 2005.
[66] P. Moin, K. Squires, W. Cabot, S. Lee, A dynamic subgrid-scale model for compressible turbulence and scalar transport, Phys. Fluids A 3 (11) (1991) 2746–2757.
[67] B. Vreman, B. Geurts, H. Kuerten, Subgrid modeling in LES of compressible flow, Appl. Sci. Res. 54 (1995) 191–203.
[68] A. Yoshizawa, Statistical theory for compressible turbulent shear flows, with the application to subgrid modeling, Phys. Fluids 29 (7) (1986) 2152–2164.
[69] E. Riber, M. García, V. Moureau, H. Pitsch, O. Simonin, T. Poinsot, Evaluation of numerical strategies for LES of two-phase reacting flows, in: Proceedings of the Summer Program, Center for Turbulence Research, NASA Ames/Stanford Univ., 2006, pp. 197–211.
[70] A. Kaufmann, M. Moreau, O. Simonin, J. Hélie, Comparison between Lagrangian and mesoscopic Eulerian modelling approaches for inertial particles suspended in decaying isotropic turbulence, J. Comput. Phys. 227 (13) (2008) 6448–6472.
[71] K. Hishida, K. Takemoto, M. Maeda, Turbulent characteristics of gas–solids two-phase confined jet, Jpn. J. Multiphase Flow 1 (1) (1987) 56–69.
[72] T. Poinsot, S. Lele, Boundary conditions for direct simulation of compressible viscous flows, J. Comput. Phys. 101 (1992) 104–129.
[73] I. Celik, A. Smirnov, J. Smith, Appropriate initial and boundary conditions for LES of a ship wake, in: Proceedings of the Third ASME/JSME Joint Fluids Engineering Conference, San Francisco, California, USA, vol. FEDSM99-7851, 1999.
[74] A. Smirnov, S. Shi, I. Celik, Random flow generation technique for large Eddy simulations and particle-dynamics modeling, Trans. ASME J. Fluids Eng. 123 (2001) 359–371.
[75] A. Sengissen, T. Poinsot, J. VanKampen, J. Kok, Response of a swirled non-premixed burner to fuel flow rate modulation, Lect. Notes Comput. Sci. Eng. – Complex Effects LES 56 (2006) 337–351.
[76] B. Vreman, Direct and large Eddy simulation of the compressible turbulent mixing layer, Ph.D. Thesis, University of Twente, 1995.
[77] J. Jiménez, P. Moin, The minimal flow unit in near-wall turbulence, J. Fluid Mech. 225 (1991) 213–240.
[78] Y. Dubief, F. Delcayre, On coherent-vortex identification in turbulence, J. Turbul. 1 (2000) 1–22.
[79] J. Hunt, A. Wray, P. Moin, Eddies, stream, and convergence zones in turbulent flows, in: Proceedings of the Summer Program, Center for Turbulence Research, NASA Ames/Stanford Univ., 1988, pp. 193–208.
[80] F. Hussain, J. Jeong, On the identification of a vortex, J. Fluid Mech. 285 (1995) 69–94.
[81] R.D. Williams, Performance of dynamic load balancing algorithms for unstructured mesh calculations, Concurr.: Pract. Exp. 3 (5) (1991) 451–481.

INSTITUT NATIONAL POLYTECHNIQUE DE TOULOUSE

Doctorat d'Université, spécialité *Dynamique des Fluides*

19 Janvier 2009

Marta GARCÍA

Développement et validation du formalisme Euler-Lagrange dans un solveur parallèle et non-structuré pour la simulation aux grandes échelles

De nombreuses applications industrielles mettent en jeu des écoulements gaz-particules, comme les turbines aéronautiques et les réacteurs à lit fluidifié de l'industrie chimique. La prédiction des propriétés de la phase dispersée, est essentielle à l'amélioration et la conception des dispositifs conformément aux nouvelles normes européennes des émissions polluantes. L'objectif de cette thèse est de développer le formalisme Euler-Lagrange dans un solveur parallèle et non-structuré pour la simulation aux grandes échelles pour ce type d'écoulements. Ce travail est motivé par l'augmentation rapide de la puissance de calcul des machines massivement parallèles qui ouvre une nouvelle voie pour des simulations qui étaient prohibitives il y a une décennie. Une attention particulière a été portée aux structures de données afin de conserver une certaine simplicité et la portabilité du code sur des differentes architectures. Les développements sont validés pour deux configurations : un cas académique de turbulence homogène isotrope décroissante et un calcul polydisperse d'un jet turbulent recirculant chargé en particules. L'équilibrage de charges de particules est mis en évidence comme une solution prometteuse pour les simulations diphasiques Lagrangiennes afin d'améliorer les performances des calculs lorsque le deséquilibrage est trop important.

Mots clés : Formalisme Euler-Lagrange, maillages non-structurés, simulation aux grandes échelles, écoulements diphasiques, équilibrage de charges, calcul parallèle.

Development and validation of the Euler-Lagrange formulation on a parallel and unstructured solver for large-eddy simulation

Particle-laden flows occur in industrial applications ranging from droplets in gas turbines to fluidized bed in chemical industry. Prediction of the dispersed phase properties such as concentration and dynamics are crucial for the design of more efficient devices that meet the new pollutant regulations of the European community. The objective of this thesis is to develop an Euler-Lagrange formulation on a parallel and unstructured solver for large-eddy simulation. This work is motivated by the rapid increase in computing power which opens a new way for simulations that were prohibitive one decade ago. Special attention is taken to keep data structure simplicity and code portability. Developments are validated in two configurations: an academic test of a decaying homogeneous isotropic turbulence and a polydisperse two-phase flow of a confined bluff body. The use of load-balancing capabilities is highlighted as a promising solution in Lagrangian two-phase flow simulations to improve performance when strong imbalance of the dispersed phase is present.

Keywords: Euler-Lagrange formulation, unstructured grids, large-eddy simulation, two-phase flows, particle load-balancing, parallel computations.

Centre **E**uropéen de **R**echerche et de **F**ormation **A**vancée en **C**alcul **S**cientifique (CERFACS)
42, avenue Gaspard Coriolis
31057 Toulouse Cedex 1 - France -